The Development of Continuous Microfluidic Immobilised Enzyme Reactor (μ-IMER) Systems and their Applications in Heterogeneous Biocatalysis

-

Kalum Thurgood-Parkes

-

Doctor of Philosophy

-

University of York

Physics, Engineering and Technology

-

March 2024

i. Abstract

Enzymes and artificial metalloenzymes (ArMs) have been demonstrated in both research and industrial settings to be highly effective tools for achieving complex chemical transformations, such as enantioselectivity chemical synthesis, that would otherwise be highly inefficient or unobtainable via classical synthetic chemistry. Nevertheless, significant optimisation is required to develop these enzyme-catalysed reactions. Traditional approaches based on batch screening remain a highly labour-intensive, costly and time-consuming process. Using microfluidic immobilised enzyme reactors could address these limitations by enabling high throughput screening of the parameter space whilst reducing optimisation costs and time, with significantly lower volumes of precious chemical feedstocks and biocatalysts. However, little work within the literature compares different types of reactors for biocatalyst screening applications. This work focuses on developing packed-bed microcolumn and planar surface microfluidic chip reactor systems to compare and evaluate the performance and limitations of each. Two His-tag based surface immobilisation strategies were explored as part of developing the microfluidic chip reactor. First, an electrografting approach resulted in a dense molecular surface coverage of 3.29×10^{14} molecules cm^{-2}, surpassing current literature values for similar processes. Second, a self-assembling monolayer based on thiol chemistries demonstrated an enzyme surface coverage of 6.86×10^{11} molecules cm^{-2}. In order to minimise the amount, a novel continuous flow control system was created to automate control of the reactor setup. Successful inflow biocatalysis was demonstrated using a microcolumn reactor consisting of cystathionine beta-lyase (CBL) immobilised onto agarose beads to catalyse the α,β-elimination reaction of S-benzyl-L-cysteine at various concentrations. Although biocatalysis was not observed for CBL immobilised on a planar surface within a microfluidic chip reactor, the work explores the limitations of such techniques to provide grounds for furthering this area of research. The work additionally aims to contribute to the broader development of microfluidic chemical production lines for telescoped biocatalysis and enzyme cascade reactions.

ii. Contents

iii. Acknowledgements

It seems only fitting that the first person I acknowledge is Professor Steven Johnson, my supervisor. I cannot put into words the depth of my gratitude and thanks to Steve or the level of support and encouragement he provided me over the three and a half years I have been under his tutelage. So, to you, Steve, thank you for your support, insights, patience, honesty, and friendship. You have always pushed me to become the best researcher I could be. I owe you more than just a pint.

Steve has surrounded himself with exceptional people to work with in his group. I am proud to have called these people my colleagues, and I continue to call them my friends. Thank you to the postdocs who supported me along the way: Dr Matt Simmons, Dr Casper Kunstmann, Dr Lisa Stevenson, and Dr Callum Silver. I would have been lost without you all. As for my peers from Steve's group, Dr Rhys Ashton, Dr Elena Mancinelli, and Miss Francesca D'Rozario, thank you for being such fantastic travelling companions during my research journey and for your support. Our group had close connections with the Krauss group, and I would like to thank them for their help and support. I would also like to thank Professor Anne Duhme-Klair, Dr Elena Blagova, Dr Alex Miller, Dr Natalia Baranska, Dr Paul Jarvis, Mr Mark Bentley, Miss Becca Neale and Mr Reyme Herman for their help during my PhD. Special thanks must go to my closest friends and colleagues during my PhD time: Dr Manuel Deckart, Dr Augusto Martins, and Dr George McKay. You stood with me throughout it all, especially when it was dark and stormy, and I know we will stay friends for life.

To those not directly linked through the University of York, my friends and family. Thank you, Emily Thompson, for always being the most amazing and supportive human. Never stop being you. To my flatmate and brother in all things other than blood, Thomas Hiddleston, I am truly blessed to have you as my friend. I know it has not been easy putting up with me during the rollercoaster of my PhD, but I could not have got through it without you, bud. Thank you for making every day one with laughter in it. To my sisters, Katy and Kez, and possibly my biggest supporters, thanks for cheering me on; better siblings do not exist. To my Nan and Grandad, you have never given up on me and are still my heroes. Lastly, I would like to thank my parents. Words will not do justice to the support, time, love and commitment you have shown me. My gratitude is truly endless. I love you and am forever in your debt for helping make my life goals a reality.

iv. Author's Declaration

I, Kalum Thurgood-Parkes, declare that this thesis is a presentation of original work, and I am the sole author. I can confirm that:

- This work has not previously been presented for an award at this, or any other, university.
- Chemical synthesis of the chemical described as LA-NTA within (Chapter 4.2) was performed by Dr Natalia Baranska, who did not participate in any work disclosed past the point of chemical synthesis.
- Expression and purification of the Gst apoprotein described within (Chapter 4.2) was performed by Dr Elena V. Blagova, who did not participate in any work disclosed past the point of providing the purified concentrated protein scaffold.
- Expression and purification of the Cystathionine beta-lyase (CBL) introduced within (Chapter 4.2) was performed by Mr Reyme Herman, who did not participate in any work disclosed past the point of providing the purified concentrated CBL enzyme.
- All sources are acknowledged as references.

Awards

- Departmental Prize for the Best 3rd Year PhD Seminar Presentation at the Electronic Engineering Departmental PhD Conference, 2022.

Additional Achievements

- York Learning and Teaching Award (YLTA) with accreditation for Associate Fellow of the HEA (AFHEA) status, 2022.

Dedicated to my Nan, Josie.

You can finally give St. Antony a break now.

All my love,

Kal x

“Education isn’t everything. For a start, it isn’t an Elephant.”

Spike Milligan

“I neither know nor think that I know.”

Socrates, *The Apology (21d)*

Chapter 1 - Introduction

This chapter introduces the context of this research and the goals the work hopes to achieve to contribute to the wider community. The chapter additionally provides an overview of the structure and contents of each chapter within the thesis.

1.1 - Heterogeneous Inflow Bio-Catalysis: Costly to configure, so why not just downsize?

Optimisation. It is a word frequently used within academic and industrial research and can be defined as 'The action or process of making the best of something'[1]. However, if one were to ask a researcher how they found the process of optimising a chemical reaction or fabrication procedure, 'The best' is unlikely to be a term they would use. Reaxys, the world's largest chemical database, has 73 million reported reactions[2]. Nevertheless, chemists and biochemists often still need to optimise the wider parameter space of these reported reactions due to the range of practical conditions, ambiguity in the protocol description and unreported procedural differences. In the case of totally new reactions, the parameter space for optimisation is even greater. As a result, optimisation via batch screening remains highly labour-intensive, costly and time-consuming.

Enantioselective chemical synthesis is often considered one of the most challenging optimisation objectives in synthetic chemistry due to most chemical reactions involving prochiral reactants that are non-stereospecific. Enantiomerically pure chemicals are essential in many industrial chemical sectors, ranging from cosmetics to pharmaceuticals, with the Thalidomide scandal of the late 1950s and early 1960s a harrowing example of how a lack of stereoselective control in drug synthesis can lead to tragic consequences.

Due to the innate ability of biological systems to produce chemicals with total enantioselectivity, enzymes that perform this feat have been proven to be an effective tool within chemical synthesis for low energy, highly efficient and enantioselective chemical processing. Nevertheless, enzymes are often expensive and time-consuming to express in the large quantities often needed when optimising inflow biocatalytic reactions. Artificial metalloenzymes (ArMs) are an emerging area of research that combines organometallic catalysis with protein scaffolds to achieve

additional catalysed enantioselective reactions, otherwise inaccessible when using wild-type enzymes. ArMs, however, suffer from the same drawback as enzymes: they are costly and time-consuming to produce.

For this reason, the immobilisation of enzymes for inflow biocatalysis is an ever-expanding field of research, offering advantages over traditional batch biocatalysis, such as passive enzyme-product separation, sustainable reusability and increased stability. Moreover, the development and application of an immobilised enzyme/ArM reactor system at the microfluidic scale would enable the high throughput screening of the inflow biocatalytic parameter space while further reducing the cost and time for optimising these reactions, using significantly smaller volumes of precious chemical feedstocks and biocatalysts.

The development of high throughput screening microfluidic reactors also has the long-term potential to form the basis of entirely novel approaches to inflow biocatalysis. The selective and 'switchable' immobilisation of enzymes and ArMs within given regions of a microfluidic device would allow for the simple creation of biocatalytic multistep microfluidic reactors, which would only require low amounts of each biocatalyst to establish. These multistep microfluidic reactors would provide a microfluidic chemical production line and a means for testing telescoped biocatalysis and enzyme cascade reactions. For this reason, the development of immobilisation strategies that could be used in a switchable surface would need to be explored to help with this long-term vision.

1.2 - The Goals of this Work

Within the wider vision and context of this work, well-defined goals were established to provide focus and structure to the progression of the research undertaken and to act as a point of reflection as to the achievements and further work required upon its completion. The key objectives of this research are as follows:

- Devise and investigate a range of strategies for immobilising His-tag containing enzymes and protein structures, focusing on methods displaying stability when formed on surfaces such as planar electrodes and ease of use.
- Demonstrate a robust protocol for surface immobilisation of a functional enzyme or protein structure via one of the established strategies.
- Design, build and characterise a continuous recirculating flow reactor system to accommodate various microfluidic reactors, which in the context of this work will include microcolumn and microfluidic chip reactors.
- Validate the potential of inflow biocatalysis using the well-established method of a bead column reactor via the His-tag immobilisation motif and a microcolumn reactor as a transitional step to a planer microfluidic chip reactor and as a proof of concept.
- Evaluate the efficacy of inflow biocatalysis using a planar microfluidic chip reactor compared to the microcolumn reactor system.

1.3 - An Outline of this Thesis

This thesis comprises seven chapters. The initial chapters introduce the theory, methods and motivation for this work, while the main body of the thesis is split into three areas of study: the chemical immobilisation of enzymes, the design, construction and application of a bead column microfluidic immobilised enzyme reactor, and the fabrication of microfluidic chip rectors and their comparative use in a microfluidic immobilised enzyme reactor.

Chapter 2 – Theory and Literature Review

This chapter summarises the fundamental scientific concepts underpinning the research and reviews the relevant literature that contributes to the experimental and innovative research presented in this thesis. The chapter is split into three main sections, each covering a specific area of related theory: an introduction to enzymes and artificial metalloenzymes and their associated kinetic theory and related use within the literature. A summary of fluid dynamics within microfluidic systems and an introduction to the design and construction of flow reactors. Lastly, a thorough review of the numerous enzyme immobilisation strategies demonstrated within the literature and an overview of the research field of microfluidic immobilised enzyme reactors (μ-IMERs) and inflow biocatalysis.

Chapter 3 – Methods

This chapter introduces the basis and application of the various analytical techniques used for the solution and surface analysis throughout this work, as well as relevant fabrication methods and standard operating procedures (SOPs). The chapter covers the fundamental science and engineering underpinning the analytical and fabrication methods and details of how they are used to allow replication of work detailed within the experimental sections.

Chapter 4 – Chemical Immobilisation Strategies

This chapter describes the process of innovating and applying His-tag affinity binding strategies for immobilising enzymes and artificial metalloenzymes. Two methods are explored in this section. The first is a diazonium salt electrografted onto planar gold electrodes, and the second

is the formation of a thiol-based self-assembled monolayer (SAM) onto planar gold-coated surfaces. Both methods are extensively characterised using various complementary analytical techniques described in the method chapter.

Chapter 5 – Column Immobilised Enzyme Reactor (IMER)

This chapter outlines the initial creation of the flow reactor setup and the assembly and, informed by the comparable immobilisation chemistries discussed in Chapter 4, the characterisation of a bead column microfluidic immobilised enzyme reactor. Accordingly, the chapter is split into two key sections. First, the design and implementation of the bespoke flow system and the associated flow control software to achieve a continuous flow reactor system compatible with various reactor designs. Second, the implementation and characterisation of the reactor system to determine the inflow enzymatic kinetics of a previously undemonstrated immobilised enzyme species within a bead microcolumn reactor.

Chapter 6 – Microfluidic Chip Reactor In-Flow Biocatalysts

This chapter comprises the design and fabrication of various PDMS microfluidic chips intended for use as a planar surface chip reactor within the continuous flow immobilised enzyme reactor system. This chapter contains two main sections. The first outlines the procedures and fabrication methods developed for producing a range of PDMS microfluidic chips, including their quantification and testing. The second addresses the integration of the planar microfluidic chip reactor into the flow system and explores the enzymatic kinetics of an initial multi-day study of the system compared to the microcolumn reactor setup.

Chapter 7 – Conclusions and Outlook

This chapter summarises the work performed within this thesis and addresses further work to explore hypothesised theorems illuminated as a direct result of this work and further applications of this research to the broader field.

Chapter 8 – Appendices

This chapter contains additional information of interest regarding the repository for the open-access flow control software and schematics of the engineered PDMS microfluidic chip mould.

Chapter 9 – Abbreviations

This chapter lists all abbreviations used to provide a convenient location for their lookup at any given point without the prerequisite of reading the entire work.

Chapter 2 - Theory and Literature Review

This chapter comprises a summary of the essential scientific theory, and a review of the relevant literature underpinning the work later disclosed. The chapter is split into three subchapters, addressing this thesis's main overarching areas of academic interest: enzymes and artificial metalloenzymes, microfluidics and flow reactors, and immobilisation strategies and microfluidic inflow biocatalysis. Through reading this chapter, a better understanding of the context for the research performed should be gained while directing the reader to other related studies and areas of interest within the literature.

2.1 - Enzymes and Artificial Metalloenzymes

This subchapter details the context, theory and literature on natural and artificial biocatalysis. The first section introduces protein structures and their expression, the structure and function of enzymes, biocatalytic thermodynamics and kinetics, and stereoselectivity in biocatalysis. The second briefly introduces organometallic catalysis and artificial metalloenzymes, standard means of developing artificial metalloenzymes within the literature, and examples of their potential use.

2.1.1 - An Introduction to Enzymes

Enzymes are a classification of proteins that facilitate the catalytic turnover of a chemical molecule (or molecules), referred to as substrates, by providing a lower activation energy route in which the reaction can occur. Naturally expressed within biological cells, enzymes perform a range of essential processes to maintain the cell and, in turn, the biological organism. These essential processes range from breaking down triglycerides (fats) by lipase enzymes[3] to synthesising deoxyribonucleic acid (DNA) by DNA polymerase enzymes[4].

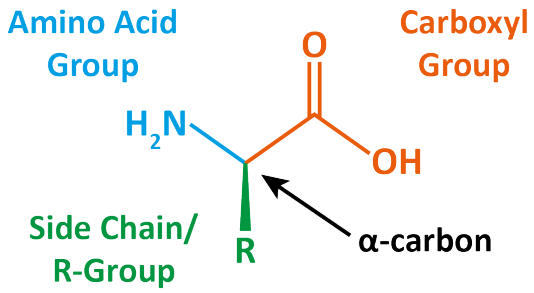

Figure 2.1 - The generic structure of an α-amino acid, consisting of an amino acid group, a carboxyl acid group and a variable side chain or R-group, all stemming from a singular carbon centre, referred to as the α-carbon.

Enzymes are globular proteins made of a polypeptide chain that consists of specific peptide subunits made up of a chain of bonded chemical building blocks called amino acids[5, 6]. There are over 500 known naturally expressed amino acids[7], with 22 of them known as the proteinogenic α-amino acids, which are used in the creation of proteins[8]. All α-amino acids can be simplified to the same generic structure, in which the functional groups are coordinated to central carbon referred to as the α-carbon (Figure 2.1). The amino acids polymerise into peptides and polypeptides through a condensation reaction between the amino acid and carboxyl groups, forming an amide linkage called a peptide bond[5, 6]. The other key component of an α-amino acid is that of the side chain group, sometimes referred to as the R-group. The side chain group

determines the hydrophobicity[9], the nature of the higher order structural folding of the polypeptide, including the various bonding interactions between other amino-acid groups within the polypeptide[10] and, in the case of enzymes, sometimes even helps facilitate the catalysis by interacting with the substrate[11].

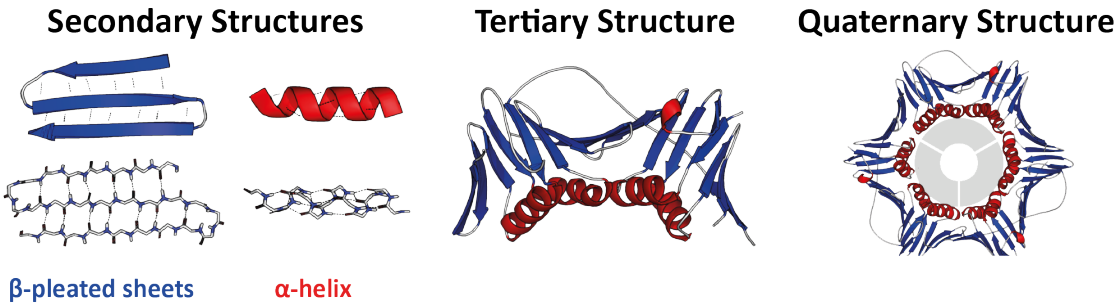

Figure 2.2 - The Polypeptide chain is folded to form secondary structures such as β-pleated sheets and α-helices. These then interact with one another to form larger tertiary structures. Then, several of these tertiary structures acting as subunits can form a quaternary structure. The example tertiary and quaternary structures shown are a subunit and the whole quaternary protein of the DNA clamp known as proliferating cell nuclear antigen (PCNA). The figure was modified under a Creative Commons licence[12, 13].

Once formed, polypeptide strands will undergo a process called folding in which they arrange themselves into the lowest possible conformational energy state, according to steric limitations and bonding interactions between individual peptides and the constituent amino acids. The first of these structural levels is the polypeptide chain, which is defined by the specific amino acid sequence. The polypeptide chain then undergoes additional folding to form secondary protein structures such as β-pleated sheets and α-helices[14] (Figure 2.2). Multiple arrangements of the secondary structures formed by the polypeptide strands will then interact to form a higher-order tertiary protein structure. Both secondary and tertiary structures of proteins are held together via hydrogen bonding and disulfide bonding between side-chain groups[14], as well as larger structural interactions such as van der Waals forces,[15] electrostatic forces[16], and hydrophobic interactions. In the case of some proteins, several of these tertiary structures consisting of one polypeptide chain each, referred to as subunits, also interact with one another to form quaternary protein structures[14].

The artificial expression of proteins is commonly achieved by inserting the gene of interest into the plasmid of a bacteria, such as *E. coli*, which will then express this protein via translation and transcription. After a period of growth, the bacteria are lysed, and the lysate is purified via centrifugation techniques to obtain just the protein of interest[17]. This procedure is called genetic recombination, and proteins expressed by these means are called recombinant proteins. Additional genetic modifications can be made to the gene before being inserted into the plasmid. A common modification made to protein structures is the addition of a polyhistidine tag, most commonly referred to as a His-tag[18]. This amino-acid motif contains several imidazole-containing Histidine groups, which have a high binding affinity to metals such as Cu^{2+} and Ni^{2+}. Therefore,

by expressing the His-tag group on a protein, the protein can be selectively isolated via this affinity for such metals, most commonly for purification via chromatography[19], but also the surface functionalisation approaches[20], as used in this work.

Enzymes consist of two simplified structural elements: the protein scaffold and the active site (Figure 2.3). The protein scaffold consists of a tertiary protein structure, except for some enzymes, which also have quaternary structures, such as pyruvate dehydrogenase[21] or cystathionine beta-lyase[22]. Although the bonding and intermolecular forces offer structural stability for the protein, they are often kinetically liable, meaning some are more easily overcome than others. This is both an advantage and disadvantage to enzymes, as it means they are relatively 'malleable' in nature and able to move dynamically, which is essential to their function. However, this also means enzymes can often be susceptible to temperature[23-25] and pH changes[24, 26] as they can disrupt these bonding interactions, causing the protein to unfold, which can lead to the denaturing of the enzyme.

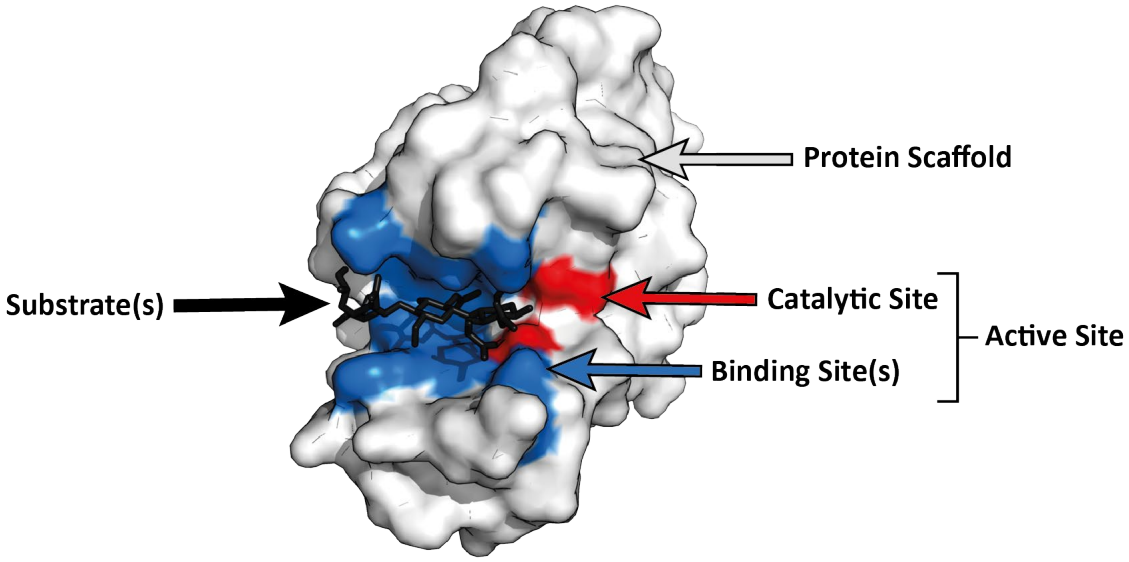

Figure 2.3 - The general structure of an enzyme, consisting of the protein scaffold, which is folded to express the active site, comprising a catalytic site and a binding site for binding specific substrates. The example enzyme given is Lysozyme, with peptidoglycan as its substrate. The figure was modified under a Creative Commons licence[27].

The protein scaffold additionally determines the particular pocket shape within the enzyme structure, which is most commonly referred to as the active site, which provides both a site for the binding and catalysis of the substrate(s). The active site is formed to bind a specific substrate, or in some cases substrates, through an electrostatically and sterically adaptable environment, which induces complementarity to the substrate(s). The observed specificity of a substrate binding to a specific enzyme was initially explained by Emil Fischer in 1894 through the so-called 'lock and key' model[28]. The model describes the enzyme as having a perfectly complimentary steric environment for the substrate, in the same way, that a lock is a stationary structure designed to accommodate its complimentary key perfectly. However, as previously described,

protein structures are anything other than stationary but are instead dynamic and malleable. It was therefore suggested by Daniel Koshland in 1958 that the lock and key model should be revised to instead an induced fit model[29].

In the induced fit model, the un-complexed enzyme has an active site approximately complementary to that of the substrate(s), but upon the substrate(s) approaching and interacting with the enzyme, the shape of the active site shifts to accommodate the substrate according to the chemical, electrostatic and steric complementarity of the binding site itself[29] (Figure 2.4). The resultant composite from this interaction is referred to as an enzyme-substrate complex, and catalysis of the substrate can occur once formed.

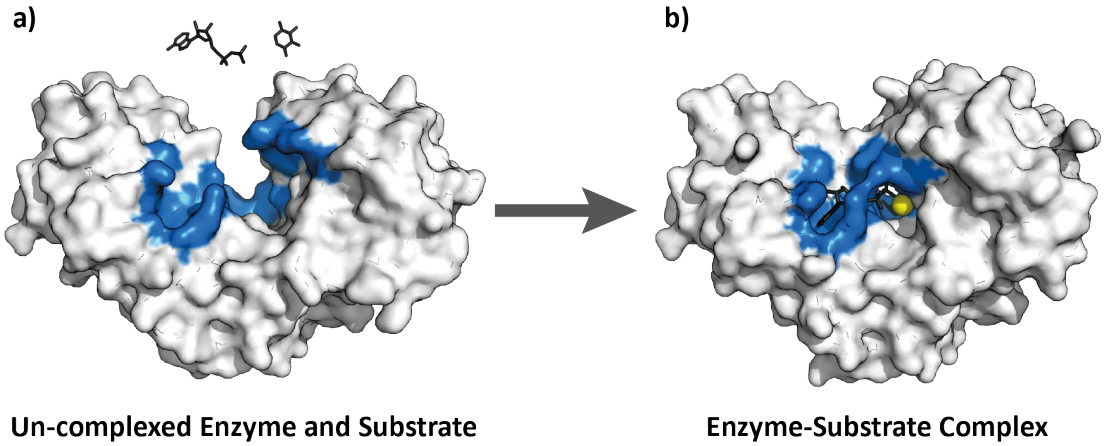

Figure 2.4 - a) The un-complexed enzyme has a binding site approximately complementary to the substrate but is not a rigid perfect fit. b) Once the complex is bound to the active site, induced fit around the complex is established, and the enzyme-substrate complex is formed. The example enzyme shown is hexokinase, with its substrates adenosine triphosphate and xylose. The figure was modified under a Creative Commons licence[30].

The enzyme's catalytic site is most commonly adjacent to the binding site. The area is responsible for interacting with the substrate to lower the activation energy of a chemical reaction that facilitates the conversion of the substrate to the product. Depending on the substrate and the reaction the enzyme catalyses, the means by which the activation energy is lowered varies from enzyme to enzyme. The main mechanisms enzymes use to achieve this lowering of activation energy are covalent catalysis[31], metal catalysis[32], electrostatic interactions[33], acid-base catalysis[34], conformational distortion[35, 36] and increasing substrate proximity[37].

Cofactors are another crucial component of an enzyme's catalytic function and are either permanently resident or bound within the catalytic site[38]. Cofactors are generally either nonprotein organic chemical molecules or metallic ions incorporated into the enzyme structure essential to the catalytic process. Cofactors that are organic chemical molecules are commonly referred to as coenzymes and are often biochemically derived from vitamins and nutrients, naturally taken up by a biological organism[39]. Metallic ion cofactors are acquired as essential trace elements from mineral uptake or metabolised from food[40]. In the case of recombinant

enzymes, if the cofactor is a permanent resident of the enzyme structure, it must be incorporated during protein folding to ensure it is present within the structure[41]. If it is bound during catalysis, like a substrate, it must instead be incorporated within the reaction buffer. Some cofactors are fully regenerated to their original state as part of the catalytic process, while others are altered and must be regenerated by an alternative biochemical reaction or process[42]. Cofactors usually participate in the enzymatic process by facilitating electron transfer[43], transferring functional groups[44] or stabilising reactive product intermediates[45]. For this reason, enzymes lacking the required cofactors do not catalytically function, making cofactor incorporation essential for successful enzymatic biocatalysis. Enzymes will often utilise several of these mechanisms for any given catalytic reaction.

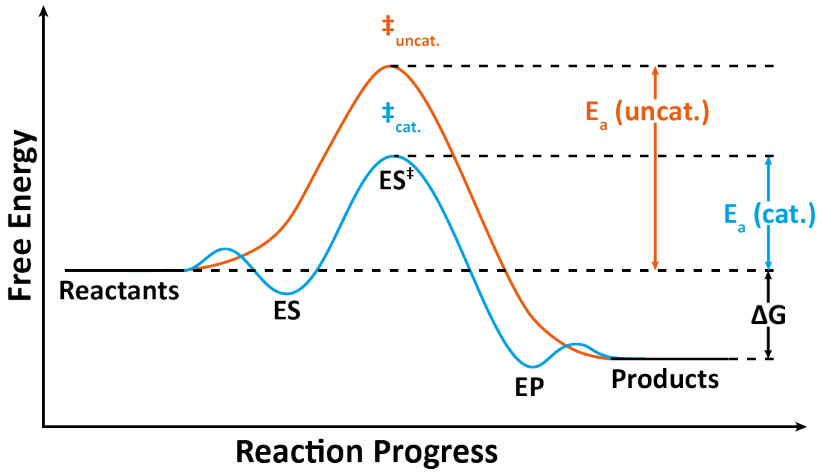

Figure 2.5 - A potential energy diagram to illustrate the difference between transition states of an un-catalysed ($‡_{uncat.}$) and catalysed reaction ($‡_{cat.}$), and their activation energies respectively (E_a (uncat.) & E_a (cat.)), As well as the change in free energy (ΔG). The lower energy states of the enzyme-substrate (ES) and enzyme-product (EP), as well as the transitional state of the enzyme-substrate complex ($ES^‡$), are additionally indicated.

Regardless of the mechanism the enzyme utilises, the thermodynamic theory behind how enzymes, or any catalyst, catalyse a reaction remains the same. The activation energy is defined as the minimum free energy (sometimes referred to as Gibbs energy) required for the reaction to occur spontaneously. In a catalysed reaction, the catalyst or enzyme provides an alternative chemical route that lowers this activation energy, increasing the rate at which the reaction proceeds. A reaction is thermodynamically viable when there is a change in free energy upon its completion (ΔG)[46]. A reaction may have several transition states, but for any reaction to occur, the reagents must have the required free energy, the activation energy (E_a (uncat.), to overcome the maximum transition state ($‡_{uncat.}$) (Figure 2.5). When a reaction is catalysed, the catalyst or enzyme provides an alternative route for the reaction to occur that goes through a transition state of lower free energy ($‡_{cat.}$). This results in an overall lower activation energy (E_a (cat.)) for the reaction to occur. How this alternative route is achieved differs drastically from catalyst to catalyst. Another thermodynamic consideration when dealing with enzymes is a free energy requirement for the association of the enzyme-substrate complex (ES) and the disassociation of

the enzyme-product complex (EP)[46]. Both energy requirements are, however, vastly smaller than the activation energy to form the transition state enzyme-substrate complex ($ES^{\ddagger}$), so it remains the most significant energy barrier required for enzyme catalysis to occur.

Catalysis in any form, enzyme or otherwise, does not affect the equilibrium of a reaction but instead lowers the activation energy to increase the reaction rate. Therefore, one of the main ways of profiling enzymatic catalysis is by monitoring the reaction's kinetics. All reactions start with a given concentration of substrate. Over time, the substrate will be turned over into a product by the enzymatic reaction, meaning that as substrate concentration decreases, product concentration will increase. In the simplest case, this reaction is first order, meaning the reaction rate is directly proportional to the concentration of the substrate. In turn, this would mean the substrate consumption rate is equal to the rate of product formation (Figure 2.6a). The reaction rate, sometimes called reaction velocity, is a function of the concentration change over time. Because of this, the rate can be determined by fitting a kinetically valid mathematical equation that closely follows the trend shown by the data. By comparing the rate fitting equation to the kinetic rate equation, it is possible to determine a value for the rate of reaction. The quality of the fit can be assessed using statistical analysis techniques, which are explained and utilised later in this work.

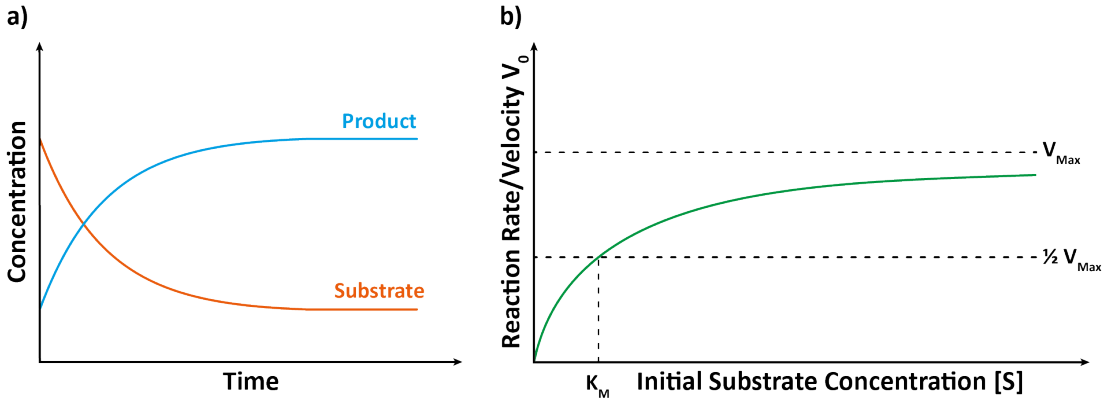

Figure 2.6 - a) The relationship between concentration and time for an enzymatically catalysed reaction. In the simplest kinetic fit, assuming the initial reaction is first order so that as product concentration increases, substrate concentration decreases, the gradient will be equal to the rate of reaction. b) a Michaelis-Menten plot showing reaction rate versus initial substrate concentration, displaying the classical hyperbola shape and the locations of the theoretical maximum rate (V_{max}), half the theoretical maximum rate ($\frac{1}{2}V_{max}$) and the substrate concentration at half the theoretical maximum rate (K_M).

For complete kinetic analysis of an enzyme species, Michaelis-Menten kinetics is often applied to determine vital kinetic parameters of the enzymatic system[47, 48]. The easiest way to consider enzymatic kinetics is through relative concentrations of the enzyme and substrate. At low relative substrate concentrations, there is an excess of available enzymes. Under these conditions, the reaction rate will increase linearly with substrate concentration. As the relative concentration of substrate increases to a point where almost all enzyme active sites are occupied or saturated, the rate is then dependent upon the efficiency of the enzyme to turn over the substrate, at which

point the rate of reaction tends towards the theoretical maximum rate of reaction, V_{max} (Figure 2.6b) [46, 49]. Increasing the substrate concentration at this point will not affect the reaction rate. The concentration of the substrate at half the maximum rate of reaction, $\frac{1}{2}V_{max}$, is referred to as K_M and is crucial to further understanding the enzyme kinetics.

As previously stated, the Michaelis-Menten equation can be used to describe the kinetic behaviour of enzymes. If a reaction were to proceed spontaneously from substrate to product, the standard enzymatically catalysed form of that reaction, with only one substrate, could be simplified to the equation[50]:

$$E + S \underset{k_{-1}}{\overset{k_1}{\rightleftharpoons}} ES \xrightarrow{k_2} E + P \qquad (2.1)$$

Where E, is the enzyme, S, is the substrate, ES, is the enzyme-substrate complex, P, is the product, and k_1, k_{-1} and k_2 are the rate constants for each step. The derivation of the Michaelis mentum equation relies upon two key assumptions. The first is that the reaction is not reversible from substrate to product. The second is the steady-state approximation, meaning the first-rate constant must be significantly slower than that of the second constant ($k_1 \ll k_2$), and therefore, the concentration of the enzyme-substrate complex is relatively constant[49]. From those assumptions and the given equation (2.1), the Michaelis-Menten equation can be derived[46, 49]:

$$V_0 = \frac{V_{max}[S]}{K_M + [S]} \qquad (2.2)$$

Where V_0 is the reaction rate or velocity, V_{max} is the theoretical maximum rate observed when the enzyme is fully saturated, and there is a significant excess of substrate, $[S]$ is the substrate concentration, and K_M is the Michaelis constant. The Michaelis constant indicates the enzyme's affinity for its substrate and is the summation of the rate constants for each step, given in equation (2.1), derived to be:

$$K_M = \frac{k_2 + k_{-1}}{k_1} \qquad (2.3)$$

The constants determined using the Michaelis-Menten equation and associated plot, as shown in Figure 2.6b, give crucial information about the enzymatic reaction but can also be used to calculate other insightful constants. One of which is that of catalytic constant (k_{cat}) which is given by the equation[46]:

$$k_{cat} = \frac{V_{max}}{[E_T]} \quad (2.4)$$

Where V_{max} is the theoretical maximum rate, and $[E_T]$ is the total enzyme concentration within the reaction. The catalytic constant represents the maximum number of substrates an enzyme can turn over into a product per unit of time when all enzyme binding sites are at full substrate saturation. From the catalytic constant of a reaction, it is also possible to calculate the catalytic efficiency, sometimes referred to as the specificity constant, by the equation[46]:

$$Catalytic\ Efficiency = \frac{k_{cat}}{K_M} \quad (2.5)$$

Catalytic efficiency indicates two critical properties of the enzyme-substrate relationship. The first is that it considers how the rate of catalysis is affected by how readily the enzyme-substrate complex is formed and is a strong indicator of the enzyme's overall efficiency in turning over a substrate into a product[51]. The second is that it indicates the specificity of the enzyme for a substrate[52]. When studying an enzyme capable of turning over multiple substrates, with all conditions and concentrations kept constant, comparing their catalytic affinities indicates how well the enzyme comparatively turns over each substrate. The higher the catalytic affinity for a substrate, the better suited the enzyme for facilitating its enzymatic catalysis. In addition to the rate of catalysis, the yield of a target product is important, as wasted substrate is detrimental to both the environmental and financial advantages of the catalytic process.

One of the most significant advantages of enzyme catalysis is that it offers high catalytic affinity and enantioselectivity. Enantioselectivity refers to a preference for expressing one enantiomer over the other when performing a chemical reaction that results in a chiral product. The exact definition of an enantiomer is a molecule which is a non-superimposable mirror image[53]. An enantiomer is a type of optical isomer, meaning a molecule that has the same chemical formula and connectivity but a differing functional group arrangement around a stereogenic carbon, which has two possible arrangements denoted as R (rectus, which means right in Latin) and S (sinister which means left in Latin) enantiomers. The biochemical significance of enantiomeric molecules was not fully appreciated until the unfortunate thalidomide tragedy during the 1950s and 1960s. Thalidomide was a racemic drug, meaning it consists of a mixture of both enantiomers, given to pregnant women as a sedative medication to help with the effects of

morning sickness. Although the (R)-enantiomer of thalidomide was indeed an effective sedative, the (S)-enantiomer, unknown to pharmaceutical industries at the time, was a teratogenic[54], causing congenital disorders to the developing embryo, resulting in significant birth defects[55]. Although this tragedy was partly due to a lack of rigorous systematic testing of the developmental toxicity within pharmaceuticals at the time, part of the issue was a lack of understanding of the crucial role that enantiomers and enantiomeric selectivity play in biological systems. Although thalidomide is one of the most well-known cases of enantiomers affecting biological systems, not all are so sinister. Another example of how different enantiomers engaged differently with biological physiology is that of limonene. (R)-limonene has the distinct smell of oranges, meanwhile (S)-limonene instead smells like lemons[56]. The reason enantiomers have such a dramatic effect on biological systems is because biology itself is enantiomerically selective, from smell receptors to protein-binding sites, biology has developed to utilise molecular chirality.

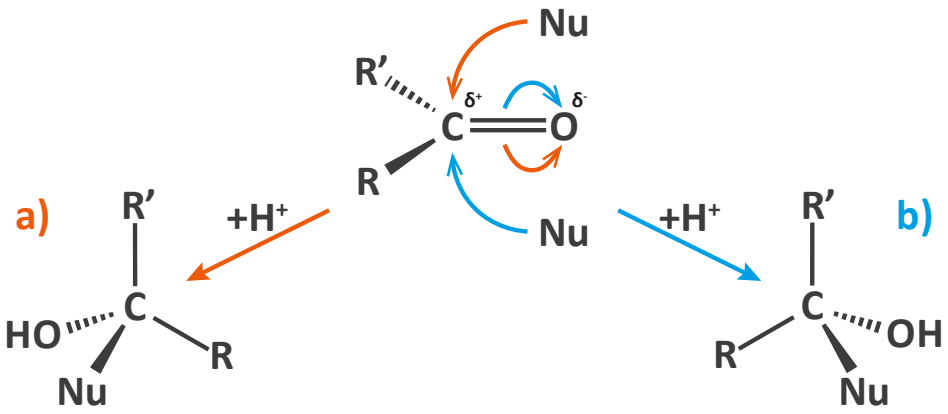

Figure 2.7 - Generalised nucleophilic addition of a ketone or aldehyde. If the nucleophile attacks the 'top plane', it will result in one enantiomer, a), and the attack of the bottom plane will yield the other enantiomer, b).

As previously mentioned, one of the primary mechanisms the enzymes utilise for catalytic turnover is that of the conformational distortion of the substrate during the enzyme-substrate complexation. Not only does this often provide an energetically favourable alternative reaction pathway, but it can also heavily favour the formation of one enantiomer over the other. To take an arbitrary example of a reaction that results in enantiomeric products, the nucleophilic addition of a nucleophile to aldehyde or ketone with differing functional groups will result in either an R or S enantiomer. This enantiomer produced depends on whether the nucleophile attacks the top or bottom plane of the carbonyl group[57] (Figure 2.7). By inhibiting access to one of these two planes by geometrically restraining the substrate, only one plane would be open to undergo nucleophilic attack, forcing only the formation of one of the enantiomeric products. Enzymes can directly catalyze specific substrates in the same way; through orientation of the active catalytic residues and conformational distortion of the substrate, the resultant product will be predominantly, if not entirely, one specific enantiomer. When determining the amount of enantiomer within a given solution, the solution is subjected to a plane of polarised light. The

light will interact with each enantiomeric molecule so that it causes an overall rotation of that plane of light in a given direction, referred to as the observed rotation, α, given in degrees, which differs depending on the molecule's chirality. The absolute rotation is also a function of concentration, c, the path length of the sample cell, l, and temperature, T. For this reason, specific rotation $[\alpha]_D^T$, is calculated for comparison of compounds under standard conditions, given by the equation[58]:

$$[\alpha]_D^T = \frac{\alpha}{l \times c} \qquad (2.6)$$

Because the rotation measured experimentally differs from compound to compound and will sometimes contain mixed enantiomers, the optical rotation is most commonly reported as a percentage, referred to as the enantiomeric excess (e.e.), given by the equation[58]:

$$\%\ ee = \frac{|observed\ \alpha|}{|\alpha\ of\ pure\ enatiomer|} \times 100 \qquad (2.7)$$

In addition to enantiomers, diastereoisomers are another key stereoisomer that can be directed by enzymatic catalysis. The preference of an enzyme or catalyst for forming a particular diastereoisomer product is referred to as its diastereoselectivity. Diastereoisomers are described in two varying notations: *cis*/*trans*-diastereoisomer or *E*/*Z*-diastereomers. Diastereoisomers only occur between two adjacently stereogenic centres, which are rotationally constrained around their bond, most commonly through an alkene double bond or the two stereogenic centres being conformationally locked by a ring structure. In the simplest case, where each stereogenic centre has an identical group, the isomer is referred to as being in a *cis*-confirmation if these two groups are within the same plane or on the same side of the conjoining bond. If these groups are not in the same plane or not on the same side of the conjoining bond, the molecule is in *trans*-confirmation. If those stereogenic centres do not share an identical functional group, it is no longer possible to classify them by these rules. Instead, each group on each stereogenic centre is ranked according to the atomic number or highest priority (for example, CH3 < CH2CH3, as the next conjoining atom/s are greater in atomic number) of the atom directly attached to the centre. If the two highest atomic numbers or priority groups are within the same plane or on the same side of the conjoining bond, they are *Z*-configuration diastereomers. If the two highest atomic numbers or priority groups are not in the same plane or on different sides of the conjoining bond, they are defined as *E*-configuration diastereomers. When discussed in the literature, mixed diastereomer products tend to be given as a percentage ratio of *cis*: *trans* or *Z*: *E*, with the percentages being experimentally determined using nuclear magnetic resonance (NMR) spectroscopy, high-performance liquid chromatography (HPLC) or gas chromatography (GC).

Given the biological importance of the enantiomeric conformation to modern medicinal drug synthesis and the anosmic characteristics that can be tailored through selective enantiomers, many industrial sectors with the pharmaceutical[59, 60] and perfume[61, 62] predominant amongst them, means there is a demand for specificity in enantiomeric products. The utilisation of enzymes is one potential route to achieve that. However, enzymatic catalysis is not always a perfect solution and can come with some significant disadvantages, if not ultimately limiting usage. While some enzymes can facilitate the catalysis of an extensive range of substrates or chemical reactions[63], many can only accommodate one specific substrate or reaction[64]. For this reason, the catalysis of a similar substrate to the intended substrate of the enzyme's biochemical function is not always possible, and when it is possible, it often incurs a significant decrease in the K_{cat} of the enzyme. Another limitation is the working conditions of the enzyme, especially when considering the solubility of the reactant or product of interest. Enzymes by natural design are best suited to aqueous solvent environments and are often not well suited to nonaqueous solvents, which often denature or lower the reactivity of the enzyme[65]. Temperature can also significantly affect the function of most enzymes. Even though increasing the reaction temperature can often lead to higher enzymatic turnover simply as a function of the system's entropy, it only holds if the system temperature is kept within the working temperature range of the enzyme. Below this point, the enzyme will be unable to perform at any significant catalytic rate; above that point, the enzyme often readily denatures[25]. The ability to synthetically engineer enzymes capable of overcoming some of these limitations, such as new catalytic reactions or thermal stability, but still utilise the advantages of an enzyme such as enantioselectivity and high k_{cat} values, would therefore open a whole new set of potential uses for biosynthetic catalysis.

2.1.2 - Artificial Metalloenzymes

Artificial metalloenzymes (ArMs) are a class of synthetic enzymes consisting of an organometallic reactive centre, or metallocofactor, incorporated into a protein scaffold to combine the reactivity and versatility of transition metal catalysis with the complex reaction control achieved by enzyme biocatalysis[66]. Organometallic catalysts comprise a reactive metal centre coordinated to at least one carbon-containing ligand. The metal centre commonly consists of a transition, alkali or alkylene metal, but only catalysts and artificial metalloenzymes containing transition metal centres will be considered in this work. The ligand consists of an ion or a molecule containing a functional group that readily binds to the metal centre to form a coordination complex. How the ligand interacts with the molecular orbitals of the metal centre determines its geometric configuration and makes the complex suitable to facilitate the catalysis of a chemical reaction. In terms of the thermodynamics and overall catalytic principle, organometallic catalysts function in the same way as enzymes, providing an alternative lower activation energy chemical route to increase the rate of a given reaction. The types of reactions performed by organometallic catalysts are broad and numerous, including palladium-catalysed cross-coupling reactions[67], metal-catalysed olefin metathesis[68] and asymmetric hydrogenation[69]. Many of these catalytic processes are not naturally carried out by enzymes within nature, meaning organometallic catalysts are often the only feasible means of achieving these chemical processes. The limitations of many organometallic catalysts are that they are usually susceptible to biocompatible conditions, have limited solvent compatibility and offer low selectivity, especially for synthesising enantiospecific products. As mentioned in the previous section, enzymes commonly display a high level of enantioselectivity in the final product, which is often due to the steric and chemical environment provided by the protein scaffold within the active site. Not only that, but they also function efficiently within more mild biocompatible conditions than many organometallic catalysts.

Many naturally occurring proteins within biology actively coordinate with metal centres for a host of reasons, including as enzymatic cofactors. It is not hard to envision that if an organometallic catalyst was instead incorporated within a protein scaffold, it might offer similar advantages to that displayed within naturally occurring enzymes. ArMs are, therefore, a result of combining biological and organometallic systems to yield a new hybridised form of catalysis. By selectively choosing the desired features from both organometallic and biological enzyme catalysts, ArMs provide a novel approach to catalysis that delivers advantages from both respective systems.

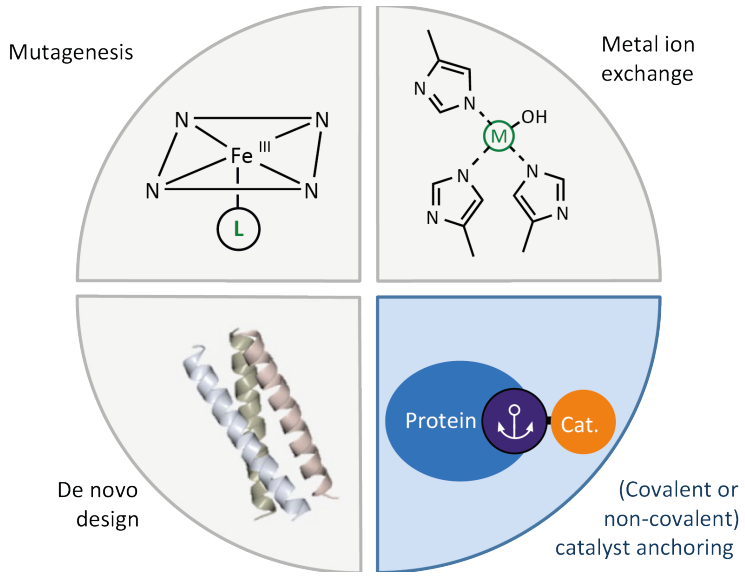

Figure 2.8 - The four main strategies for developing artificial metalloenzymes. The figure is taken from the literature[70].

It is generally accepted that there are four main ways of developing artificial metalloenzymes: *de novo* design, mutagenesis, metal ion exchange and catalyst anchoring (Figure 2.8). *De novo* design, meaning 'from the beginning', is the development of new wholly artificial, engineered ArMs, primarily relating to the protein scaffold structure, which is not just redesigned or repurposed but instead designed totally from the beginning. *De novo* design of ArMs is often significantly challenging as it requires a thorough understanding of the desired end protein structure, down to the amino acid level, and complete control over folding into its secondary and tertiary structures. It not only requires an understanding of these fundamental principles to form a new unnaturally expressed protein structure successfully but also to provide an appropriate binding site for the substrate and essential enzymatic cofactors and ensure the structure gives the desired enhancements attributed to protein scaffolds.

Despite the complexities, many such *de novo* designed ArMs have been demonstrated in the literature[71]. One such example is the work of Cangelosi *et al.*[72], where a single-stranded three α-helix protein structure, α_3DH_3, was designed, recombinantly expressed, and successfully folded with a three Histidine - Zn^{II} coordination site that demonstrates catalytic activity for the successful hydration of CO_2. The α_3DH_3 ArM showed catalytic efficiencies within 1-3 orders of magnitudes of the natural carbonic anhydrase enzyme and faster than similar small-molecular catalysts with no notable product inhibition, an issue commonly found in the small-molecular catalysts for this reaction. The development of a fully *de novo* ArM is fundamental to the development of the field as a whole, informing future design of protein scaffolds.

The development of ArMs through mutagenesis describes the genetic modification of naturally expressed enzymes or protein scaffolds to improve its normal mode of catalysis, such as enhanced efficiency or selectivity. Mutations made to the protein scaffolds of naturally occurring

enzymes can be selective or random. Selective mutagenesis is often employed in enzymes where the protein structure and catalytic process are well-characterised and understood. Selective mutagenesis allows the consideration of possible modifications that may be made to the structure of the protein scaffold, partially within the active site, that may alter the enzyme's functionality beneficially, such as allowing it to perform alternative catalytic reactions or increase its enzyme promiscuity. When the catalytic mechanism or the structure of an enzyme is less understood, random mutagenesis of a given enzymatic species[73] or even an already established ArM[74] can prove to be an effective method of building a library of potential protein scaffolds for both computational and experimental screening of new biocatalysis. A groundbreaking example of mutagenesis for the development of ArMs, is the work of Coelho *et al.*[75]. In the work, it is outlined that nature has developed an extensive range of enzymes for performing monooxygenation (oxene transfer) reactions on olefin's (alkenes), but no natural enzymes for the cyclopropanation (carbene transfer) of olefin's, which is a mechanistically a similar reaction. The catalytic site of the iron heme-containing enzyme cytochrome $P450_{BM3}$ had an analogous structure to that of iron porphyrins, which is a commonly used catalyst in organometallic carbene-transfer reactions. Although iron porphyrins can catalyse organometallic carbene-transfer reactions, they do so with the potential of producing up to three differing stereoisomer products. Coelho *et al.* theorised that cytochrome P450 could be genetically engineered to catalyse cyclopropanation reactions but with significant regio- and stereoselective control, as displayed in their catalysis of monooxygenation reactions. From work they had already performed on the directed evolution of $P450_{BM3}$, an extensive library of 92 modified $P450_{BM3}$ variants was available for screening the catalysis of the cyclopropanation reaction.

Ten of these variants were fully characterised, and 5 showed an improvement in total turnover numbers (TTNs), which can be defined as the number of moles of product generated divided by the number of moles of biocatalyst used for the reaction[76], from the P450 wild-type. Trends in the structure of these variants were used to inform additional mutations of residues within the active site. The final P450 catalyst variants showed varying TTN, regio- and stereoselectivity values for a range of cyclopropanation reactions of styrenyl substrates, but all far exceeding the performance of the wild-type. One of the most notable and remarkable variants contained a singular mutation from the wild-type P450 variant. This single modification not only made it fully active for catalysing cyclopropanation reactions, but it also displayed a staggering stereoselectivity for the trans product (*cis* 1: *trans* 99) and enantioselectivity for the major diastereoisomer (-96% $e.e._{trans}$, calculated from (*R*, *S*) - (*S*, *R*) enantiomers). The work fully illustrates the potential advantages of using mutagenesis for ArM design, even single modifications to existing enzymes changing the properties of an enzyme to form a new ArM, but also showcases the advantages ArMs offer to the broader chemistry community as a whole in

the production of both regio- and stereoselective products unavailable through wild-type enzyme catalysis.

Using a metal ion exchange is one of the more simplistic approaches to developing ArMs from naturally expressed enzymes. The basic premise of the strategy is that the metal ion cofactor in a preexisting, naturally occurring metalloenzyme is replaced with an alternative metal ion species. The pivotal step in this method is the successful structural retention of the protein scaffold structure without the presence of its native metal ion species bound. A metalloenzyme lacking its metal ion component is called an apoenzyme or apoprotein. There are two main ways of obtaining apoenzymes: recombinant protein expression without the metal ion present and dialysis of the metal ion species from the preexisting metalloenzyme. Although recombinant protein expression without the metal ion is sometimes possible, depending on the metalloenzyme, this approach can often interfere with the correct folding of the protein structure[77]. It is often more straightforward and therefore preferred to express the wild-type enzyme, including the original metal ion centre and use the dialysis process to extract this centre after expression, leaving the apoenzyme vacant to coordinate the new desired metal ion complex. Within the work by Jing *et al.*[78], the zinc^{II} ion within the enzyme carbonic anhydrase (CA) was replaced with a rhodium^{I} ion to be used in the selective hydrogenation of *cis*-stilbene into bibenzyl. The natural Zn^{II} ion was removed by means of dialysis using the zinc chelator 2,6-pyridine dicarboxylate, to which they estimated 90-95 % of the zinc was removed from the CA in solution. The purified CA apoenzyme was suspended in a solution of $[Rh\text{-}(cod)_2]BF_4$ to form the ArM via another dialysis process. This initial attempt revealed that the uptake of Rh ions was, on average per CA, 6.5 and 7.5 times higher than expected, depending on the CA strand used. This author hypothesised that histidine and lysine side chains on outward-facing surface residues might coordinate Rh ions, explaining this extra uptake. Site-directed mutagenesis alone or combined with chemical modifications of the histidine groups showed a significant decrease to an average of only 1.3 Rh per CA, confirming that the additional Rh ion uptake was due to histidine side chains on outward-facing surface residues. Despite showing a slower hydrogenation process (55% conversion within a 12-hour reaction versus 80% for the unbound Rhodium), the best of the resulting Rhodium CA ArMs showed 20:1 stereoselectivity for the *cis*-stilbene over the *trans*-stilbene, as opposed to the 6:1 stereoselectivity of the unbound Rh complex.

The last strategy for developing ArMs is covalent or non-covalent anchoring. This method relies on two primary components: a catalytic organometallic centre (not just a reactive metal ion like in metal ion exchange) and a surrogate protein scaffold commonly referred to as an apoprotein. The catalytic organometallic centre, usually similar to a known and well-characterised

homogeneous catalyst, acts as the main site of catalytic reactivity as an artificial cofactor. This element also contains a group that allows it to be anchored to the protein scaffold via covalent or non-covalent means. The protein scaffold contains a defined pocket within the 3D structure to which the metal centre can be bound. This pocket is analogous to the active site of a natural enzyme, providing a means of size exclusion and forced substrate orientation to drive stereoselective product formation. The binding pocket also contains the reciprocal binding group for anchoring the catalytic organometallic component. In a covalently anchored strategy, part of the ligand structure responsible for the formation of the catalytic organometallic centre is covalently bonded to the inner binding pocket of the protein scaffold, often through a mixture of mutagenesis and chemical modification[79] or the incorporation of a metal binding ligand during protein expression[80]. The metal centre can subsequently be coordinated to the ligand, establishing the organometallic catalytic centre within the protein scaffold. Alternatively, a non-covalent strategy can be employed to incorporate the organometallic catalytic centre. One of the most used non-covalent interactions is that of affinity pair bonding, such as the affinity pairing of streptavidin-biotin[81, 82], where one element of the pair is incorporated into the protein scaffolds binding pocket and the second element incorporated onto one of the organometallic catalyst centres ligands, enabling the non-covalent anchoring of the catalyst into the protein scaffolds binding pocket.

In work by Raines *et al.*[70] they proposed that when using an anchoring strategy, non-covalent anchoring offers certain advantages, such as not needing to rely on the chemical reactivity of the active groups within the protein scaffold to contribute towards the catalytic process. By not needing to modify the protein scaffold, particularly the catalytic binding site, it can be optimised independently of the catalyst before and during the formation of the artificial metalloenzyme. The other advantage of non-covalent anchoring is the potential of reverse binding of the organometallic catalytic centre to the protein scaffold. The reversible binding is particularly desirable for artificial metalloenzymes as the metals used within the organometallic catalytic centres are often high-value and precious earth metals. Therefore, reversibility means the organometallic catalytic centres can be recycled, and the empty apoprotein can also be regenerated through the non-covalent affinity binding of new catalytic centres. They, therefore, explored a redox controllable non-covalent anchoring strategy for the ArM. Iron-siderophore cognate periplasmic binding proteins (PBPs) can be found naturally within bacteria and provide the function of selective iron uptake. PBPs function naturally by strongly binding essential mineral Fe^{III} ion complexes through forming stable siderophore complexes, which can be taken into a microorganism. Once within the microorganism, reducing the Fe^{III} to Fe^{II} leads to the iron siderophore complex becoming less thermodynamically stable and more kinetically liable, leading to the dissociation of the Fe^{II} into the cell. Raines *et al.* proposed that modifying

siderophores with a well-established organometallic catalyst could then, through means of its natural ability to coordinate to iron centres reversibly, form a metal centre non-covalent anchoring strategy to the protein scaffold, giving a redox switchable artificial metalloenzyme assembly.

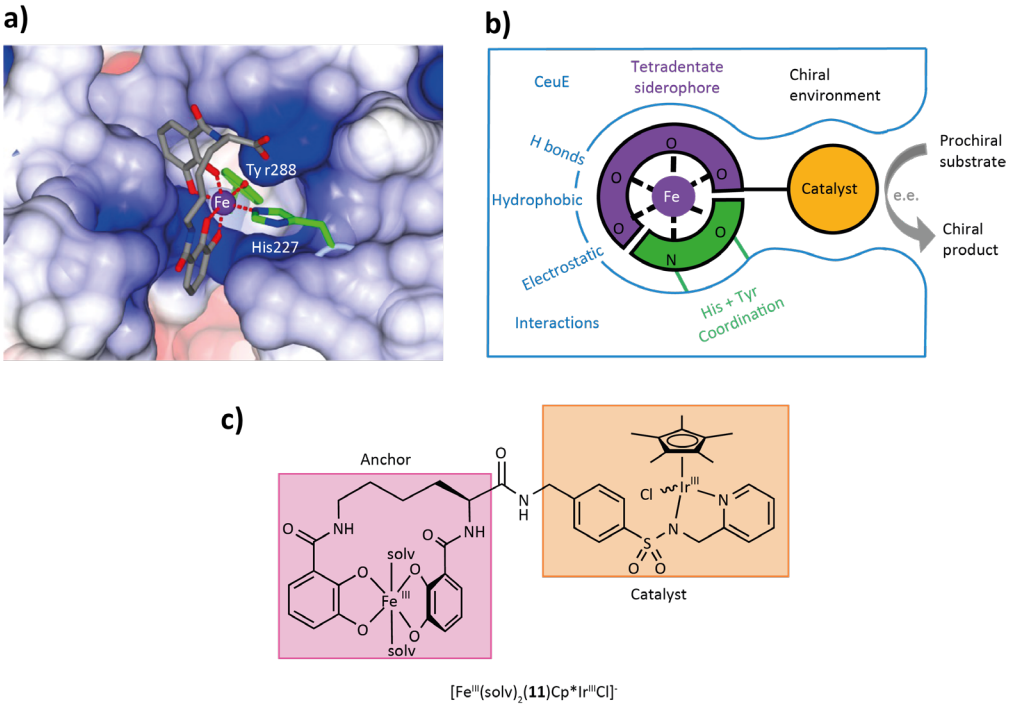

Figure 2.9 - Details on the ArM structure and design. a) The determined crystal structure for $[Fe^{III}(AZOTO)]^{2-}$⊂CeuE (PDB code: 5OAH) overlayed with azotochelin tetradentate siderophore binding. The CeuE is the electrostatic surface representation, Fe in purple, C within the Tyr288 and His227 in green, C within azotochelin is grey, O is red, and N is blue. b) A schematic for the non-covalent siderophore anchoring ArM strategy. C) The molecular structure of the azotochelin–catalyst conjugate, $[Fe^{III}(solv)_2(11)Cp^*Ir^{III}Cl]^-$. Figures are taken from the literature[70].

The work focused on the CeuE, which is the iron-siderophore PBP of *Campylobacter jejuni*, acting as the ArM protein scaffold, and the azotochelin (AZOTO), the siderophore of *Azotobacter vinelandii.* The work set out to modify the azotochelin siderophore with a well-established organometallic catalyst. The siderophore could then be selectively bound and unbound via the Fe-siderophore binding interaction within the apo-CeuE protein scaffold, which will conformationally dictate stereoselective catalysis (Figure 2.9b). Before modifying the azotochelin, active binding and dissociation of the azotochelin siderophore to the CeuE apoprotein were confirmed. By soaking apo-CeuE crystals with the $[Fe^{III}(AZOTO)]^{2-}$ complex, a protein structure with the bound siderophore was acquired via crystal X-ray diffraction (XRD), which showed the orientation and binding interactions within the protein coordination site (Figure 2.9a).

Additionally, optical spectroscopy of the $[Fe^{III}(AZOTO)]^{2-}$⊂CeuE construct showed a clear λ_{max} peak at 547 nm, which was lost upon reduction of the Fe^{III} species to Fe^{II} using sodium dithionite. The Fe^{II} indicator, ferrozine, was also added, leading to the solution changing to an intense magenta colour, indicating the presence of Fe^{II} and the successful dissociation of the azotochelin

and the CeuE. After letting the Fe^{II} to oxidise through prolonged exposure to air, the reforming of the $[Fe^{III}(AZOTO)]^{2-}\subset$CeuE construct was observed through the reappearance of the spectroscopic peak at 543 nm characteristic of the CeuE complex peak rather than the free $[Fe^{III}(AZOTO)]^{2-}$ complex which had a peak absorption λ_{max} at 572 nm. The fully assembled ArM system was then characterised and optimised, demonstrating a reduced turnover number (TON), which is the number of substrates converted per catalytic site before the enzyme is rendered inert, compared to the unbound siderophore. Despite this decrease in TON, there was a significant increase in the enantioselective production of the *R*-salsolidine product, showing an e.e. of 35.4 ± 0.1 %. The His227 residue within the binding site was identified as the predominant contributor to this increase in enantioselectivity.

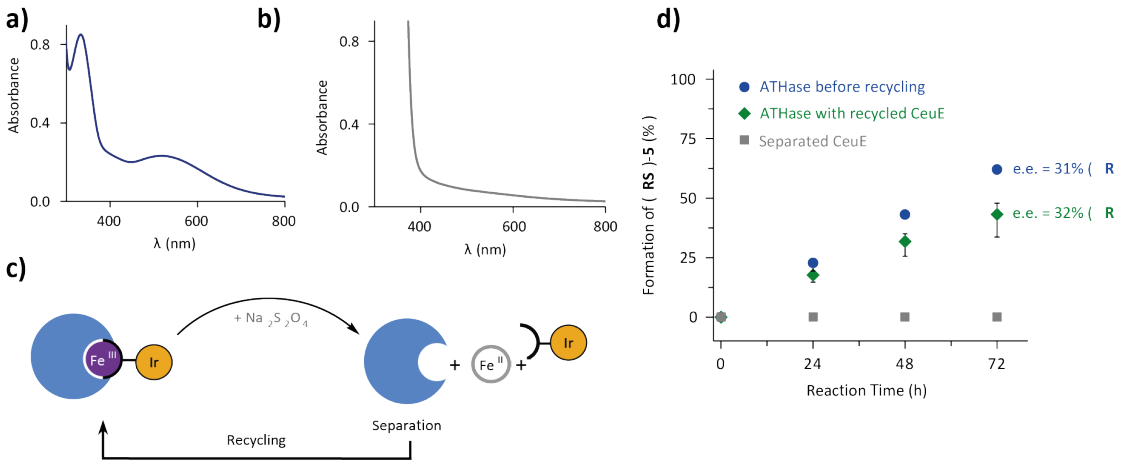

Figure 2.10 - a) Visual absorbance spectrum of the $[Fe^{III}(11)Cp^*Ir^{III}]\subset$CeuE ArM in solution. b) visual absorbance spectrum of the ArM after being dissociated by adding the reducing agent sodium dithionite. c) A schematic to represent the reduction of the Fe^{III} coordination centre for the chemically actuated release of the catalytic-siderophore conjugate, followed by the recovery and recycling of the CeuE apoprotein. d) The kinetic plots for forming *R*-salsolidine product over time for the original ArM, the ArM with recycled CeuE and the separated CeuE as a negative control. Figures are taken from the literature[70].

This work's particular area of interest is the reversible nature of the catalytic anchoring to the apo-protein through the iron-siderophore motif. The successful complexation and dissociation were first confirmed using visual absorbance, showing the clear profile for the $[Fe^{III}(11)Cp^*Ir^{III}]\subset$CeuE ArM (Figure 2.10a) and its absence upon its actuated dissociation (Figure 2.10b), through the reduction of Fe^{III} to Fe^{II} by sodium dithionite. After confirming the dissociation of the siderophore from the apoprotein through these means, the apo-CeuE was filtered and reconstituted for recycling using centrifugal microfiltering (Figure 2.10c). The successful isolation and integrity of the apo-CeuE were confirmed using SDS–polyacrylamide gel electrophoresis, circular dichroism and UV–visible spectroscopy before being re-complexed with fresh $[Fe^{III}(solv)_2(11)Cp^*Ir^{III}Cl]^-$ to reform the ArM. The kinetic activity of the $[Fe^{III}(11)Cp^*Ir^{III}]\subset$CeuE ArM for the enantioselective catalytic formation of *R*-salsolidine was tested before recycling and after dissociation, recycling and re-complexation, in addition to just the filtered and reconstituted apo-CeuE, as a negative control (Figure 2.10d). Although the rate

of catalytic conversion was slower in the recycled [Fe^{III}(11)Cp*Ir^{III}]⊂CeuE ArM, the stereoselectivity was maintained with an e.e. of 32. No turnover was observed in the negative control. The successful isolation of the catalysis-siderophore conjugate was only achieved to a small degree (15 % recovery) and at the detriment of the CeuE, which precipitated when one of the extraction solvents, ethyl acetate, was used.

Although the [Fe^{III}(11)Cp*Ir^{III}]⊂CeuE ArM impacted the reaction TON compared to the uncoordinated siderophore–catalyst conjugate, it showed significant improvements to the enantioselectivity, demonstrating the viability of ArMs. However, the real advantage that the work by Raines *et al.* demonstrated over other strategies for the development of ArMs was the switchable nature of the catalytic centre. Organometallic catalysts can become less active or inactivated due to poisoning or decomposition. Removing and recovering these precious metal catalysts, such as iridium, is not only financially and environmentally beneficial, but due to the possible retention and recycling of the protein scaffold, which is also expensive and time-consuming to express, the advantage to this reusable strategy is twofold.

As expressed in the work, the inability to successfully recover both the apo-CeuE and the catalysis-siderophore conjugate was not achievable in the extraction solvent used. However, the separation would be drastically simplified if the protein were immobilised, such as in an immobilised enzyme reactor (IMER) system. For this reason, one of the goals of this thesis was to investigate approaches to immobilise CeuE and a thermophilic homologue of CeuE, *G. stearothermo-philus* (Gst)[83] into a microfluidic flow device and demonstrate redox switchable binding of catalysis-siderophore conjugates for inflow biocatalysis and will be discussed in detail in a later chapter.

2.2 - Microfluidics and Flow Reactors

This subchapter includes an introduction to microfluidic theory, the basics of microfluidic device design and a summary of the range of microfluidic applications. The second half focuses on the simplified breakdown of flow reactor setups, the key areas of their design and construction, and a generalised review of their use within the literature and real-world applications.

2.2.1 - What is microfluidics?

Microfluidics is an area of research which focuses on systems in which fluid flow is confined to channels in the sub-millimetre range, and the flow properties begin to differ drastically from that of classical "macroscale" flow. This divergence from what is expected by classical fluid flow is one of the essential reasons that microfluidics are such a point of interest within many fields of research. Microfluidic research can draw its origins from microelectronic fabrication and analytical separation techniques such as gas chromatography[84], liquid chromatography[85] and electrophoresis[86]. The drive to develop analytical devices that use minimal sample quantities and were significantly smaller than conventional equipment led researchers to create capillary-like microchannels within silicon chips. It was the area of microelectronics that gave researchers the tools required to fabricate channels of this size with high precision and reproducibility.

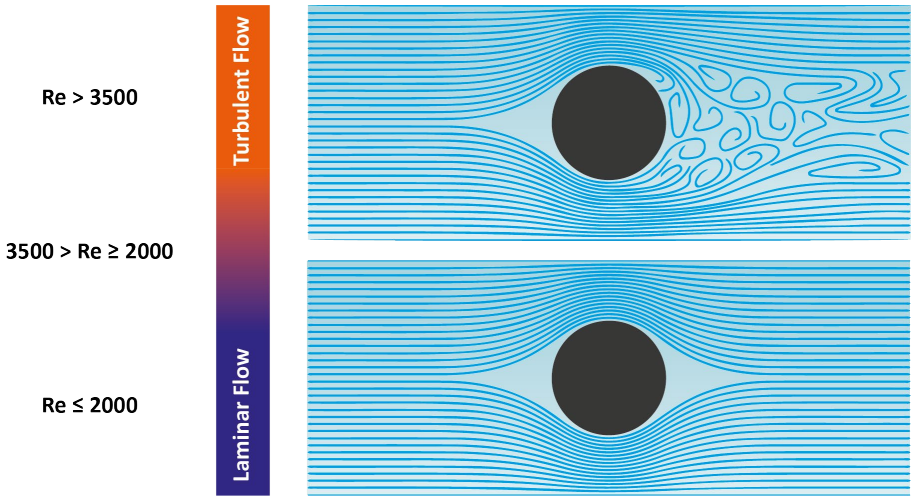

Figure 2.11 - A visual representation of the differing flow profiles between turbulent and laminar flow, including the approximate Reynolds number ranges. Figure modified from an original source[87].

Before the rise of microfluidics, many academics extensively studied and profiled the mechanics of microscale fluid flow. Arguably, one of the most significant differences between 'macroscale' and microscale flow is its flow profile. First discussed by Osborne Reynolds in 1883[88], laminar

and turbulent flow is essential to understanding how a liquid flows within microfluidic systems. Turbulent flow is usually observed within 'macroscale' fluidics, where when a flow current meets a spherical obstruction, vortices arise within the flow profile; hence, the description of it being turbulent flow. One of the only exceptions to this within 'macroscale' fluidics is when the fluid is highly viscous. In the case of microscale flow, the flow profile will not form vortices but instead goes around the obstruction to continue a linear flow profile, hence the name laminar flow (Figure 2.11). The nature of the flow profile is predicted using the dimensionless quantity known as the Reynolds number (Re). The following equation defines Reynolds number[89, 90]:

$$Re = \frac{Inertial\ forces}{Viscous\ forces} = \frac{\rho v d_h}{\mu} \quad (2.8)$$

Where ρ is the density (kg.m^{-3}) of the fluid, v is the velocity (m.s^{-1}) of the fluid, d_h is the hydraulic diameter (m) of the flow profile, or in reality, the fluidic channel and μ is the dynamic viscosity (Ns. m^{-2}) of the fluid. In turn, d_h can be defined by the equation:

$$d_h = \frac{4A}{P} \quad (2.9)$$

Where A is the Cross-sectional area of the channel (m^2), and P is the wetted perimeter of the channel (m).

Re, as defined in Equation (2.8), is the ratio of the inertial forces, which are the forces acting upon the fluid whose motion is described by the non-inertial frames of reference, such as the acceleration or rotation, to the viscus forces, which are the forces between the channel walls and the fluid flowing past it, acting in opposition to the direction of flow. Applying this equation to a given frame of reference within a microfluidic device makes it possible to calculate the Reynolds number of the flow at that given point. From this equation, it can also be deduced that increasing any of the inertial forces and decreasing the viscous forces will each individually cause an overall increase in the Reynolds number. Figure 2.11 shows how the expected cross-sectional flow profiles would look for turbulent and laminar flow if the path is met by a circular obstruction. Generally, a large Reynolds number, Re > 3500, indicates turbulent flow and a lower Reynolds number, Re ≤ 2000, indicates laminar flow. The flow profile for the middle ground, 2000 ≤ Re < 3500, is often referred to as transient flow[91]. Transient flow arises when flow parameters such as velocity or pressure are inconsistent, resulting in an erratic flow profile which is neither laminar nor turbulent.

From the equation for the Reynolds number (2.8), it can be deduced that within microfluidic devices, where hydraulic diameters are intrinsically small due to the size of the microfluidic channels, the Reynolds number is expected to be low, meaning the dominant flow regime most

commonly observed is laminar flow. When designing a microfluidic device, one of the first things that should be considered is the laminar flow and its impact on the flow profile within the channels. The result of laminar flow is a dramatic change in many flow profile properties from that of a turbulent flow regime. For example, in the turbulent flow regime, the meeting of two fluid flows results in the rapid mixing of the two streams due to the chaotic movement of the flow.

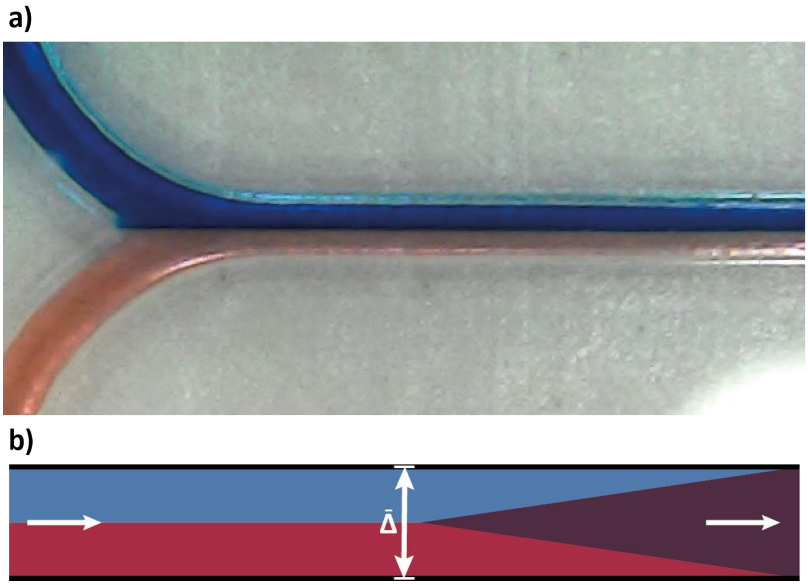

Figure 2.12 - An example of how diffusion dominates as the primary means of combining flows over mixing. a) is an example of laminar flow in a Y-shaped microfluidic channel made during this work. b) is a diagram demonstrating how the diffusion occurs over the time in flow for a given channel width, $\bar{\Delta}$.

In contrast, in a microfluidic channel, inertial forces are lower due to the diameter of the channels; viscous forces, therefore, predominate, which prevents the mixing of fluids. With no chaotic convection currents within the fluid flow, mechanical mixing cannot occur.

If two separate flows are combined to meet side-by-side within one laminar flow channel (Figure 2.12), the mixing of the two flows is diffusion-limited. The time, t, taken for diffusion to occur can be calculated using Einstein's diffusion equation[92]:

$$t = \frac{\bar{\Delta}^2}{2D} \qquad (2.10)$$

Where, $\bar{\Delta}$ is the diameter of the channel, and D (m^2) is the diffusion coefficient ($m^2.s^{-1}$). As the two streams can only mix via diffusion down the concentration gradient, this equation determines the rate of mixing for flow within a given width of channel and fluids with defined diffusion coefficients. It can also be seen that decreasing the diameter of the channel will also decrease the time for diffusion to occur and, therefore, increase the rate of mixing.

Despite the absence of chaotic convection currents in laminar flow, it is possible to design microfluidic channels so that additional inertial forces induce mixing through ordered convection

currents. Referred to as Dean vortices, these currents arise due to the combination of centripetal and centrifugal forces acting upon the fluid flowing with a parabolic velocity profile as it undertakes a corner or spiral[93]. According to Newton's second law, centripetal force is the net force acting on a body moving in a circular path and is directed towards the centre of rotation. According to this law, the centripetal force is a function of the body's mass and acceleration. The centripetal force can also be described by the angular velocity of a body about the centre point of the path's curvature. Centrifugal or inertial forces, again described by Newtonian mechanics, are the forces that act on the object when it is considered in a rotating frame of reference, that act away from the centre of rotation, as opposed to inwards as with centripetal force. The magnitude of this force is also a function of the radius of the curvature, the mass and the angular velocity of the body/fluid.

Experiments initially conducted by Dean in 1927 demonstrated that within a laminar flow regime, the maximum point of velocity for a fluid undertaking radial curvature shifts from the centre of the channel outwards towards the concave (outer) wall. This shift in the maximum point of velocity induces a strong pressure gradient along the horizontal middle plane of the channel, causing an imbalance in the flow pressure and velocity, known as Dean instability[94]. To compensate for this imbalance in pressure, a secondary flow profile forms perpendicular to the direction of the primary flow. This secondary flow profile consists of vortices above and below the horizontal middle plane of the channel (Figure 2.13).

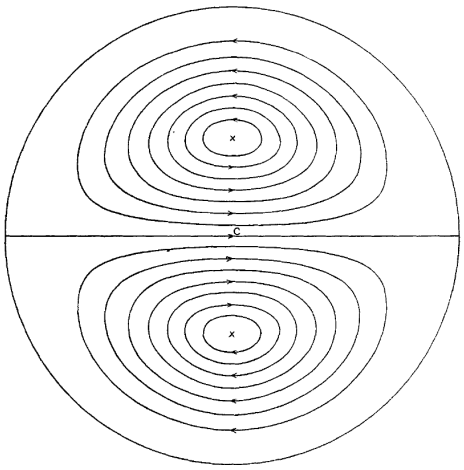

Figure 2.13 - Dean's original diagram[93] to illustrate Dean vortices, the lines showing the movement of the fluid within a cross-section of the spiralled channel. The LHS is representative of the convex wall, and the RHS is that of the concave wall.

Dean Vortices can be described by the non-dimensional number, known as the Dean number (De), and act to quantify the Dean force generated in the secondary flow of curved microchannels [93, 95]. The Dean number is defined by the equation:

$$De = Re\sqrt{\frac{d_h}{2r}} \qquad (2.11)$$

Where Re is Reynolds number as defined in equation (2.8), d_h is the hydraulic diameter (m) as defined in equation (2.9), and r is the radius of curvature of the path of the channel (m). The magnitude of this secondary flow is heavily contingent upon the cross-sectional area of the channel and the radius of its curvature. The cross-sectional area is also essential in defining the critical Dean number at which Dean vortices will occur, in addition to its role in forming secondary Dean vortices [95].

Channels with a low Dean number will show no or little of the secondary flow profile, but as the Dean number increases, the position of maximum velocity will shift closer to the convex wall. Ultimately, primary Dean vortices form at high Dean numbers to compensate for increased pressure and velocity gradients across the flow profile. If the Dean number increases beyond this point, the increasing centripetal and centrifugal forces cause the central point of the primary Dean vortices to shift closer to the concave side of the channel. This shift, in turn, leads to extra areas of pressure gradient within the flow. To compensate for this, an additional pair of vortices form to redistribute the pressure, splitting the cross-sectional flow profile into four quadrants of vortices (Figure 2.14). Dean vortices demonstrate how non-chaotic convection currents can be induced within a laminar flow channel by controlling the channel geometry, in this case, a curved channel of defined cross-sectional area.

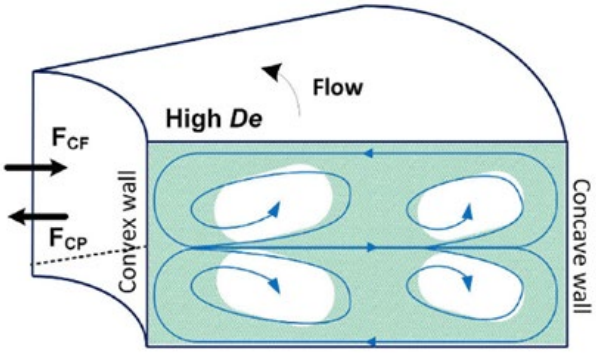

Figure 2.14 - A diagram to show how additional vortices form in flow profiles with high Dean numbers. F_{CF} and F_{CP} represent the centrifugal and centripetal force, respectively. Figure taken from the literature[95].

Another commonly employed means of overcoming the lack of mixing within a laminar flow regime is the introduction of herringbone patterning into one of the planes of the fluidic channel. First demonstrated by Stroock *et al.*[96], staggered herringbone mixers (SHMs), similar to spiral

mixers, work through the induction of transverse flow effects within the laminar microfluidic channel, generating quantifiable chaotic mixing.

In contrast to spiral mixers, where transverse flow is generated through centripetal and centrifugal forces that create a pressure gradient within the flow profile that is compensated for by the transverse flow, the axial pressure differential in herringbone mixers is instead generated through building anisotropic resistance to the laminar flow using asymmetric ridged features on one of the channel faces (Figure 2.15A). The ridged features, referred to as a herringbone pattern, are created within microfluidic channels using soft photolithography (3.3.1 - Soft Photolithography). The oblique angle of the herringbone ridges to the y-axis of the channel determines the degree of induced axial pressure gradient, which in turn causes the spiral cross-sectional flow profile and the asymmetric offset to that of the central channel that governs the direction of the streamline flow within the transverse flow effect. In the work by Stroock *et al.,* the direction of the herringbone pattern was alternated to increase the induced chaotic mixing further as it inverted the streamlined flow direction between ½ and 1 cycle (Figure 2.15B), only to repeat. Herringbone structures were not pursued as a microfluidic mixer within this work because serpentine channels were deemed a more simplistic means of inducing mixing in the first instance while increasing the channel footprint on the functionalised surface.

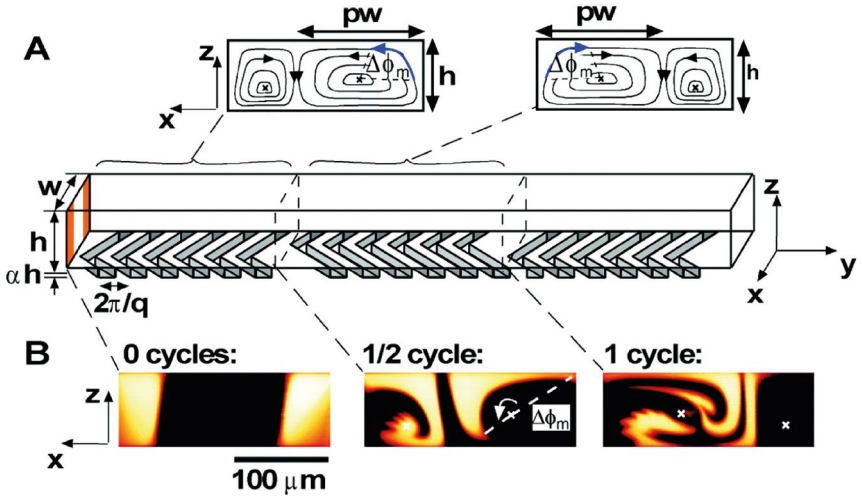

Figure 2.15 - The design of a staggered Herringbone mixer (SHM). A) the two mixing regions, with the asymmetric herringbone pattern and therefore streamline flow direction switching between regions, as illustrated above each respective area. B) The cross-sectional flow profile of the channel at the ½ and 1 cycle point as determined by confocal micrograms of two fluorescent streams introduced at either side of the channels x-z plane. Figure modified from the literature[96].

Fabrication of microfluidic channels is often time-consuming and costly due to the high degree of precision required for engineering small features in the micrometre range, from approximately 1 µm to 1 mm[97]. One of the most common approaches to fabricating microfluidic devices is via a master or mould fabricated using high-precision fabrication methods, from which many microfluidic devices can be cast, saving time and cost and ensuring reproducibility. There

are multiple ways of fabricating microfluidic device masters[98], including microcutting[99], laser ablation[100] and industrial etching techniques[101]. However, two other primary means of fabrication, soft photolithography (3.3.1 - Soft Photolithography) and stereolithography (3.3.2 - Additive Manufacturing via Stereolithography (SLA)), were used within this work and are covered extensively in this thesis's methods chapter. Once fabricated, the microfluidic chip is usually cast using a curable polymer such as PMMA[102], Polyimide[103] or PDMS. PDMS microfluidic chips are exclusively used in this work, cast from soft photolithography and stereolithography fabricated masters. Further details on casting PDMS microfluidic devices/chips are given in the method section (3.4.1 - Casting of PDMS Microfluidic Chips).

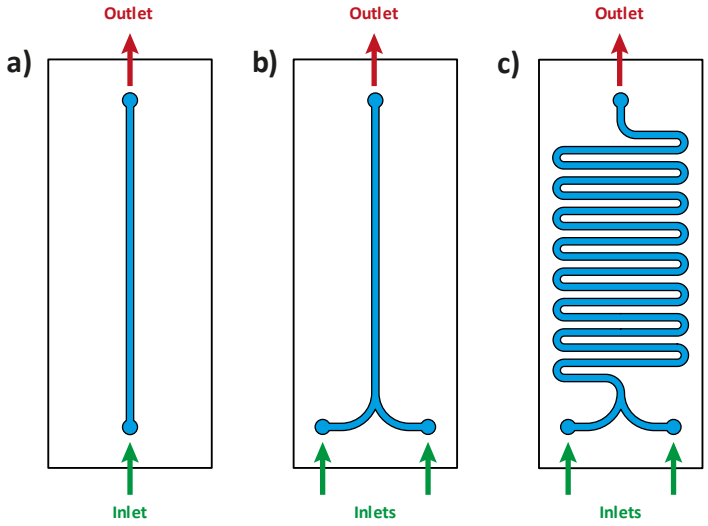

Figure 2.16 - Simple microfluidic chip designs commonly used within the literature. a) single inlet linear channel. b) a double inlet (Y-junction) linear channel. c) a double inlet (arbitrarily chosen as an example) serpentine channel.

When designing a microfluidic chip, the pattern chosen for the microfluidic pathways is of primary importance and should be designed according to the desired function of the chip. The most simplistic pattern for a microfluidic device is a linear channel with one inlet and one outlet (Figure 2.16a). A microfluidic chip like this tends to be used for the most straightforward experiments, where the flow rate controls the residence time a solution/chemical species remains within the microfluidic channel between the inlet and the outlet. Two inlet, Y-channel linear channels (Figure 2.16b) are often employed for diffusion-controlled reactions, such as generating concentration gradients[104] or monitoring biomolecular interactions[105]. This Y-junction design channel can also be used for droplet generation[106], an area of microfluidics that has a range of applications, from microorganism detection to biomolecular synthesis [107, 108]. A third typical design of a microfluidic device is that of a serpentine channel, a meandering channel between inlet(s) and outlet(s) (Figure 2.16c). The meandering nature of the channel inherently increases path length and, therefore, the maximum residence time when compared to a linear channel at the same flow rate on the same-sized chip. Serpentine channels also have a larger footprint and increase exposure to the bottom substrate attached to form the channel. Within a

serpentine channel, there are also multiple radial paths, which can introduce ordered convection currents and increase mixing in the solutions, often a desired feature of many microfluidic devices. For these reasons, serpentine channels are used for microfluidic mixing, longer residence time microfluidic reactors, and inflow particle management such as inflow particle focusing[109] or particle separation[110].

Linear and serpentine channel microfluidic devices are only two of a considerable scope of potential designs, all with different purposes and applications, and computer-aided design (CAD) can be used to inform the optimal channel geometry[111]. One of the critical considerations when designing and fabricating a microfluidic device is the channel aspect ratio. It is essential to first consider the material used for the master substrate and the casting material, as their viscoelastic properties, both cured and uncured, will limit the aspect ratios of the design. As a general fabrication rule for PDMS devices, the aspect ratio (height: width) should be between 1:10 and 10:1; less than 1:10 results in sagging of the PDMS, while an aspect ratio greater than 10:1 is inherently unstable.

It is also essential to consider the physical and chemical conditions to which a microfluidic device must be exposed, in addition to considering physical requirements, materials and designs, working temperatures, flow rates and internal flow pressures. Increases in system pressure can result from higher flow rates, which cause a greater compression of the fluid, which in turn exerts pressure on the device walls. Due to the viscoelastic nature of PDMS, it can accommodate small fluctuations in system pressure better than most high-strength materials, but if subjected to prolonged higher pressures, it can often fail at contact points (inlets and outlets) or sealing points within the device (the clamped seal or the substrate bonding interface). Solvent and substrate chemical/biochemical compatibility with the chosen device materials is also a key consideration when designing a microfluidic device. If the materials are not chemically compatible with the desired application, the microfluidic device can degrade, leading to leaks, experimental anomalies and reactant/product leaching. PDMS is a material known for solvent swelling and its incompatibility with many organic solvents. Although it displays low amounts of swelling in aqueous buffers[112], it can often absorb/leach small molecule hydrophobic reactants[113] over long periods of use and reuse.

Microfluidic devices have been used for a range of applications, including biomolecular analysis[114], cell separation[115], nanoparticles synthesis[116], inflow crystallisation[117], cell microbiome culturing/organ-on-chip[118] and various drug discovery applications (including lab-on-chip designs)[119]. In relation to the work performed within this thesis, microfluidics has also been used in the design of immobilised microfluidic enzyme reactors (IMERs)[120], supporting the use of microfluidics in this work.

2.2.2 - The Design and Applications of Flow Reactors

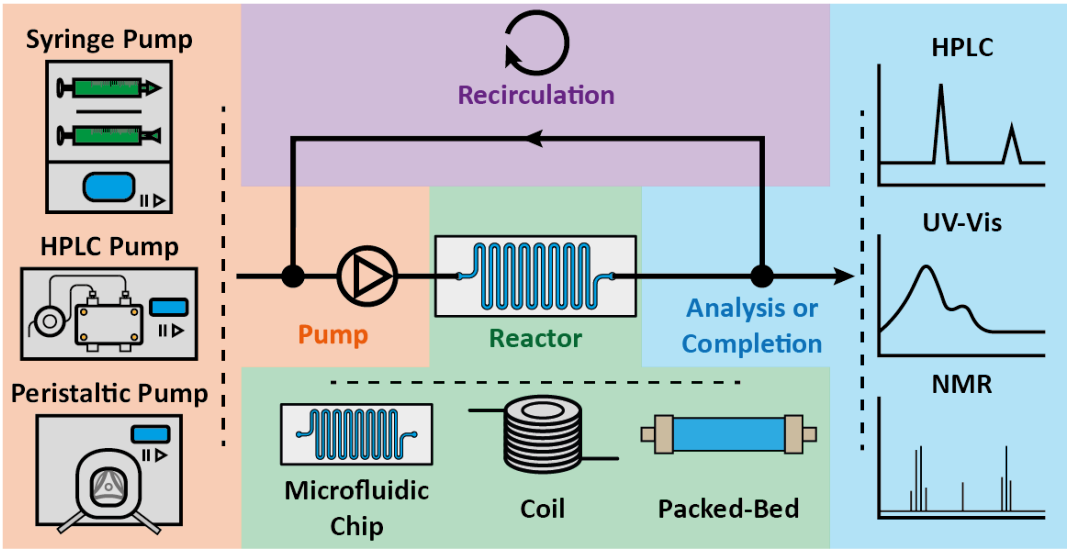

Figure 2.17 - A schematic breaking down a generic reactor setup into its most simplistic components with examples: a means of pumping/driving the fluidics (orange), a reactor in which the chemical processing takes place (green), the ability to run or recirculate the reactant (purple) continuously, and a means to analyse and monitor product formation, and collect it upon completion (blue).

Flow/process chemistry is an incredibly vast and well-established field that has been in industrial use for many years and continues to grow[121-123]. Flow chemistry can be summarised as an automated means of inflow chemical processing with high levels of system and reaction condition control. Although these systems' complexity varies drastically, a flow reactor's standard fundamental elements will be presented here. These four essential elements consist of a means of driving the fluidics (often referred to as fluid delivery), a reactor in which the chemical processing occurs), product analysis typically focussed on quantification to determine reaction completion, product collection, and in the case of this work particularly the recirculation of unreacted reagents (including system automation and control) (Figure 2.17).

2.2.2.1 - Flow reactors: Fluidic pumps

Numerous mechanical pump types are used to drive fluid flow, with various advantages and disadvantages according to their precision, flow speeds, fluid capacity, operating conditions, chemical compatibility and cost. One common form of pump used within reactors is the syringe pump. The syringe pump consists of a syringe driven by a drivescrew attached to the pump motor to infuse (push the fluid forward) or withdraw (pull the fluid back) the fluid from the syringe. The accuracy, size of the syringe, and flow speed will vary depending on the model/brand and the

cost of the pump. One of the advantages of syringe pumps is that the desired volume and chemical compatibility are determined by the syringe attached to the pump, which can be additionally chosen to best fit the reactor conditions without requiring an entirely new pump or fluid handling module. An often-quoted disadvantage of syringe pumps is volume limitation due to the size of the syringe for continuous flow[123]. However, dual-driver systems, which can handle two syringes simultaneously, can be used in parallel with valves to create a continuous flow system, similar to the inner workings of dual-piston in-parallel HPLC pumps.

As the name suggests, HPLC pumps were initially developed for HPLC systems, offering high pressures (and therefore flow rates) at high accuracy and often with good chemical compatibilities. There are numerous internal designs for HPLC pumps, such as single-piston reciprocating, dual-piston in-parallel and dual-piston in-series pumps[124], but all work through the movement of a motorised cam-driven piston which withdraws and infuses the fluid according to directional valves, providing continuous fluid flow. The disadvantages of HPLC pumps are that they are one of the most expensive options, they are often limited to either a high or low operating pressure range and not both, and their piston seals are susceptible to damage from particles and gas bubbles[123].

Peristaltic pumps work through the concept of peristalsis (the act of compression and relaxation propagated down a given length of tubing) to provide pumping through the positive displacement of the fluid. This displacement is usually achieved using a motorised roller, which compresses the flow tubing and traps the fluid between two roller groves (like the meshed teeth of a gear), which then rotate, pushing the fluid through the tube and creating a vacuum that pulls more fluid between the rollers. One of the advantages of peristaltic pumps is that the fluid only makes contact with the tubing, lowering dead volumes and giving options for chemical compatibility by selecting the tubing material accordingly. Additionally, peristaltic pumps are comparatively inexpensive and can often run several individual flow channels at the same flow parameters at any given time. However, the fluid flow is pulsed, the magnitude of which depends on the number of grooves within the roller.

A pressure pump is another form of displacement pump that uses overpressure (or vacuum) to push/pull fluid from a sealed reactant-containing vessel (or collection vessel for vacuum systems). Pressure pumps usually utilise a feedback loop with an inline pressure sensor to adjust the overpressure to ensure a constant flow rate or system pressure. This feedback loop makes pressure-driven systems one of the most accurate regarding pressure, smoothness of flow and flow rates. Unfortunately, pressure pumps are often costly and are not best suited for high throughput purposes, such as reactor systems, as it is hard to achieve a closed loop system required for reactant recirculation as pressure pumps work through the application of a pressure

gradient across the system, which cannot be achieved in a closed system without complex considerations.

2.2.2.2 - Flow reactors: Fluidic reactors

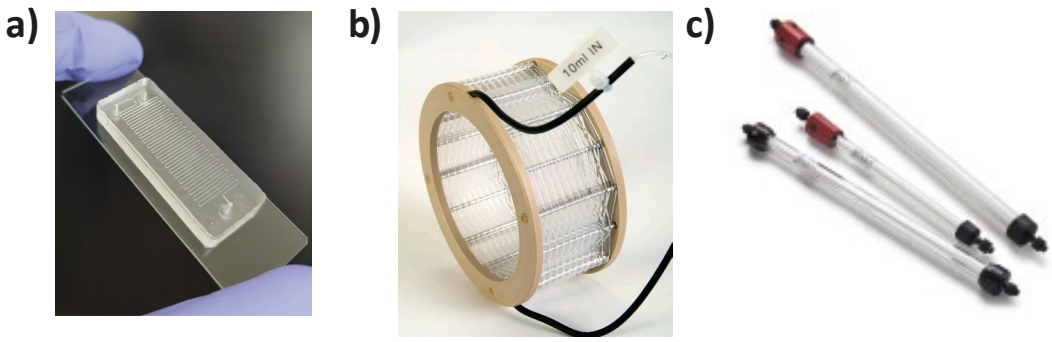

Figure 2.18 - Examples of the types of reactors used within flow reactor setups: a) PDMS microfluidic chip reactor fabricated in this work, b) PFA tubing coil reactor[125] and c) size exclusion columns (SECs)[126] often repurposed as packed-bed reactors.

Various types of reactors can be used within a flow reactor, but in line with the work performed within this thesis, this work will only focus on micro-reactors, the most commonly used being microfluidic chip, coil and packed-bed reactors. In the reactor, chemical processing occurs with control over reaction conditions such as temperature, light exposure, and mixing. In the case of catalytic flow setups, it is also the location at which the catalyst is present, either homogeneously or heterogeneously.

Microfluidic chip reactors consist of a set of fluidic channels created using microfabrication techniques, which can be sealed to create a small 'chip' in which the fluid will follow the fabricated pattern (Figure 2.18a). Temperature control can be achieved by placing the chip onto a heated platform, submerging it in a water bath, or building heating elements into the bottom substrate[127]. The fabrication and theory of these chips are extensively covered within this work (2.2.1 - what is microfluidics? & 3.3 - Fabrication Techniques). The primary advantage of microfluidic chip reactors is that the fluidic pattern can be designed according to the desired function of the flow reactor, allowing nuanced control over the flow profile, mixing and scope for much more complicated bespoke reactor systems. Soft lithography/stereolithography also allows multiple chips to be fabricated easily and rapidly, enabling chip upscaling by creating several reactor devices which can be used in parallel. One of the main issues with microfluidic reactors is that they require a significant amount of advanced fabrication expertise and equipment and significant time to optimise when created from the ground up. If purchased from a retailer, they are often costly and deprive the user of the distinct advantage of experimenting with the chip design.

Coil reactors consist of a set length of tubing wrapped around a central core, similar to a cotton reel, which is either heated or placed within a water bath to provide temperature control (Figure 2.18b). Coil reactors tend only to be used for either single-phase or liquid-gas phase chemical reactions due to the only surface exposed to the flow consisting of the inner tubing, but heterogeneous catalysis has been demonstrated using inflow nanoparticles[128] or through the coil material acting as the catalyst[129]. Their simplicity also makes them inexpensive to acquire and maintain; tubing of any chemical compatibility and diameter can be chosen, and the distance-controlled residence time/ reactor volume can be controlled through the length of the chosen coil.

Packed bed reactors are modified from columns used in chromatography systems, such as immobilised metal affinity chromatography (IMAC) and HPLC columns (Figure 2.18c). These columns can be packed with a solid heterogeneous catalyst or agarose beads modified with a solid enzyme/catalyst. Like coil reactors, packed-bed reactors are only applicable in set scenarios such as heterogeneous catalysis but are often very effective in these applications, offering a high surface area to volume ratio of the catalytic species to the solubilised reactant. Often, the columns of packed-bed reactors can be regenerated easily by the column being cleared and repacked with fresh solid material. The volume of the column determines the size of the packed-bed reactor and the amount of solid catalytic material used. The volume of the column is often a limiting factor for costly optimisation processes, such as initial high throughput screening, as some columns are relatively large compared to the preferred small volume of reactant solution or costly to functionalise when immobilising biocatalysts such as enzymes. Another disadvantage of packed bed reactors is that they often produce extremely high back pressures due to the flow-restricting nature of the packed column, which can often lead to leaks and inconsistencies in the flow reactors' performance[130]. System backpressure can be overcome by introducing a backpressure regulator to the flow reactor system, but it should be carefully considered to ensure chemical compatibility with the chemical reaction being performed.

2.2.2.3 - Flow reactors: Flow recirculation

Many continuous reactors are designed for the reaction to be completed in one pass of the reactor to produce a continuous flow of product. Longer residence times in single-pass reactors can be achieved by decreasing the flow rate[131]. However, the flow rate is limited by the operating parameters of the pump driving the system, and in turn, the residence time is determined by this flow rate range and the volume of the reactor system. So often, alternative means are

needed to increase residence times further. Recirculation allows for an incremental increase in the overall residence time and control of flow rate and reactor channel length. In the case of heterogeneous catalytic reactors, assuming that the catalyst has high reusability without activity loss, recirculation allows the use of smaller-volume reactors, which contain less of the catalyst. However, recirculation increases the complexity of the reactor through the need for automatic control systems to regulate the flow parameters, such as pump volumes, flow rates/pressures, number of cycles through the reactor and temperature conditions, in addition to the actual passive function of the reactor setup such as valve actuation and, if implemented, inline reagent analysis.

2.2.2.4 - Flow reactors: Product analysis

Approaches to determine the point of completion and analysis of the end product are often required. In the most simplistic case, the reaction can be left for an excessive amount of time in order to ensure completion. More complex systems collect aliquots of the reaction solution at precise time points, which can subsequently be analysed offline to determine the point of reaction completion. Such approaches also allow the determination of the reaction kinetics, potential side reactions, and optimisation of the reactor setup. Implementation again requires reactor control systems to define the time points at which aliquots are taken while accounting for the loss of system volume due to aliquot removal. Inline analysis can also be performed in which the reaction solution passes through an analytical system without requiring the reactant solution to be removed from the system. In such systems, analysis can performed at set time intervals or even continuously. Inline analysis is the least intrusive, labour-intensive and systematic approach to analysing flow reactions, but usually, such systems are specialised, expensive and complex to set up[121]. The sort of analytical techniques that have been used, in line or otherwise, for the quantification and characterisation of continuous reactor solutions are IR spectroscopy, UV-Vis spectroscopy, HPLC, GC, NMR and mass spectrometry (MS)[121, 122, 132, 133].

2.2.2.5 - Flow reactors: Applications

The applications of flow reactors can be categorised as transformers, generators and chemical assembly systems.[121] Transformers perform chemical transformations by enabling chemical reactions between given reagent species. Transformer reactions can be achieved through direct reaction, catalysis or biocatalyst. Some examples of transformation reactions demonstrated

within flow reactors include catalytic aerobic oxidation of alcohols to aldehydes and ketones[134], the selective reduction of esters into aldehydes[135] and enzymatic phosphorylation of alcohols[136]. Many of these reactions can be achieved classically through batch production. However, flow synthesis offers significant advantages over batch production, such as experimental condition optimisation analysis, continuous production of a product with the ability to readily upscale the reaction and precise control over the experimental conditions through reactor residence time, flow rate/system pressure, compensation of reaction atmosphere (such as under air, nitrogen or argon) and temperature ramping.

Generators are a class of reactors that perform the continuous *in situ* generation of highly reactive and often hazardous chemical intermediates and species, which can be later reacted inflow under highly controlled chemical and environmental (temperature, atmosphere and pressure) conditions to yield the desired product. Examples of some of the processes and reagents generated using generator continuous flow reactor setups are diazomethane formation for insertion of methyl and methylene groups[137], ethyl diazoacetate production for reaction aldehydes to yield 2-keto esters[138] and photochemical generation of phosgene for the conversion of alcohols into chloroformates and carbonates[139]. Once again, these reactions can be performed via batch chemical synthesis, but as previously stated, the reactive chemical intermediates are unstable, hazardous or both. The ability to generate these reagents in situ under highly controlled environmental conditions significantly mitigates risk, as they are not directly handled and can be quenched before disposal within the reactor setup. It also ensures the rapid consumption of unstable products.

Chemical assembly systems (CAS) are flow reactors that combine multiple combinations of transformer, generator or transformer and generator systems to achieve a chemical production line, in which the starting reagent will undergo multiple processes to achieve a more complex product or array of products within a reactor. CASs have been used for various processes, from the synthesis of entire amino acid libraries[140] to the optimised, multistep synthesis of pharmaceutical targets[141]. Given the complexity of chemical product assembly in CASs, it is increasingly common to see control systems developed to automate the production line[133]. Recently, control systems have been demonstrated to automate the reaction and enable self-optimisation in real-time through advanced data analysis models and inline chemical analysis feedback[132].

2.3 - Immobilisation Strategies and Microfluidic Inflow Biocatalysis

This section consists of an introduction and in-depth literature review of enzyme immobilisation strategies and the field of microfluidic immobilised enzyme reactors (µ-IMERs). The first section includes a detailed summary of enzyme immobilisation, including an in-depth literature review of each method. The second section includes an introduction to the specific field of µ-IMERs, the area of study to which the work within this thesis belongs, and a review demonstrating current and novel applications for µ-IMERs.

2.3.1 - Chemical Immobilization Strategies for Enzymes

Immobilisation of enzymes onto a surface is employed in protein purification, biosensors, drug delivery and heterogeneous enzymatic catalysis. Accordingly, there are a significant number of substrate materials and strategies in order to facilitate immobilisation. Immobilisation can be broken into two categories: surface immobilisation and enzyme encapsulation.

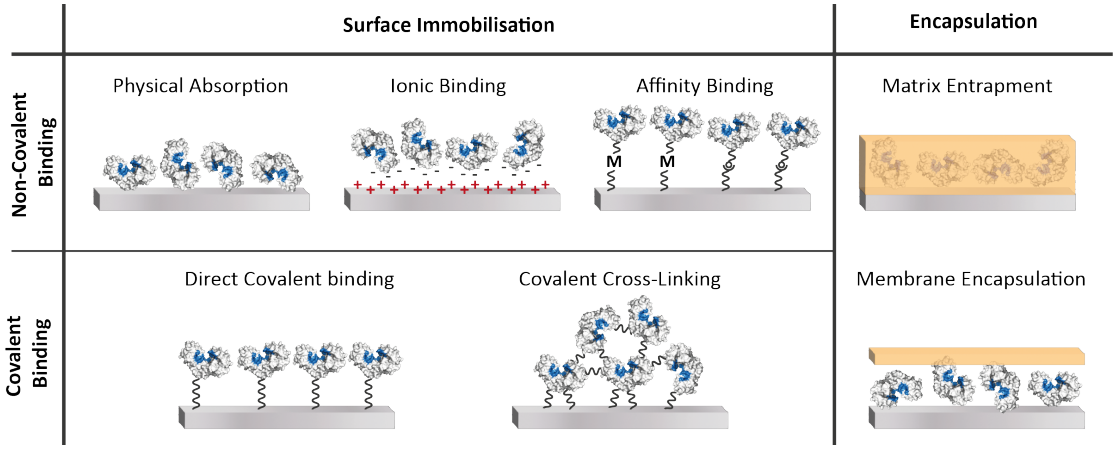

Figure 2.19 - Schematic diagram illustrating the various immobilisation strategies for enzymes and their associated categories. Inspiration for the figure from Ref.[120] and the hexokinase enzyme used under a Creative Commons licence[30].

Encapsulation methods utilise the confinement of the enzyme within a media while still allowing free movement of the substrate and the resultant product through the media. Enzyme encapsulation can be broken down into two predominant techniques: matrix entrapment and membrane encapsulation.

Matrix entrapment is a means of immobilisation where the enzyme is physically suspended in a matrix scaffold, such as a covalent-organic framework (COF)[142], metal-organic framework (MOF)[142] or hydrogel[143], which allows the diffusion of smaller molecules such as the substrate

and product. Matrix entrapment can be an effective and often uncomplicated means of enzyme immobilisation, with the additional benefit of offering a 'protective' layer from otherwise unfunctional acidic[144] or high temperature[145] conditions. Nevertheless, it is not without its complications, with a need for optimisation to ensure correct matrix porosity[144] and a risk of inhibiting the enzyme with potentially toxic constituents of the matrix[142]. The encapsulation of enzymes into MOFs has been a common area of study within the literature; with their ease of synthesis and well-established methods for tuning the pore size, where the enzyme would be trapped, they have been shown to be excellent enzyme matrixes[144-146]. There are many ways of achieving encapsulation of enzymes within MOFs; for example Liang *et al.*[145] suspended multiple enzymes, including lipase, horseradish peroxidase and urease in the MOF, Zeolitic imidazolate framework-8 (ZIF-8), a composite consisting of 2-methylimidazole coordinating to Zn^{2+} ions.

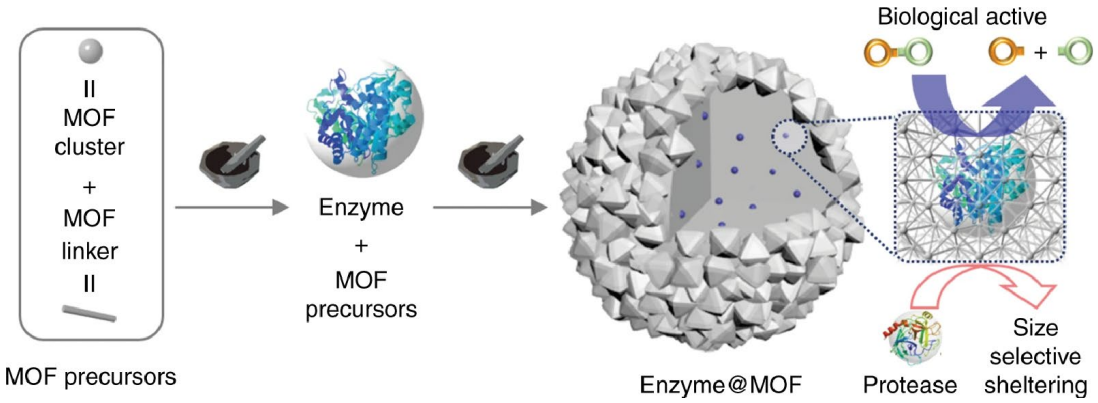

Figure 2.20 - A schematic to demonstrate the mechanochemical method of using MOFs for the matrix entrapment of enzymes while maintaining their biocatalytic functionality. The figure was taken from the litrature[144].

An alternative approach to encapsulating enzymes within MOFs is a solid-state mechanochemical strategy, as Wei *et al.*[144] show. In this strategy, enzymes are encapsulated via the ball milling method, where the enzyme and the desired MOF scaffold are solubilised and vigorously shaken in a reaction vessel that contains a solid zirconia ball which grinds the reactants into a paste (Figure 2.20). The resultant paste can then be washed under centrifugation and dried at room temperature to form the encapsulated enzyme-MOF matrix. Incredibly, it has been shown that the enzymes are undamaged despite the mechanical process. In work by De Hoog *et al.*[143], the enzymes Candida antarctica lipase B (CALB) and glucose oxidase (GOx) were separately entrapped within a polymersome hydrogel consisting of the block copolymers of polystyrene-poly(isocyanoalanine-(2-thiophene-3-yl-ethylamide)) (PS-PIAT). The CALB-loaded polymersome hydrogel was formed by incubating a mixture of Milli-Q water-solubilised CALB enzyme and PS-PIAT solution in THF overnight, with some additional filtration and resuspension steps. Once formed, CALB-loaded polymersome hydrogel was loaded into a gravity driven batch reactor, and the inflow activity of the immobilised lipase enzyme demonstrated, with a steady activity of 118+16 FI min^{-1}, in relation to the fluorometric assay of 6,8-difluoro-4-methylumbelliferyl

(DiFMU) octanoate (non-fluorescent) being hydrolysed to 6,8-difluoro-7-hydroxy-4-methylcoumarin (fluorescent) via the immobilised CALB enzyme.

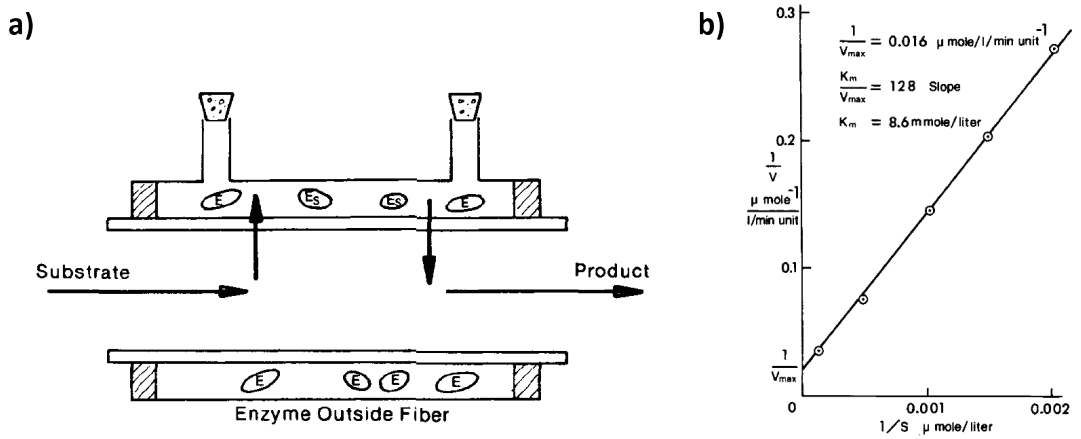

Figure 2.21 - a) The mini tube hollow fiber-dialyser flow reactor schematic. b) Lineweaver-Burk plot used to calculate the Michaelis constant, k_M, and determine V_{max}. The figures are taken from the literature[147].

In membrane encapsulation, the enzyme is immobilised and separated from the bulk reaction solution employing a semipermeable membrane such as porous hollow fibres,[147] that permits the free movement of substrate and product. Moreover, membrane encapsulation allows the use of relatively unpurified enzymes, as the membrane separates the unpurified enzyme from the reactant-product bulk solution, so the immobilisation is unaffected by protein impurites[147]. The disadvantage is that membrane-encapsulated systems are often rate-limited by bulk diffusion of substrates and products across the separation membrane. In early enzyme reactor work by Davis[147], the enzyme alkaline phosphatase (ALP) was encapsulated in the outer chamber of a miniature hollow fiber-dialyser.

A through-chamber in the middle of the fibre dialyser allowed the flow of the substrate, p-nitrophenylphosphate, and converted product, p-nitrophenol (Figure 2.21a). The system successfully demonstrated inflow catalysis, but as the units of enzyme concentration were not given, a TON could not be calculated, but other parameters, such as a Michaelis constant of 0.0086 M, were obtained (Figure 2.21b). Bulk diffusion across the porous hollow fibre membrane of the substrate and product was shown to be the rate-limiting step.

Rather than encapsulating the enzymes, surface immobilisation of enzymes focuses on binding the enzyme onto a solid surface. Surface immobilisation can be broken down into two subcategories: covalent and non-covalent binding.

Covalent binding is where the enzyme is bound to the surface via a covalent bonding interaction. There are two widely accepted approaches to covalent binding of enzymes: direct covalent binding and covalent cross-linking.

In direct covalent binding, reactive side chains on the enzyme surface are covalently bound to chemical moieties introduced onto the solid substrate surface. Direct covalent binding can be achieved using various chemical strategies such as EDC-NHS coupling/carbodiimide reactions[148] and Schiff base reactions[149]. The advantage of direct covalent bonding is that it offers a uniform monolayer of enzymes and stable tethering to the surface. However, as the bonding to the enzyme occurs via a commonly expressed reactive functional group within the protein structure, such as thiol, amine and carboxyl groups[150], the directionality of the binding cannot be controlled. This lack of control over binding location and orientation can affect the enzyme's functionality, blocking access to the active site and potentially causing the enzyme to denature.

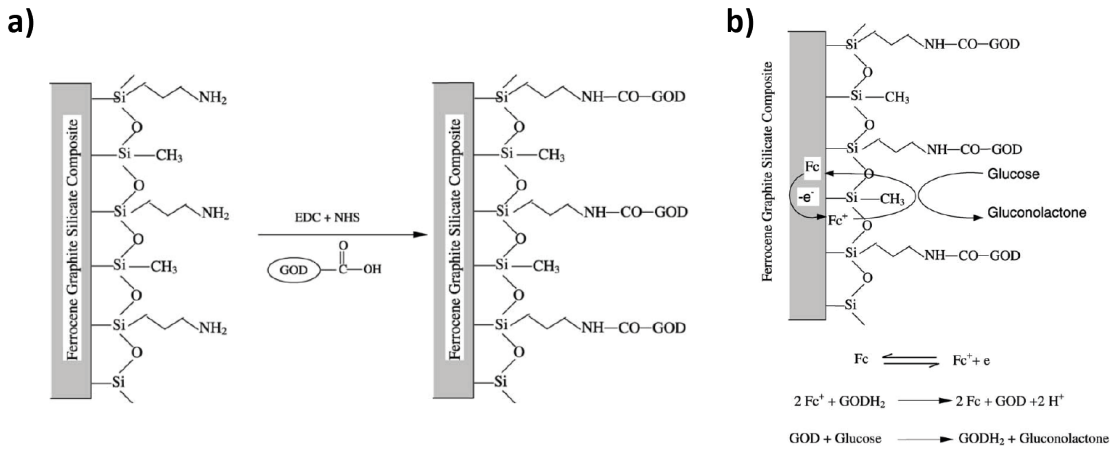

Figure 2.22 - a) The reaction scheme for the carbodiimide chemistry direct covalent immobilisation of glucose oxidase (GOD) onto a pre-functionalised hybrid sol-gel carbon composite electrode. b) The proposed electrochemical relationship of the catalytic reaction between the GOD and the encapsulated ferrocene within the electrode composite forms the basis of the glucose biosensor. The figures are taken from the literature[148].

In work by Yang *et al.*[148], a hybrid sol–gel carbon composite electrode was used in conjunction with carbodiimide chemistry for the direct covalent binding of the enzyme glucose oxidase (GOD). Here, direct covalent bonding of the enzyme occurs between free amine groups present within the backbone of the carbon sol–gel silicate composite electrode surface and carboxylic acid groups present within the protein structure of the GOD enzyme. The carboxylic acid residuals are reacted with 1-ethyl-3-(3-dimethylaminopropyl) carbodiimide hydrochloride (EDC) and *N*-hydroxysuccinimide (NHS) to form semi-stable NHS-Esters on the GOD enzyme that readily react with the surface-bound amine groups, to form a covalent amide bond, immobilising the enzymes to the surface (Figure 2.22a). The approach demonstrated a glucose biosensor in which the immobilised GOD enzyme catalyses glucose's oxidation to gluconolactone, forming a $GODH_2$ enzyme complex. The redox-active ferrocene, within the graphite silicate composite, then oxidises the $GODH_2$ complex back to GOD and 2 H^+ ions. The oxidative peak of the ferrocene can be monitored via cyclic voltammetry to measure glucose concentration (Figure 2.22b). As no direct kinetic studies of the activity of the immobilised enzymes were performed, it is hard to

assess the amount of enzyme that was denatured or otherwise rendered catalytically inactive due to the covalent bonding process.

In covalent enzyme immobilisation via cross-linking, sometimes referred to as cross-linking polymerisation, instead of covalently bonding the enzyme to the desired surface, cross-linker chemical reactions are used to immobilise the enzymes to the substrate and to one another, forming an interlinked network of cross-linked enzymes on the surface. Glutaraldehyde cross-linking reactions are a commonly employed chemical strategy for the covalent cross-linked immobilisation of proteins. The immobilisation uses glutaraldehyde to cross-link between reactive functional groups of the enzyme protein scaffold and another reactive polymeric agent, such as polyallylamine hydrochloride[151] or paraformaldehyde[152], forming a covalently cross-linked polymeric network that immobilises the enzymes. Covalent cross-linking offers an energetically stable means of immobilising enzymes, but due to it being a polymerisation reaction, it does not result in a near monolayer, but instead, a dense network of immobilised enzymes, the density of which can be hard to control. Also, due to the bonding interactions occurring with reactive functional groups on the enzyme surface, the probability of denaturing the enzyme is increased due to having no control over the directionality of the immobilisation. However, the increased concentration of enzymes that can be immobilised can often compensate for the loss of catalytically active enzymes caused by the immobilisation process.

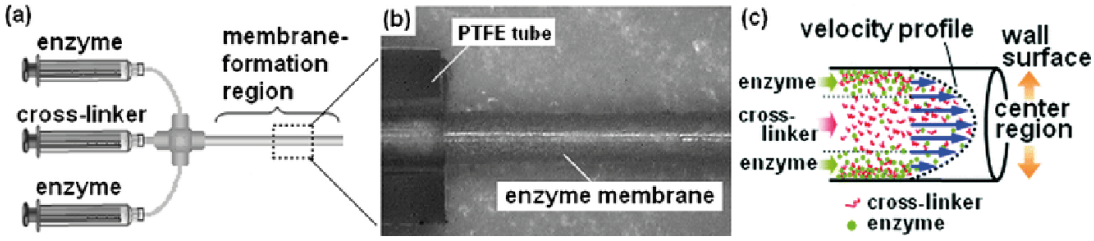

Figure 2.23 - a) The syringe-microfluidic tubing arrangement, with two syringes loaded with α-chymotrypsin solution, going into a cross junction connector perpendicular to the syringe loaded with the cross-linker solution and the outlet into the membrane-forming PTFE tube. b) the dried enzyme crosslinked membrane exposed from the PTFE tubing; when wet, it expands to line the tubing. c) the proposed schematic of the cross-linked polymerisation of α-chymotrypsin and the cross-linker agent within the microfluidic channels laminar flow profile. The figures are taken from the literature[152].

In work by Honda *et al.*[152], a glutaraldehyde (GA) and paraformaldehyde (PA) cross-linker agent was used for the covalent cross-linked immobilisation of the enzyme α-chymotrypsin onto the inner surface wall of a polytetrafluoroethylene (PTFE) tube, in the form of a surface lining polymerised membrane for its use in a microfluidic continuous flow reactor. This polymerised membrane was achieved by loading the solubilised PA and GA into a syringe connected to a four-way cross junction across from the PTFE tubing to be functionalised. The remaining ports on the four-way cross junction were then connected to syringes containing the solubilised α-chymotrypsin (Figure 2.23a). Due to laminar flow within the PTFE tubing, the enzyme and cross-linker agent each form diffusion-limited flow streams (Figure 2.12), the outer streams containing

the enzyme and the inner stream containing the cross-linker agent. As the system is left to flow over several hours, the enzyme adsorbs onto the hydrophobic PTFE wall, and as the cross-linker slowly diffuses into the enzyme flow stream, the GA bonds to the reactive functional groups of the α-chymotrypsin protein scaffold and the PA to form Schiff bases, which results in the formation of a covalently cross-linked polymer membrane onto the wall of the PTFE tubing (Figure 2.23b & c). This polymer membrane will continue to grow and thicken as other enzymes covalently cross-link to other enzymes immobilised within the membrane. Once fully formed, the membrane was treated with the reducing agent, sodium borohydride, to reduce the Schiff bases to more stable secondary amines. The GA-PA cross-linked α-chymotrypsin reactor was shown to have a Michaelis constant, K_m = 0.50 mM and a theoretical maximum rate V_{max} = 0.77 mM min^{-1}, successfully demonstrating the feasibility of this covalent cross-linker immobilisation strategy. The immobilisation strategy was also shown to significantly increase resistance to enzyme digestion over 40 days without affecting the enzymatic yield.

Non-covalent approaches to enzyme immobilisation can be categorised as nonspecific physical absorption, ionic binding, and affinity binding.

Nonspecific physical adsorption of enzymes is the simplest method for immobilising an enzyme to a surface, relying on attractive forces between the enzyme and the immobilisation surface such as van der Waals forces, hydrogen bonding and electrostatic forces of attraction, and hydrophobic interactions. Nonspecific immobilisation of enzymes has been demonstrated on various surfaces, often carbon-based, such as carbon nanotubes (CNTs)[153], nanodiamonds[154] or graphene oxide[155]. One of the advantages of this method, other than being simple, is that it usually only requires mild conditions and, therefore, causes minimal alteration to the protein scaffold and damage to the enzyme's catalytic function. The relatively low energy demands of the predominant forces within nonspecific physical adsorption mean the process is reversible to some degree, but this, in turn, means the enzyme can undesirably desorb from the surface. This low surface binding affinity is particularly an issue with any ionic, pH or temperature changes to the flow medium and system, as these can often more readily disrupt the physical adsorption interactions. Physical absorption of an enzyme to a surface is, therefore, more commonly used in conjunction with a secondary, more thermodynamically favourable immobilisation stage[152]. Cang-Rong *et al.*[153] immobilised the enzyme amyloglucosidase (AMG) via nonspecific physical adsorption onto single-walled carbon nanotubes (SWNTs) and multi-walled carbon nanotubes (MWNTs). Immobilisation was achieved simply by agitating the CNTs in AMG for 2 hours at 4 °C, followed by reconstitution via centrifugation to obtain the SWNT-AMG and MWNT-AMG conjugates (Figure 2.24). The activity of the CNT-AMG conjugates for the enzymatic hydrolysis of starch was quantified by monitoring the optical absorbance of a starch-iodine complex. While

this study successfully demonstrates nonspecific physical adsorption of amyloglucosidase onto carbon nanotube structures, the longevity, stability or buffer compatibility of these systems, were not quantified which would potentially demonstrate the inherent issues with this form of immobilisation.

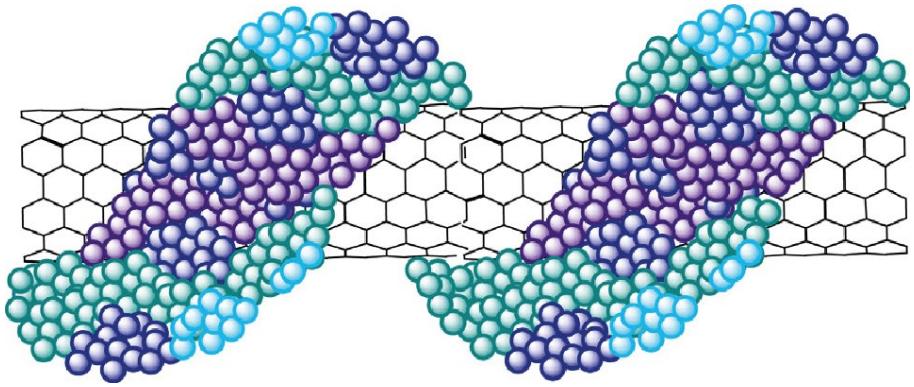

Figure 2.24 - A proposed diagram for the physical absorption of enzymes around a carbon nanotube, taken from the literature[153].

Ionic binding of enzymes relies on electrostatic interactions between charged functional groups within the enzyme and the opposing complementary charge on the immobilisation surface. Creating a surface that carries a complimentary charge to that of the enzyme and is stable in the desired solvent/buffer is essential to a good ionic binding strategy. Depending on their overall charge polarity, the chemicals used to coat surfaces to this effect are commonly called polycations or polyanions. Examples used within the literature are polyethylenimine (PEI)[156], polycationic electrolyte hexadimethrine bromide (HDB)[157] or polyelectrolyte polydiallyldimethylammonium (PDDA)[158] coatings. Like nonspecific physical adsorption, ionic binding offers reversibility of binding through buffer pH control but is typically more energetically stable.

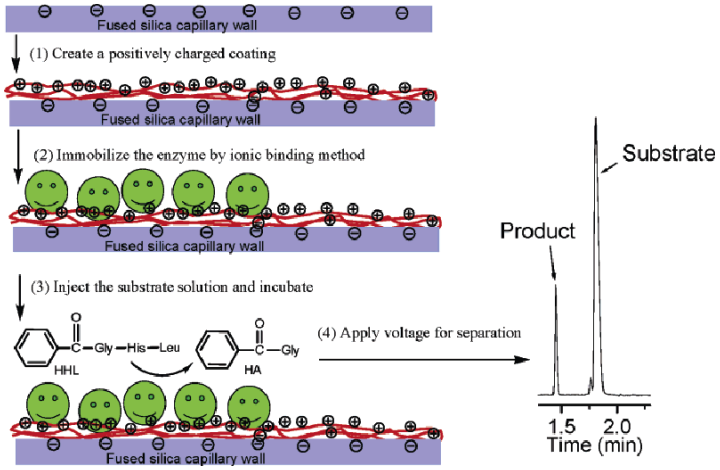

Figure 2.25 - Schematic to demonstrate the ionic binding method employed for the immobilisation of angiotensin-converting enzyme (ACE) onto a silica capillary channel wall for use as an enzymatic microreactor, as well as the subsequent assay reaction and means of characterisation. The figure is taken from the literature[157].

In work by Tang *et al.*[157], angiotensin-converting enzyme (ACE) was immobilised using ionic binding onto the wall of a fused silica capillary via a coating of the polycationic electrolyte, hexadimethrine bromide (HDB) to create an enzyme microreactor for enzyme inhibitor screening. The silica capillary was first prepared through a sodium hydroxide pretreatment to ensure the wall carried an overall negative charge that could then support the lining of the capillary walls with the polycationic electrotype HDB solution to create a positively charged coating. Once washed, the ACE solution (at pH 8.0) could then be loaded into the capillary and left to incubate, the enzyme ionically binding to the positively charged HDB coating (Figure 2.25). The catalytic activity of the ACE microcolumn was determined by following the enzymatic turnover of hippuryl-His-Leu (HHL) into hippuric acid (HA) using mass spectrometry (MS). While enzymatic activity was observed, the Michaelis constant was found to be lower than literature-reported values. Moreover, there was a 40% loss of activity over 300 cycles of substrate injections and a similar loss in activity following storage in buffer for ten days. By comparison, the free enzyme in solution was reported to lose activity after three days. While the long-term activity of the immobilised enzyme was improved compared to the enzyme in the solution phase, the loss of reactivity could be due to the loss of enzyme from the surface over time.

Affinity binding offers a more stable yet reversible method of immobilising enzymes that relies on ligand-metal binding or specific interactions between biochemical pairs with a high affinity for their formation. Moreover, the binding element can be conjugated to the enzyme and localised to a specific area of the enzyme's tertiary structure, meaning the active site can be left unaffected by the binding and even orientated away from the surface. This localisation of the conjugation is achieved by genetically modifying the protein structure, enzymatically assisted conjugation or utilisation of both, which can modify the protein conformation and influence enzymatic catalysis.

Complementary bio-molecular affinity uses a well-characterised binding interaction observed within biological systems. Antigen/antibody bonding interactions are one possible type of bio-chemical coupling reaction used to immobilise enzymes. Antigen/antibody pairs, such as the antigen Immunoglobulin G (IgG) and its paired antibody, anti-Immunoglobulin G (anti-IgG), have evolved to bind via non-covalent bonding interactions and sterically complementary structures specifically. By immobilising IgG onto a surface, it is possible to bind an enzyme conjugated to anti-IgG via the two molecules' specific interaction with one another[159]. Other commonly used complementary bio-molecular interactions for affinity binding are biotin-streptavidin[160], Strep-tag II[161] and DNA-directed immobilisation (DDI)[162, 163]. The enzyme is conjugated in DDI to a specific single-strand DNA (ssDNA) motif, and the ssDNA strand complementary to the enzyme-

conjugated DNA motif can then be immobilised to the desired surface[162 163]. The enzyme can subsequently be immobilised through Watson-crick base pairing between the ssDNA strands.

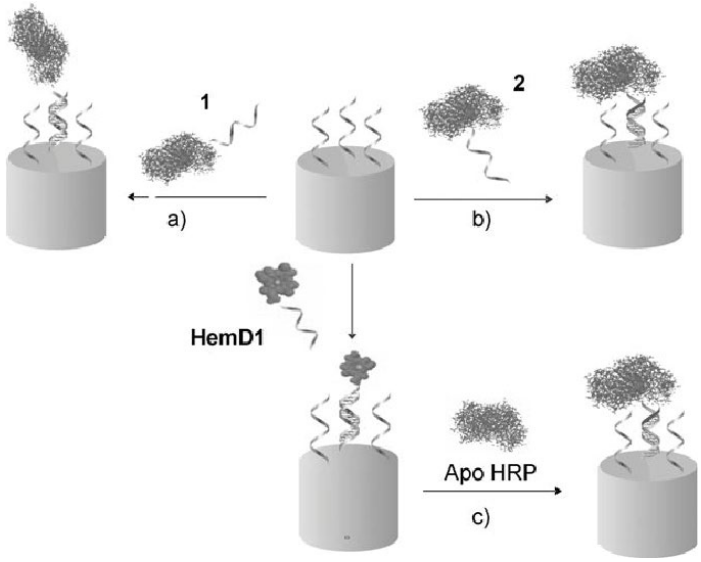

Figure 2.26 - A schematic to show the various methods of DDI affinity binding used within the work by Fruk *et al*. a) the covalent cross-linking of the oligonucleotide and the HRP approach to the DDI. b) the apo-HRP approach to the DDI. c) the *in situ* apo-HRP approach to DDI. The figure is taken from the literature[163].

An example of DDI for enzyme immobilisation was shown by Fruk *et al.*[163], where horseradish peroxidase (HRP) was modified with a single-strand DNA motif and coupled to a complementary strand of DNA, which was immobilised to a gold electrode surface through thiol-gold binding. The HRP-DNA conjugates were achieved via two different routes. The first used covalent cross-linking between any Lys-NH_2 residue on the HRP and a thiolated oligonucleotide (D1) using the heterobifunctional cross-linker sulfo-succinimidyl-4-(*N*-maleimido-methyl)-cyclohexan-1-carboxylate (sSMCC) (Figure 2.26a). The second used a modified HRP in which the prosthetic heme (protoporphyrin IX) group (apoprotein) had been removed. A heme apoprotein modified with the same complementary thiolated oligonucleotide was reconstituted within the heme-free HRP (Figure 2.26b). This reconstitution could be performed in solution or on the surface via the immobilised DNA-conjugated heme (Figure 2.26c). By monitoring the steady-state cathodic current within the solution due to the oxidation of *ortho*-phenylendiamine (PDA) in the presence of the immobilised HRP and hydrogen peroxide (H_2O_2), the kinetic parameters for each strategy were determined. For the first covalent cross-linking method, a K_{cat}' of 104 ± 1 pmol cm^{-2} s^{-1}, a K_M' of 44.6 ± 0.4 µM and a catalytic efficiency of 23 ± 1 × 10^{-4} cms^{-1} were obtained. For the second apo-HRP method, a K_{cat}' of 141 ± 1 pmol cm^{-2} s^{-1}, a K_M' of 56.5 ± 0.4 µM and a catalytic efficiency of 7.2 ± 0.5 × 10^{-4} cms^{-1} were obtained. While this demonstrates that the enzyme's activity is retained after immobilisation, there is a significant loss in catalytic efficiency compared to the free HRP enzyme. However, this could, in part, be due to the electrochemical approach used to quantify the kinetics of the immobilised enzyme. The work also demonstrated that the double-

stranded DNA could be melted and the surface could be regenerated, demonstrating the reversibility of this technique.

Enzyme immobilisation via metal chelate affinity exploits a genetically modified ligand tag expressed within the protein scaffold, allowing the enzyme to coordinate readily with a specific metal centre. The metal centre is additionally coordinated to another multidentate ligand with a high binding affinity, which is bound to the desired immobilisation surface. Metal chelate affinity as a strategy for the immobilisation of enzymes can be split into four key factors: the genetic addition of the affinity tag to the protein scaffold (the protein tag), the metal centre, the surface-bound ligand group and the surface immobilisation technique.

Protein affinity tags were initially developed for protein purification via immobilised metal affinity chromatography (IMAC) and remain their primary use. IMAC consist of resin-packed chromatography columns, which can coordinate and immobilise the tagged protein onto the resin matrix using metal chelate affinity binding. In this way, the expressed protein/enzyme is purified from the other proteins, amino acids and other undesired by-products of the protein expression process. Once rinsed, the protein can be 'stripped' from the column by interrupting the metal affinity interaction, resulting in a pure protein product. The same strategy provides a convenient and obvious means of enzyme immobilisation for purposes other than purification. Protein affinity tags are commonly expressed as recombinant proteins (2.1.1 - An Introduction to Enzymes) by genetic engineering the protein scaffold by inserting an additional peptide sequence to either the N-terminus or C-terminus of the protein polypeptide chain. The end at which the tag is expressed will depend on the specifics of the protein structure and the proximity to its critical features, such as the active site of an enzyme. This localisation of the tag motif means immobilisation via affinity binding offers a distinct advantage in that it gives control over the enzyme orientation upon binding.

The affinity tag contains several amino acids, which are selected with the correct conformational arrangement and appropriate functional groups that would coordinate to a metal centre as a multidentate ligand to increase the binding affinity according to the Chelate effect[164]. These desired characteristics have driven the development of standardised affinity-tag designs which demonstrate exceptionally high stability and affinity. The most commonly used is the His-tag[18], a peptide chain usually consisting of six histidine (His) groups but can comprise of ten or more. It has been shown that His demonstrates the strongest coordination interactions to both Cu^{2+} and Ni^{2+} metal ions[165], hence its use over other amino side groups. The greater the number of His groups, the greater the chelate effect and its potential to coordinate to multiple metal centres, further strengthening the protein immobilisation.

Various divalent metal ions can be used for the metal chelate affinity binding of proteins/enzymes. The most commonly used are Cu^{2+}, Ni^{2+}, Zn^{2+} and Co^{2+} [165]. When choosing which divalent metal to use, there are two observed trends to consider: affinity and specificity. The greater the affinity of the metal-tag interaction, the more considerable the amount of protein successfully immobilised, and *vice versa*. The observed binding affinity trend is $Co^{2+}<Zn^{2+}<Ni^{2+}<Cu^{2+}$ [165-167]. Specificity relates to the selective nature of the ligands to the divalent metal ion, where a decreased specificity means an increased likelihood that the metal ion will bind species other than the affinity tag expressed on the desired enzyme. The observed trend of binding specificity is $Cu^{2+}<Ni^{2+}<Zn^{2+}<Co^{2+}$. It should be noted that the relationship between affinity and specificity is reversed; therefore, when choosing which bivalent metal ion to use, there is a trade-off between these two desired properties. For the immobilisation of enzymes engineered with metal chelate affinity tags, Ni^{2+} is the most commonly chosen ion, as the amount of immobilised enzyme is often critical to ensure high catalytic activity.

Strategies for immobilising the metal centre to a surface the tagged enzyme can coordinate are broad and varied within the literature. The first factor to consider is how the metal centre can be bound to the surface. The metal centre to surface tethering will depend upon the chosen substrate material, and multiple approaches for different materials have been demonstrated, including thiol SAMs for attachment to Au surfaces[20, 168, 169], diazonium electrografting for use on electroactive electrodes[20, 170] and the use of NTA functionalised agarose gel[171]. The most common chemistry used to achieve coordination site vacancy and strong divalent metal ion chelation is nitrilotriacetic acid (NTA). NTA and its functional variants strongly chelate multidentate ligands, which coordinate to 4 of the 6 possible vacant coordination positions of the octahedral Ni^{2+} molecular geometry. The NTA functional group is typically placed on the opposing end of a molecular chain anchored to the solid support surface. Ni-NTA functionalised surfaces have become synonymous with His-tag binding due to their widespread use within IMAC purification, especially with agarose and Sepharose packed bead columns, which are functionalised with terminal NTA groups and charged with Ni^{2+} ions.

Although not used for the explicit immobilisation of enzymes, instead as a means of immobilising His-tagged proteins as a whole, work by Bellare *et al.*[20] provides two potential routes of functionalising an electrode surface with an outward-facing terminal NTA group, to which a ferrocene functionalised His-tag and a fluorescently tagged His-tagged protein (recombinant *Staphylococcus aureus* Protein A), could be immobilised via Cu^{2+} metal chelate affinity binding. The goal was to investigate two strategies that could be used for binding and releasing His-tag functionalised biomolecules and informed some of the strategies later explored and demonstrated within this thesis for the immobilisation of enzymes and ArMs.

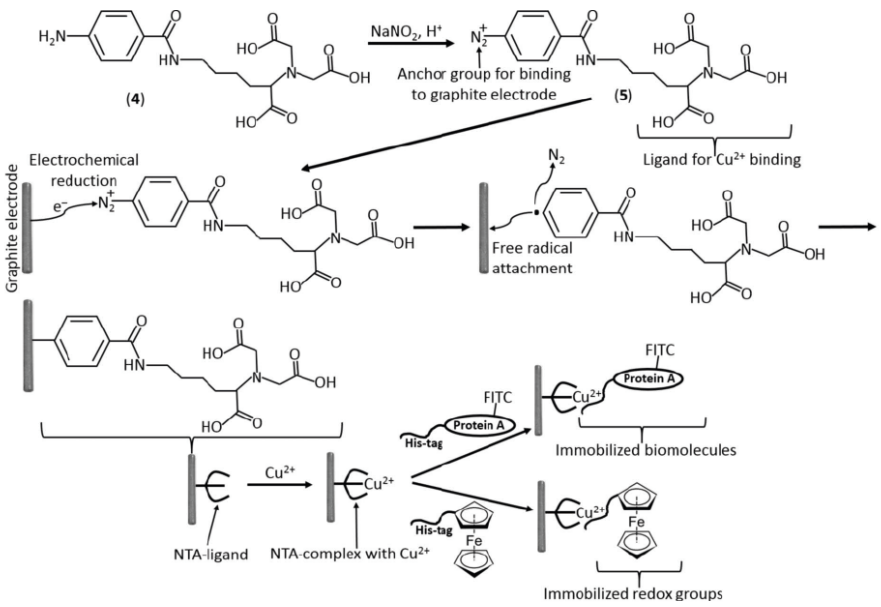

Figure 2.27 - Diazonium electrografting strategy for the grafting of the NTA-ligand, to then be used for NTA-Cu^{2+} chelate affinity immobilisation of both fluorescently tagged Protein A and a ferrocene-modified His-Tag. The figure is taken from the literature[20].

The first strategy for forming an NTA-ligand functionalised electrode used diazonium salt electrografting to covalently bond the NTA ligand via its terminal aryl group to the electrode surface (Figure 2.27). The starting compound NTA-ligand (Figure 2.27 - 4) first underwent *in situ* conversion of its aromatic amine group to form the diazonium salt NTA-ligand (Figure 2.27 - 5). The pre-polished pencil graphite electrode was then exposed to the solution, and a current was supplied via the means of cyclic voltammetry (0 to –1 V potential range (vs Ag/AgCl reference electrode) at 50 mV sec^{-1} for 30 cycles.). Applying this potential causes the diazonium species to become electrochemically reduced to form a radical aryl species and nitrogen gas. Free radical species that diffuse near the electrode will then interact with the surface of the graphite electrode to stabilise the highly reactive radical and form a significantly more energetically favourable covalent bond between the aryl group and the surface. This process forms a dense layer of the NTA-ligand electrografted to the surface of the electrode, which is then charged with Cu^{2+} ions to form the desired Cu-NTA complex for His-tag immobilisation. It should be noted that the radical species can often interact with other aryl species, including those bound to the surface, to form branched dendritic multilayers instead of a near monolayer[172].

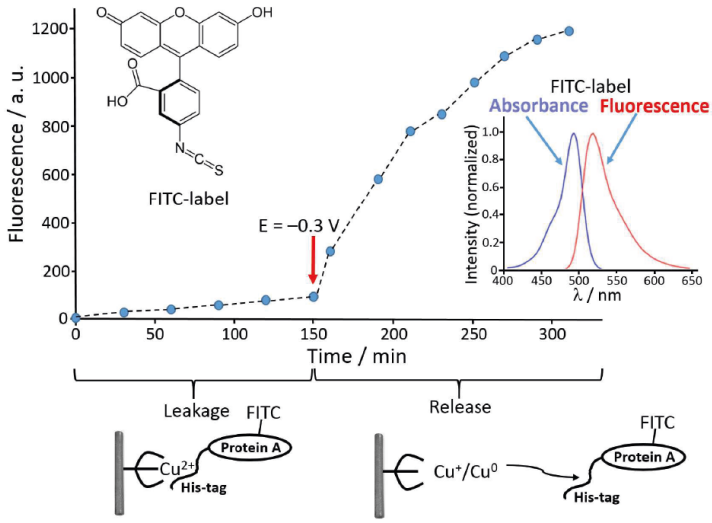

Figure 2.28 - Fluorescent profile for FITC-labelled Protein A within the electrolyte solution over time, before and after the electrochemically actuated release of the protein from its immobilisation to the Cu^{2+} NTA-ligand electrografted graphite electrode surface. The absorbance and fluorescence spectra for the FITC label are also displayed. The figure is taken from the literature[20].

The functionalised electrode surface was characterised using cyclic voltammetry at various stages of functionalisation leading up to the capture and release of a ferrocene-modified 6-His tag. After immobilising the His-tag ferrocene, a current peak at around 0.5 V vs Ag/AgCl was observed and ascribed to the coordinated ferrocene complex. This current peak subsequently reduced in magnitude following the application of a reductive potential of -0.3 V vs Ag/AgCl for 20 minutes, which is associated with reducing the Cu^{2+} ions to Cu^{1+} and releasing the His-tag ferrocene. The successful electrochemical release was further supported by an experiment to measure the electrolyte solution's fluorescence before and after the electrochemically actuated release of the FITC-labelled His-tagged protein A (Figure 2.28). Despite the slow desorption of the FITC-labelled protein A from the surface and into solution prior to electrochemical release, after applying the -0.3 V reductive potential, there was a significant increase in solution fluorescence. These experiments clearly illustrate that the protein was successfully immobilised on the surface using the metal chelate strategy for His-tag protein immobilisation and that, for the most part, they can be successfully released from the immobilisation surface.

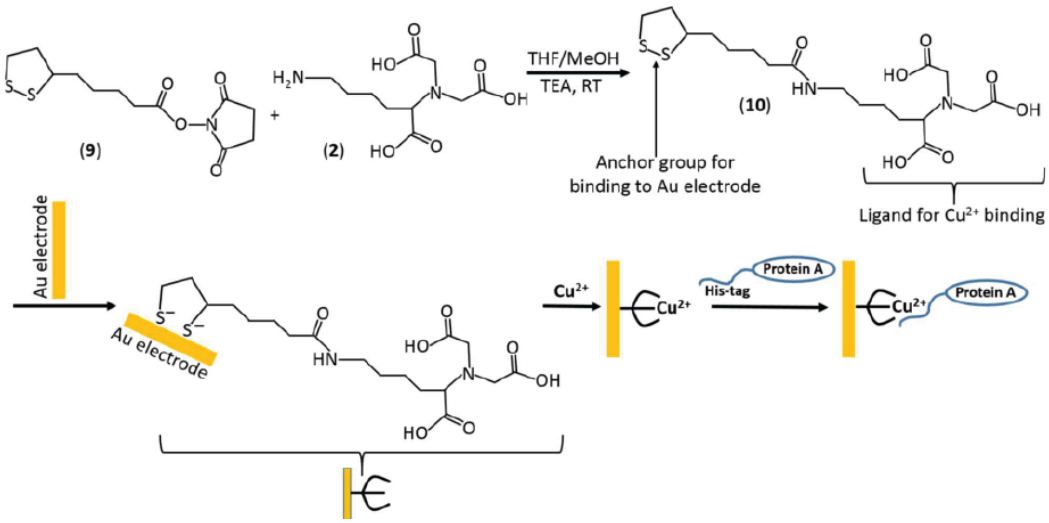

Figure 2.29 - The formation of the lipoic acid (thiol)-NTA-ligand, 10, to then be used for the Au-thiol functionalisation approach forming a SAM of NTA-ligands to be then used for NTA-Cu^{2+} chelate affinity immobilisation of the fluorescently tagged Protein A. The figure is taken from the litrature[20].

The second immobilisation strategy used the formation of an Au-thiol self-assembled monolayer (SAM), with the non-thiolated end of the ligand containing an NTA group (Figure 2.29). The strategy first required the prior formation of a lipoic acid-NTA-ligand (LA-NTA) (Figure 2.29 - 10), after which the disulphide bonds in the lipoic acid groups were reduced using Tris(2-carboxyethyl)phosphine hydrochloride (TCEP) to facilitate the formation of Au-thiol bonds. The solution was then drop cast onto the Au electrode surface and incubated overnight at 4 °C and 100 % humidity. During this time, the LA-NTA self-assembles on the surface of the gold electrode to form the desired LA-NTA SAM functionalised electrode surface. The surface was then charged with Cu^{2+} ions to form the desired Cu-NTA-complex functionalised surface for His-tag immobilisation.

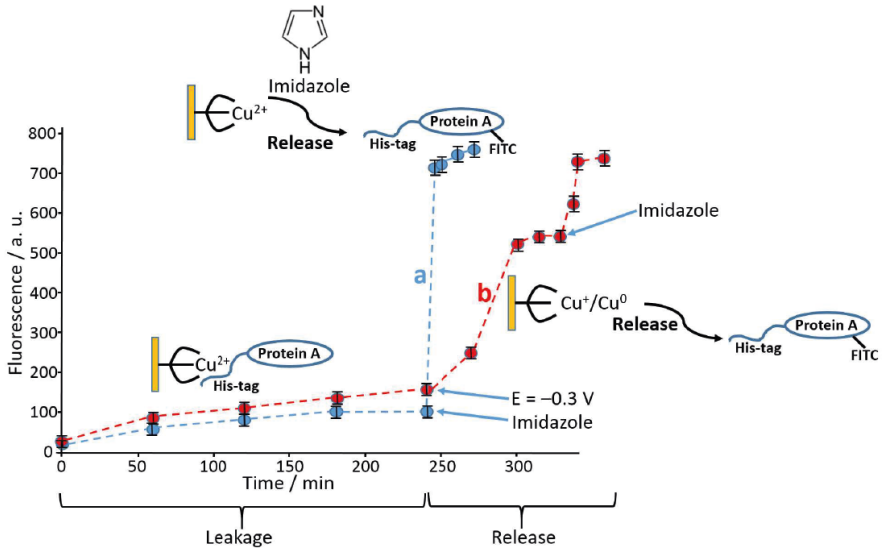

Figure 2.30 - Fluorescent profile for FITC-labelled Protein A within the electrolyte solution over time, before and after the chemically, a, electrochemically, b, actuated release of the protein from its immobilisation to the LA-NTA-Cu^{2+} gold electrode surface. The figure is taken from the literature[20].

Again, fluorescent measurements of the electrolyte were used to evaluate the reduction of the Cu^{2+} cation for the release of immobilised FITC-labelled Protein A (Figure 2.30). As with the electrografted method, the leaching of protein A was seen prior to its release. Electrochemical release by applying -0.3 V potential showed a significant increase in the electrolyte solution's fluorescence (Figure 2.30b). The chemical release of the His-tagged protein using imidazole was also explored, which showed a significant and dramatic increase in solution fluorescence that saturated at a higher value than was observed with electrochemically induced release (Figure 2.30a). This result was ascribed to the inefficiency of the electrochemical reduction. However, it could also be explained by non-specifically bound protein, which is less likely to be affected by the electrochemical potential but may be affected by the ionic nature of the imidazole solution, which can often disrupt non-specific binding interactions between proteins and functionalised surfaces.

This thesis used a similar electorgrafting and the same LA-NTA SAM approach for metal chelate affinity binding of a His-tagged enzyme and artificial metalloenzyme.

When considering the surface coverage of immobilised enzymes discussed later in this work, an approximation of protein size can be helpful to contextualise and rationalise these values. To get a cross-sectional area of a protein to compare to surface coverage, first, an approximate protein volume, V, needs to be calculated through the equation[173]:

$$V = \frac{\bar{\nu} M}{N_A} \qquad (2.12)$$

Where $\bar{\nu}$ is the partial specific volume (which is commonly assumed to be 7.3×10^{20} nm^3 g^{-1} for protein structures[173], and is used for calculations in this work), M is the protein mass (in Da/ g mol^{-1}) and N_A is Avogadro's constant.

The calculation of the protein radius can be drastically reduced in complexity by simplifying the protein shape to a sphere of radius r_{min} which can be calculated from the volume of a sphere equation[173]:

$$r_{min} = \left(\frac{3V}{4\pi}\right)^{\frac{1}{3}} \qquad (2.13)$$

Using the r_{min} and the continued simplification of the protein being spherical, the maximum cross-sectional area of the protein can then be found using the equation for the area of a circle:

$$A = \pi {r_{min}}^2 \quad (2.14)$$

Despite cross-sectional areas calculated via these methods being a significant oversimplification, as the shape of proteins is fully dynamic, the value holds merit as it gives an approximate value within an order of magnitude, allowing comparison with measured protein molecular coverage values to indicate whether the proteins are immobilised in mono- and multilayer assemblies.

2.3.2 - Microfluidic Immobilised Enzyme Reactor (µ-IMER)

As the name suggests, a microfluidic immobilised enzyme reactor (µ-IMER) is used in the literature to describe a chemical reactor system consisting of surface immobilised enzymes integrated with a microfluidic scale reactor. Continuous flow µ-IMERs offer many advantages over classical batch biocatalyst setups, such as fast mass transfer, small profile, high reproducibility, amenable to upscaling, low energy chemical operating conditions (such as lower temperature and pressure requirements), superior heat transfer, fine control over mixing, lower catalytic and substrate material requirements, increased stability, and rapid experimental optimisation.

µ-IMER systems have been demonstrated for various applications, from reactors for chemical sysnthesis[131, 174-176] and chemical processors for protein anaylsis[177] to tools in synthetic polymer characterisation[178]. Here, a review of a µ-IMER for continuous catalytic chemical synthesis is provided but would refer the reader to recent review articles on using µ-IMERs as continuous bioreactors for chemical conversion[120, 179] and analytical devices[179-181].

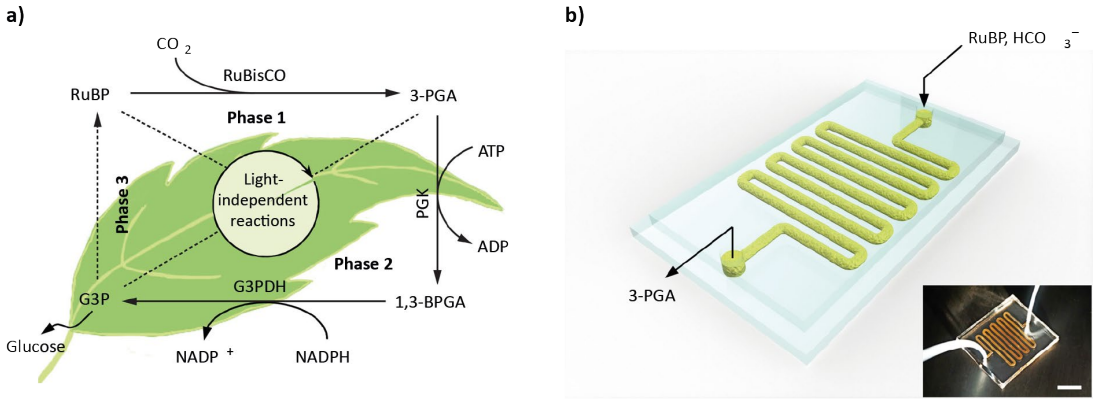

Figure 2.31 - a) Schematic of the biochemical light-independent reactions of the Calvin cycle responsible for glucose production, Phase 1 being the reaction of interest within this work. b) a 3D diagram of the microfluidic reactor used within this work, along with a photograph of the built RuBisCO immobilised microfluidic reactor (RIMR) with a 1 cm scalebar. Figures are taken from the literature[131].

Zhu *et al.*[131] compared a µ-IMER system for producing a precursor to glucose (a high-demand material for food production) to the traditional bulk reaction system. The precursor, 3-phosphoglyceric acid (3-PGA), is the phase 1 product of the first light-independent stage of the Calvin cycle (Figure 2.31a) and is produced by the biocatalysed reaction of CO_2 and ribulose 1,5-bisphosphate (RuBP). The reaction is catalysed by the enzyme Ribulose-1,5-bisphosphate carboxylase/oxygenase (RuBisCO). Here, RuBisCo was immobilised in a PDMS chip reactor (Figure 2.31b), referred to as the RuBisCO immobilised microfluidic reactor (RIMR).

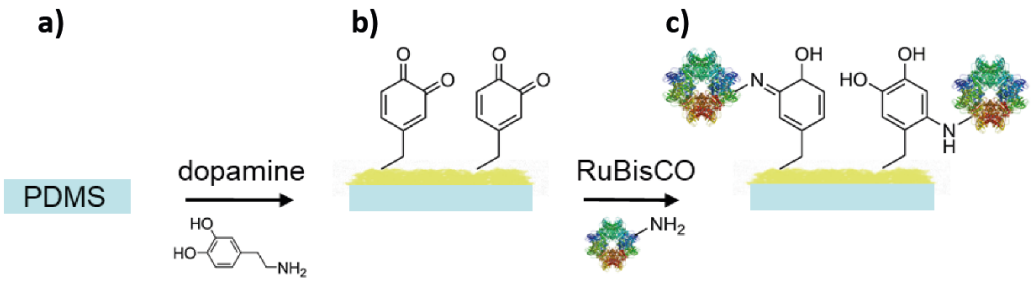

Figure 2.32 - Schematic of the proposed RuBisCO immobilisation strategy, illustrating a) the unfunctionalised PDMS chip, b) the exposed catechol groups within polydopamine functionalised inner channels of the chip and c) the immobilisation of RuBisCO [131].

The immobilisation strategy consisted of functionalising the inner channel walls of a PDMS microfluidic chip using the biochemical adhering agent dopamine, which will polymerise and coat surfaces in a polymeric layer of polydopamine under basic conditions (Figure 2.32b). The polydopamine was subsequently functionalised with RuBisCo through the reaction of catechol groups to that of thiol and amine groups on amino acids within the protein scaffold structure[182] via Michael addition or Schiff base reactions[183] (Figure 2.32c).

The formation of 3-PGA was quantified by coupling the product with a biochemical assay that leads to the oxidation of NADH, which has a distinct absorption peak within the UV-Vis range. The enzyme kinetic parameters of the RIMR system were compared to that of the conventional bulk reaction under identical conditions and comparable enzyme concentrations. The Michaelis constant, K_m, was notably higher for the RIMR than that of the bulk reaction (0.070 ± 0.012 compared to 0.049 ± 0.008 mM, respectively). This increase indicates a lower substrate affinity in the immobilised RuBisCO enzyme than the free enzyme. The authors comment that this is a '*common and intrinsic weakness of immobilized enzymes, owing to the steric hindrance introduced by the coverage of some active site by the support*' and can potentially lose '*flexibility to bind the natural ligands during catalysis*'. This statement highlights the limitations of non-specific immobilisation approaches such as polydopamine and the need for alternative approaches that enable immobilisation of the enzyme in the correct orientation to expose the active site.

Despite this loss in kinetic performance upon the enzymes' immobilisation, the work demonstrates some of the significant advantages of the RIMR over the free solution phase enzyme. For one, a study where the catalysis was tested daily showed that after 15 days, the RIMR demonstrated a 7.2-fold increase in longevity compared to the bulk reaction, with a 43 % retention of activity compared to 6 %, respectively. Additionally, the RIMR system showed significantly greater thermal stability, with a 6.7-fold larger maintained activity at 70 °C compared to the bulk reaction, with a 67 % relative activity compared to 10 %, respectively. The work also demonstrates that if a set concentration of RuBisCO is used in volumes of substrate solution above 600 µL, and at a continuous production of approximately 360 µmol g^{-1} RuBisCO, the

enzymes in solution reach saturation and no increase to production is observed past this point. In comparison, the RIMR shows a continuous increase in 3-PGA production with the volume of collected product, with no signs of enzyme saturation. This difference is attributed to an ever-increasing ratio of the RuBisCO quantity (which remains the same) to the bulk volume of reactant solution, which reaches a saturation point. On the other hand, the RIMR is unaffected due to the constant removal of product and refreshment of reactant solution to the immobilised enzymes, which also reduces feedback inhibition, displaying another advantage of the RIMR system over the bulk reaction.

The work by Zhu *et al.* showcases the advantages, potential and versatility of μ-IMERs from displaying increased stabilities, reusability, longevity and performance over classical systems, in addition to the advantages stated at the start of this subchapter. One area that has not been extensively researched within the area of μ-IMERs is flow automation and recirculation for enzyme reactors, most comprising simple single-pass continuous reactors. As previously discussed within the general flow reactor section (2.2.2 - The Design and Applications of Flow Reactors), automation and flow recirculation can offer distinct advantages over straight pass-through reactors, such as lower amounts of the enzyme being required, quantification of enzyme kinetics per cycle, immediate reaction scale-up, longer potential reaction times and an ability to display increasingly impressive reactor stability. For this reason, the development and demonstration of a simple, low-cost, automated recirculating μ-IMER setup were one of the aims of the work within this thesis.

Chapter 3 - Methods

This chapter comprises several subchapters introducing the various analytical techniques, fabrication methods, and standard operating procedures (SOPs) used and innovated in this work. Analytical techniques have been addressed according to whether they were applied to analyse a surface or a solution medium, regardless of their capability to analyse other mediums. In addition to providing an introduction to these techniques, the chapter also explains the theory of operation and the method for data analysis. The fundamental principles and details of the microfabrication process are also discussed within this chapter, including detailed protocols and experimental conditions required to replicate the later disclosed results. The final section of this chapter details the standard optimised treatment or synthetic procedures used repeatedly throughout the research and will be referred to within the relevant chapters accordingly. If a process is not disclosed within this chapter, it will be included in the relevant section of the experimental chapter.

3.1 - Surface Chemistry Characterisation Techniques

Unlike its solution phase counterpart, surface chemistry is notoriously hard to characterise with a singular technique; this is often because singular techniques come with their own advantages and many limitations[184]. Using multiple surface analysis techniques in collaboration instead can often overcome their singular limitations while corroborating results. Although some of these techniques described can also be used for solution phase characterisation, such as cyclic voltammetry and Fourier-transform infrared spectroscopy, in the context of this work, they were used exclusively for surface characterisation. This sub-chapter outlines the theory and application of the surface analysis techniques within this work.

3.1.1 - Quartz Crystal Microbalance with Dissipation monitoring (QCM-D)

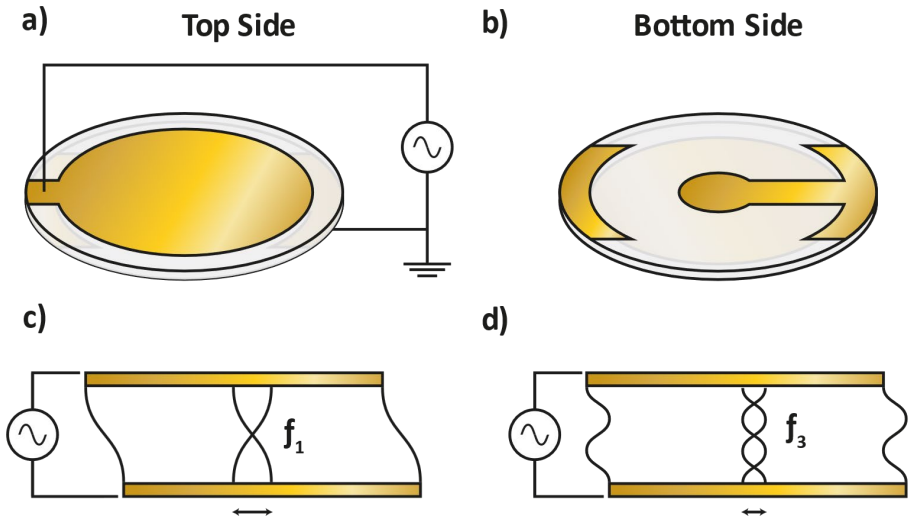

Figure 3.1 - The standard configuration of a QCM-D sensor, with a top face exposed to a liquid phase where the surface chemistries of the sensor can be modified. a) an oscillating signal is applied through the piezoelectric quartz via the top and bottom electrodes. b) the bottom side consists of the two electrode contact points. c) and d) various harmonics within the sensor can be probed via the analytical system, allowing for a more nuanced analysis of varying depths of the surface formed on the QCM-Ds top face.

Quartz Crystal Microbalance with Dissipation monitoring (QCM-D) is one of the few techniques that allow real-time information about the assembly of chemistry on surfaces, allowing for quantification of the mass that is bound[185], as well as giving insight into the kinetics of this process[186] and the viscoelastic nature of that chemistry[187]. One of the QCM-D system's main components is the quartz crystal sensor. The sensor consists of a circular disc of the piezoelectric material quartz, with the top surface comprising a modifiable layer, usually a metal, oxide or polymer, which sits above an electrode with an adhesion layer between the two, respectively

(Figure 3.1a). All QCM-D studies within this thesis used gold for the top functionalised surface. The bottom side of the quartz sensor consists of two electrode contact points, one connecting to the top side electrode and the other to the bottom (Figure 3.1b). When mechanical stress is applied to piezoelectric materials, it causes a net change in the overall electrical field established in the material[188]. This relationship also works in reverse; the piezoelectric material can undergo mechanical deformation by applying electrical energy. Thus, when an alternating voltage is applied between these two electrodes, the piezoelectric quartz between them oscillates at a distinct frequency. The quartz crystal thickness determines this resonant frequency, which can be monitored in real-time alongside the various harmonic overtones implicit with the oscillations (Figure 3.1c& d)[189].

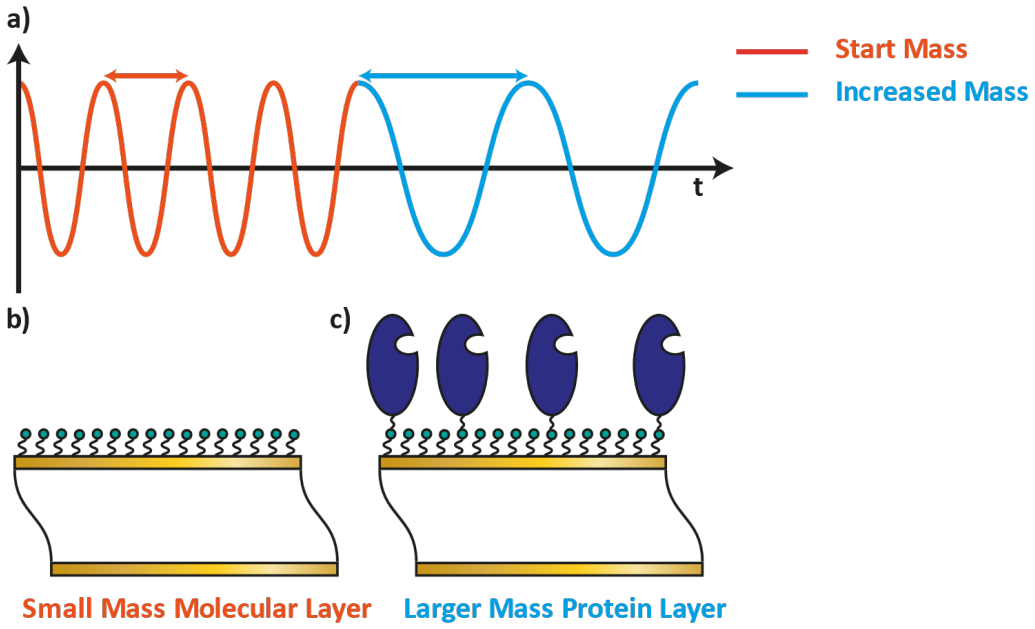

Figure 3.2 - Mass and frequency are linked through the physical properties of the quartz. a) The QCM-D sensor resonates at a set frequency according to its starting mass. When the mass of the sensor increases, it results in a decrease in resonant frequency. b) The surface layer is where the mass is altered via means such as chemical functionalisation. c) When the mass increases at the surface, the sensor frequency decreases accordingly.

When a mass is applied to the sensor's surface, it causes compression of the mechanical deformation, which in turn causes a drop in the frequency monitored in real time via the applied electrical signal (Figure 3.2). In the experiments performed within this work, the changing mass on the surface of the QCM-D sensor is due to either the chemical functionalisation of the surface or the desorption of molecules from that surface. The more significant the change of mass on this interface, the greater the resultant change in the frequency. The relationship between the frequency and the mass at the surface is most simplistically described by the Sauerbrey equation[190] (3.1), where Δm is mass change (ng), C is the calibration or mass sensitivity constant (ng/(cm2· Hz)), Δf is the frequency change (Hz) and n is the overtone number. It should be noted, the fundamental and harmonic overtones respond differently to changes in

mass at different depths and can be used to provide additional information about the structure of a surface-bound layer.

$$\Delta m = -C\frac{\Delta f}{n} \quad (3.1)$$

The calibration or mass sensitivity constant, C (ng/(cm^2· Hz)), is derived from the physical properties of the QCM-D sensor itself, where A is the piezoelectrically active crystal area (cm^2), μ_q is the shear modulus/ stress of the crystal (g/(cm·s^2)), ρ_q is the crystal density (g/cm^3), and f_o is the resonant frequency (Hz) (3.2). By knowing the properties of the 5 MHz sensors used within this work, C is calculated to be 17.7 ng/(cm^2· Hz)[189].

$$C = \frac{A\sqrt{\mu_q \rho_q}}{2{f_o}^2} \quad (3.2)$$

The dissipation factor or dissipation, D, is often defined as the inverse of the Q-factor or quality factor, Q^{-1} [191]. For this reason, dissipation can be described as the bandwidth, defined as twice the half-width at half-maximum 2Γ, divided by the resonant frequency of the piezoelectric oscillator, f (3.3).

$$D = Q^{-1} = \frac{2\Gamma}{f} \quad (3.3)$$

Another way of defining dissipation that could be considered more insightful in terms of its use in QCM-D is that it is equal to the energy lost (dissipated) per oscillation divided by the total energy within the oscillating system. This energy loss per single oscillation can be attributed to the physical dampening of the piezoelectric crystal oscillatory motion[192]. Dissipation can thus be used to probe the viscoelastic properties of the surface-bound layer. If the surface-bound layer is rigid, energy loss due to dampening effects are low due to minimal inflow drag and more efficient conservation of vibrational energy, giving a low dissipation[193]. In the opposite case, when the layer is soft/viscoelastic, there is more significant inflow drag, and the conservation of vibrational energy is reduced, leading to an increased dampening in the oscillating system and a higher dissipation[194] (Figure 3.3). By monitoring changes in the dissipation, it is possible to infer many viscoelastic properties of the surface-bound layer and how these properties change in the event of changes to that layer.

The Sauerbrey equation (3.1) best describes evenly distributed rigid surface bound layers[189]; the moment this layer deviates from these properties, the more the equation approximates the bound mass[195]. The Sauerbrey equation does not account for the viscoelastic properties of longer, less tightly packed layers, leading to inaccuracy when applied to such systems. The validity of the

Sauerbrey equation is determined from analysis of both the magnitude of the dissipation and the amount of separation in the frequency response of the harmonic overtones[196]. In cases where these two indicators are large, more complex viscoelastic models need to be applied for a more accurate calculation of the surface-bound mass[197]. One of the most commonly used viscoelastic models is the Kevin-Voigt model, which gives insight into the mass, density and thickness of viscoelastic surface-bound layers[198]. Although this can be interesting and informative, applying this model to a given experiment requires assumptions regarding the molecular layer's mechanical properties, which are often poorly defined. As a result, only the Sauerbrey equation was used here to approximate mass and density changes within the QCM-D studies.

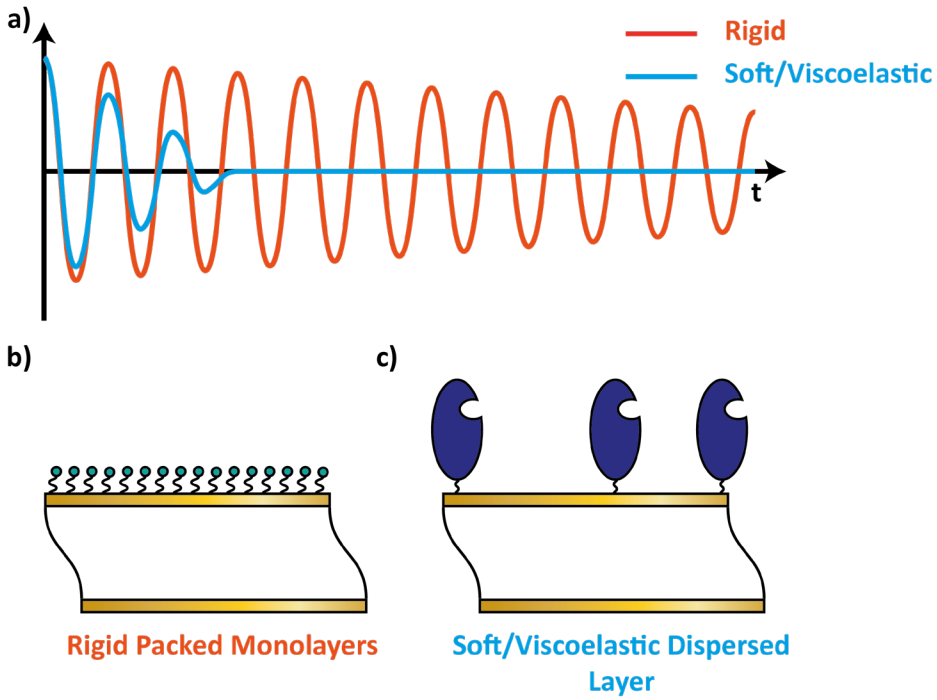

Figure 3.3 - The effect the viscoelastic properties of the surface-bound layer have on the dissipation of the QCM-D sensor. a) & b) A thin and rigid layer has little vibrational dampening and, therefore, a low dissipation. a) & c) A soft or viscoelastic and dispersed layer has large amounts of vibrational dampening and, therefore, a higher dissipation.

In QCM-D experiments performed within this work, a Biolin Scientific QSense Analyze was used in conjunction with 5 MHz Biolin Scientific Gold QCM-D Sensors (QSX 301). Before use, all sensors were cleaned with Piranha solution (3.4.2 - Piranha Solution for Substrate Cleaning). Flow cells and tubing were washed after each experiment using Hellmanex III cleaning solution and mQ water. All experiments were run in flow using a peristaltic pump operating at a flow rate of 75 uL min^{-1}. The temperature of the QCMD chambers was maintained at 21° C. All QCM-D data displayed within this work is taken from the seventh harmonic unless otherwise specified.

3.1.2 - Polarisation Modulation Infrared Reflection Absorption Spectroscopy (PM-IRRAS)

The relationship between electromagnetic (EM) radiation and the energy of molecular interactions must first be explored before understanding any form of molecular spectroscopy. One of the fundamental principles of wave-particle duality is that EM radiation can be considered both a particle and a wave[199]. Therefore, EM radiation can be described as an oscillating electric and magnetic field in which the frequency, v , is equal to the speed of light, c, divided by the wavelength of the radiation, λ (3.4).

$$v = \frac{c}{\lambda} \qquad (3.4)$$

The same EM radiation can also be described as a photon, where the energy of the photon, E, is equal to Planck's constant, h, times its frequency, v (3.5).

$$E = hv \qquad (3.5)$$

The properties of molecules, particularly the bonding interactions between the constituent atoms, have a discrete ground state energy resulting from their electrical, translational or quantum mechanical properties. When these molecules are irradiated with EM radiation where the energy of that photon is precisely equal to that of the difference between the ground state and an excited molecular state, the energy of the photon is absorbed by the electron for that transition to occur. The absorption of these discrete energies of the EM radiation can be considered in terms of the frequency or wavelength as described by (3.4) and (3.5). By subjecting a molecule to a spectrum of EM radiation, discrete absorption frequencies are observed and can be used to identify specific molecular interactions characteristic of that molecule. These principles form the basis for all types of molecular spectroscopy.

One of these properties of molecules, the molecular or bond vibrations of the molecule, have quantised vibrational energies and transitions between vibrational energy levels within an energy range of approximately 1-50 kJ mol^{-1} (100 – 4000 cm^{-1})[200], depending on the particular vibrational interaction. This range of energies matches the energy of infrared (IR) radiation, a specific subset of the EM spectrum. An analogy to consider when looking at the vibration of chemical bonds is that the bond between the two atoms is like a spring, where the atoms are bound but can move relative to each other in an oscillating fashion[201]. Due to the nature of bonding and atomic interactions, how the atoms in a bond can vibrate is limited within 3D space, according to its degrees of freedom. There are six ways in which atoms in a molecule can

potentially vibrate, referred to as the modes of vibration. There are three main categories of vibrational mode, each with two different symmetries, namely symmetrical and asymmetrical stretching, scissoring and rocking in-plane bending, and twisting and wagging out-of-plane bending[164] (Figure 3.4).

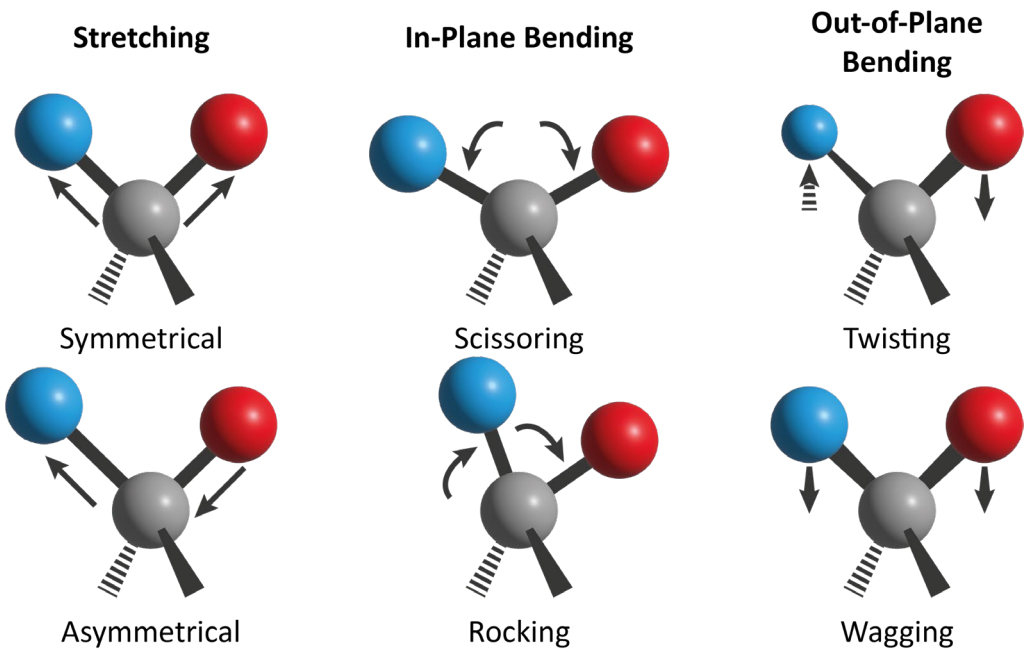

Figure 3.4 - The six potential modes of vibrational movement for a molecule, with the three categories of vibrational mode given in bold at the top of the figure.

Although molecules can potentially undergo any of these vibrational modes, depending on the nature of the vibrating functional group, some modes will dominate, while others might not be possible due to the conformational constraints of the molecular bonding interaction. In regards to IR spectrometry, only vibrational modes that cause a resultant periodic change within the dipole moment of the bond will absorb discrete energies of IR radiation, which is why they are often referred to as IR active[202]. It is commonly observed that functional groups with greater bond polarity, such as carbonyl-containing groups[203], are more susceptible to a stronger absorbance of IR radiation resulting from these periodic changes in dipole moment.

The vibrational modes within any molecule are determined according to the conformational bonding arrangement and the overall change in the dipole moments of its bond. These characteristics also govern the discrete energy levels of any given molecular bond vibration, thus determining the wavelengths at which the IR radiation is absorbed. It is, therefore, possible to distinguish individual bonding interactions, particularly the specific chemical groups they belong to, according to the wavelength of IR radiation absorbed by a given molecule.

Subjecting a chemical sample to EM radiation across the IR range and observing which of these wavelengths are absorbed (or transmitted) makes it possible to identify the presence of specific IR active chemical functional groups through inference and literature comparison. Usually, IR

spectrum plots, as per convention, are given in terms of absorbance, or transmission, versus the wavenumber (cm^{-1}), which is the inverse of the wavelength.

Fourier-transform infrared spectroscopy (FT-IR) is a means of obtaining high-resolution infrared spectroscopic data over a wide range of wavelengths within significantly smaller timeframes than that of classically scanning a range of wavelengths using a monochromator, which is particularly crucial with time-sensitive samples. Faster sample rates are achieved through a signal containing multiple modulated wavelengths established through constructive and destructive interference of IR radiation exposed to the sample, and the resultant signal is detected and deconvoluted using a Fourier transform mathematical function. This signal encoding is most commonly achieved using a Michelson interferometer[204], which consists of an IR radiation source which directs a collimated beam into a beam splitter. Half the beam is refracted into a stationary mirror, the other half is transmitted into a moving mirror, and then recombined upon reflection from the mirrors into the beam splitter and directed along to the sample or to undergo additional optical processing before irradiating the sample, and is finally then passed into an optical detector (Figure 3.5). The movement of the mirror within the interferometer causes a change in the path length, resulting in a phase change within that beam of radiation. When the two beams recombine via the beamsplitter, the interference with the stationary mirror beam will differ depending upon the phase of the moving mirror beam. If the moving mirror beam is in phase with the stationary mirror beam, it will interfere constructively. Conversely, if the beam is out of phase, it will destructively interfere with the stationary mirror beam, and between each extreme, a range of interference patterns will be generated[205]. For each of the many wavelengths of light given off by the IR source, these interface patterns will be generated, resulting in a complex signal pattern all related to the movement of the moving mirror[205, 206].

The overall detected interference pattern is referred to as an interferogram. The interference of radiation generated by this method, which gives the interferogram and interferometer its name, is also related to how many wavelengths of light can be probed simultaneously by an FT-IR spectrometer. Each time the moving mirror is moved back and forth, it is called a scan. Because the signal-to-noise ratio is proportional to the square root of the summation of the number of scans, an increased number of scans will result in an overall noise reduction[205]. When a Fourier transformation is applied as a mathematical operation to the resultant interferogram, it resolves into a spectrum relating to the transmission determined by the sample and wavelength of light selected and generated by the IR source[205, 207].

Within this work, a specific subcategory of IR spectrometry called polarisation-modulation infrared reflection-absorption spectroscopy infrared spectrometry (PM-IRRAS) was used

exclusively. PM-IRRAS is a technique that specialises in the surface analysis of thin, surface-bound chemical layers on reflective metal substrates[208], such as an Au-on-Si substrate. It is particularly powerful in this regard because it has very high surface sensitivity and selectivity for the surface chemistry, largely mitigating otherwise predominant and undesired signals from surrounding gaseous molecules such as water and carbon dioxide[209].

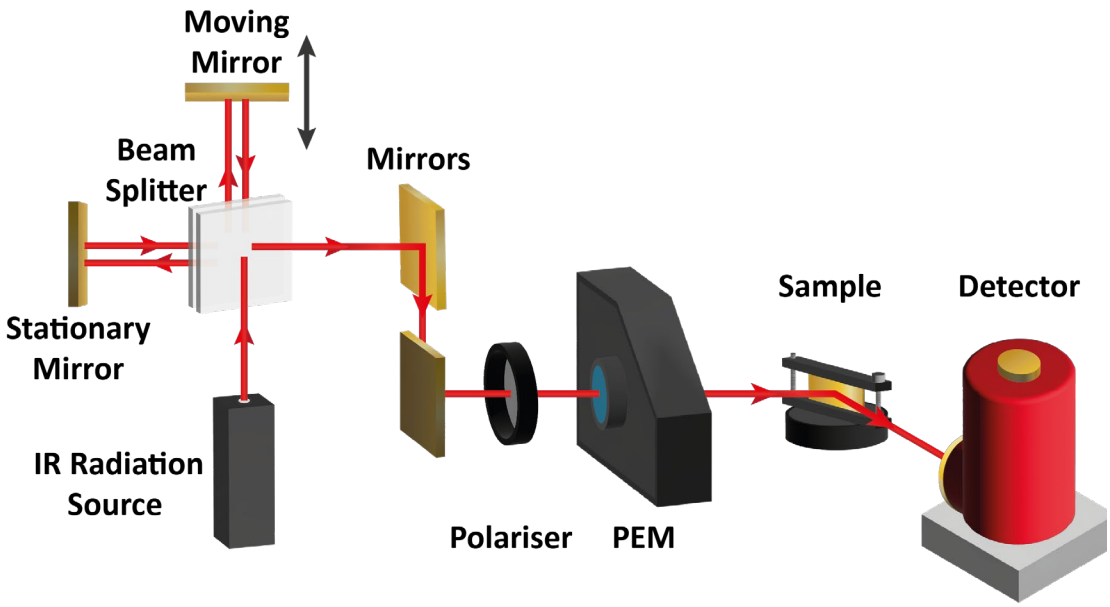

Figure 3.5 - The components and standard beam path setup for a PM-IRRAS system. The beam splitter, stationary mirror, moving mirror, and other elements make up the interferometer within the setup, and the polariser and photo-elastic modulator (PEM) allow the setup to perform PM-IRRAS measurements.

The standard setup f##or an FT-PM-IRRAS system is that a coherent IR radiation light source is passed through the interferometer (which consists of a beam splitter and a stationary and moving mirror, as previously described) to generate the FT-IR signal 'encoded' IR beam. This beam is then directed through a polariser into a photo-elastic modulator (PEM), which causes alternating linear states of polarised IR radiation[210], precisely modulating between the p- and s-polarisation. The incident radiation is then reflected off the sample surface, with an angle of incidence of approximately 80°, but can range from 70 to 89°[211]. The reflected radiation is then directed into a liquid nitrogen-cooled photodetector (Figure 3.5).

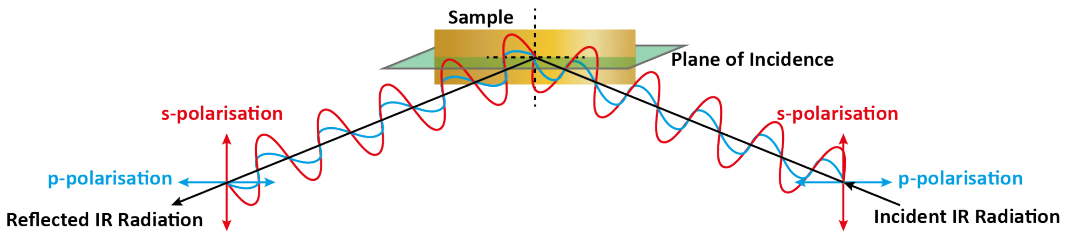

Figure 3.6 - The p- and s-polarised IR radiation orientations relative to the sample and the plane of incidence.

The key to why PM-IRRAS gives such a sensitive analysis of surface chemistry is understanding how each polarised state of the IR radiation interacts with the sample.

s-polarised radiation, which is perpendicular to the plane of incidence, displays close to no difference with an altered angle of incidence (Figure 3.6). Because it is also parallel to the substrate, it results in no net amplification of IR radiation[212]. Conversely, p-polarised radiation, which is parallel to the plane of incidence, is strongly affected by the angle of incidence. Because of this dependence and the high grazing angle of the system (80 to 89°), the p-polarised IR radiation combines the incident and reflected radiation to give the net amplification compared to that of the original incident radiation, which is the origin of the enhanced sensitivity of the technique[213].

The selectivity of this technique is derived from the fact that only p-polarised radiation interacts with molecules close to the surface of the sample and only those that have functional groups with bond dipole moments in the directional normal to that of the surface of the sample. This property of PM-IRRAS is often referred to as the surface selection rule[213, 214]. By combining the intensity of both the p and s-polarised radiation, PM-IRRAS provides a signal that does not require a reference, as the s-polarised radiation does not contain any spectrographic information regarding the sample, but instead only the 'background' signals, such as water and carbon dioxide within the air[215]. Then, subtracting the intensity of the s-polarised radiation from the p-polarised radiation results in a signal relating solely to that of the sample.

This work used a Bruker Vertex 70 FT-IR module spectrophotometer coupled to a Bruker PMA50 PM-IRRAS module for all IR measurements. All substrates used for PM-IRRAS consisted of Au-on-Si, comprising a titanium adhesion layer (25 nm) and a gold top layer (75 nm), with the Au surface working as the reflective plane and having an approximate surface area of 30 by 20 mm. The detector was kept at a constant temperature of -196 °C via liquid nitrogen, and the sample was held at a stable room temperature of 21 °C. The system was vented with dried compressed air for at least 12 hours before measurements. The parameters for spectra acquisition were set to a resolution of 4 or 8 $cm^{-1,}$ depending on requirements, with 500 scans and 36 background scans. Deconvolution of the FT-IR interferogram via a Fourier-transform algorithm and additional signal processing was carried out using Bruker OPUS software.

3.1.3 - Cyclic voltammetry (CV)

Cyclic voltammetry (CV) is an electrochemical technique used for the analysis of analytes susceptible to reductive and oxidative changes to their configuration, commonly referred to as redox properties[216]. In this case, reduction is defined as a gain of electrons and oxidation is defined as a loss of electrons from the analyte species. Cyclic voltammetry most often uses a three-electrode electrochemical cell to characterise the redox active species of interest[217]. All electrodes within the cell are immersed within the electrolyte solution, which freely carries charge from one electrode to the others. The working electrode is the surface at which the closed circuit interacts with the analyte, which can be either in solution or bound to the surface of the working electrode. It is essential that the working electrode provides a constant potential via the electrolyte solution to a secondary electrode referred to as the counter electrode. The purpose of the counter electrode is to provide a means for charge to flow to and from the working electrode to complete the cell. The counter electrode must consist of a chemically inert material so it will not interact with the analyte and is highly conductive, not to inhibit the flow of electrons; for this reason, materials such as platinum are used[218]. When only considering a chemical cell consisting of a working electrode and the counter electrode, it is difficult to maintain a constant potential between these electrodes when both are responsible for monitoring current and potential[219], unless at low currents[220]. This issue is why a three-electrode approach is the most common configuration for potentiostat chemical cells when a higher current is used (Figure 3.7).

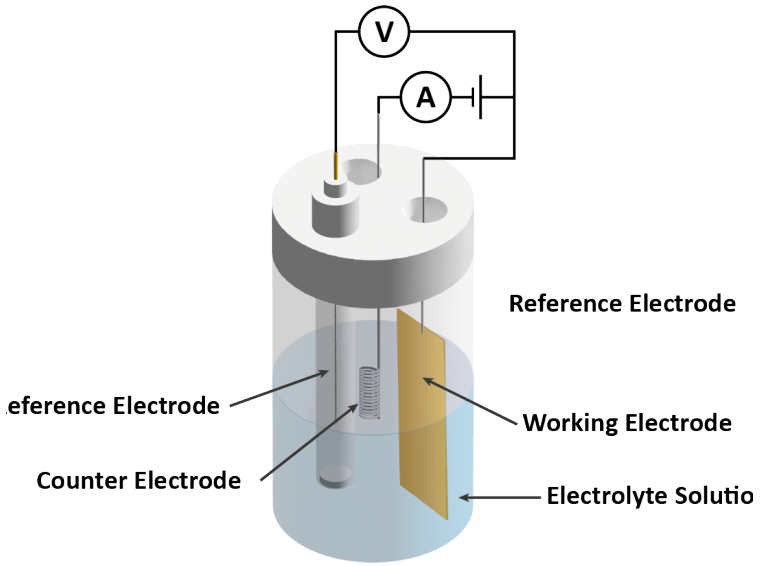

Figure 3.7 - The standard configuration of a three-electrode chemical cell used with potentiostats for techniques such as cycling voltammetry and impedance spectroscopy, with a simplistic circuit diagram demonstrating each electrode's analytic relevance.

In the case of a three-electrochemical cell, a reference electrode is added, which contains an isolated half-cell chemical reaction with a well-quantified redox potential[217]. A commonly used reference electrode, and the reference electrode used for all electrochemical experiments within this work, is an Ag/AgCl reference electrode. An Ag/AgCl reference electrode consists of a silver chloride coated silver wire suspended in a concentrated potassium chloride solution, isolated from the bulk electrolyte solution of the cell via a porous frit[164, 221], sometimes referred to as a salt bridge[222]. The sole purpose of the reference electrode is to provide a stable reference potential from which the working potential of the working electrode can be measured and controlled due to no intended current passing via the reference electrode[217, 219]. The transfer of current, or flow of electrons, is monitored and controlled via the counter (or auxiliary) electrode[35], which can then fluctuate in potential to account for the current needed at the working electrode. A much more stable and accurate redox profile for the analyte can be achieved by decoupling the current and potential, monitoring and delivering them indervdually via these two electrodes.

The example species that will be used throughout the section to illustrate concepts regarding electrochemistry and cyclic voltammetry is that of ferrocene. Ferrocene has been chosen as it is often used as the standard reference compound for calibrating electrochemical cells[223, 224] due to its distinct and nearly ideal redox reversibility[224]. It is also used as the reference compound of choice for studies in later chapters of this work.

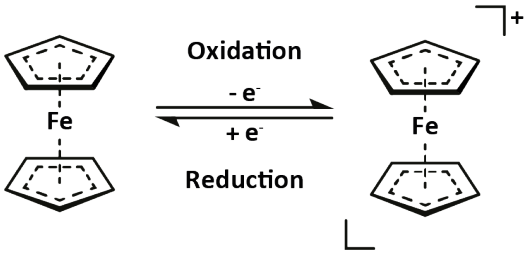

Figure 3.8 - Redox equation of ferrocene to a ferrocenium ion.

As mentioned previously, redox reactions consist of the oxidation and reduction of an analyte species, and in the case of ferrocene, this is the oxidation of ferrocene to a ferrocenium ion and its reduction back to ferrocene (Figure 3.8). Through a three-electrode chemical cell and potentiostat, it is possible to obtain a cyclic voltammogram, a plot of the current against the potential, in which the potential is scanned as a function of time and controlled versus the reference electrode. When considering only the oxidation or reduction reaction, it is commonly referred to as a voltammogram. However, when the voltage is cycled to probe both the oxidation and reduction reactions, it is referred to as a cyclic voltammogram[216]. It is worth noting that there are two standard conventions for plotting cyclic voltammograms. The first convention, as declared by the International Union of Pure and Applied Chemistry (IUPAC), stipulates that the oxidative or anodic scan runs from left to right, meaning from negative to positive potential

values, and the reductive or cathodic scan runs from right to left, meaning from positive to negative values. In comparison, the US standard convention dictates that the potential is plotted in the opposite direction[225]. All cyclic voltammograms within this work conform to the IUPAC standard convention.

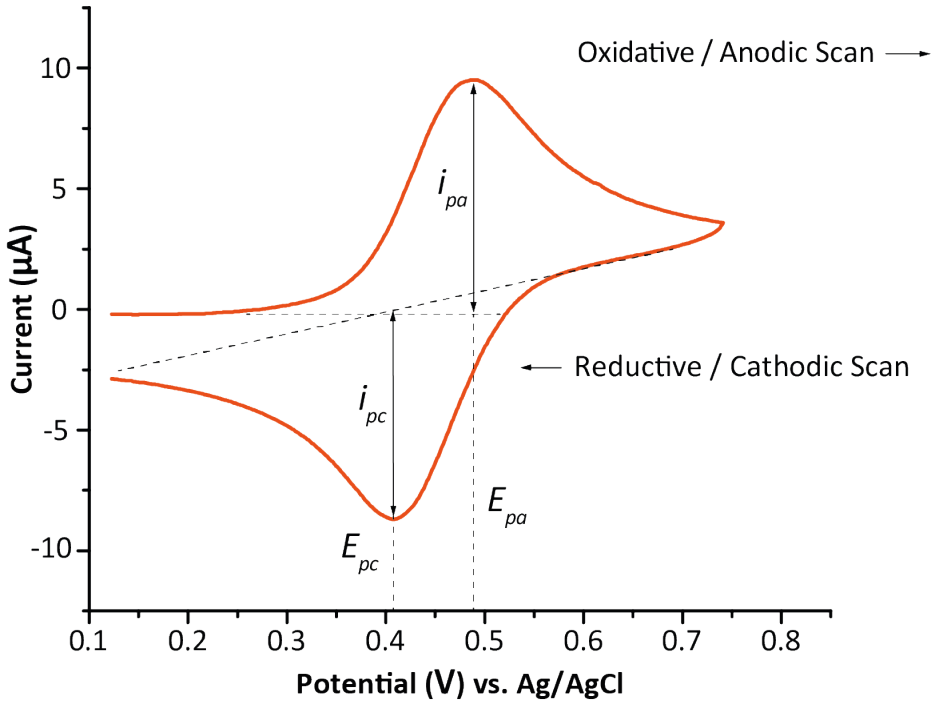

Figure 3.9 - The cyclic voltammogram of ferrocene, as the analyte, to explain the various properties obtainable from this analytical technique. The figure was modified from an original[226].

There are standard values associated with the interpretation of a cyclic voltammogram. When considering ferrocene as an example, the potential first scans in the oxidative or anodic direction before being reversed in the reductive cathodic direction, resulting in the classical ferrocene redox voltammogram, often referred to as 'duck-shaped'. The potential at which the current peaks in the anodic scan gives the anodic peak potential, E_{pa}, and its height the anodic peak current, i_{pa} (Figure 3.9). In the reverse scan direction, the peak associated with the cathodic scan has a position related to the cathodic peak potential, E_{pc}, and the height associated with the cathodic peak current, i_{pc}[225].

In the case of fully reversible redox reactions, such as observed ideally for ferrocene in solution, the anodic and cathodic peak currents should be of equal value, only differing by i_{pa} being a positive value and i_{pc} being negative[227]. When this is not the case, the analyte in question does not undergo a reversible redox process, suggesting an irreversible change has been made to the compound.

The reduction, or electrochemical potential, E, of a chemical cell reaction is described by the Nernst equation[217]:

$$E = E^0 - \frac{RT}{nF} \ln Q \quad (3.6)$$

Where E^0 is the standard cell potential, R is the universal gas constant, T the temperature in Kelvin, n is the number of electrons transferred, F is the Faraday constant, and Q is the reactant quotient, which is the concentration ratio of the potential products that arise from the reduction process. The Nernst equation forms the basis of many calculations regarding the concentration of analytes consumed during electrochemical redox reactions, such as electrografting, a technique used and later addressed in this work.

When using electrochemical methods to functionalise working electrodes, it is essential to discriminate in-solution and surface-bound redox active analytes. In the case of a simple redox reaction species, such as ferrocene, it is possible to determine if the species is bound to the surface or free to diffusion in solution by performing a range of cyclic voltammograms with varying scan rates. The square root of the scan rate (the voltage change over time) is directly proportional to the Faradaic current, i_p, a relationship described by the Randles–Ševčík equation:

$$i_p = 0.446 n F A_{sur} C^0 \left(\frac{nFvD_o}{RT}\right)^{1/2} \quad (3.7)$$

Where n is the number of electrons transferred, F is the Faraday constant, A_{sur} is the surface area of the working electrode, C^0 is the initial concentration of the analyte, v is the scan rate, D_o is the diffusion coefficient, R is the universal gas constant and T the temperature in Kelvin. Assuming all variables other than the scan rate are kept constant, the Faradaic current should vary linearly with the square root of the scan rate. This linear trend only holds if the analyte can diffuse through the solution, as the analyte concentration will vary with voltage according to the Nernst equation. For this reason, the faster the scan rate, the greater the concentration gradient at the working electrode and the higher the Faradaic current[217].

In the case that the analyte is not free to diffuse through the solution but is instead bound to the surface of the working electrode, the Randles–Ševčík equation is no longer valid, and the Faradaic current is instead described by the equation:

$$i_p = \frac{n^2 F^2}{4RT} v A_{sur} \Gamma \quad (3.8)$$

Where n is the number of electrons transferred, F is the Faraday constant, R is the universal gas constant, T is the temperature in Kelvin, v is the scan rate, A_{sur} is the surface area of the working electrode, and Γ is the surface coverage. This relationship is not based on diffusion but on the assumption that the analyte is bound or absorbed directly to the surface of the working electrode[217, 228]. Assuming the temperature is constant, the scan rate should be directly proportional to the Faradaic current. If this relationship holds experimentally, it strongly indicates that the analyte is bound to the electrode surface instead of being free to diffuse in solution. Both these equations have been employed within this work to validate the functional groups during the process of building immobilisation chemistries onto gold electrodes and are later discussed in detail.

In addition to determining if redox active species are free to diffuse or surface-bound, cyclic voltammetry via the equation (3.9) can additionally be used to calculate the surface coverage of redox-active groups immobilised on an electrode surface, Γ_{mol}, (mol cm^{-2}):

$$\Gamma_{mol} = \frac{A_s}{nvFA} \qquad (3.9)$$

Where A_s is the integrated area under the observed Faradaic oxidation or reduction peak, n is the number of electrons that participate in the electron transfer reaction, v is the scan rate, F is the Faraday constant, and A is the area of the working electrode. Within this work, A_s was calculated from the area under the baseline subtracted reduction or oxidation peak of interest, using the Simpsons rule, with the integration spacing, dx, set to one, which equates to the spacing between each acquired datapoint. Using this calculated value of Γ_{mol}, it is possible to convert the value to molecule surface coverage, $\Gamma_{molcules}$, using the equation:

$$\Gamma_{molcules} = N_A \Gamma_{mol} \qquad (3.10)$$

Where N_A is Avogadro's constant. For the electrografting process later described within this work (4.1 - Diazonium Electrografting Immobilisation Strategy), the number of electrons participating in the reaction is assumed to be one electron per molecule. The calculated value of $\Gamma_{molcules}$, is the number of molecules electrografted over the entire working electrode area. The initial electrografting process is assumed to form a dendric multilayer, not a near monolayer. For the ferrocene probe experiments described within the same chapter, the number of reaction participating electrons is assumed to be one electron per molecule, and the surface is assumed to be a near-monolayer, giving a more accurate value for molecule surface coverage.

This work used a BioLogic SP-300 potentiostat for all CV experiments. All experiments were performed using an Au-on-Si working electrode with a working area of approximately 20 by 20

mm. A Cu wire and silver epoxide connection or an electrical contact pin provided contact to the working electrode surface. A Pt counter electrode and an ALS RE-1CP Ag/AgCl/Saturated KCl (0.197 V) Reference electrode were used, all assembled within an ALS SVC-3 voltammetry cell.

For the electrografting of diazonium species, standard experiments were performed with a scan rate of 100 mV s^{-1} and a scan range of -0.2 to 0.6 V vs Ag/AgCl reference electrode with five repeat scans. The reaction solution acted as the electrolyte in these experiments.

For ferrocene immobilisation studies, standard experiments with a scan rate from 50 to 1000 mV s^{-1}, increasing in increments of 50 mV s^{-1} with a 15-second interval between scans. The set scan range was either 0.0 to 0.8 V or 0.1 to 0.7 V vs Ag/AgCl reference electrode with five repeat scans. These experiments used sodium phosphate buffer [100 mM] at pH 7.0 as the electrolyte.

3.1.4 - Stylus Profilometry

Various techniques, such as scanning electron microscopy (SEM) and atomic force microscopy (AFM), are regularly used for nanoscale surface characterisation. However, they are less relevant when characterising step heights of micro-scale fabricated features, which are an order of magnitude larger than the working range of these techniques.

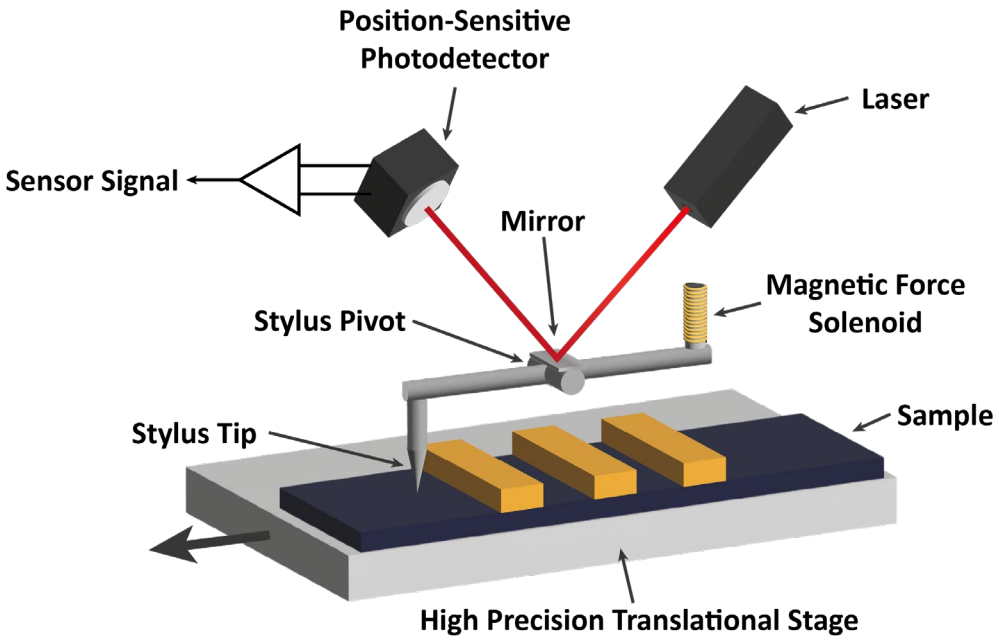

Figure 3.10 - The basic configuration of a stylus profilometer with respect to a microfabricated sample for height profiling.

Stylus profilometry, therefore, stands as one of the best standards for characterising surface topography and feature step heights within the micrometre range while ensuring high sensitivity[229]. The basis of the technique is that a counter-levered stylus tip is applied to the surface of the substrate, and a defined torque is applied, referred to as a set point[230]. This force is maintained by a magnetic force solenoid coupled with a feedback loop, so as the stylus is driven across the surface of the sample in the X and Y axis, the cantilever moves according to the exact changes on the surface in regard to the Z axis. Mirrors mounted above the cantilever pivot reflect a laser onto a position-sensitive photodetector. As the stylus is scanned across the surface and is deflected in height by the surface topography, so does the angle of reflection of the beam, which is interpreted by the position-sensitive photodetector and the signal converted to the change in height of the surface (Figure 3.10). As the stylus traces the path along the sample, a reconstruction of the exact surface topography can be recorded, allowing a profile of both surface roughness and height of any feature that has been fabricated.

In stylus profilometry, it is critical that the stylus tip is physically in contact with the surface. Depending on the shape and size of the tip, the resolution and performance of the resultant profile will vary accordingly due to the degree of contact with the surface and the scale of the features relative to the tip[230]. Using a sharper tip makes it possible to resolve smaller features than that of a broader tip. Moreover, when the torque applied through the tip to the surface is too high, it can damage the surface. The nature of the material of which the surface is made also needs to be considered, as any materials, such as those with viscoelastic properties, will deform upon applying the stylus tip, meaning the profile cannot be correctly determined.

Stylus profilometry within this work was performed with a Bruker Dektak XT, with a 2 µm radius stylus tip, 10 mg stylus force and a 524 µm stylus scan range.

3.2 - Solution Characterisation Techniques

Molecular spectroscopy techniques and some of their inherent theory have already been discussed. Some of these techniques instead rely on the solubilisation of the analyte in order to function. These techniques can then be used in conjunction with an assay, which allows for the quantification of an otherwise undetectable chemical product. This sub-chapter will focus on ultraviolet-visible spectroscopy used in this work.

3.2.1 - Ultraviolet-Visible Spectroscopy (UV-Vis)

As already discussed in the PM-IRRAS section (3.1.2 - PM-IRRAS), the absorption of EM radiation by excitation of electrons from the ground to higher energy states within chemical molecules allows the characterisation of molecules using molecular spectroscopy. Ultraviolet-visible (UV-Vis) spectroscopy is a related optical spectroscopy technique used to identify and quantify given chemical species.

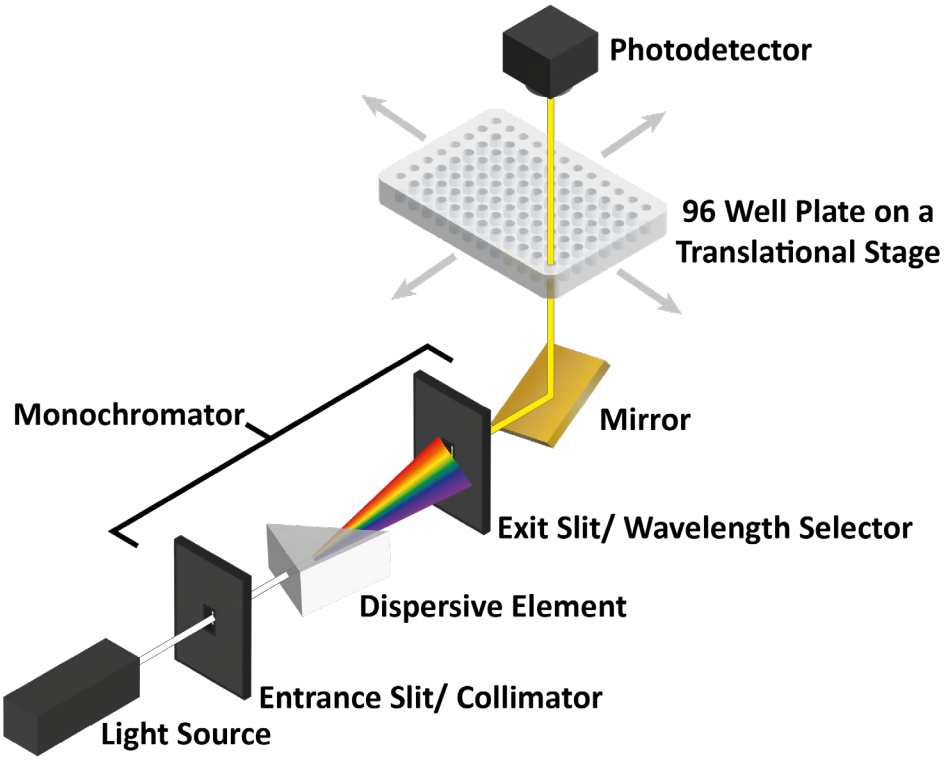

Figure 3.11 - A UV-Vis spectrophotometer's components and standard beam path setup. This setup is also the same for most molecular spectrophotometers but with alternative light sources within another spectral range and monochromators that select these alternative wavelengths accordingly.

While IR spectroscopy focuses only on the infrared section of the electromagnetic spectrum, UV-Vis spectroscopy is concerned with radiation absorption in the UV and visible light regions. Being of higher energy than IR radiation, UV-Vis spectroscopy covers an energy range of approximately 50-1000 kJ mol^{-1} [164], and it is the electronic transitions within a molecule in this energy range that are responsible for absorbing the incident radiation.

The UV-Vis spectrophotometer used within these studies was a specialised plate reader UV-Vis spectrophotometer, which is compatible with a standard biological assay of 96-well plates containing 96 individual 100 µl cells (Figure 3.11). The first element of a UV-Vis spectrophotometer is a light source which emits radiation within the UV-Vis range of the electromagnetic spectrum. The radiation from the source then passes through a monochromator, which consists of an entrance slit that acts as a collimator. It gives a light beam of smaller spatial cross-section that then passes into a dispersive element, either a prism or diffraction grating, which disperses the radiation into its spectrum of discrete wavelengths, which are then individually selected via the exit slit or wavelength selector of the monochromator, resulting in narrow bandwidth radiation[231]. A mirror reflects this through the analyte within a specified well within the well plate and then into a photodetector. The well plate is mounted on a translational stage that does not inhibit the beam path but is automatically moved to place the cell of interest into the beam path for the sample to be analysed. The stage movement is automated to allow the selection of a different well within the well plate, and the process is repeated. This automation allows a plate reader spectrometer to deliver fast multi-sample analysis by loading the well plates with up to 96 samples at any given time. Where full spectral analysis is required, as opposed to measurement at a single wavelength, the monochromator will scan through discrete wavelengths within the range specified, and the light intensity for each wavelength will be recorded by the photodetector to produce a plot of absorbance (or transmission) versus wavelength.

The UV-Vis spectrophotometer was used within this work to characterise and quantify the concentration of molecular species in the solution phase. As discussed previously, absorption spectra contain information regarding the chemical composition of a sample. In addition, the intensity of absorption, or transmission, at each wavelength is determined by the number of absorptions that take place. This, in turn, is a function of the concentration of the analyte, the probability that a specific transmission will occur, the path length through the solution, the incident radiation intensity and the fraction of molecules that are in the correct ground state to absorb the incident radiation[164].

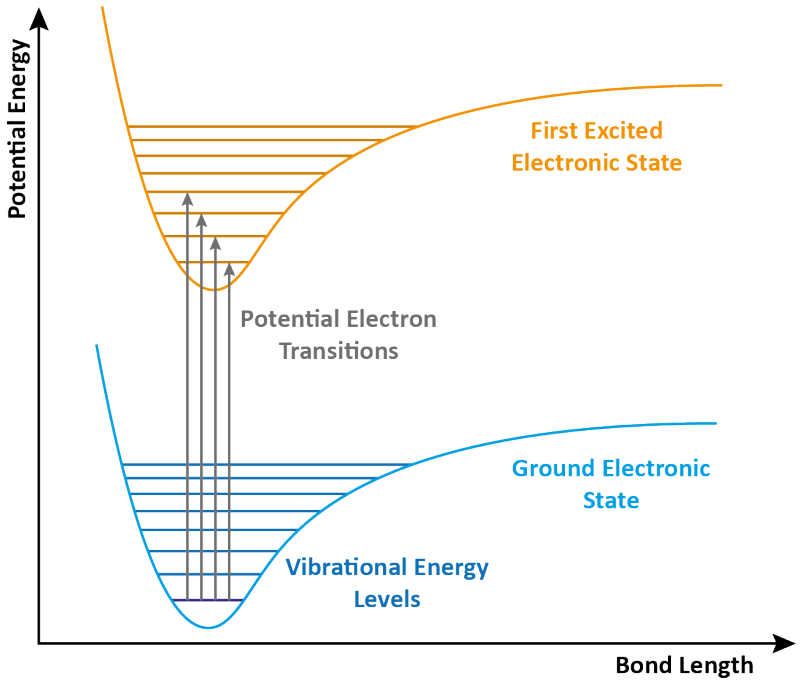

Figure 3.12 - Morse curves to show potential electron transitions due to irradiated excitation in a diatomic molecule, resulting in broad peaks as seen in UV-Vis spectrometry.

Each transition from the ground electronic state of the electron within the bonding interaction can potentially transition to a range of excited electronic states. The reason for this can be best explained using Morse curves, which best describe diatomic molecules modelled as two masses on a spring acting as harmonic oscillators but still act as a good approximation for understanding potential electron transitions in more complex molecular systems. Within any given electronic state, an electron within a bond is confined within a potential energy well, similar to an inverted Maxwell Boltzmann distribution curve and has a set of possible vibrational energy levels. These energy levels can vary with the inter-atomic distance or bond length (Figure 3.12), referred to as the Franck–Condon principle[232, 233]. When the molecule is irradiated, the wavelength and, therefore, the energy of that radiation has the potential to match one of the potential electron transitions, and various electron transitions can occur. These transitions differ according to the vibrational energy of the initial electron state and the vibrational energy level equivalent to the energy of the incident radiation. Therefore, for any UV-Vis active sample analysed using UV-Vis spectroscopy, the resultant absorption peak is often broad due to the many variations in vibrational energy levels and the many potential discrete electron transitions, leading to a wide range of absorb wavelengths of the incident radiation. As these absorption peaks are closely spaced in energy and thus wavelength, they merge, and the resultant peak is much broader[234].

Transmission, T, through a given concentration of analyte in solution can be defined as a function of the intensity of the radiation after passing through the given solution, I_t, divided by the original intensity of the radiation, I_0 (3.11).

$$T = \frac{I_t}{I_0}$$

(3.11)

Since the transmission and the concentration of the analyte are not a linear relationship, when calculating analyte concentration using UV-Vis, absorbance, A, is instead considered, which is linear with concentration. Absorbance can be expressed in terms of transmission via the given equation:

$$A = -log_{10}T$$

(3.12)

The standard setup for a spectrophotometer allows for the acquisition of values for the intensity of the transmitted radiation before and after passing through a given analyte solution. In that way, the absorbance of the analyte at the given concentration of a solution can be calculated using a spectrometer via the given combined equation[235, 236]:

$$A = log_{10}\left(\frac{I_0}{I_T}\right)$$

(3.13)

The Beer-Lambert Law is used to relate, via absorbance, the intensity of the radiation before and after passing through a solution of uniform concentration and given path length, where ε, is the absorption coefficient of the analyte, c is the concentration for the analyte, and l is the path length of the radiation through the analyte solution[235, 237] (3.14).

$$A = \varepsilon cl$$

(3.14)

The absorption coefficient can be calculated using a known concentration of the analyte, which can, in turn, be used to calculate an unknown concentration for the analyte using that absorption coefficient for the maxima peak and the known path length, using a UV-Vis spectrometer to acquire the maxima peak position of the absorbance.

Generating a calibration plot using a known dilution series of the analyte (or a reference compound with a similar absorbance coefficient) gives a linear plot of the absorbance versus the concentration. Evaluation of the linear equation that fits the Beer-Lambert Law shows that the line gradient equals the absorption coefficient times the path length through the solution. Knowing the path length of the radiation through the sample makes it possible to calculate an experimentally obtained absorbance coefficient, which can then be used for concentration determination using UV-Vis spectroscopy[238].

In this work, calibration curves of the desired analyte or reference compounds were calculated to obtain the concentration of products during flow catalysis and proteins, the procedures for which are later outlined in this work, including an assessment of their efficacy. Ellman's reagent

thiol assay, coupled with UV-Vis spectroscopy, was used to quantify a biocatalytically generated thiol product; the procedure and related chemistry are described within the experimental chapter (5.2.1 - Microcolumn μ-IMER Experiments using CBL Immobilised Agarose Beads). A Biotek Synergy H1 UV-Vis plate reader spectrophotometer was used for all UV-Vis measurements with a 1 nm resolution and a double orbital shaking step for 1 minute at a speed of 282 cycles per minute (CPM) between each measurement.

3.3 - Fabrication Techniques

The fabrication of devices and various engineered components was a significant element of the work presented within this thesis. The methods used to undertake the design, engineering and fabrication of these components are outlined within this chapter.

3.3.1 - Soft Photolithography

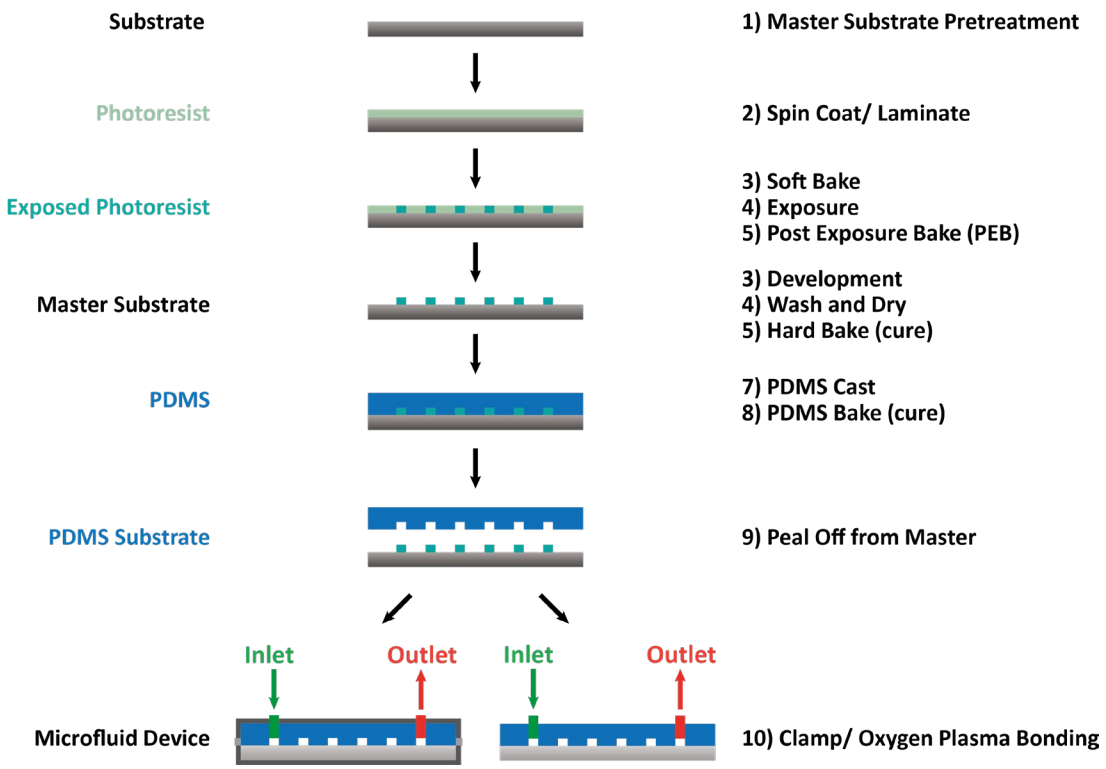

Figure 3.13 - A schematic diagram of the soft photolithography process used for the fabrication of microfluidic chips.

Soft photolithography is the name given to the lithographic fabrication of stamps, devices and structures in soft polymer or elastomeric materials[239]. The most commonly used material is polydimethylsiloxane (PDMS), the composite used in this work. Soft photolithography can be used for multiple purposes, but in terms of the context of this work, it will be discussed as a means of creating microfluidic devices or chips. Soft photolithography can be split into two main processes: the first is fabricating a master substrate, which acts as a mould, and the second is the casting of microfluidic chips within PDMS from the master substrate. In terms of microfluidic chip fabrication, there is additionally the step of forming a sealed microfluidic device between

the cast PDMS substrate and another planar sealing substrate, commonly a glass microscope slide or silicon wafer.

The surface roughness of an unpolished glass microscope slide is typically around 1.2 nm[240], and for the polished silicon wafers used in this work, surface roughness is quoted as <0.2 nm[241]. Concerning microfabricated microfluidics used in this work, the minimum feature size used was 70 µm in height, which is three orders of magnitude greater than the surface roughness of an average unpolished microscope slide, let alone a silicon wafer and, therefore, is unlikely to impact the fabrication of microfluidic chips, unlike nanofabrication where sub-nanometre surface roughness is required. In contrast, when choosing a substrate material for protein or enzyme functionalisation, the surface roughness will affect the uniformity and self-assembly of the immobilised layer[242], which is unsurprising considering CBL, the primary enzyme used within this work, has an estimated diameter of 4.82 nm (4.2.1 -SAM Formation and Residence Time Optimisation of CBL). It is difficult to quantify the impact surface roughness would have on both the structure of the immobilisation enzyme layer and on the overall enzyme activity; thus, in the first instance, it was deemed prudent to minimise the effect surface roughness might play on the immobilisation process through using polished silicon wafers, due to their significantly lower surface roughness.

When undertaking master substrate fabrication, the base substrate, made of either glass or silicon, as discussed, is subject to pretreatment as a point of start. This pretreatment usually consists of an aggressive cleaning step, such as plasma ashing or piranha cleaning, followed by solvent washers to ensure no surface contaminants are present on the surface that could affect the lithographic process (Figure 3.13 - 1)[243, 244].

Once cleaned, the substrate is then spin-coated or laminated with a photoresist, depending upon its mode of application (Figure 3.13 - 2). Photoresist is the term given to a chemical mixture consisting of a polymer monomer and a solvent to act as a thinning agent[245]. Sometimes, the polymer monomer is UV activated, meaning it is self-polymerising upon UV activation. In other cases, the photoresist contains a photoactivated catalytic chemical, such as a photoacid, which increases the acidity of the solution[246] when irradiated. The increased acidity then catalyses the cross-linking polymerisation of the monomers, such as is the case for SU-8[244], where the photoacid catalyses the epoxide ring opening required for polymerisation of the constitute polymer. Usually, negative photoresists are used to produce the master substrates for microfluidic chip reactors, which is a concept explained in greater detail below, but it is to say that the photoresist that is not exposed to radiation will dissolve during development. A spin-coated negative photoresist, such as SU-8 2050, is applied to the surface of the substrate, which is then mounted to a spin coater. The spin coater holds the sample in place via a vacuum seal

while rotating at a set speed for a given time, causing the resist to spread to form a layer of consistent thickness. Depending on the desired thickness of the photoresist, the speed and time length can be varied according to the manufacturer's specification[244] or an optimised in-house process. The substrate then undergoes a soft bake, which causes solvents within the photoresist to evaporate, increasing the layer's viscosity. A laminate resist, such as SUEX K-200, is instead already a predefined thickness. The resist is enclosed between two polyethylene terephthalate (PET) sheets; one side is opaque and is removed before exposure, the other is clear, to be removed before lamination . The clear PET sheet on one side is removed, and the exposed resist is applied gently to the surface of the substrate. This is then enclosed between larger polyester sheets before being passed through a temperature and speed-controlled laminator, which laminates the resist onto the substrate. The speed and temperature vary according to the thickness of the resist and is set according to the manufacturer's specification[243] or an optimised in-house process. Laminated resists do not require a soft baking step.

The substrate, now covered in photoresist, is then exposed to UV radiation. Both laminated and spin-coated resists are treated the same from this point onwards, except the polyester sheet covering the top of laminated samples is removed before the sample is exposed (Figure 3.13 - 4). Two main methods of exposing patterns in soft photolithography are a mask aligner and a direct laser writing system. A mask aligner primarily consists of a UV light source, a photomask, a means of focusing the light via the mask and a holder for the substrate[247]. The system works by the mask impeding the path of the UV light onto the sample, except at predetermined openings within the mask, which mirror the desired pattern that will be exposed within the photoresist. The dose, which is a general term used to describe the amount of energy from the UV radiation the photoresist is exposed to, is controlled by the light intensity and the length of time that the UV source irradiates the sample. In a direct laser writing system, the pattern is instead exposed onto the surface of the substrate via a collimated beam of UV radiation generated by a UV laser source[248]. This beam is focused onto the substrate, which is attached to a high-precision translational stage. The desired pattern to be exposed onto the surface of the substrate is drawn in computer-aided design (CAD) software and converted into a write path, which the translational stage will follow to create the desired exposure pattern within the resist on the substrate. The dose of a direct laser writing system is determined by the modulation (percentage power of the UV laser) and speed at which the laser traverses the substrate surface. In this work, a direct laser writing system was used.

Once exposed, the substrate undergoes a post-exposure bake (PEB), which consists of maintaining the samples at a fixed temperature for a defined period of time according to the manufacturer's specification[243, 244] or an optimised in-house process. The PEB ensures that all

exposed and cross-linked areas of the photoresist are fully polymerised before development. It is an important side note that the sample should be cooled slowly following baking, as rapid changes in temperature can cause thermal shock in the newly polymerised photoresist, leading to poor fabrication quality.

The sample is then developed, a step in which the substrate is immersed within a solvent (or developer) specified by the manufacturer[243, 244] and gently agitated for a fixed length of time, determined according to the exposure dose and thickness of the resist. Any resist that has not been polymerised during exposure is soluble within the developer, causing it to slowly dissolve to leave only the desired pattern that was exposed (Figure 3.13 - 6).

The samples are finally washed with at least one other solvent to remove residual resist and developer from the substrate's surface and carefully dried under nitrogen[243, 244].

Depending upon the photoresist used and the optimised procedure for the resist, a hard bake step is sometimes required, in which the sample is heated at a set temperature within an oven for a given length of time. Hard baking is sometimes performed to ensure the substrate is dry and free of solvents[243, 244].

At this point, the master substrate has been successfully fabricated, and it is then possible to cast PDMS microfluidic chips from this master substrate. Silicone polymers, such as PDMS, consist of an elastomer and a curing agent mixed in given ratios to achieve different viscoelastic properties within the cured microfluidic chip. Once mixed, the still viscous PDMS solution is degassed before being carefully poured over the master substrate and cured in an oven at a set temperature and time to polymerise the PDMS layer (Figure 3.13 - 10). Once finished, the PDMS substrate can be peeled from the master substrate, leaving a microfluidic chip in which the master substrate has cast the pattern of the desired flow channels (Figure 3.13 - 11). Holes can then be punched at any fluidic inlets and outlets of the chip, or in cases where more sophisticated master substrate chip jigs are used, inlet and outlet holes are predetermined by the jig itself.

Once the PDMS substrate has been fabricated via this process, it is possible to form the enclosed microfluidic device/ chip. The PDMS substrate can either be bonded or clamped to a flat base substrate, such as a glass slide or silicon wafer, forming the base of the microfluidic device. A standard method of bonding for a PDMS substrate to the glass substrate is oxygen plasma bonding[249], in which both the bonding surface of the PDMS and glass substrate are subjected to oxygen plasma ashing, which aggressively oxidises the surface, resulting in an increased concentration of silanol groups. Due to the high polarity of the silanol groups, when the substrates are brought in contact with one another, the silanol groups on each surface undergo a condensation reaction to form O-Si-O bonds between the two substrate surfaces, forming a

tight seal[250]. An alternative strategy is mechanically clamping the PDMS substrate to the base substrate. Although this sounds like a simplistic solution, it is often more challenging due to issues that arise with the need to apply even clamping pressure across the PDMS surface. At regions where the substrates are clamped to a too higher pressure, the fluidic channels can collapse, and extremely high back pressures will be observed within the device. Conversely, if the substrates are clamped with too little pressure, they will not correctly seal causing fluid to leak from the channels. Clamped microfluidic devices therefore need engineered solutions to evenly distribute the correct pressure to seal but not crush the PDMS substrate.

The photoresist used within this work was MicroChem SU-8 2050, which was applied to a silicon substrate using an Electronic Micro Systems Ltd 6000 Spin coater. DJ MicroLaminates SUEX® K-200 was used in conjunction with a GBC Pro-Series 3600 laminator for fluidic devices fabricated using laminated resists. The CAD design of all patterns was generated using Autodesk Inventor and converted to a beam write path using Kloe Design. All direct laser writing was performed using a Kloe DILASE 650 direct laser writing system.

The SU-8 2050 photoresist standard operating procedure was modified from the manufacturer data sheet[244] through in-house optimisation and is as follows:

20 by 50 mm surface area Si substrates were first cleaned using Piranha solution as per the SOP (3.4.2 - Piranha Solution for Substrate Cleaning). The cleaned substrate was then mounted on the spin coater using a vacuum seal. Approximately 3 mL of the resist was poured directly onto the surface before being spun first at 500 rpm for 10 seconds with an acceleration of 100 rpm per second, followed by a second step of 1750 rpm for 30 seconds with an acceleration of 300 rpm per second. The substrate was soft-baked at 65 °C for 3 minutes, then at 95 °C for 9 minutes, then left to return to room temperature. This process gave samples with a resist thickness of approximately 85 µm. The optimal expose dosage of SU-8 samples was found to be a modulation of 100 %, a write speed of 1 mm s^{-1} and a Δ focus adjustment of +30 µm. It is worth noting that when SU-8 resist was used, the direct laser writing system was significantly misaligned, so the quoted exposure dose exceeded what would be expected for this thickness. The sample then underwent a PEB by heating on a hot plate to 65 °C for 3 minutes, then ramped to 95°C for 10 minutes and left to cool overnight. MICROPOSIT EC Solvent (40 mL), which is commercially branded 2-methoxy-1- methylethyl acetate, was used to develop the sample by immersion and agitation within the solvent for 7 minutes. The sample was washed in fresh MICROPOSIT EC Solvent (40 mL) for 7 minutes, followed by an IPA wash for another 10 seconds before being dried under nitrogen. The sample was finally hard-baked for 60 minutes at 180 °C to ensure full annealing of any cracked surfaces that might have appeared during development. Master substrate features were checked using stylus profilometry and an optical microscope.

The SUEX K-200 photoresist standard operating procedure was modified from the manufacturer data sheet[60] through in-house optimisation and is as follows:

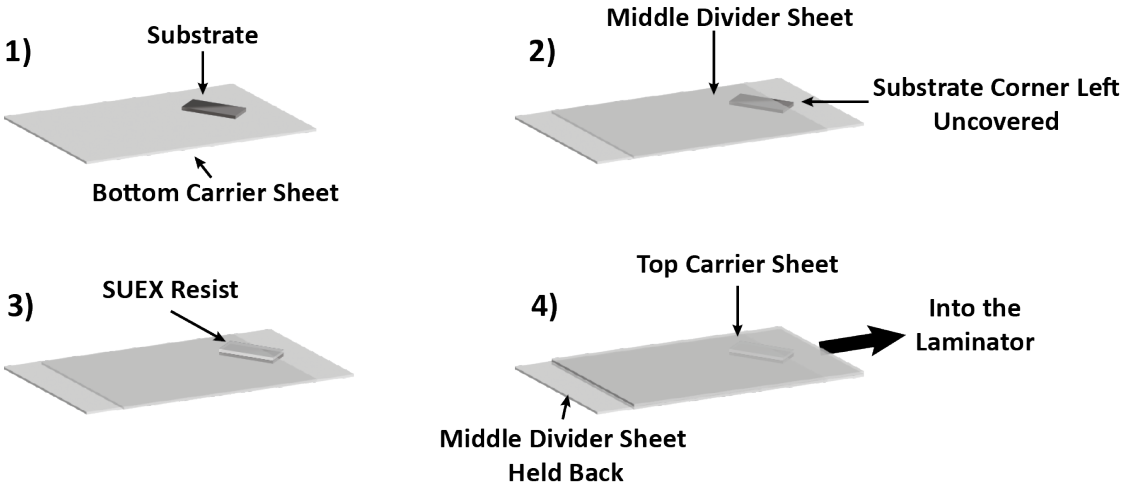

Figure 3.14 - Schematic for the step-by-step assembly of the substrate and SUEX with Mylar sheets before lamination.

The SUEX K-200 photoresist was cut to the correct substrate size using a Laserscript LS6090 PRO Laser cutter operating at a speed of 45.0 mm s^{-1}, max of 15 % and percentage power min of 10 %. To laminate samples, they must first be placed between carrier sheets, and the substrate and SUEX reisit separated by a divider sheet. The carrier sheets ensure that smaller samples enter with the correct orientation and do not get stuck within the laminator. The divider sheet provides a bubble-free adhesive of the SUEX resist and the substrate during lamination, especially with larger samples. All sheets are comprised of Mylar (BoPET or Biaxially-oriented polyethylene terephthalate) and were carefully rinsed in acetone and left to fully dry prior to their use within the lamination process, free of any creases or residual photoresist to ensure no defects or contamination occurred. The Si substrate was carefully placed on a bottom carrier sheet at a 45 ° angle to the top edge of the sheet (Figure 3.14 - 1). Over this, a Mylar divider sheet was placed, leaving the topmost corner of the substrate uncovered (Figure 3.14 - 2). The clear PET cover sheet on the SUEX was then removed, and the SUEX was placed carefully over the footprint of the Si substrate. At this stage, the SUEX was only in contact with the substrate in the top corner, which was exposed by the Mylar divider sheet (Figure 3.14 - 3). The top carrier sheet was then carefully placed on top of the assembly (Figure 3.14 - 4) and carefully passed into the laminator, which had been set to a temperature of 65.6 °C (as confirmed experimentally) and a lamination speed of 2, ensuring that the corner where the SUEX was in contact with Si substrate entered the rollers first. The rollers were allowed to pull the substrate through the laminator while the Mylar divider sheet was held in place so that the SUEX was gradually brought into contact with the Si substrate. This process forces air from the interface between the SUEX and substrate, minimising the formation of bubbles. The upper PET sheet was kept in place after lamination and removed immediately before exposure.

The exposure dosage of SUEX K-200 samples was a modulation of 88 %, a write speed of 5 mm s^{-1} and a Δ focus adjustment of + 100 µm. The sample then underwent a PEB of 35 minutes at 85 °C within a pre-heated oven and left to cool to room temperature overnight. For development, the sample was immersed in a gently stirring bath of 2-methoxy-1- methylethyl acetate or PGMEA (40 mL) for 40 minutes, followed by a second step in a gently stirring bath of clean PGMEA (40 mL) for 20 minutes. The sample was then washed and immersed in a bath of IPA for 5 minutes before being gently dried under nitrogen. Hard-baking of the master substrate was not required, and features were again checked using stylus profilometry and an optical microscope.

3.3.2 - Additive Manufacturing via Stereolithography (SLA)

Stereolithography (SLA) or resin printing is one of the primary forms of 3D printing, alongside fused deposition modelling (FDM) and selective laser sintering (SLS)[251]. 3D printing is the term given to taking computer-aided design (CAD) models and exporting them via specialist software to a printer that can reproduce the model as a physical 3D object through additive manufacturing. In this project, only stereolithographic 3D printing has been utilised, and it will be the only 3D printing process covered in this chapter. SLA printers work on the premise of exposing discrete localised areas of UV polymerising resin via a beam of UV radiation to build up a layer-by-layer physical representation of the CAD model design.

3D models designed within CAD software are rendered into more simplistic wire-mesh models, which can then be converted to printing commands for the 3D printer via a process called slicing. Slicing refers to the model being broken down into individual layers corresponding to the working Z-axis resolution of the 3D printer[252]. Each sliced layer is then converted into G-code, which is a numerically controlled programming language that the 3D printer interprets into physical movements that result in the printing of the model, one sliced layer at a time.

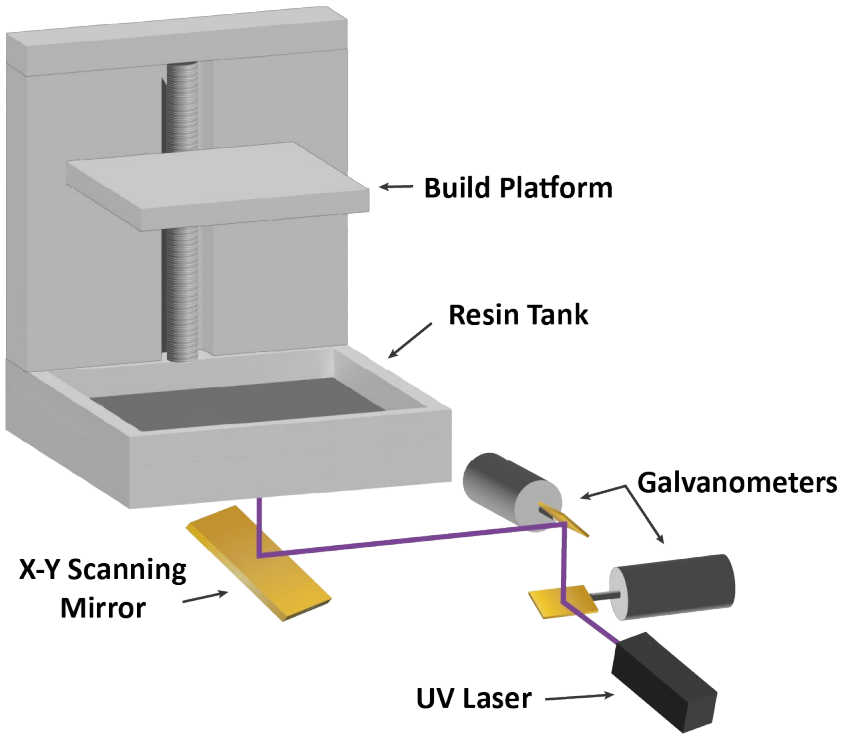

Figure 3.15 - The setup of a standard SLA 3D printer, including the internal optical components, based on the configuration of Form Labs Form 3+ 3D printer used in this work.

There are multiple designs of SLA 3D printers, but this work will focus only on a 'bottom-up' printer design, such as the Form Labs form 3+, as used within this work. In a 'bottom-up' printer,

the photo-activated resin sits in a tank with a flexible membrane acting as its base, which is optically transparent to UV radiation[251] (Figure 3.15). A build platform parallel to the Z-axis is then lowered into the resin tank and approaches the membrane, leaving a gap equivalent to that of the working Z-axis resolution of the printer, which is also the thickness of each sliced print layer. A collimated UV laser beam is then directed across the XY writing plane of the membrane via the assistance of galvanometers and an XY scanning mirror to ensure accurate movements of the laser beam. The resin within the tank consists of a mixture of photo-activated monomers and oligomers. As it is exposed to UV radiation, the oligomers polymerise at the position local to the UV laser beam as it writes the desired pattern of the layer within the XY plane between the membrane and the build platform. The build platform then moves away from the membrane, leaving the newly polymerised solid layer bonded to the surface of the build platform. The build platform is then positioned at a fixed distance from the membrane to leave a gap equal to that of the working resolution of the printer, which is then filled via displacement by the UV-curable resin. At this point, the process can be repeated, and the next sliced layer of the model is built onto the surface of the previous layer attached to the build platform. In this way, the 3D CAD model can be built layer by layer onto the surface of the build platform. Once completed, the printed part can be removed from the platform and washed in a solvent such as isopropanol (IPA). The washing ensures that any excess, uncured resin on the printed model is removed, as it should be soluble within the washing solvent before it is dried and cured further via heating and UV light exposure[253].

Various resins can be selected to achieve a printed model with the desired physical properties, such as toughness, chemical compatibility and durability. Within this work, SLA 3D printing was used for general engineering solutions such as printing a bespoke microfluidic chip PDMS clamp and a scaffold for microfluidic components within the flow reactor. In addition, stereolithography was used to fabricate larger (> 300 µm diameter channels) microfluidic master substrates. These were then used for casting PDMS substrates, as described in the section regarding soft photolithography (Figure 3.13 - 9).

All SLA 3D printing was performed using a FormLabs Form 3+, FormLabs Form Wash, and FormLabs Form Cura and was printed in Tough 2000 resin. All CAD designs were generated using Autodesk Inventor Professional, and models were sliced using FormLabs Preform. The standard operating procedure for printing, as taken from the manufacturer[254], is as follows:

A clean build platform was mounted within the printer, and the print was started following the model's upload. The time required for printing was proportional to the model's size, the print's resolution and the number of sliced layers. Upon completion of printing, the build platform was detached, and the printed models were removed. The models were then agitated gently within a

'dirty' IPA wash bath for five minutes, followed by a 'clean' wash bath for another five minutes. All models were placed within a vortexed IPA wash bath for 10 minutes. The models were then dried under nitrogen and left within the curer for 60 minutes at 70°C, with temperature ramping from 21°C (room temperature).

3.4 - Standard Operating Procedures (SOPs)

Any standardised protocols used throughout this work and across various experiments are outlined within this subsection or otherwise contained in the subsections prior or their respective experimental chapters.

Within this work, standard phosphate buffered saline (PBS) buffer consists of 0.01 M phosphate buffer, 0.0027 M potassium chloride and 0.137 M sodium chloride, pH 7.4 at 25 °C.

3.4.1 - Casting of PDMS Microfluidic Chips

The in-house devised standard operating procedure (SOP) for preparing and casting PDMS microfluidic devices is as follows:

PDMS chips were fabricated using SYLGARD™ 184 Silicone Elastomer, with a 1:7 ratio of curing agent to elastomer base by weight. The mixture was vigorously mixed before 30 minutes of degassing within a vacuum desiccator. The liquid PDMS was then poured into the PDMS microfluidic chip jig, in which the master substrate of choice was already mounted and degassed again for a further 30 minutes. The PDMS was subsequently baked in an oven at 65 °C overnight but was fully cured within 4-5 hours. Before use, the formed PDMS microfluidic chip was removed from the mould and washed in mQ water, followed by ethanol and dried under nitrogen. Punching holes into the PDMS chip was not required within this work, as the bespoke PDMS microfluidic chip jig automatically formed channel inlets and outlets as part of the casting process.

Several approaches were employed to seal the PDMS microfluidic manifold to a glass substrate. The standard in-house standard operating procedure (SOP) for plasma oxygen bonding substrates is as follows:

Plasma oxygen bonding was used to covalently attach the PDMS microfluidic devices to a standard microscope slide glass substrate. The glass and PDMS surfaces were washed for 5 minutes in mQ water, followed by ethanol, and then dried under nitrogen. For the plasma oxygen treatment (ashing), the microscope slide glass substrate was treated at 20 % power for 2 minutes using a Henniker plasma HPT-200, followed by the PDMS separately subjected to 100 % power for 20 seconds. Upon plasma oxygen exposure, the PDMS chip was carefully laid channel slide

down onto the glass substrate, and pressure was applied gently and evenly to the top of the chip, successfully sealing the device to the glass slide to create the microfluidic device.

PDMS chips used as microfluidic reactors that did not require plasma oxygen bonding were instead clamped firmly to the enzyme-functionalised Au-on-Si substrate via a bespoke microfluidic chip clamp (6.2 - In-Flow Biocatalysis in a Planar Surface Microfluidic Chip).

3.4.2 - Piranha Solution for Substrate Cleaning

Piranha solution is an aggressive cleaning and etching agent for organic compounds, usually used with glassware and substrates, that consists of sulphuric acid and hydrogen peroxide. The formation of the active chemical within Piranha is described by the equation[255]:

$$H_2O_2 + H_2SO_4 \rightleftharpoons H_2O + H_2SO_5 \quad \textbf{(3.15)}$$

Peroxymonosulfuric acid or Caro's acid[256], H_2SO_5, is highly acidic and an extremely strong oxidising agent, and reacts energetically with organic molecules, breaking them down to the point of degradation. In this work, piranha solution was the primary form of cleaning used for substrates. The in-house devised standard operating procedure for this process is as follows:

Three large beakers of mQ water were prepared, and the fume hood/ wet deck sink was filled two-thirds with town water as a precautionary step. Lab coats, face shields and long acid-resistant rubber gauntlets over nitrile gloves were worn at all times. All organic solvents (including those stored in the fume hood) were moved well away from the working area. All labware containers used were made of glass, not plastic.

Hydrogen peroxide solution at 30 % (w/w) in H_2O (20 ml) was added slowly to sulfuric acid (60 ml) in a 1:3 ratio, respectively, to form the active Piranha solution, which then spontaneously heats and effervesces. The substrate was then submerged in the Piranha solution for 7 minutes, rotated to expose the reverse face and submerged for an additional 7 minutes. The substrate was then carefully removed from the solution and washed twice in succession in the mQ water baths. In addition, all tweezers or implements used to manipulate the substrate were washed similarly. The substrate was kept underwater until the correct disposal of the piranha solution had been performed.

Once the piranha solution was thoroughly disposed of, the substrate was immersed in ethanol before being dried under a stream of nitrogen. The cleaned substrate was used directly or stored under ethanol until use.

3.4.3 - Enzyme Functionalisation and Packing Procedure for Bead Columns

The functionalisation of sepharose beads via the His-Tag motif on expressed enzymes was used regularly for the later stages of this work. The in-house devised standard operating procedure is as follows:

Cytiva Ni Sepharose 6 Fast Flow beads (approx. 20 mg) were suspended in a solution of cystathionine beta-lyase [1 mg/ml, 20.7 µM] made up in standard PBS buffer (0.8 mL) and left gently agitating for 1 hour. Protein concentrations were determined before and after the process using a Bradford Assay.

The functionalised beads were then concentrated by centrifugation, the enzyme-containing supernatant decanted, and the beads resuspended in standard PBS buffer (1 mL). This washing, centrifuging and decanting process was repeated twice more before the beads were packed into the microfluidic column and washed with further standard PBS buffer (1 mL).

3.4.4 - Lipoic Acid Self-Assembled Monolayer (SAM) Procedure

A standard operating procedure (SOP) for functionalising Au substrate surfaces with an LA-NTA self-assembled monolayer was devised for the His-Tag binding of enzymes. This procedure was used in the case of both QCM-D experiments to further characterise this enzyme immobilisation method and on Au-on-Si substrates for planer microfluidic chip reactors. Before functionalisation, Au-on-Si substrates or Au QCM-D sensors were cleaned using Piranha solution (3.4.2 - Piranha Solution for Substrate Cleaning). The standard operating procedure was modified from the literature[20] and is as follows:

(2S)-2-[bis(carboxymethyl)amino]-6-[5-(dithiolan-3-yl)pentanoylamino]hexanoic acid, abbreviated to LA-NTA (9.0 mg, 20 µmol) was dissolved in a 1 to 1 solvent mixture of mQ water (0.5 mL) and ethanol (0.5 mL). Tris(2-carboxyethyl)phosphine hydrochloride abbreviated to TCEP (20.0 mg, 70 µmol) was then dissolved in mQ water (200 µL) before being added slowly to the original solution and then being mixed via vortex for 60 seconds. The reaction mixture was then carefully drop-cast onto the surface of the Au-on-Si substrate or Au QCM-D sensor and incubated overnight at 4 °C, suspended over a shallow bath of 1:1 Ethanol-mQ Water mix in a sealed container, to maintain a humid environment and reduce the rate of evaporation. The substrates were then washed with consecutive ethanol and mQ water wash steps, which were repeated a

further two times before being dried under a stream of nitrogen. This results in an LA-NTA self-assembled monolayer functionalised substrate, which was validated through further QCM-D and PM-IRRAS experiments.

3.4.5 - Ni regeneration of the LA-NTA SAM and His-Tagged Enzyme Immobilization Procedure

An SOP for the further functionalisation of LA–NTA self-assembled monolayer functionalised substrates prior to their use in planer microfluidic chip reactors was devised in-house, including the preparation, Ni regeneration and enzyme immobilisation of the surface.

Ethylenediaminetetraacetic acid (EDTA) dipotassium salt dihydrate (1.719 g, 4.25 mmol, 425 mM) was dissolved in standard PBS buffer (10 mL), and the LA-NTA SAM functionalised substrate submerged in the solution and gently agitated on a sample mixer for 2 hours at 400 RPM and room temperature. The substrate was then washed with consecutive PBS buffer and mQ water wash steps, which were repeated twice before being dried under a stream of nitrogen.

Nickel(II) chloride (0.143g, 1.10 mmol, 100 mM) was dissolved in mQ water (6 mL) and then drop-cast onto the LA-NTA SAM functionalised substrate for 20 minutes at room temperature. The substrate was then washed three times with mQ water and dried under a stream of nitrogen.

CBL Enzyme [100 ug/ml, 2.07 µM] in PBS Buffer (2 mL) was then carefully drop-cast onto the surface of the Ni regenerated LA-NTA SAM functionalised substrate for ***strictly*** *5 minutes at room temperature. The substrate was washed with PBS Buffer three times and stored under PBS Buffer until used for inflow biocatalysis. The substrate was validated through further QCM-D and PM-IRRAS experiments at each step.*

3.4.6 - Preparation of the Standard CBL µ-IMER Running Buffer

This SOP outlines the preparation of the S-benzyl-L-cysteine substrate running buffer used in all reactor and control experiments involving the enzyme cystathionine beta-lyase (CBL).

S-benzyl-L-cysteine (42.4mg, 200 µmol) was partially dissolved in standard phosphate-buffered saline solution (10 mL). To this solution, 5,5'-dithiobis-(2-nitrobenzoic acid) or DTNB (8 mg, 20 µmol) in standard phosphate-buffered saline solution (10 mL) and the resultant solution vortexed until any prevailing precipitate dissolved. The solution was then passed through an MCE syringe

filter (0.22 µm pore size, 25mm diameter) to ensure no particulates remained in the solution, to yield the substrate running buffer comprised of S-benzyl-L-cysteine [10 mM] and DTNB [1 mM] in standard PBS.

Chapter 4 - Chemical Immobilisation Strategies

A requirement inherent to any µ-IMER is a means of immobilising an enzyme on a surface suitable for catalysis of the solubilised substrates while remaining stable within the fluidic flow. The strategy required for the immobilisation is subject to the requirements of the reactor and the enzyme used in the process. Naturally, an enzyme with a higher stability is much more likely to be compatible with multiple immobilisation strategies without significant detriment to its structural integrity and reactivity. In contrast, other enzymes with lower stability will readily unfold or be rendered inert following immobilisation.

One of the intrinsic advantages of working with any in-house expressed recombinant protein or enzyme is that they have often undergone mutagenesis to express a binding tag motif, such as a His-tag, for ease of purification. This motif can be left uncleaved following purification, which gives the designer of the enzymatic reactor the flexibility to use the tag as the means of enzyme immobilisation. As described in the theory section, metal affinity binding immobilisation via genetically incorporated protein-binding motifs often provides a convenient, reversible and orientationally selective means of enzyme immobilisation. If the enzyme has previously been immobilised using affinity binding for purification, its structural stability after using this approach is often also validated, decreasing the risk of immobilisation incompatibility. Both the Gst apoprotein and the natural enzyme, CBL, used within this work were expressed with a His-tag motif, which was left un-cleaved. For the advantages already discussed, immobilisation methods that utilised Ni^{2+} His-tag affinity binding were chosen in the design of all µ -IMER systems within this work.

The selected natural enzyme, Cystathionine beta-lyase (CBL), is expressed within biological systems to catalyse the α,β-elimination reaction of L-cystathionine to produce homocysteine, pyruvate and ammonia[257]. The enzyme was chosen due to the collaborator in biology who performed the enzyme expression and purification, Reyme Herman, having an excess of the His-tag containing CBL and had already confirmed its stability, high catalytic activity and promiscuity for alternative substrates for solution phase catalysis within their work[258], making it a perfect candidate to use during the optimisation of the immobilisation protocol and also the IMER system as a whole. The use of CBL allowed for confirmation of the immobilisation approach while protecting precious stocks of the GST apoprotein and opened the opportunity for rapid enzymatic testing of immobilisation strategies and the entire flow reactor system. Additionally, as the use of CBL in a µ-IMER is novel, it provides an additional example of a µ-IMER system to

the broader community. Another choice in experimental design made early on in the project was to pursue multiple strategies for immobilisation. Not only does this maximise the chance of successful immobilisation, but it gives the opportunity to develop different methods for different applications. Therefore, this chapter is split into two parts that detail the approaches investigated. Specifically, the first part discusses a bespoke electrografted near monolayer approach; the second is a more simplistic, self-assembled monolayer approach to enzyme functionalisation of surfaces, where both utilise his tag affinity binding. The chapter is structured to reflect the evolution of the strategies, including the obstacles, solutions, discoveries and choices made when pursuing these immobilisation strategies for their potential incorporation in the end µ-IMER system.

4.1 - Diazonium Electrografting Immobilisation Strategy

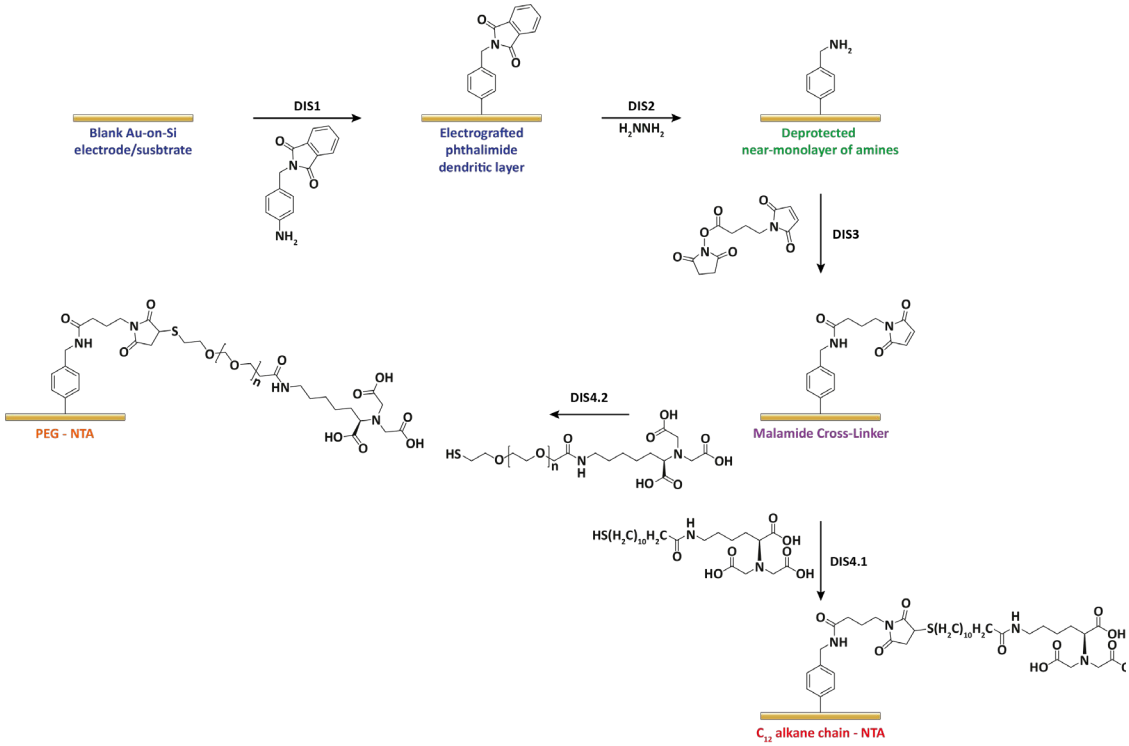

Figure 4.1 - The schematic for the diazonium electrografting strategy, including the potential polyethylene glycol (PEG)-NTA and alkane-NTA thiol linkers.

When first considering the potential directions of this research, reversible immobilisation strategies were a recurring theme due to the implicit advantages, such as the regeneration, recyclability and reusability of crucial components such as the protein scaffold and precious metal catalytic centres. For example, the reversible siderophore ArMs demonstrated by Raines *et al.*[70] would be used within the project. This work confirmed the switchable nature of the siderophore apoprotein complex but also revealed the difficulty of reconstituting the protein scaffold and metal catalytic centre via solution phase purification. Through the use of a switchable immobilisation strategy, such as metal affinity binding, a twofold reversible binding strategy could be achieved, with a set redox profile to actuate the binding of the siderophore and another binding approach to switch the His-tag immobilisation of the apoprotein to the surface reversibly. This approach would allow the regeneration, recycling and switching of the catalytic centre and the separate reconstitution of the protein scaffold. For this to be possible, the difference in electrochemical potential for redox switching of the metal centre used for the affinity surface binding and the iron centre of the siderophore complex would need to be sufficient so that both could be actuated individually. Therefore, if the enzyme were immobilised onto an electrode surface via a redox-active centre, it would offer a potential means of electrochemically actuating both reversible binding systems independent of one another

without the need for chemical reduction and oxidation flow steps. It should be noted that although chemical redox switching of the siderophore-ArM complex had been shown, electrochemical redox switching was still undemonstrated.

To develop this electrochemical redox approach, the immobilisation strategy required to functionalise the surface with NTA groups would need to be resistant to degradation across various electrochemical potentials. For this reason, a diazonium electrografted approach was selected, which would allow the step-by-step assembly of a highly stable NTA functionalisation layer, with room for selective optimisation of its properties through aspects such as the chemical composition of the chain-linker strand (Figure 4.1). The proposed electrografted diazonium immobilisation strategy (DIS) was split into four reaction steps, not including nickel charging or protein immobilisation. 1) Electrografting a diazonium salt of a phthalamide-protected benzylamine molecule onto an electrode surface, followed by 2) the hydrazine-aided deprotection of the phthalamide group to leave a near monolayer of benzylamine chemically bonded to the surface. 3) the de-protected amine was then conjugated via an NHS-ester coupling reaction to a short cross-linker molecule, which terminated in a maleimide group. 4) this maleimide group could be cross-linked to a thiol-containing chain-NTA molecule, with a chain consisting of alkane or polyethylene glycol (PEG) monomeric units. Au-on-Si wafers (approximate surface area of 30 by 20 mm) comprising a titanium adhesion layer (25 nm) and an active gold upper layer (75 nm) were used as the working electrodes within all electrografting procedures within this work. The procedure, optimisation and characterisation of each of these steps are discussed in the following sections. Prior to the surface being functionalised, the Au-on-Si working electrode first underwent the following ozone-cleaning procedure:

The Au-on-Si electrode substrate was subjected to UV-ozone treatment for 10 minutes, followed by sonication in Hellmanex III solution (2 % v/v) and twice in fresh mQ water for 10 minutes per step and dried under nitrogen between each step. The electrode substrate was then subjected to UV-ozone treatment for a further 30 minutes before being fully immersed in ethanol for 30 minutes and then finally dried under nitrogen.

4.1.1 - Initial Electrografting Diazonium Strategy (DIS1.1)

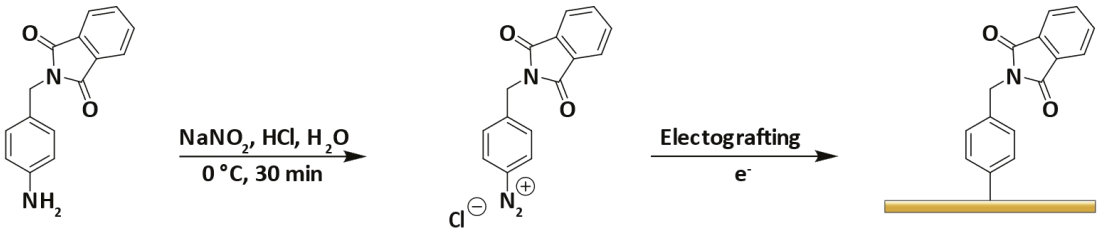

Figure 4.2 - The reaction schematic for the benzyl phthalide multilayer functionalisation of an Au-on-Si electrode surface via the *in situ* formation of a diazonium salt species followed by electrografting under the initially proposed reaction conditions.

Electrografting of the diazonium salt was inspired by work performed by Yates *et al.*[172] that demonstrated electrografting of a phthalamide-protected benzylamine diazonium cation species to form a dendritic multilayer structure on the surface of a disc electrode. Through the hydrazine deprotection of the phthalamide group, Yates *et al.* showed that the surface was functionalised with a near-monolayer of chemically bonded para-position benzylamine.

The strategy demonstrated by Yates *et al.* was adapted within this work to investigate an alternative reaction route for the formation of the diazonium species. First, various solvent mixtures were tested to determine which would best suit the solubilisation of 4-N-Phthaloylglyaminomethyl aniline (Table 1).

Solvent	Volume used (µL)	Soluble?
H_2O	20 & 100	No
DMSO	20 &100	No
H_2O : DMSO - 1:1	20 &100	No
CH_3CN	20 & 100	No
MeOH	20 & 100	Sparingly Soluble (not very)
DMF	20	Yes

Table 1 - The various solvents at differing volumes were tested to dissolve 4-N-Phthaloylglyaminomethyl aniline (3.0 mg) and the resultant solubilities.

These preliminary experiments showed 4-N-Phthaloylglyaminomethyl aniline (3.0 mg) to be highly insoluble in numerous solvents, with dimethylformamide (DMF) yielding the best results in which the reactant mostly dissolved but not entirely. However, the solubility in DMF was sufficient enough that the solution could be added dropwise to the nitrous acid solution (required to activate the diazonium for electrografting) upon which any remaining solid substrate

rapidly dissolved. Using this information, the initial operating procedure for this reaction, DIS1.1 (Figure 4.2), was established and tested:

In an Eppendorf tube, sodium nitrate (9.9 mg, 144.0 µmol) was dissolved in mQ Water (480 µL). HCl (0.5 M, 9.00 mL) was added, and the solution was mixed via vortex for 2 minutes. To this resultant nitrous acid solution, 4-N-Phthaloylglyaminomethyl aniline (3.0 mg, 12.00 µmol) in DMF (120 µL) was added carefully dropwise and gently agitated at 0 °C for 30 minutes. The surface for functionalisation was then submerged in the diazonium salt solution (<1 mM). The surface was used as the working electrode, a Pt wire as the counter electrode, and an Ag/AgCl / KCl (sat'd) reference electrode at a scan rate of 100 mV/s between -0.20 to 0.70 V vs Reference for the electrografting configuration.

A stable electronic contact with the Au-on-Si working electrode, where a constant signal was observed throughout the CV scanning, was achieved using a copper wire bonded to the top of the gold-plated surface of the working electrode using a silver epoxide adhesive. This method provided a consistent and reliable electronic contact to the working electrode surface and was thus used throughout. It is worth noting that care was needed to ensure the silver epoxide was not exposed to the electrolyte solution, as it could have contaminated the electrolyte solution and the electrode surface. In order to mitigate this risk of contamination, the total volume of electrografting solution in the electrochemical cell was optimised to 9.6 ml. Doing so ensured that approximately 20 mm of the total 30 mm length of the working electrode remained immersed within the solution, ensuring the contact point remained dry.

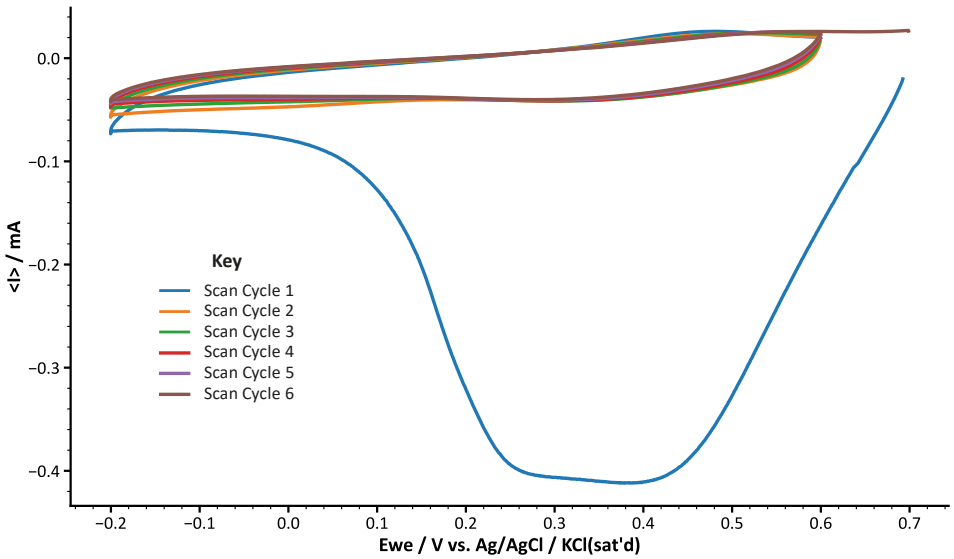

Figure 4.3 - The CV of the initial test conditions for diazonium salt electrografting to form a benzyl phthalamide multilayer. An Au-on-Si surface (2 cm^2) was used as the working electrode, a Pt wire as the counter electrode and an Ag/AgCl / KCl (sat'd) reference electrode at a scan rate of 100 mV/s across -0.20 to 0.70 V vs Reference.

The resulting cyclic voltammogram obtained during the electrografting process showed a significant and broad reduction peak around 3.5 V vs Ag/AgCl KCl (sat'd) within the first cycle, with no significant oxidation peak (Figure 4.3). Several more potential cycles proceeded the initial one, none displaying any additional redox peaks. This result indicated that deposition via diazonium electrografting is complete within the first initial reduction scan. Simpson's rule was used to approximate the area under the baseline corrected peak, which could then be used in the equations derived from Faraday's laws of electrolysis (3.1.3 - Cyclic voltammetry (CV) - Equation (3.9)) to estimate the molecular coverage, i.e. the number of molecules per unit area. This thesis uses the same method for all CV-based surface coverage calculations. For the electrografting process, molecular coverage is not simply dependent on the number of molecules directly attached to the surface of the electrode, as the process forms a dense multilayer. Instead, the calculated surface coverage includes the number of molecules electrografted to the surface and molecules bound within the multilayer. Later surface coverage studies involving ferrocene, and within the next chapter for protein binding, assume a near-monolayer planer surface. The estimated molecular coverage was calculated to be 2.42×10^{15} molecules cm^{-2}, which, due to its magnitude, supports the formation of a dense dendritic multilayer. The magnitude agrees with published densities[259] of 1.81×10^{15} molecules cm^{-2} for similar diazonium electrografted aryl species. Despite yielding a significant resultant density, further optimisation of this process was explored, such as rapid use of the *in situ* generated diazonium salt and an improved electrode cleaning process.

4.1.2 - Improved Electrografting Diazonium Strategy (DIS1.2)

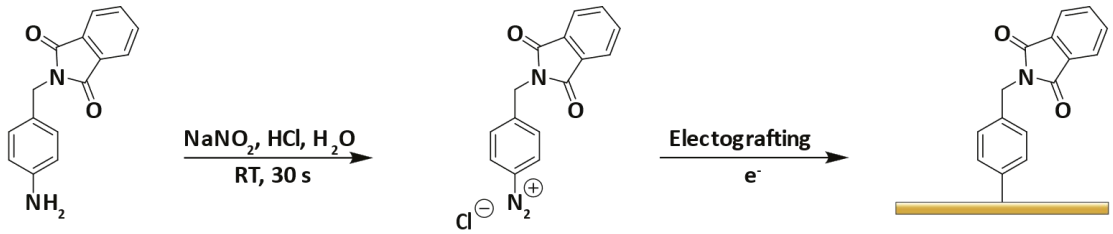

Figure 4.4 - The reaction schematic for the benzyl phthalide multilayer functionalisation of an Au-on-Si electrode surface via the *in situ* formation of a diazonium salt species followed by electrografting under experimentally optimised reaction conditions.

The first area explored was the reaction conditions for *in situ* diazonium salt formation. When diazonium salts are formed for solution-phase reaction with solubilised reagents, the concentrations of diazonium salt are often much more significant than those used for electrografting. Diazonium compounds are thermally unstable and are often explosive in nature[260]. For electrografting, the concentration of the diazonium species can be significantly lower as the reaction with the diazonium salt is electrochemically driven, making working with the compounds significantly safer. The diazonium species at the concentration used within this work was shown to be non-explosive, even at room temperature, but was still handled with extreme care. It was suspected that the 30-minute length of the *in situ* formation step at a low concentration led to significant decomposition of the active diazonium species despite being kept at 0° C. Therefore, after ensuring relative thermostability of the diazonium compound in low molarity solutions at room temperature under controlled ventilated conditions, a new reaction scheme was developed, DIS1.2, for a much faster 30-second preparation at room temperature (Figure 4.4). The resultant CV for the electrografting using this new experimental procedure showed a significantly larger reduction peak (Figure 4.5b) and an almost twofold increase in molecular coverage with a calculated value of 4.54×10^{15} molecules cm^{-2} compared to the original strategy.

Although this optimisation significantly improved the observed density of electrografted diazonium, it was still deemed prudent to confirm the effect of using a more aggressive and thorough process for the pre-reaction cleaning of the Si-on-Au working electrode. Therefore, a piranha cleaning protocol (3.4.2 - Piranha Solution for Substrate Cleaning) was performed, and the sample was subjected to the same optimised diazonium salt generation conditions, DIS1.2.

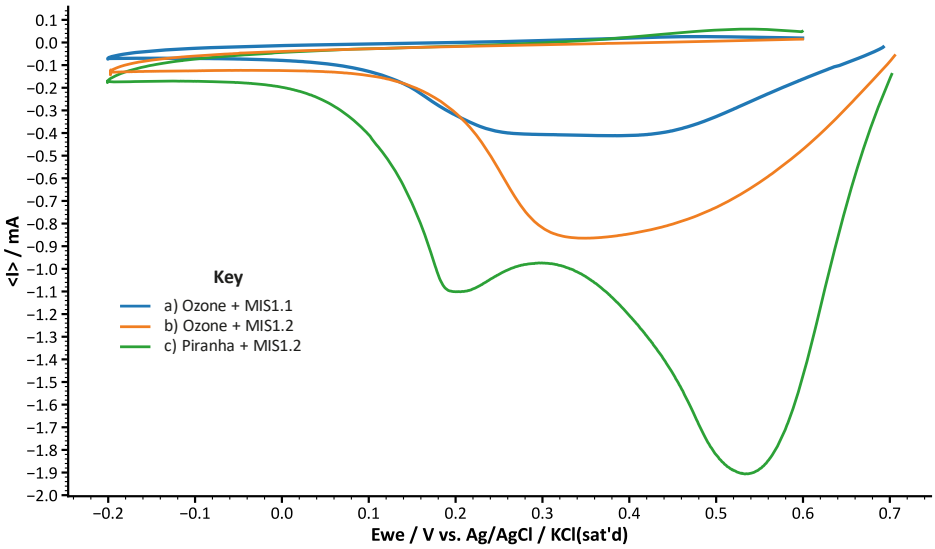

Figure 4.5 - The diazonium electrografting CV reduction peaks for comparing a) the original on optimised reaction with ozone cleaning, b) the optimised reaction conditions with ozone cleaning, and c) the optimised reaction conditions with piranha cleaning. In each CV, an Au-on-Si surface (2 cm^2) was used as the working electrode, a Pt wire as the counter electrode and an Ag/AgCl / KCl (sat'd) reference electrode at a scan rate of 100 mV/s across -0.20 to 0.70 V vs Reference. Only the first of six repeat scans has been plotted for clarity; all other scans displayed no additional peaks.

Due to the peak's increased magnitude, the calculated molecular coverage of 9.52×10^{15} molecules cm^{-2} (Figure 1.5c) was over twice that of the sample that had only been subject to ozone cleaning. The resultant reduction voltammogram also displays two reduction peaks, the first at 0.53 V vs Reference and the second at 0.20 V vs Reference. One explanation for the presence of a double peak is that one relates to the initial formation of the surface-bound species, and the second is associated with electrografting at a different site, such as a different area on the electrode or the interaction with already bound aryl groups[261]. A more compelling explanation for this phenomenon is given by Lee *et al.*[262], who observed the same pattern for the electrografting of aryldiazonium ions onto glassy carbon electrodes. They attribute the presence of the first reduction peak to the lower energy, surface-catalysed reaction and the reduction peak at a more negative electrode potential to the higher energy, solution-catalysed reaction of the diazonium salt species. The work additionally demonstrated that the catalysed reaction could only occur at clean surfaces and that in the absence of the surface catalytic pathway, only the more negative potential peak for the uncatalysed reaction is observed. Critically, the higher energy reduction peak does not occur exclusively due to direct grafting to the electrode surface, and a dendric multilayer structure still forms at the high potential peak. The fact that the double peak was only observed within this work after piranha cleaning of the substrate further supports the explanation and hypothesis proposed by Lee *et al.*.

4.1.3 - Hydrazine Deprotection of a Phthalimide Protecting Group (DIS2)

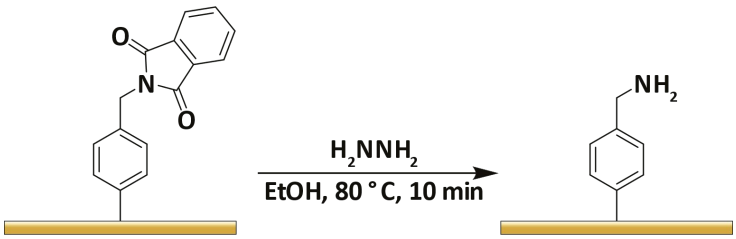

Figure 4.6 - The reaction schematic for the hydrazine deprotection of the phthalamide group to liberate the dendritic multilayer structure, leaving a benzylamine near-monolayer.

After the surface had been successfully electrografted, the same strategy used by Raines *et al.*[70] was utilised to de-protect the phthalamide group, leaving a near monolayer of benzylamine groups as opposed to the dendritic multilayer that results from the electrografting process (Figure 4.6). The procedure used for this process is as follows:

Hydrazine monohydrate (775 µL, 16.0 µmol) in ethanol (10 mL) was heated to 80 °C under reflux. The solution was then removed from the heat, and the N-benzyl phthalimide functionalised Si-on-Au surface was submerged for 10 minutes. The surface was then cooled to room temperature and submerged in ice-cold ethanol for 30 seconds before being rinsed with ice-cold mQ water and dried under a stream of nitrogen, yielding the benzylamine near-monolayer "hydrazine-treated" surface.

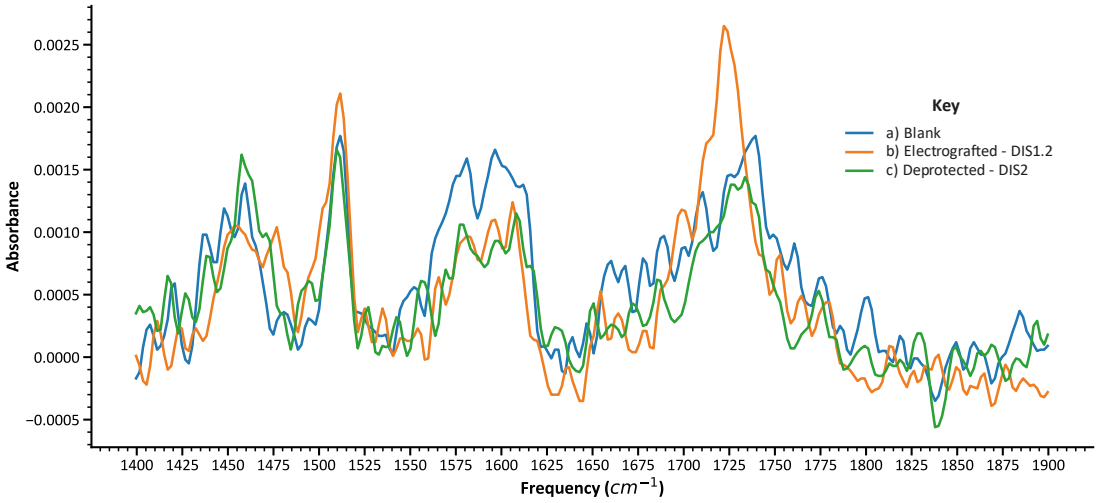

Figure 4.7 - PM-IRRAS spectra of the same Au-on-Si working electrode after a) piranha cleaning (blank control), b) aryl diazonium electrografted and c) hydrazine deprotection. The spectrum was acquired with a spectral resolution of 7 $cm^{-1,}$ and the data was processed with a polynomial baseline subtraction.

Two methods were utilised to test the validity and effectiveness of the deprotection. First, PM-IRRAS was used to evaluate the chemical composition of the electrode surface at multiple stages of the surface functionalisation process, namely the blank Au surface of the working electrode, the surface after electrografting and the surface after the deprotection step (Figure 4.7).

An IR absorption peak at 1724 cm^{-1} was observed on the electrografted surface (Figure 4.7b). This peak was not observed on the surface of the bare Au surface (Figure 4.7a). The starting compound (Figure 4.4 - First molecule) was reported in the literature to give a C=O at 1754 cm^{-1} using KBr IR[263]. The similarity to this literature value suggests the absorbtion peak on the electrografted surface is likely associated with the tertiary amide C=O stretching peak of phthalimide groups within the electrografted multilayer, with the slight downshift in frequency likely a result of the change in molecular structure and a more sterically hindered local environment resulting from the dendritic multilayer. PM-IRRAS performed on the sample after undergoing the hydrazine protection step did not contain the C=O stretching peak, alluding to the removal of a detectable portion of the dendritic multilayer. Additional analytical methods were employed to complement the IR data to confirm the successful deprotection of phthalimide-protecting groups. The electrografted surface, being an active working electrode, opened options for the use of electrochemical methods to probe the state of the surface chemistry. Ferrocene is regularly used as an electrochemical probe and reference compound due to its reversible and distant redox CV profile. Moreover, using electrochemical measurements, it is possible to determine if a reversible redox active molecule, such as ferrocene, is immobilised or free to diffuse in solution (3.1.3 - Cyclic voltammetry (CV)) and to calculate the density of immobilised redox groups. In this work, NHS-ester-modified ferrocene was immobilised to the electrode-bound unprotected benzyl amines (Figure 4.8); the same reaction chemistry proposed within this surface functionalisation strategy, DIS3 (Figure 4.4).

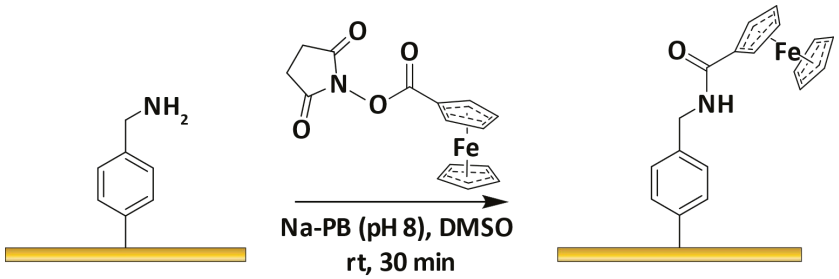

Figure 4.8 - The reaction schematic for functionalising the benzylamine surface with ferrocene via an NHS-ester cross-linker reaction.

The experimental procedure was developed in-house for the ferrocene NHS-ester cross-coupling reaction to the benzylamine surface and is as follows:

NHS ester Ferrocene (4.9 mg, 15.00 µmol) in DMSO (200 µL) was added dropwise to sodium phosphate buffer (pH 8, 10 mL, 0.01 M) and then mixed via vortex for 2 minutes. In this solution, the benzylamine functionalised Au-on-Si surface was then submerged fully for 30 minutes at room temperature. The functionalised surface was removed and washed with mQ water followed by ethanol and then dried under nitrogen gas, giving the ferrocene functionalised Au-on-Si surface.

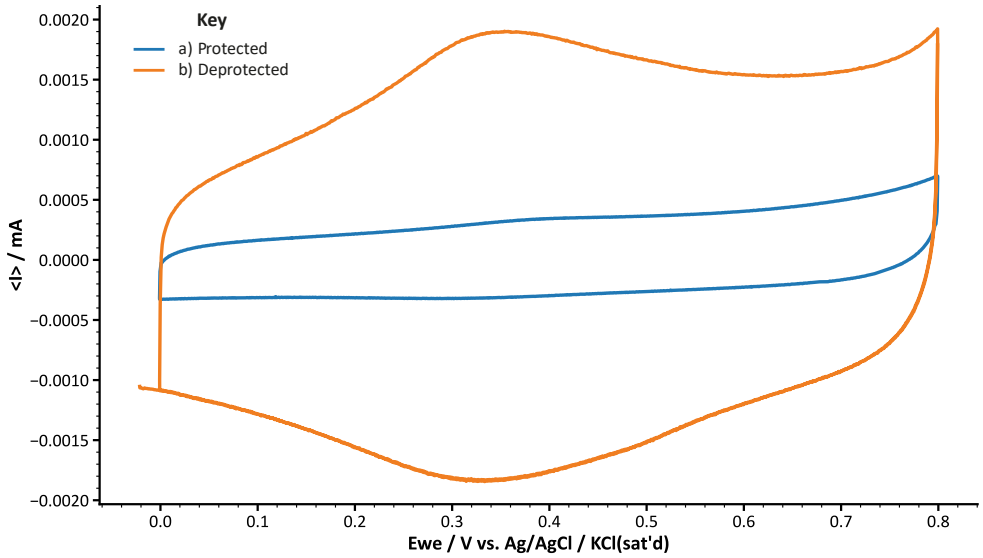

Figure 4.9 - Cyclic voltammogram of electrode surfaces which had undergone the NHS-ester ferrocene functionalisation, where a) had undergone the hydrazine deprotection step DIS2 and b) had not undergone deprotection as a control. Other than this, both electrodes underwent identical treatment. In each CV, an Au-on-Si surface was used as the working electrode, a Pt wire as the counter electrode and an Ag/AgCl / KCl (sat'd) reference electrode at a scan rate of 500 mV/s across 0.00 to 0.80 V vs Reference. The second of six repeat cycles was used for plotting and analysis.

The ferrocene NHS ester cross-linker functionalisation reaction was performed on two electrografted electrodes; the first had undergone hydrazine deprotection, and a second acted as the control, which was electrografted with the diazonium but not subject to deprotection. Both electrodes' CV profiles were collected at a voltage scan rate of 500 mV/s. The de-protected electrode surface displayed a significant CV profile characteristic of a reversible redox couple such as ferrocene (Figure 4.9b). The same characteristic profile was absent in CVs for the protected multilayer electrode (Figure 4.9a), which suggests that the deprotection step was successful in exposing an amine for reaction with the NHS-modified ferrocene while on the still protected multilayer electrode surface; binding could not occur via this route and little non-specific binding was observed. Further CVs were collected at various voltage scan rates to confirm the ferrocene's immobilisation to the electrode surface (Figure 4.10).

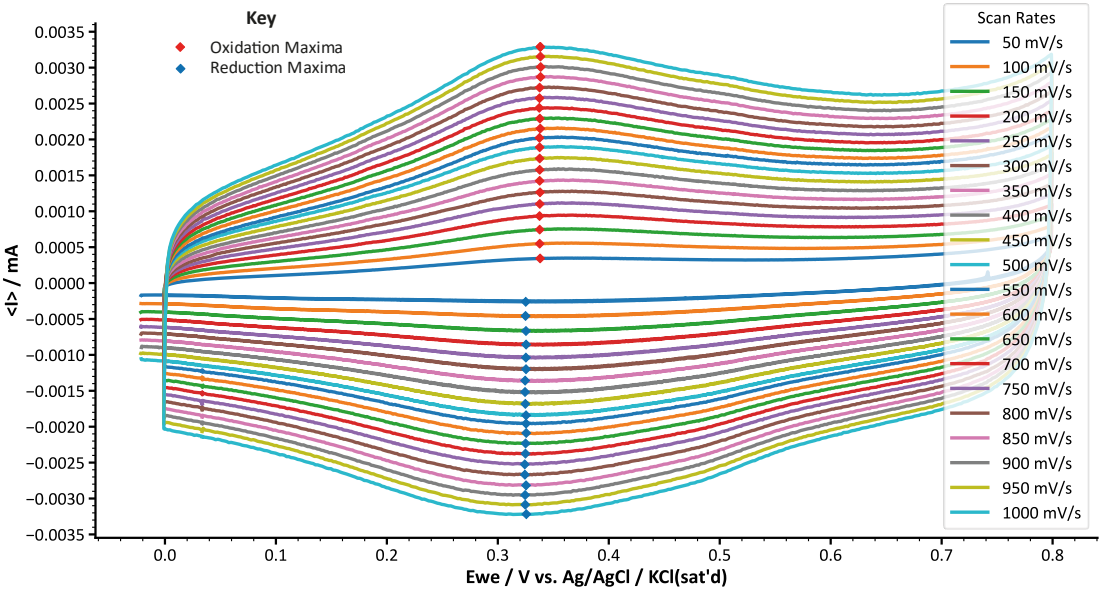

Figure 4.10 - The cyclic voltammogram of the ferrocene functionalised working electrode at scan rates between 50 and 1000 mV/s, incrementing in 50 mV/s steps, with a 15-second wait step between scans. The oxidation and reduction current maxima peak positions used in later analysis have additionally been labelled. In each CV, an Au-on-Si surface was used as the working electrode, a Pt wire as the counter electrode and an Ag/AgCl / KCl (sat'd) reference electrode at various scan rates across 0.00 to 0.80 V vs Reference. The second of six repeat cycles was used for plotting and analysis.

As expected, the magnitude of the redox peaks increased with the scan rate. An approximation of the surface coverage for each scan rate could be determined using the equation derived from Faraday's laws of electrolysis. Calculations showed the surface coverage of the immobilised ferrocene to be $2.16\times10^{14} \pm 7.84\times10^{13}$ molecules cm^{-2}. The obtained value for surface coverage is in the same order of magnitude as other strategies for immobilisation of ferrocene following electrografting, namely 1.51×10^{14} molecules cm^{-2} reported by Yates *et al.*[172] and 2.41×10^{14} molecules cm^{-2} reported by Bellare *et al.*[20].

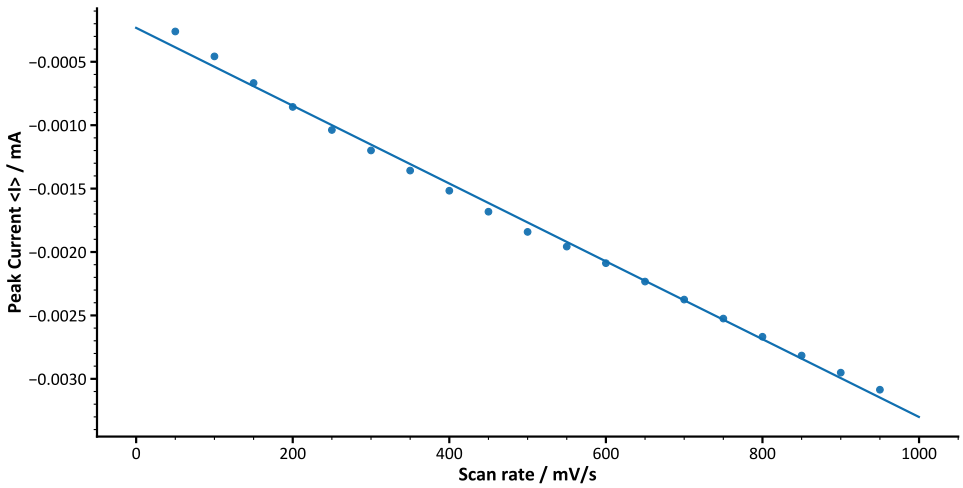

Figure 4.11 - The plotted relationship between the current maxima of the reduction peak and the scan rate for initial reaction conditions. Fitting was achieved using OLS linear regression with an R^2 value of 0.998.

For ferrocene immobilised on an electrode surface, a plot of peak current versus scan rate should follow a linear relationship according to the equation outlined within the method section (3.1.3 - Cyclic voltammetry (CV) - Equation (3.8)). The fitting of a linear equation to each dataset was achieved using an ordinary least squares (OLS) linear regression model.

In the case of the plots comparing peak current against scan rate, a clear linear trend was observed for the reduction peaks (Figure 4.11), with an expected negative gradient. Inspection of the quality of the linear function fit to the experimental data (R^2 = 0.998) further supported the veracity of a linear relationship between peak current and scan rate and, therefore, successful immobilisation of the ferrocene to the surface.

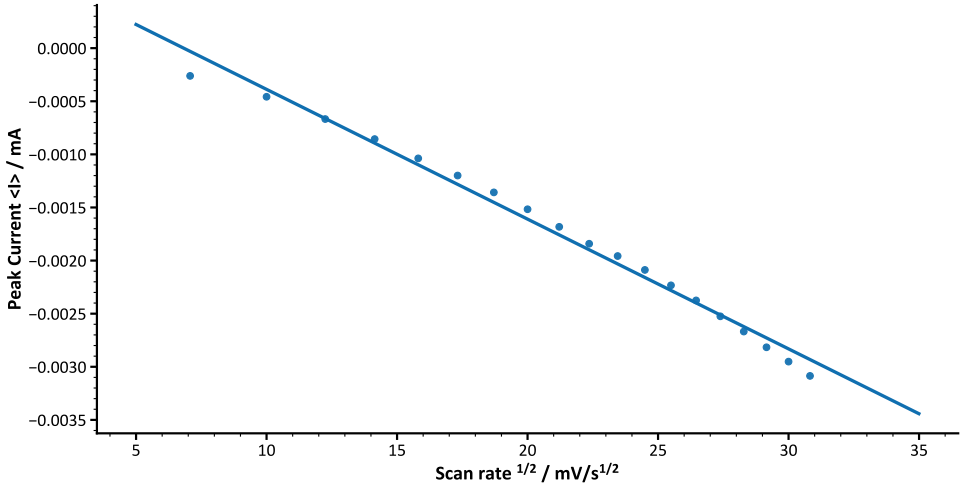

Figure 4.12 - The plotted relationship between the current maxima of the reduction peak and the square root of the scan rate for initial reaction conditions. Fitting was achieved using OLS linear regression with an R^2 value of 0.984.

For completeness, the peak current against the square root of the scan rate was also plotted for the reduction peaks. A directly proportional relationship between these two parameters indicates a freely diffusing redox active species (3.1.3 - Cyclic voltammetry (CV) - Equation (3.7)). Critically, the plots of peak current against the square root of scan rate did not as firmly match the linear fit for the reduction peak (R^2 = 0.984) (Figure 4.12), further confirming successful immobilisation of the NHS-labelled ferrocene on the de-protected diazonium monolayer.

One of the prominent issues observed with the described procedure was that the ferrocene NHS ester had sparingly soluble characteristics within the solvents disclosed within the reaction procedure. Therefore, additional work was performed to optimise the reaction conditions upon concluding this electrochemical ferrocene study. The resultant optimised reaction procedure is as follows:

NHS ester Ferrocene (4.9 mg, 15.00 µmol) in dimethylformamide (DMF, 400 µL) was added dropwise to sodium phosphate buffer (pH 8, 10 mL, 0.01 M) and then mixed via vortex for 2 minutes. In this solution, the benzylamine functionalised Au-on-Si surface was then submerged fully for 30 minutes at room temperature. The functionalised surface was removed and washed with mQ water followed by ethanol and then dried under nitrogen gas, giving the ferrocene functionalised Au-on-Si surface.

Using DMF instead of DMSO significantly increases the solubility of the NHS ester ferrocene species. When the same scan rate CV study was performed, a larger electrode area was used than the previous study to increase the number of ferrocene species being probed and, therefore, reduce experimental noise and uncertainty. The same method of analysing the resultant CV plots at each scan rate gave a significantly improved surface coverage of $3.29\times10^{14} \pm 1.95\times10^{13}$ molecules cm^{-2}, surpassing Bellare *et al.*'s[20] previously reported surface coverage by almost 1.4 times.

Two additional statistical analysis methods were applied for the data obtained using the optimised procedure to assess the validity of plot-fitting relationships further. The first, residual analysis, illustrates how the experimental data deviates from the model fit to the data. The second quartile-quartile (QQ) plot analysis compares the distribution of the experimental data (sample quartiles) to that of a theoretical distribution of the fitted model (theoretical quartiles). The fitting of a linear equation to each dataset was once again achieved using an ordinary least squares (OLS) linear regression model, and the subsequent residual and QQ plot analysis was included with the plots.

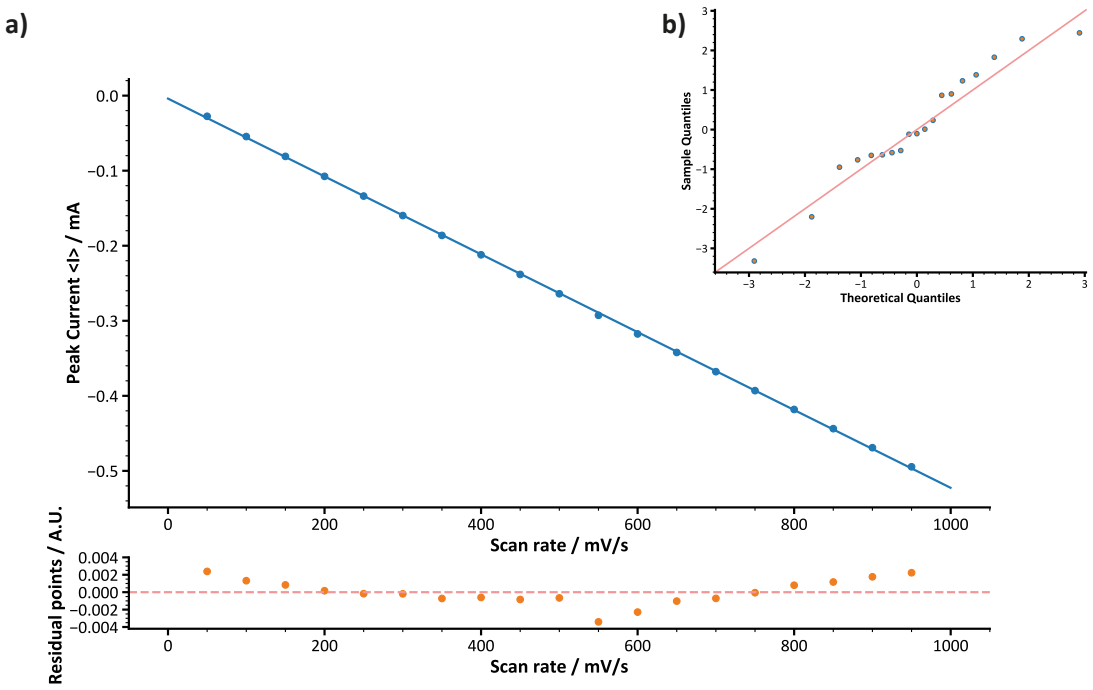

Figure 4.13 - Plotted relationship between the current maxima of the reduction peak and the scan rate with residual analysis a) and Q-Q plot statistical analysis b). Data from the optimised reaction showed significantly lower noise, and the OLS linear regression fitting gave an R^2 value of 1.000, only further validating the prior experimental results.

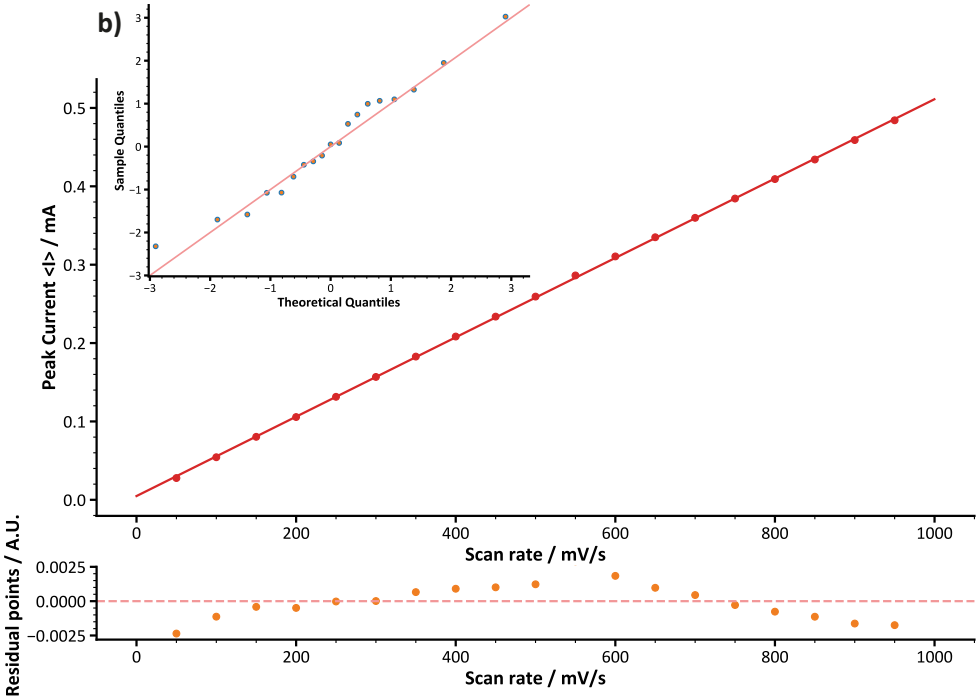

Figure 4.14 - The plotted relationship between the current maxima of the oxidation peak and the scan rate with residual analysis a) and Q-Q plot statistical analysis b). Data from the optimised reaction showed significantly lower noise, and the OLS linear regression fitting gave an R^2 value of 1.000, only further validating the prior experimental results.

The data obtained from the optimised procedure followed the same trends observed within the previous experiment but with significantly lower background noise. The results for this repeat

experiment demonstrated an even stronger correlation, with an R^2 value of 1.000, for both the reduction and oxidation peak current maxima versus scan rate, with inspection of the residuals for both showing a narrow distribution and slight deviations about the norm (Figure 4.13a and Figure 4.14a respectively) and the Q-Q plot analysis for both plots clearly show that the normal quartile distribution is well described by the fitted linear model (Figure 4.13b and Figure 4.14b respectively).

Critically, the plots of peak current against the square root of the scan rate did not as significantly match a linear fit for either the reduction peak, with an R^2 value of 0.975 (Figure 4.15a) or the oxidation peak, with an R^2 value of 0.974 (Figure 4.16a). The obtained residuals for both redox peaks showed the deviations about the norm to be an order of magnitude than that of the current maxima versus scan rate plot, with an apparent curved divergence in the distribution. The QQ plot for the reduction (Figure 1.15b) and oxidation (Figure 1.16b) peaks also showed that the fitted linear model poorly describes the normal quartile distribution, with the same curved deviation from the trend again emerging in the analysis.

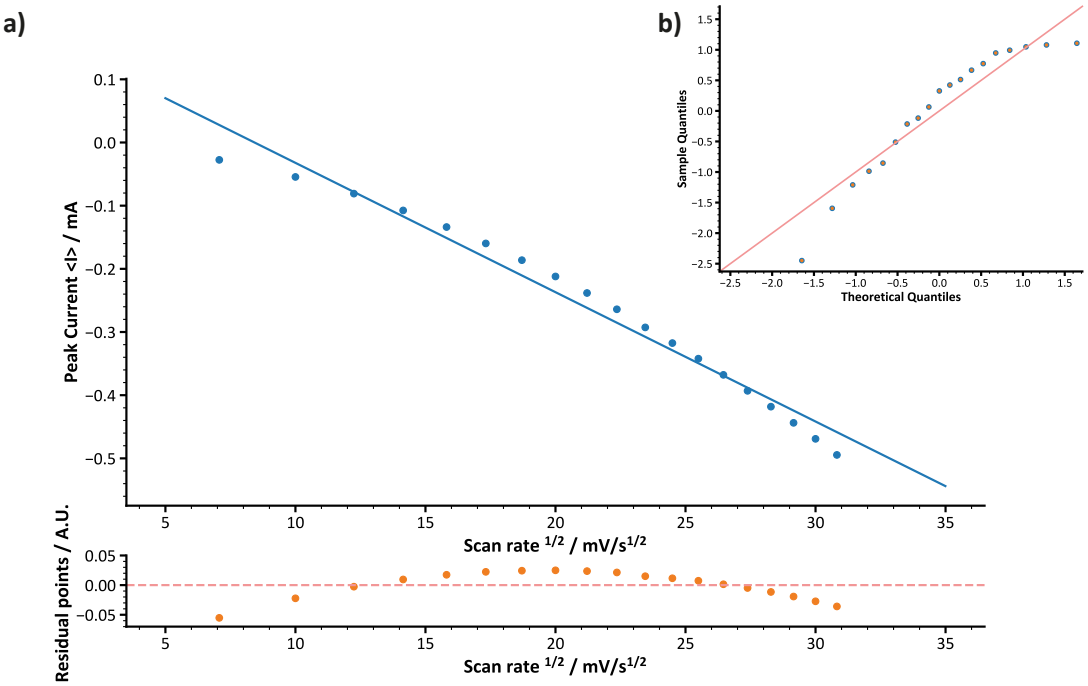

Figure 4.15 - The plotted relationship between the reduction peak's current maxima and the square root of the scan rate with residual analysis a) and Q-Q plot statistical analysis b). Data from the optimised reaction showed significantly lower noise, and the OLS linear regression fitting gave an R^2 value of 0.975, only further validating the prior experimental results.

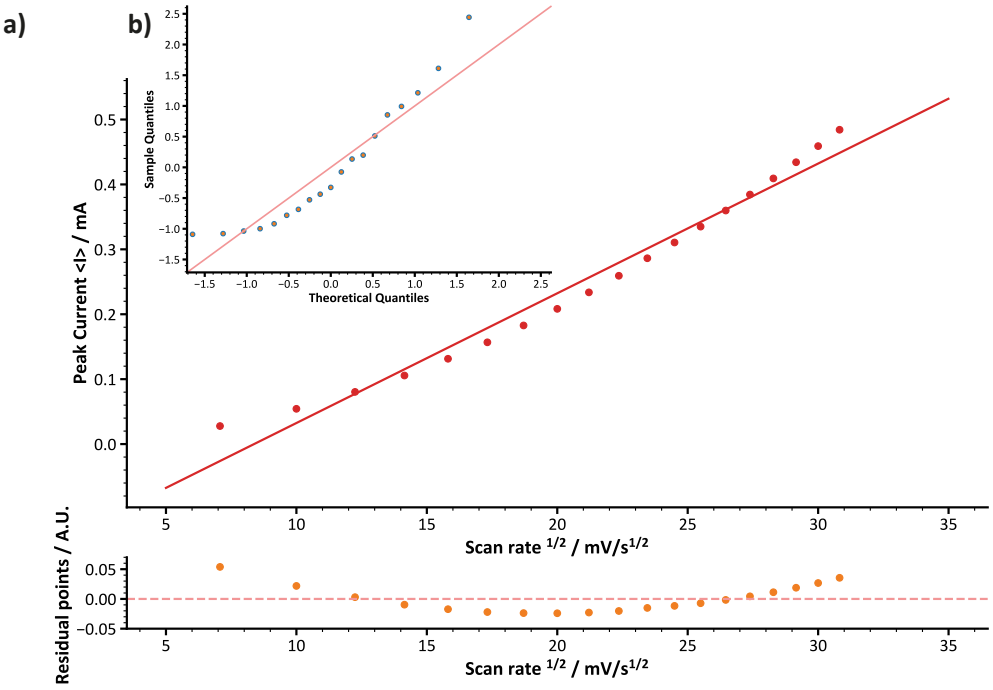

Figure 4.16 - The plotted relationship between the oxidation peak's current maxima and the square root of the scan rate with residual analysis a) and Q-Q plot statistical analysis b). Data from the optimised reaction showed significantly lower noise, and the OLS linear regression fitting gave an R^2 value of 0.974, only further validating the prior experimental results.

The additional statistical analysis only further validated the experimental results' legitimacy, indicating that the ferrocene was immobilised to the electrode surface through the apparent correlation of peak current and scan rate, and supported the invalidation of the data correlating peak current to the square root of the scan rate, which continued to support that the ferrocene was immobilised and not free to diffuse.

The ferrocene immobilisation experiments not only demonstrated the successful deprotection and formation of the near monolayer of benzyl amines, corroborating with the PM-IRAAS results, but also that this layer could successfully form covalent amide bonds via an NHS ester coupling reaction, as was required in the next functionalisation step, BIS3.

4.1.4 - NHS-Ester Cross-linking of a Melamine Terminated Linker (BIS3)

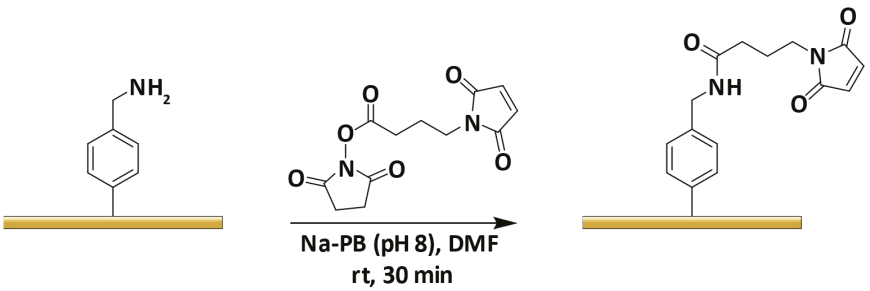

Figure 4.17 - The reaction schematic for the functionalisation of the benzylamine surface, with a short chain maleimide terminated linker molecule, via an NHS-ester cross-linker reaction.

After confirming the successful deprotection and feasibility of using NHS-ester cross-linking to functionalise the surface-tethered benzylamine, a new reaction was established to functionalise the surface with terminal maleimide groups (Figure 4.17) to allow the final coupling of the NTA terminated strands. The experimental procedure developed in-house for this reaction was as follows:

N-Succinimidyl 4-Maleimidobutyrate (4.2 mg, 15.00 µmol) in dimethylformamide (DMF, 1400 µL) was added dropwise to sodium phosphate buffer (NaPB, pH 8, 9 mL, 0.01 M) and then mixed via vortex for 2 minutes. In this solution, the benzylamine functionalised Au-on-Si surface was then submerged fully for 30 minutes at room temperature. The functionalised surface was removed and washed with mQ water, followed by ethanol, then dried under nitrogen gas, giving the maleimide functionalised Au-on-Si surface.

The N-Succinimidyl 4-Maleimidobutyrate was found to be insoluble in DMSO. Instead, DMF was shown to successfully solubilise the compound, allowing its addition to the NaPB. PM-IRRAS analysis of the resultant surface did not yield any significant peaks to confirm the presence of the resultant coupled molecule, such as the carboxyl groups within the formed amide or maleimide group. Moreover, an electrochemical study was undertaken to confirm the presence of the maleimide group by coupling to a thiol-modified ferrocene group. No significant CV redox peaks associated with ferrocene were observed. This absence of peak could be due to the ferrocene group being located too far from the electrode surface for the successful transfer of electrons or simply an unoptimised procedure for the thiol maleimide reaction to immobilise sufficient ferrocene species to be detectable.

Although the strategy till this point had proved to form a stable and densely packed maleimide layer, assuming similar to immobilisation that of the ferrocene NHS-ester species, preparation of the surface prior to this step took a significant length of time. Moreover, the reaction processes

required high levels of experimental care due to the high-hazard chemicals involved. It was, therefore, decided that a more straightforward and less hazardous immobilisation strategy would be pursued to allow the progression of other aspects of the work.

Although electrografting as an approach for the immobilisation of proteins has been demonstrated within the literature, the exact reaction procedures presented here are novel and can produce high molecular density monolayers, so they can still be considered a sizeable contribution to the field of surface functionalisation.

4.2 - Thiol Self-Assembled Monolayer (SAM) Immobilisation Strategy

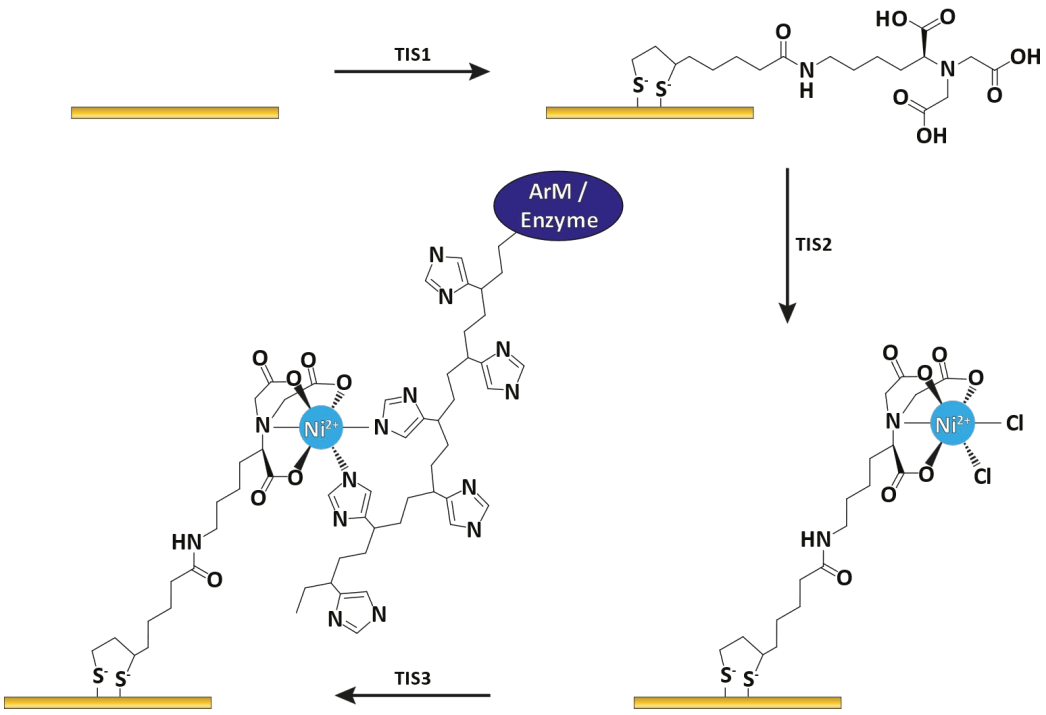

Figure 4.18 - A generalised schematic for the thiol self-assembled monolayer (SAM) functionalisation of an Au-on-Si surface (TIS1), including the additional steps of charging the surface with nickel ions (TIS2) and enzyme immobilisation (TIS3). Note: A simplified skeletal chemical structure has been illustrated for the 6-His tag motif to maintain greater visual clarity.

The second immobilisation strategy was inspired and optimised from the thesis by Bellare *et al.*[20]. The strategy utilises gold-thiol bonding interactions to establish a self-assembled monolayer on the surface of a gold substrate, where the un-bound terminal end of the molecule consists of an NTA group to which nickel can then be coordinated and the enzyme immobilised via the His-tag binding interaction (Figure 4.18). The initial procedure for the synthesis of the lipoic acid-nitrilotriacetic acid self-assembled monolayer (LA-NTA SAM) (TIS1) was provided by Natalia Baranska, a collaborator in the Department of Chemistry at the University of York, who additionally performed solution synthesis of the SAM forming molecule, LA-NTA. This procedure was later replaced with an optimised version of the synthesis outlined within the work of Bellare *et al.*[20]. The narrative of the subchapter describes the confirmation and optimisation of the His-tag affinity binding of CBL via the LA-NTA SAM layer.

4.2.1 - SAM Formation and Residence Time Optimisation of CBL

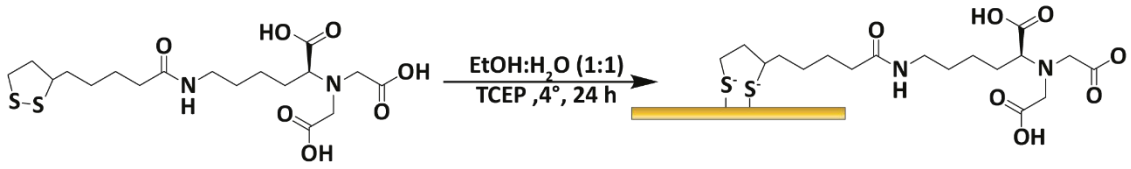

Figure 4.19 - The chemical reaction schematic with the initial reaction conditions, modified from the literature[20].

The procedure used for the LA-NTA SAM functionalisation of the Au-on-Si surfaces and Au QCM-D sensors (TIS1) (Figure 4.19), used within this section can be found in the methods chapter of this thesis (3.4.4 - Lipoic Acid Self-Assembled Monolayer (SAM) Procedure). Further immobilisation steps, such as Ni ion binding (TIS2) and CBL His-tag binding (TIS3), were performed in flow for QCM-D sensor surfaces and via drop-casting for PM-IRRAS substrate surfaces, the conditions for which are also discussed within the methods chapter of this work. An initial QCM-D study was performed to establish the profile and reversibility of the CBL binding via the LA-NTA strategy. All approximations for molecular surface coverage were calculated using the Sauerbrey equation and the given shifts in frequency, as described within the methods section of this work (3.1.1 - Quartz Crystal Microbalance with Dissipation monitoring (QCM-D) - Equation (3.1)).

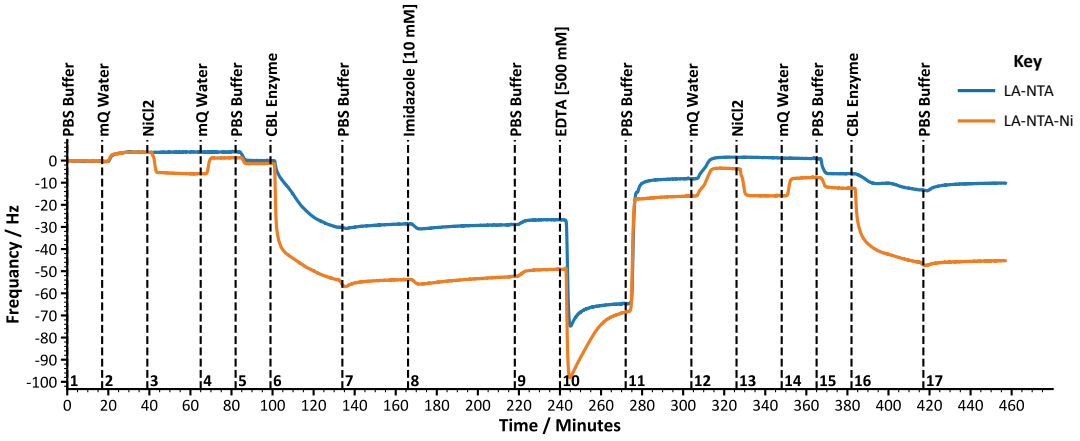

Figure 4.20 - QCM-D experiment for CBL surface functionalisation via Ni His-tag affinity binding to the LA-NTA SAM formed under optimised formation conditions, with the time stamps given at each injection event and the $NiCl_2$ injection absent from the LA-NTA surface (blue). Experiments were run in duplicate. The experiment was performed at 21 °C at a flow rate of 75 µl min^{-1}. Key of time-stamp solutions: PBS Buffer - Standard Phosphate buffered saline @ pH 7.4, mQ Water - mQ filtered water, $NiCl_2$ - $NiCl_2$ [100 mM] in mQ water, CBL Enzyme - CBL Enzyme [100 ug/ml, 2.07 µM] in PBS Buffer, Imidazole [10 mM] - Imidazole [10 mM] in PBS Buffer and TWEEN (0.1 % v/v) and EDTA [500 mM] - EDTA [500 mM] in PBS buffer.

All QCM-D experiments were performed at 21 °C at a flow rate of 75 µL min^{-1}. Due to nickel chloride being insoluble in standard PBS buffer, the system running buffer required switching to mQ water before and after the nickel chloride injection step to prevent precipitation of the nickel chloride within the QCM-D flow cell modules. In addition to $NiCl_2$ solution and CBL enzyme

solution injection steps, the QCM-D studies also utilise solutions of imidazole [10 mM] in standard NaPB as a washing agent and EDTA [500 mM] in NaPB, which acts as a stripping buffer via the ability to strongly chelate the His-tag bound nickel ions, resulting in the de-coordinating and liberation of the affinity bound enzyme. Imidazole wash steps and EDTA stripping are standard practices when purifying proteins using IMAC columns. Here, the imidazole wash step was included to help remove non-specifically bound enzymes and the EDTA stripping buffer was used to investigate the reversible nature of the affinity binding strategy.

The first QCM-D study compared the binding of CBL to the LA-NTA SAM functionalised surface (Figure 4.20 & Figure 4.21), with and without exposure to $NiCl_2$ solution, referred to as LA-NTA-Ni and LA-NTA, respectively. These conditions were run in duplicate and demonstrated high experimental reproducibility and reliability. For the LA-NTA-Ni surface, a 55.7 Hz reduction in the resonant frequency was observed upon exposing the sensor to the CBL enzyme solution [2.07 µM] (Figure 4.20 - 6). This reduction in frequency is indicative of the deposition of mass on the surface, as expected for the Ni His-tag immobilisation of the CBL enzyme, and corresponds to a calculated molecular surface coverage of 1.89×10^{12} molecules cm^{-2}, or equivalently 1.89 CBL enzymes per 100 nm^2 area.

The CBL enzyme used in this study has a published molecular mass of 48363.77 Da[258]. Therefore, the simplified spherical protein volume, V, the approximated minimal radius, r_{min}, and cross-sectional area for the CBL enzyme, A, can be calculated as 58.6 nm^3, 2.41 nm and 18.2 nm^2 respectfully using equations (2.12), (2.13) and (2.14), described earlier within this work (2.3.1 - Chemical Immobilization Strategies for Enzymes). Considering an experimentally determined surface density of 1.89 CBL enzymes per 100 nm^2 area and an estimated cross-sectional area of 18.2 nm^2, the surface density is sufficiently diffuse to assume the CBL enzymes are assembled into a protein monolayer. It should be noted that the surface density is higher than is often observed for protein monolayers, and further studies to confirm that CBL enzymes are ordered into a protein monolayer would still need to be performed.

In contrast, the LA-NTA surface showed only a 29.0 Hz reduction in the resonant frequency following exposure to the CBL enzyme solution, consistent with a reduced density of immobilised enzyme. Moreover, while the frequency for both sensors recovers slightly (by 3.5 Hz) after washing with running buffer and imidazole washing buffer, a significant mass of protein remains attached to both surfaces. Given that this LT-NTA functionalised QCMD sensor was not coordinated with Ni ions and therefore unable to bind specifically to the His-tag engineered into the CBL, the mass of enzyme immobilised on the LT-NTA surface is assumed to be non-specifically bound instead. This non-specific binding could either be to the LT-NTA molecules or exposed surface regions of the QCMD sensor, if not a combination of both. The initial rate at which the

frequency decreased upon exposure to the CBL enzyme solution was much greater for the LA-NTA-Ni surface than for the LA-NTA surface, indicative of different immobilisation kinetics.

When exposed to EDTA solution [500 mM], a significant reduction of 45.3 Hz and 49.6 Hz in frequency was observed for the LA-NTA and LA-NTA-Ni surfaces (Figure 1.20 - 10), respectively. A large and rapid QCM-D frequency shift is often observed following a change in buffer, particularly to a concentrated solution or a solution containing large mass molecules. This phenomenon is often called the 'buffer effect' or 'bulk shift' and is associated with the density and viscoelasticity of the solution and the interaction of the solution with the surface rather than the binding of molecules to the surface. Upon the surface reaching the adjusted resonant frequency following the buffer effect, a vast difference in the kinetics of dissociation of CBL from the surface was observed, evidenced by the decreasing frequency profile. Specifically, the rate at which CBL was lost from the LA-NTA surface was significantly slower than dissociation from the LA-NTA-Ni surface. After returning to the PBS running buffer (Figure 4.20 - 11), the resonant frequency of the LA-NTA-Ni sensor had recovered to be only 14.9 Hz lower than before exposure to the CBL enzyme solution. Comparatively, the LA-NTA surface returned to 6.3 Hz below the resonant frequency observed before exposure to CBL. The decrease but incomplete recovery of the resonant frequency implied that not all the CBL enzyme was liberated when the surface was exposed to the EDTA stripping buffer.

Following regeneration of the LA-NTA-Ni surface with $NiCl_2$ solution, a second injection of CBL enzyme solution (Figure 4.20 - 16) was administered to the surfaces to evaluate whether it was possible to again immobilised CBL on the surface, hence demonstrating the switchable enzymatic binding. A 34.8 Hz decrease in the resonant frequency was observed for the LA-NTA-Ni surface, displaying similar binding kinetics to the first CBL enzyme injection but with a decrease in the total mass of the immobilised CBL enzyme. Conversely, the LA-NTA surface's binding kinetics differed drastically from the initial CBL enzyme injection, showing only a 3.5 Hz overall decrease in the resonant frequency. This moderate decrease in frequency suggests that very little enzyme was immobilised on the LA-NTA surface. The lack of non-specific binding following this second CBL step compared to the first CBL injection (3.5 Hz compared to 29 Hz) raised questions about the probable cause, and as this phenomenon was not observed for the LA-NTA-Ni surface if this could be utilised to reduce the non-specific binding of CBL. Therefore, the two considerations taken from this experiment into the next were that a shorter CBL incubation step might reduce the amount of non-specific binding in the $NiCl_2$ exposed sensor and that some aspect of the EDTA stripping and re-immobilisation of the protein was affecting the non-specific binding interaction.

In order to optimise the TIS3 step of this immobilisation strategy, it was theorised that minimising the time the surface was exposed to protein solution would reduce the amount of non-specific binding. Instead of a 30-minute incubation time for the CBL enzyme solution injection, this was reduced to just 5 minutes. A 46.2 Hz reduction in the resonant frequency was observed for the LA-NTA-Ni surface upon exposing the sensor to the CBL enzyme solution (Figure 4.21 - 6), with a calculated surface coverage of 9.45×10^{11} molecules cm^{-2} (9.45×10^{-3} molecules nm^{-2}), which given the previously calculated approximate CBL enzyme cross-sectional area of 18.2 nm^2 shows the result to still be feasible for a protein monolayer. In contrast, the LA-NTA surface showed only a 24.4 Hz reduction in the resonant frequency during exposure to the CBL enzyme solution. The immobilisation kinetics observed for both surfaces showed a sharp drop in frequency, with none of the same plateauing profile as was seen in the experiment with a 30-minute CBL enzyme residence time. The frequency recovered slightly for both surfaces upon returning to the running buffer and following the imidazole washing injection, with a more significant 10.0 Hz increase for the LA-NTA-Ni surface, compared to 2.3 Hz for the LA-NTA surface (Figure 4.21 - 7 & 8). Any CBL enzyme bound via His-tag affinity binding would not be expected to dissociate under these conditions, so it can be assumed that a greater mass of the non-specifically bound enzyme was removed for the LA-NTA-Ni surface than that of the LA-NTA surface.

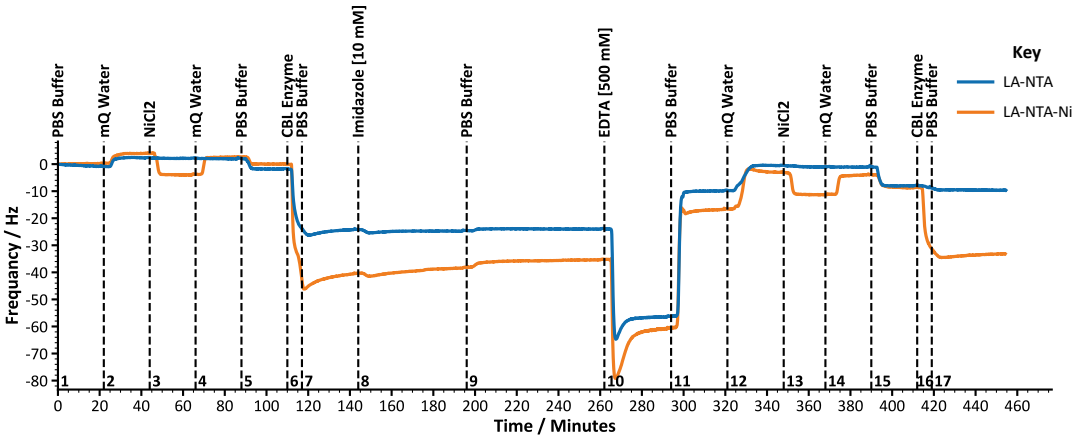

Figure 4.21 - QCM-D experiment for CBL surface functionalisation via Ni His-tag affinity binding to the LA-NTA SAM formed under time-optimised formation conditions, with the time stamps given at each injection event and the $NiCl_2$ injection absent from the LA-NTA surface (blue). Experiments were run in duplicate. The experiment was performed at 21 °C at a flow rate of 75 µl min^{-1}. Key of time-stamp solutions: PBS Buffer - Standard Phosphate buffered saline @ pH 7.4, mQ Water - mQ filtered water, $NiCl_2$ - $NiCl_2$ [100 mM] in mQ water, CBL Enzyme - CBL Enzyme [100 ug/ml, 2.07 µM] in PBS Buffer, Imidazole [10 mM] - Imidazole [10 mM] in PBS Buffer and TWEEN (0.1 % v/v) and EDTA [500 mM] - EDTA [500 mM] in PBS buffer.

The dissociation profiles in both surfaces after exposure to the EDTA stripping buffer (Figure 4.21 - 10) resembled the same dissociation pattern as the previous experiment (Figure 1.20 - 10), with the LA-NTA surface once gain showing a comparative difference in frequency of -8.5 Hz compared to the surface prior to being subjected to CBL enzyme solution. The LA-NTA-Ni again showed a greater difference of -17.9 Hz, indicating a significant, if incomplete, CBL enzyme mass loss after EDTA stripping buffer exposure.

Finally, upon nickel regeneration and re-exposure to CBL solution (Figure 4.21 - 16), a significant shift in the resonant frequency of 25.9 Hz was again seen for the LA-NTA-Ni surface, indicating the mass increase due to re-immobilisation of the CBL enzyme binding to the LA-NTA-Ni surface. The LA-NTA surface, however, only led to a negligible 1.5 Hz reduction in frequency after the CBL enzyme solution, demonstrating a minor increase in non-specifically bound CBL, reaffirming the potential to optimise the LA-NTA surface against non-specific binding interactions for the functionalised surface. The altered behaviour of the LA-NTA surface, from demonstrating a high capacity for non-specific binding of CBL to minimal binding, only occurred after subjecting the surface to the EDTA stripping buffer. It was theorised that this behaviour change may directly result from the surface being exposed to the EDTA solution.

4.2.2 - Exploring EDTA's Inhibition of Non-Specific Binding on an LA-NTA Surface

A final QCM-D experiment was devised in which four sensors, each with differing conditions, would be run in parallel to test the ability to use EDTA to inhibit non-specific protein binding. In addition to the LA-NTA and LA-NTA-Ni surfaces, two additional surfaces were also evaluated: 1) an LA-NTA-EDTA-Ni surface, which was first subjected to an EDTA solution [500 mM] wash step prior to the $NiCl_2$ solution [100 mM] to evaluate whether exposing the surface to EDTA prior to charging the surface with Ni ions had any effect on the CBL enzyme binding. 2) an LA-NTA-EDTA surface, which was first subjected to an EDTA solution [500 mM] wash step, but the surface was not charged with Ni ions to directly compare the LA-NTA surface in real time to a surface exposed to EDTA before the CBL enzyme solution.

In addition to the QCM-D experiment, the reactions were also followed on four separate Au-on-Si substrates, which were functionalised through drop casting, as opposed to inflow functionalisation, and analysed at each step using PM-IRRAS to support the QCM-D data. The drop cast procedure for nickel ion regeneration and CBL immobilisation can be found in the methods chapter (3.4.5 - Ni regeneration of the LA-NTA SAM and His-Tagged Enzyme Immobilization Procedure).

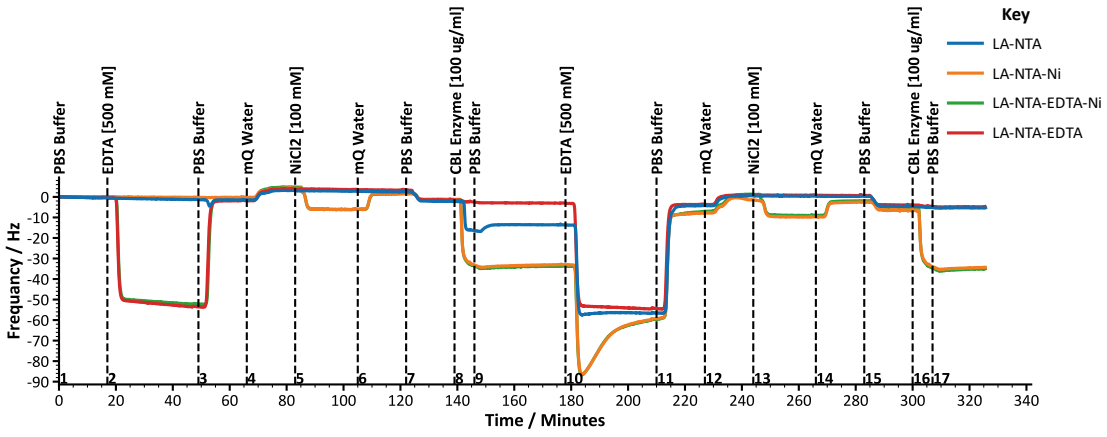

Figure 4.22 - QCM-D experiment for CBL surface functionalisation via Ni His-tag affinity binding to the LA-NTA SAM formed under time-optimised formation conditions for determining the effect of EDTA on CBL immobilisation. The key indicates the differences between each surface and the solutions to which they were exposed. The experiment was performed at 21 °C at a flow rate of 75 µl min^{-1}. Key of time-stamp solutions: PBS Buffer - Standard Phosphate buffered saline @ pH 7.4, mQ Water - mQ filtered water, $NiCl_2$ - $NiCl_2$ [100 mM] in mQ water, CBL Enzyme - CBL Enzyme [100 ug/ml, 2.07 µM] in PBS Buffer, Imidazole [10 mM] - Imidazole [10 mM] in PBS Buffer and TWEEN (0.1 % v/v) and EDTA [500 mM] - EDTA [500 mM] in PBS buffer.

Relative frequency shifts between the QCM-D sensors functionalised with LA-NTA-EDTA-Ni and LA-NTA-Ni were found to be almost identical, other than the absence of frequency decrease due to the buffer effect of the initial EDTA injection (Figure 4.22 - 2) to the LA-NTA-EDTA-Ni surface.

A 33.5 Hz and 33.0 Hz decrease in frequency was observed for the LA-NTA-EDTA-Ni and LA-NTA-Ni surfaces, respectively, for the first CBL enzyme immobilisation (Figure 4.22 - 8). Using these values to estimate the mass of bound CBL enzyme on each surface yielded molecular surface coverage values of 6.86×10^{11} molecules cm^{-2} for the LA-NTA-EDTA-Ni surface and 6.75×10^{11} molecules cm^{-2} for the LA-NTA-Ni surface. Both these surfaces showed identical dissociation kinetics upon exposure to the second EDTA stripping buffer (Figure 4.22 - 10). Upon returning to PBS running buffer (Figure 4.22 - 11), a 5.8 Hz and 6.4 Hz reduction in frequency relative to the resonant frequency prior to CBL immobilisation was observed. These small decreases in frequency implied that only a slight amount of CBL remained bound after the EDTA stripping buffer, giving values significantly lower than in previous experiments. After recharging the surface with Ni and exposing both surfaces to the second CBL enzyme solution (Figure 4.22 - 16) showed a decrease in the frequency of 30.7 Hz compared to the initial resonant frequency (corresponding to an approximate surface coverage of 6.28×10^{11} molecules cm^{-2}) for the LA-NTA-EDTA-Ni surface and 29.1 Hz for the LA-NTA-Ni surface (corresponding to a surface coverage of 5.94×10^{11} molecules cm^{-2}). All surface coverage values indicate a monolayer of proteins, given the previously calculated approximation of the CBL enzyme cross-sectional area of 18.2 nm^2.

This slight difference in the amount of CBL immobilised between the first CBL and Second CBL enzyme injection was likely due to the low density of CBL enzyme remaining on the surface after exposure to the EDTA stripping buffer. The reason these values did not perfectly match up can be explained by the additional CBL enzyme loss from the surfaces during the $NiCl_2$ re-energisation of the LA-NTA SAM.

The LA-NTA surface showed the same characteristic non-specific binding upon exposure to the CBL enzyme buffer. It was observed that the time at which the decrease in frequency plateaued at 13.7 Hz coincided with the time the peristaltic pump was stopped to switch the injection solutions (Figure 4.22 - 8). The frequency decrease and CBL solution flow relationship indicate that the non-specific binding observed on the LA-NTA surface is also intrinsically linked to the flow profile used during functionalisation. This relationship is later supported within the PM-IRRAS data, where the same surface was functionalised using drop casting, but no bound CBL enzyme is observed within the post-CBL solution exposure spectrum. Upon the solution returning to the PBS buffer, the frequency recovered slightly, resulting in a decrease in frequency after subjection of the CBL enzyme of 11.2 Hz, which corresponds to an approximate surface coverage of 2.28×10^{11} molecules cm^{-2} for CBL non-specifically bound to the LA-NTA surface. Injection of the second EDTA stripping buffer showed an almost total dissociation of any non-specifically bound CBL (Figure 4.22 - 10), with a negligible 2.0 Hz decrease in frequency compared to the frequency prior to CBL solution exposure and no apparent dissociation kinetics. A

frequency decrease of only 0.8 Hz was observed when the sensor was exposed to the second CBL solution (Figure 4.22 - 16), indicating only a small mass change on the surface and minimal non-specific binding.

The LA-NTA-EDTA surface showed no significant change in frequency other than solvent buffering effect shifts. A decrease in the resonant frequency of only 1.6 Hz and 0.7 Hz was observed when the surface was exposed to the first and second CBL enzyme buffers, respectively (Figure 4.22 - 8 & 16), indicating a nearly total absence of mass change on the surface. This lack of mass change suggests significant suppression of non-specific binding when the surface was pretreated with the EDTA stripping solution.

Following the characterisation of the LA-NTA surfaces through QCM-D, characterisation using PM-IRRAS was performed to provide additional insight and complementary analysis of drop-cast surfaces mirroring that of the inflow functionalised QCM-D sensor surfaces.

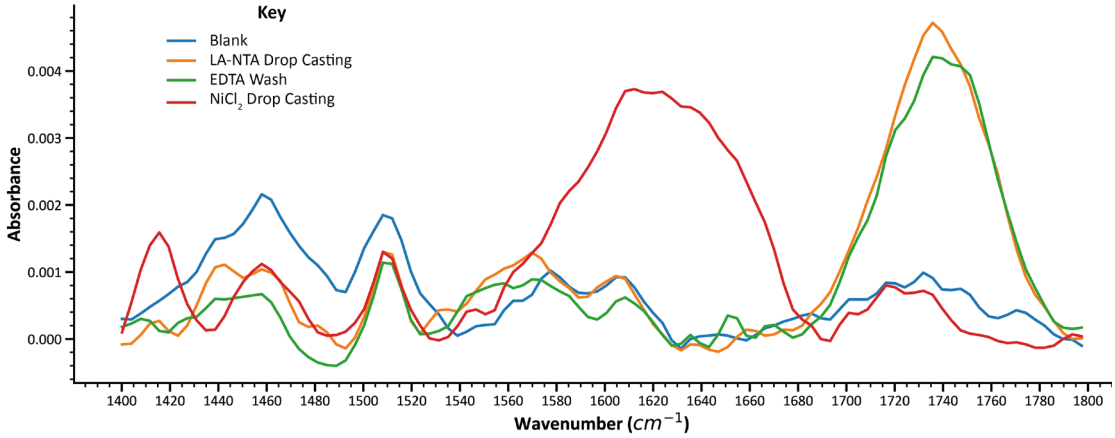

Figure 4.23 - PM-IRRAS analysis of various functionalisation steps, including an EDTA [500 mM] wash step and $NiCl_2$ [100 mM] coordination, under the final LA-NTA SAM formation conditions. The data was acquired with a spectral resolution of 14 cm^{-1} and processed with a polynomial baseline subtraction.

Comparison of the blank Au-on-Si substrate surface after undergoing the piranha cleaning protocol (3.4.2 - Piranha Solution for Substrate Cleaning) to that of the same surface after LA-NTA SAM functionalisation results in a clear broad carbonyl C=O stretch peak at 1736 cm^{-1} (Figure 4.23 - LA-NTA Drop Casting). An EDTA-washed step resulted in a slight change in peak shape but no significant shift or change in magnitude (Figure 4.23 - EDTA Wash). Due to the comparatively small mass change of the LA-NTA SAM sensor surface upon the coordination of nickel ions, the changes are unobservable using QCM-D. Therefore, PM-IRRAS proved to be an effective analytical tool for tracking the coordination of the nickel ion to the NTA group, as a significant 128 cm^{-1} downshift of the C=O stretch peak was observed, the peak shifting to 1608 cm^{-1} (Figure 4.23 - $NiCl_2$ Drop Casting).

Immobilisation of the CBL enzyme onto the functionalised Au-on-Si PM-IRRAS substrate via drop casting resulted in a spectrum with a significantly increased signal absorbance and much broader peaks resulting from the multiple vibrational environments within the protein structure (Figure 4.24 - First CBL Drop Casting). The spectrum consisted of two significant peaks; the first, at 1662 cm^{-1}, is characteristic of amide I functional groups[264] in proteins consisting primarily of C=O stretching vibrations and the second, at 1547 cm^{-1}, is characteristic of amide II functional groups[264] in proteins consisting primarily of N-H bending when coupled to C-N stretching vibrations[264, 265].

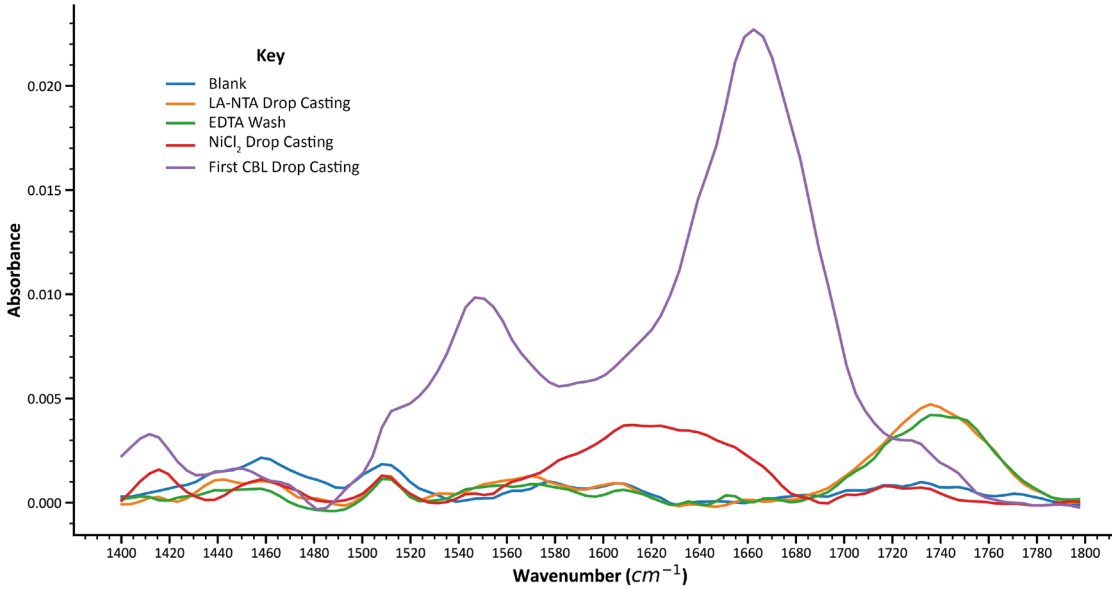

Figure 4.24 - PM-IRRAS analysis of various functionalisation steps as a continuation of the previous figure (Figure 4.23), including CBL [100 ug/ml, 2.07 µM] immobilisation under the final LA-NTA SAM formation conditions. The data was acquired with a spectral resolution of 14 cm^{-1} and processed with a polynomial baseline subtraction.

When the same LA-NTA surface but without the $NiCl_2$ drop-casting step was subjected to CBL [100 ug/ml, 2.07 µM] in standard PBS buffer for 5 minutes, the resultant PM-IRRAS spectrum showed no CBL protein IR peaks, the only difference to the blank LA-NTA surface being a slight drop in the absorbance for the C=O stretch peak at 1736 cm^{-1} (Figure 4.25 – First CBL Drop-Casting). This result corroborated the sudden frequency plateau upon the peristaltic pump and resultant flow stopping within the QCM-D flow module, implying that the formation of the non-specific binding was linked to the surface being exposed to CBL in flow. The turbulent washing process for the drop cast surfaces was also a likely factor in why no CBL protein was observed in the PM-IRRAS spectrum, compared to the laminar washing regime within the QCM-D. Suggested further work to explore both these possibilities will later be discussed in more detail within the further works chapter. The work would consist of the LA-NTA surface being subjected to CBL enzyme buffer inflow on an Au-on-Si PM-IRRAS sensor, with and without the same turbulent washing procedure, to see if non-specific binding is still observed.

When the LA-NTA-EDTA surface was recreated using drop casting on an Au-on-Si surface, little difference was seen in the resultant IR spectrum, other than a slight change in peak shape but no significant shift or change in magnitude (Figure 4.25 - EDTA Wash), as was observed in the first PM-IRRAS experiment (Figure 4.23 - EDTA Wash). When subjected to CBL drop casting for a second time following the EDTA wash, no IR peaks associated with the CBL protein structure were observed (Figure 4.25 - Second CBL Drop Casting).

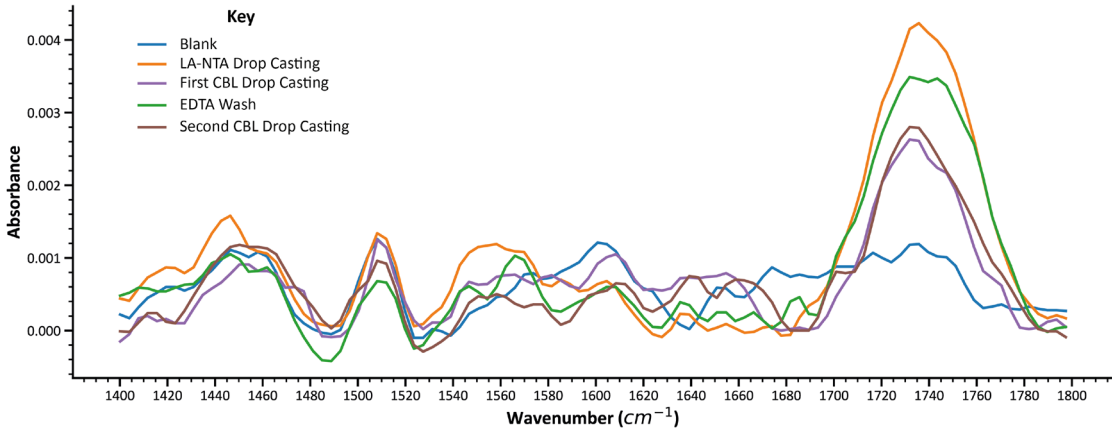

Figure 4.25 - PM-IRRAS analysis of various functionalisation steps without $NiCl_2$ coordination or an EDTA wash step in the first instance. The experiment consisted of the blank surface analysis, followed by the LA-NTA functionalisation, a first CBL [100 ug/ml, 2.07 µM], an EDTA [500 mM] wash step and then a second CBL [100 ug/ml, 2.07 µM] step to showing a lack of CBL enzyme peak. The data was acquired with a spectral resolution of 14 cm^{-1} and processed with a polynomial baseline subtraction.

To ensure that the results of the IR experiment showing the lack of non-specific CBL binding were not a result of an issue with the functionalised LA-NTA SAM surface, the same substrate that was used in the previous experiment (Figure 4.25) was subjected to $NiCl_2$ drop-casting (Figure 4.26 - $NiCl_2$ Drop Casting) which showed the same characteristic downshift of the C=O stretch peak resulting from the complexation of NTA groups to nickel ions, as was seen in a prior PM-IRRAS experiment (Figure 4.23 - $NiCl_2$ Drop Casting). The nickel-charged LA-NTA surface was next subjected to CBL drop casting for a third time. However, unlike the previous exposures, the resultant IR spectrum showed the distinct characteristic protein peaks of the CBL (Figure 4.26 - Third CBL Drop Casting), with the same peaks at 1662 cm^{-1} indicative of amide I groups and at 1550 cm^{-1} indicating amide II groups, as observed in the previous IR experiment (Figure 4.24 – First CBL Drop Casting). For completeness, a final EDTA wash step was performed on the substrate, with the resultant spectrum still displaying the characteristic protein peaks of the CBL enzyme but at a slightly lower magnitude of absorbance. Although PM-IRRAS can be used quantitatively to some extent, it is not best suited for the technique, especially in the case of this experimental setup. Therefore, the observed protein peaks could have resulted from a comparatively small amount of protein that could not be removed from the surface, as seen in the equivalent QCM-D experiments.

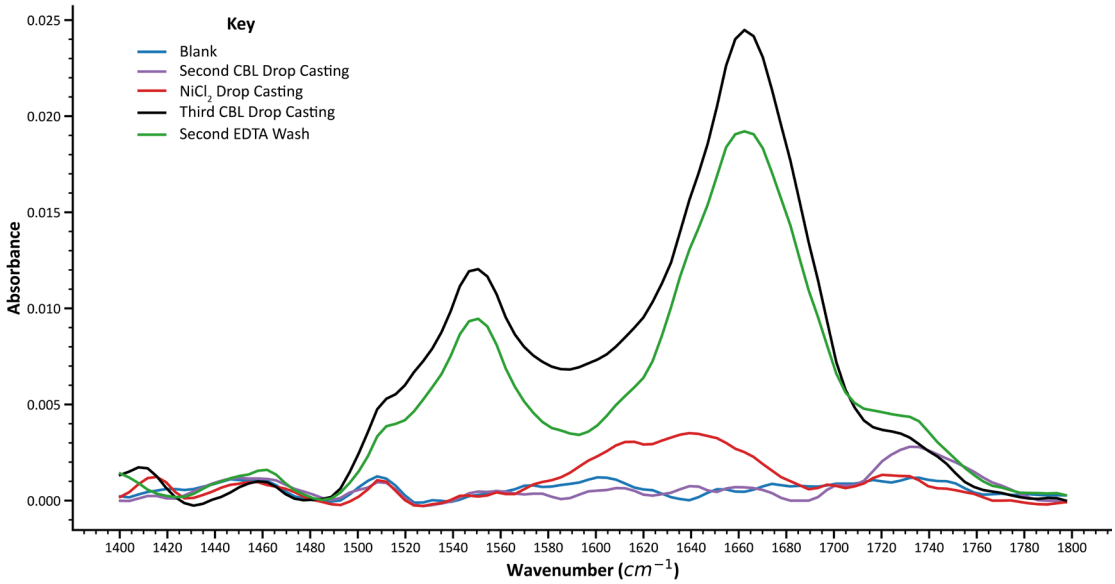

Figure 4.26 - PM-IRRAS analysis of various functionalisation steps as a continuation of the previous figure (Figure 4.25), demonstrating successful CBL [100 ug/ml, 2.07 µM] immobilisation and peak presence after a $NiCl_2$ [100 mM] coordination step, and the lack of CBL removal after an EDTA [500 mM] wash step. The data was acquired with a spectral resolution of 14 cm^{-1} and processed with a polynomial baseline subtraction.

The QCM-D studies and corroborating PM-IRRAS data showed that the EDTA pretreatment of the LA-NTA surface blocked nearly all non-specific binding of CBL. Differences in the QCM-D and PM-IRRAS data suggest that inflow immobilisation of the CBL enzyme onto the LA-NTA surface is directly linked to the inflow non-specific binding, but further work would be required to confirm this hypothesis. The current proposed theory of why the EDTA pretreatment of this surface results in this observed protection from non-specific binding in flow has two elements. Firstly, the EDTA chelates to and removes any non-specific metal ions that may already be bound to the LA-NTA surface. Removal of these non-specific ions stops any non-specific coordination of the His-tagged protein via coordination to these ions, as they are no longer present on the surface. Secondly, the EDTA modifies the SAM. This modification could be achieved by changing the overall surface charge, through the EDTA forming some level of bonding interaction to the surface (such as hydrogen bonding), or through EDTA inserting itself into the layer. However, from the current analytical data regarding this observed suppression of CBL non-specific binding after EDTA pretreatment of the SAM surface, it is not possible to ascertain which of these speculated theories, or combination of theories, if any, are responsible but remains an interesting observation that warrants further study. Therefore, one of the areas of further work for this thesis would be to explore further this observed phenomenon caused by the EDTA

pretreatment, to test the proposed theories as to its cause and to see if it holds true for other NTA-modified surfaces and other proteins.

This complimentary series of QCM-D and PM-IRRAS studies demonstrated that through using the optimised LA-NTA functionalisation strategy and a lower CBL exposure time, the CBL enzyme could, for the most part, successfully be chemically actuated to dissociate and reversibly bind to the Au-on-Si substrate surface. This work provided the means by which an Au-on-Si substrate could be functionalised to construct a planer surface microfluidic chip reactor for the IMER system, the reactor infrastructure for which next needed to be designed, developed and tested.

Chapter 5 - Column Immobilised Enzyme Reactor (IMER)

Before any inflow biocatalysis could be performed, an immobilised enzyme reactor (IMER) system, compatible with multiple microfluidic reactors, alongside a system control software capable of providing repeatable and reliable experimental processes, needed to be established. The first section of this chapter outlines the design and construction of the reactor system used in this work, including the engineered valve controller and system control software. The second section of this chapter focuses on implementing and characterising an immobilised enzyme microcolumn reactor, determining the enzymatic kinetics of a previously undemonstrated immobilised enzyme species for inflow biocatalysis.

5.1 - Flow Reactor Design and Construction

There are numerous aspects to the design of a flow control system, all of which affect and change how the system functions and the parameter space in which it can operate. Here, a system was required that could be used to control fluid flow through a range of IMERs (including packed bead bed columns and microfluidic devices integrated with an enzyme-functionalised planar surface). A considerable component of this research was thus focussed on establishing a simplistic, low-cost, and automated flow reactor setup that could be integrated with external analytical equipment to quantify the inflow catalysis of the immobilised artificial metalloenzyme and enzymatic species.

5.1.1 - The Core System Design

The first challenge was creating a microcolumn where the beads could be physically held stationary during fluid flow within the reactor. Numerous approaches to creating packed bead bed reactors have been demonstrated in the literature, including using microfluidic chips[266] and modified IMAC columns[267]. However, integrating functionalised beads within a microfluidic chip is challenging owing to the need for on-chip integrated frits to prevent bead loss. Moreover, IMAC columns are typically designed for significantly larger solution volumes than were desired for this microcolumn. Here, an alternative microcolumn was developed based on approaches used in HPLC injection valves, which have sample loops of HPLC tubing of a specific volume with inline small pore filters to remove particulates that might damage the HPLC system. By using these two elements in tandem, a fixed volume of HPLC tubing could be connected to an inline, 10 µm pore HPLC filter to provide a low-cost and simplistic means in which the functionalised agarose beads, with a particle polydispersity of 45-165 µm[268], could be packed to create the desired microcolumn.

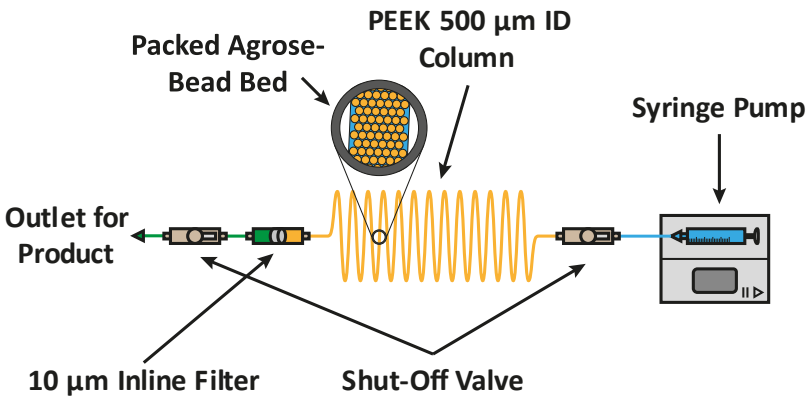

Figure 5.1 - The schematic for the initial single-pass microfluidic flow reactor setup, designed to test the in-house column reactor with agarose beads for packing without leakage, blockages or function-limiting backpressure.

The simplest possible design, using only the essential flow reactor components, would result in a single-pass flow reactor consisting of a single syringe pump connected via a Luer lock to the in-house designed bead microcolumn reactor (Figure 5.1). This design was built exclusively to test the fundamental viability of the proposed microcolumn design. The microcolumn consisted of a fixed length of VICI JR-T-6002 peek tubing (267 mm length, 0.5 mm ID, 52.5 µL volume) connected to an IDEX 10 µm pore size inline solvent filter. IDEX shut-off valves were also included at either end of the column. Following the pre-packing of the column with beads via a syringe, the shut-off valves were then used to isolate the column to allow connection to the pre-loaded running buffer syringe pump without risk of bead or solution loss. BD Plastipak 10ml sterile Luer Lock syringes were used within all flow reactor setups, and the syringe pumps were calibrated for the internal diameter of the syringe piston. The pre-packed microcolumn was left to infuse with standard PBS buffer for three hours, and it confirmed that there were no leaks, no loss of beads through filter failure and that the resultant back pressure from the volume of beads loaded was not debilitating.

5.1.2 - Design of a Passive Continuous Recirculating IMER System

One of the main limitations of single-pass reactors is that they ideally require the substrate solution to be fully catalysed within a single pass through the reactor column. In the case of an IMER, complete conversion of a substrate solution in a single pass requires a large amount of enzyme to be immobilised on the beads within the reactor. If the enzyme has a low TON, the high concentration of enzyme required can often outweigh the advantages of using a microfluidic reactor setup. A simple way to mitigate this disadvantage is by circulating the reaction substrate back through the reactor, increasing the amount of substrate turned over within the reaction mixture with each pass. Such continuous processing of the substrate solution demands less enzyme to achieve total catalysis of the substrate and gives the distinct advantage of being able to quantify the amount of product formed enzymatically per cycle and, therefore, profile the kinetics of the enzyme within the given IMER system. One of the main disadvantages of a recirculating IMER is the increased complexity, which is one of the reasons they are relatively uncommon within IMER literature.

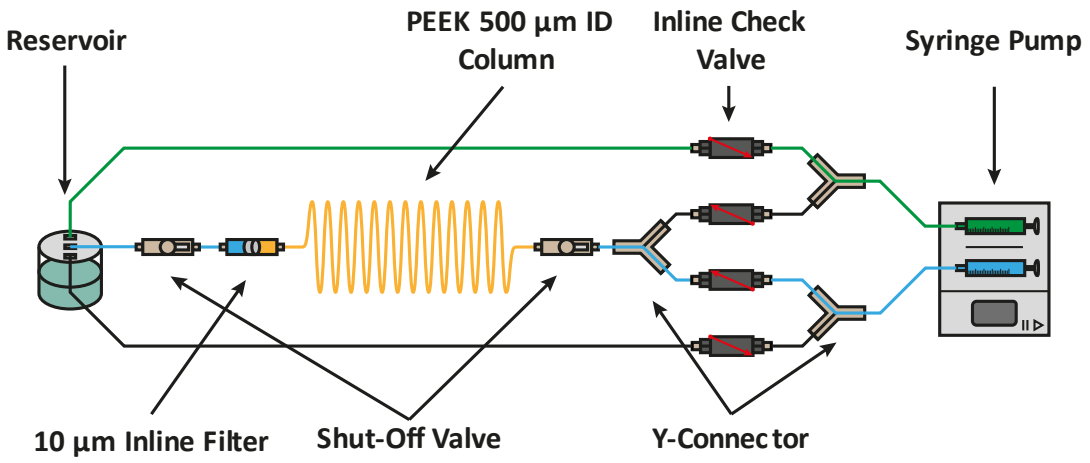

Figure 5.2 - The schematic for the initial recirculating bead column IMER design, which took inspiration from parallel piston HPLC pumps for how continuous flow was achieved.

Here, an engineering strategy utilised in some HPLC pumps, referred to as a dual-piston in-parallel system, was investigated to achieve recirculation of the reaction solution while maintaining continuous flow.

The concept behind the dual-piston in-parallel HPLC pump is shown in Figure 5.2. As one piston withdraws (pulls in) fluid from the inlet, the second infuses (pushes out) the fluid from the outlet. Upon each piston reaching maximum extension, both switch roles, such that the previously infusing syringe is now withdrawing and vice versa. The process is achieved using inline check

valves, which restrict the direction in which the fluid flows following infusion and withdrawal from the pistons, so fluid can only travel out from the outlet and in from the inlet.

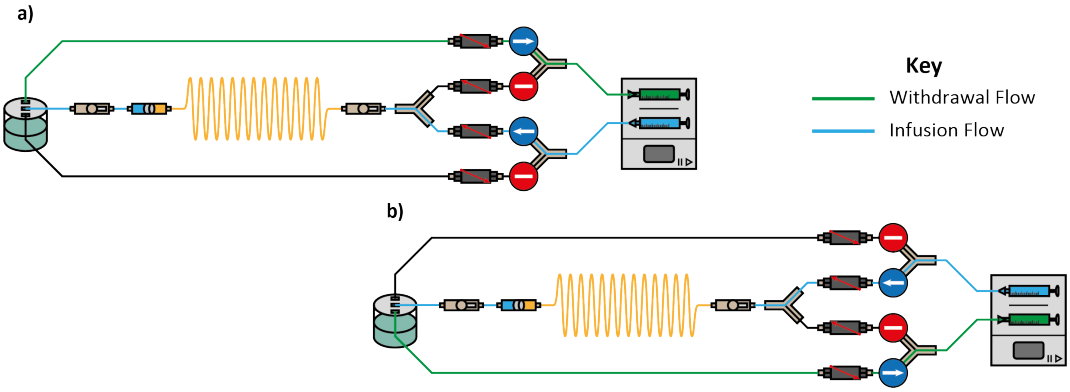

Figure 5.3 - Schematic to demonstrate the two possible pumping states for the passive inline check valve-based continuous recirculating IMER system, whether the infusion path of flow through the column reactor is represented in blue and the withdrawal path of flow from the fluid reservoir is represented in green. The dual syringe driver determines the polarity of flow, where one syringe is always withdrawing, and the other is always infusing, giving the two possible states of pumping: a) and b).

This approach to engineering HPLC pumps was translated to the IMER system design shown in Figure 1.3. As one syringe begins to withdraw, a passive IDEX inline check valve permits flow from the reservoir, while the second inline check valve connected to the syringe seals, restricting withdrawn flow from the microcolumn reactor. Simultaneously, the second syringe begins to infuse with the third inline check valve, permitting flow through the reactor, while a fourth inline check valve restricts infused flow to the reservoir (Figure 5.3a). When the syringes reach their programmed end volume, the pumping state is switched, such that the syringe that was withdrawing is now infusing and vice versa (Figure 5.3b). The system can be switched repeatedly between these two pumping states, allowing continuous recirculation of the reaction solution through the reactor.

Although the system presented in Figure 1.3 achieves the desired recirculation function, it suffers from several limitations. These limitations will be discussed throughout the next subchapters alongside improvements implemented to achieve more reliable, inflow enzymatic catalysis.

In order to explain the workings of the flow reactor system more clearly throughout this work, specific terms first need to be established. A loop/cycle refers to the point at which the total system volume passes through the reactor once. A syringe-step refers to the dual syringe driver's single synchronous withdrawal and infusion step. Extraction refers to a solution removed from the total system volume, usually at the end of a cycle, to determine the amount of product formed through offline analysis.

Upon testing the system for several cycles by manually programming the syringe-steps via the user interface of the Chemyx 4000x syringe pump, it was quickly realised that the inline check valves were not performing as expected. Specifically, fluid flow was not observed from the

reactor outlet upon switching from the first syringe-step to the second. Instead, fluid flow was observed from the alternate reservoir inlet (Figure 5.4a).

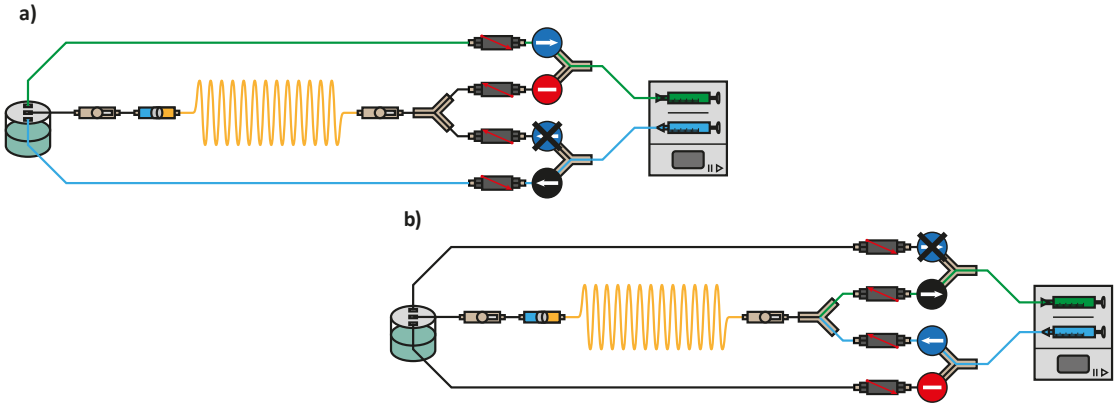

Figure 5.4 - Flow schematics to illustrate the observed issues found when using the passive inline check valves within the devised continuous flow setup, a) where the inline check valves remained open, causing fluid to flow directly to the reservoir and not from the reactor and b) after including a higher flow rate valve cracking step, the inline check valve did not stop the flow from the infusing syringe directly to the withdrawing syringe, hence negating flow through the reactor.

Due to the slow (75 µL min^{-1}) flow rate used within these tests, it was suggested that a high enough cracking pressure, which is the pressure required to close an inline check valve, was not achieved, so the valve remained open instead, allowing backflow to occur. To increase the cracking pressure, an initial cracking step prior to the main flow step, where the flow rate was increased to 1000 µL min^{-1} for 5 seconds, was introduced. Including these cracking steps resulted in a high amount of backpressure from the microcolumn reactor. To mitigate this, wait steps of 2 minutes were introduced immediately after the cracking step. Although introducing cracking steps did stop backflow through the reservoir inline check valves, no flow through the reactor was observed, and backflow proceeded directly to the withdrawing syringe instead (Figure 5.4b). Although the use of passive inline check valves, in theory, simplified the design of the cyclic flow system, the system did not function as intended. A likely reason the system was not viable could have been a result of siphoning at one of the y-connectors or slight pressure differences across the system (although the tubing lengths were carefully chosen to balance fluidic pressure). Regardless of the reason, an alternative strategy was required to achieve flow direction switching between the two states of pumping.

5.1.3 - Incorporating 3/2-Way Active Solenoid Valves

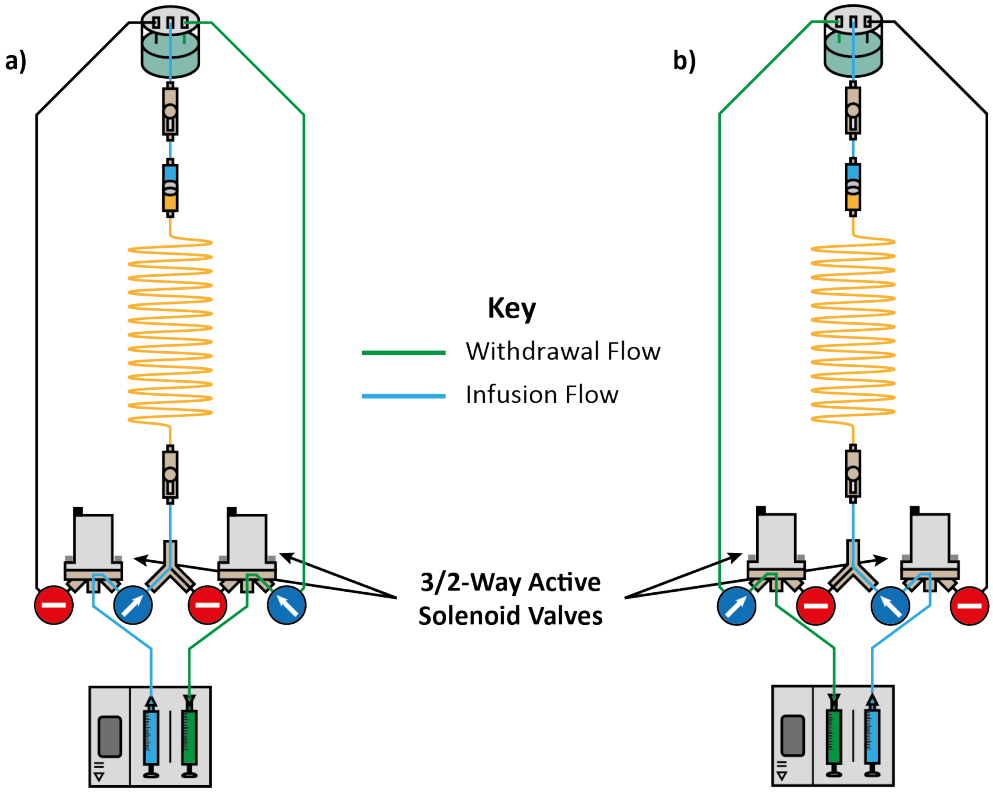

Figure 5.5 - Schematic to demonstrate the two possible pumping states for the 3/2-way active solenoid valve continuous recirculating IMER system, where the infusion path of flow through the column reactor is represented in blue, and the withdrawal path of flow from the fluid reservoir is represented in green. The dual syringe driver determined the polarity of flow, where one syringe was always withdrawing and the other was infusing, giving the two possible states of pumping: a) and b).

An alternative approach to direct fluid flow during withdrawal and infusion cycles was developed based on 3/2-way active solenoid valves. The valves used within this work were Burkert Type 6724 3/2-way Impulse Whisper Solenoid Valves. When provided with a 500 ms 24 V pulse, an internal solenoid causes the latching of the valve to either an NO ⇆ COM or NC ⇆ COM configuration dependent on the polarity of the provided potential, with the COM being the common fluidic orifice and the NO and NC the selected orifice. The concept behind using the 3/2-way active solenoid valves was that if they were actively actuated to synchronise with the switching of the pump between infusion and withdrawal, it would be possible to achieve actively directed switching between the reactor and reservoir fluidic pathways, delivering a more controlled continuous IMER system (Figure 5.5).

The Burkert Type 6724 valves selected for this purpose are designed primarily for an original equipment manufacturer (OEM) market, meaning Burkert does not manufacture any control system by which the valves can be actuated. Therefore, in order to use the Type 6724 valves, a bespoke valve control system was engineered using an RS PRO 36W AC/DC Adapter power supply

(24 V, 1.5A), a custom power distribution circuit board and an sb components Raspberry Pi Pico relay board with the required Raspberry Pi Pico microcontroller.

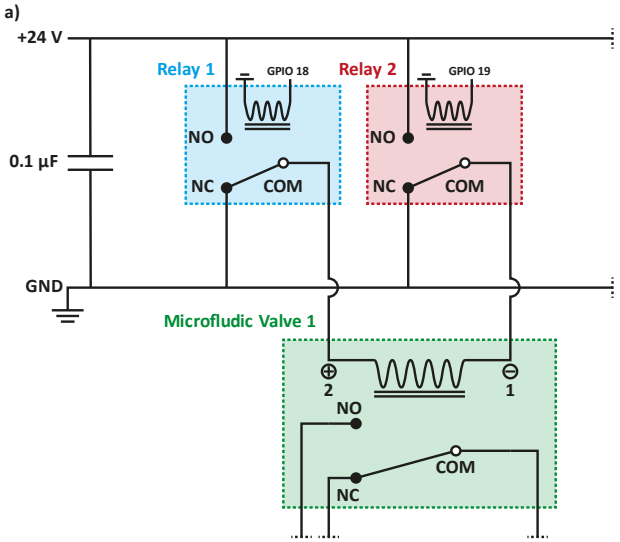

b)

Relay 1	Relay 2	Impulse 500 ms			
		Power Output	1	2	Valve Output
NC	NC	0 V	-	-	-
NC	NO	-24 V	+	-	NO ⇆ COM
NO	NC	+24 V	-	+	NC ⇆ COM
NO	NO	0 V	-	-	-

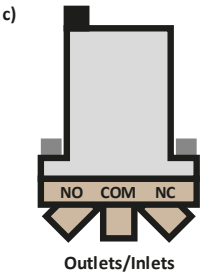

Figure 5.6 - a) The circuit diagram for the designed valve controller, including the electronic relays actuated by the Raspberry Pi Pico GPIO pins 18 & 19, and the fluidic pseudo-circuit diagram for the fluidic outlet/inlet switching, as indicated on the valve diagram c). b) a table outlining the various configurations of the two relay controls, the resultant power output to the valve, the polarity of the potential difference across the valve terminals, 1 & 2 and the resultant outcome this causes for the fluidic output on the valve, according to the valves specification sheet[269]. A second pair of relay valves were configured identically but connected to GPIO 20 and 21 of the microcontroller in order to control the second microfluidic valve.

The electronic engineering requirements for the valve controller were determined according to the specification sheet of the Burkert Type 6724 valves[269], which stipulated the resultant valve configuration output according to the polarity of the potential difference applied across the two power terminals 1 (labelled - on the valves) and 2 (labelled + on the valves) (Figure 5.6b & c). The 500 ms pulse of potential at 24 V was generated using microcontroller-actuated relays. When supplied with an external actuating power signal (in this case, supplied by the microcontroller), the internal solenoid switches the COM (common) contact from the NC (normally closed) contact to the NO (normally open) contact. In the valve controller, the NC contacts of the relays are connected to a 24 V power rail (supplied from a 24 V, 1.5 A power supply) and the NC contacts are connected to the ground rail. The COM contact of relay 1 is connected to the positive terminal of the valve (2), while in relay 2, COM is connected to the negative terminal of the valve (1) (Figure 5.6a). It is, therefore, possible to control and schedule the desired latched fluidic configuration of the valve by closing/opening relay 1 or 2 via microcontroller signals using this proposed electronic system. A basic operating system was coded in microPython (8.2 -Appendix 2 - Flow Control System Code - main.py) to continuously run on the microcontroller, enabling timed and synchronous control of the valves latching positions. Though supplying serial commands from a connected computer via a USB connection, the microcontroller operating system could interpret the commands to actuate the selected valve to the desired latch position.

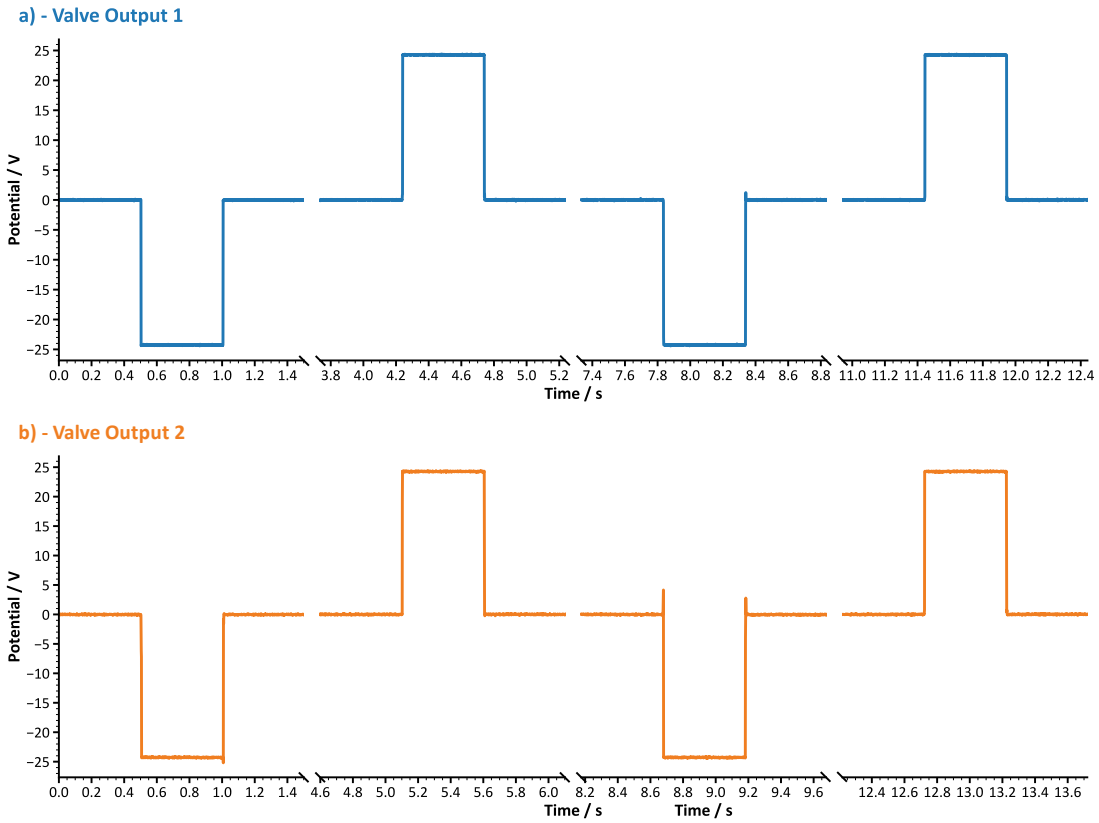

Figure 5.7 - Logged potential difference over time for the two valve output channels of the valve controller system, a) valve output 1 and b) valve output 2, in order to quantitatively analyse the profile of the outputted signal from the device to the valve when actuated via a bespoke control software on a PC. Negative 500 ms pulses actuate NO ⇆ COM switching, and positive 500 ms pulses actuate NC ⇆ COM stitching. A PicoLog 1216 12-bit DAQ at a 1 ms/s sample rate was used to obtain these measurements via connection to each valve's JST PHR male connector outputs.

In order to quantitatively ensure the valve controller functioned as designed, the output signal of each channel on the valve controller was profiled using a PicoLog 1216 12-bit DAQ (at a 1 ms/s sample rate) (Figure 5.7). From the measurement, clear +/- 24 V signal pulses with 500 ms plateaus were observed corresponding to switching between the NC position (-24 V) and the NO position (+24 V). A slight overshoot of the potential was observed intermittently upon the relay switching (e.g. Figure 5.7 - Valve 1 at 8.35 s, Valve 2 at 1.00, 7.70 and 9.17 s). These transient potential spikes did not affect the correct function of the valve at any given point during experiments using the valve controller.

A 3D-printed housing was designed and fabricated to enclose and protect the exposed electronic circuitry (Figure 5.8). LEDs were integrated into the housing lid to indicate the valve controller's current fluidic latching state. To ensure that the LED indicators showed the correct valve latching state, the coded initiation sequence for the valve controller was written to set both valves automatically to a specific defined state. In addition, the flow control software on the PC would also set both valves to a specific state prior to initiating the flow experiment. The LEDs were actuated via GPIO connections on the microcontroller, and each was assigned to a set valve and state of valve latching with the microcontroller operating system.

a)

b)

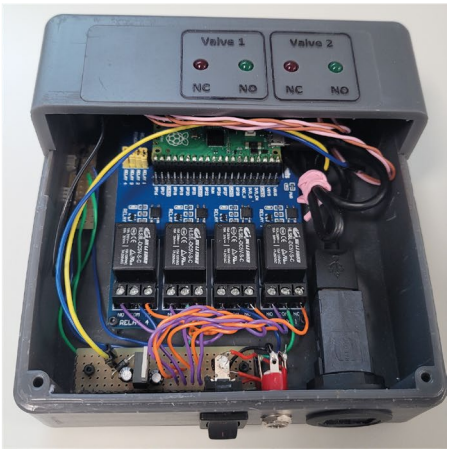

Figure 5.8 - a) The outer casing for the valve controller with the LED readout indicating each valve's current latched fluidic configuration. b) The valve controller with the inner circuitry exposed.

5.1.4 - Microfluidic flow control system (µFCS) Software and Reactor

One of the most significant disadvantages of using an actuated pump and valve within the flow setup is the increased complexity of the system design; in contrast to a system based on passive inline check valves, a digital control system is required to automate and synchronise all system components.

The digital control system served three primary purposes: to connect and interface with the pump and the valve controller, to establish the essential parameters of the flow reactor and the automated aspects of the intended flow reaction experiment and lastly, to provide a means of tracking flow cycles, extraction timings for offline analysis and overall reaction time stamping.

Connection to each device was established through individual serial port connections, and the software handled these connections by creating individual connection classes/objects that contained the common inherited parent class connection variables and the device-specific serial command definitions from the device-specific child class. The set serial commands within these definitions were determined via documentation provided by the pump manufacturer[270] as per the pump's internal operating system, and the valve controller serial commands were determined as per its bespoke operating system.

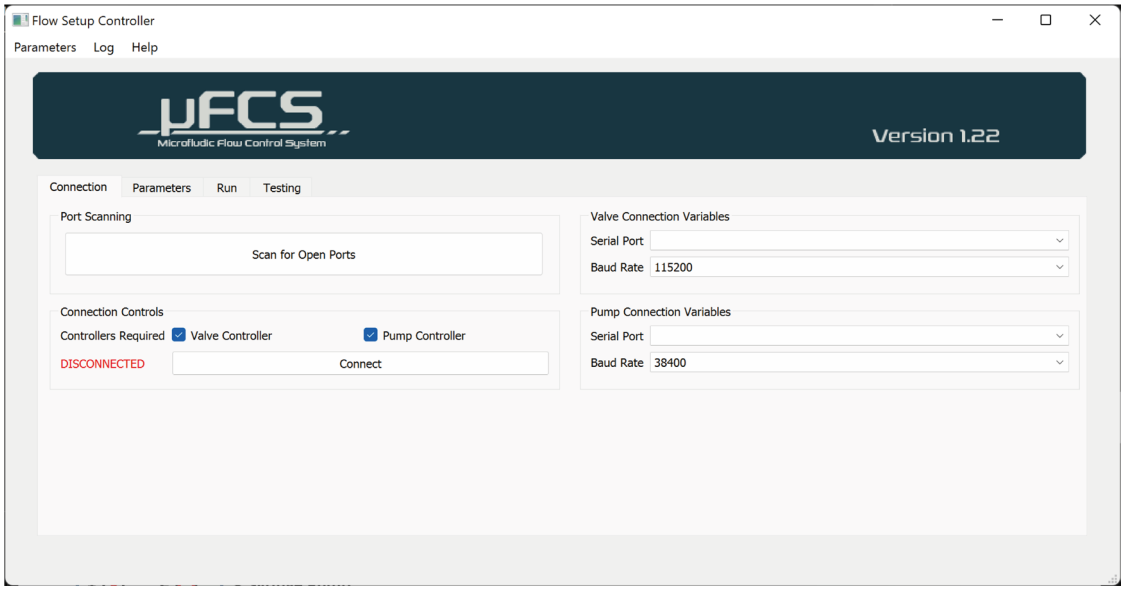

Figure 5.9 - A screenshot of the Connection page of the µFCS UI, used for the assignment of serial ports and baud rates of each device and the button which allows for the connection and disconnection of the devices.

In order to make the process of using the reactor setup and its control system as simplistic as possible, a user interface (UI), named the Microfluidic Flow Control System (µFCS), was designed for the front end of the control software using Qt designer and PyQt5. Images of each page of the µFCS have been provided (Figure 5.9 - Figure 5.11) to more clearly explain the defined

parameters and operation of the control software. The code for the software functionality described within this subsection can be found in an open repository (8.2 -Appendix 2 - Flow Control System Code).

The first page of the interface contained the connection controls and connection variable assignment (Figure 5.9). The connection interface allowed the user to scan for any open serial ports as declared by the systems operating system (Microsoft Windows, Apple OS or Linux), then manually assign one of these serial ports to one of the devices and set the desired baud rate for the connection. The software contained an internal data file storing each device's known manufacturer ID and product ID. From this, the software automatically assigned the correct device to each variable and displayed it next to the serial port number. If multiple pumps or valve controllers were used, the user would still have the option to switch them manually within this interface. Lastly, the interface had a button that allowed the user to connect and disconnect to each device. The system was programmed such that a flow reaction would not start until connections to both valves and the pump were made and confirmed by the software. If the connection was lost during a flow reaction, the system was designed to try to reconnect continuously, and the event and timestamp printed within the flow reaction timestamp log, which is created and saved by the user at the start of a new flow reaction experiment. The connect button was linked to the connect definition, which initiates the device and creates the connection class for each device. The class would be terminated upon disconnection, and the port connection would be closed.

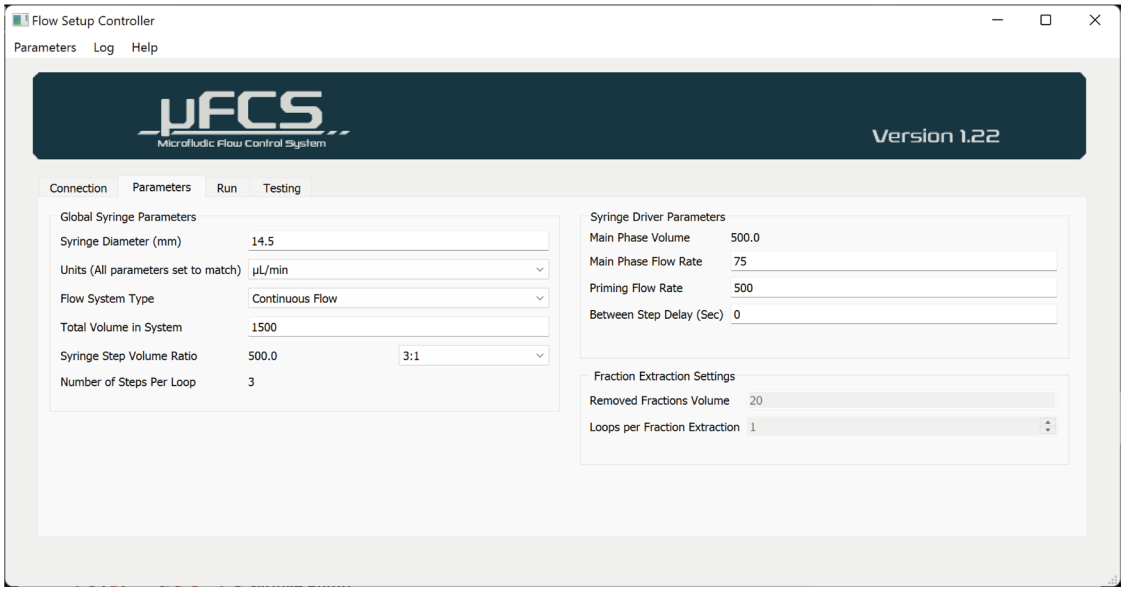

Figure 5.10 - A screenshot of the Parameters page of the µFCS UI, used for defining the various required parameters of the flow reaction, including the pump configuration, volumes used, the flow system type (continuous or fraction extraction), the number of syringe-steps per loop and the fraction extraction settings (only available if fraction extraction was set in flow system type).

The '*parameters*' page of the µFCS interface allowed the user to define the various parameters of the flow reactor and its experiment. These parameters included those required by the syringe

pump to establish the flow profile as a whole and the flow system type, which also determined the availability of the fraction extraction settings. The global syringe parameters established initial parameters for the pump, such as the syringe diameter, total volume and flow rate. When inputting the total volume of reactant solution at the start of an experiment, the software gave the user the option of choosing either two (syringe-step volume ratio of 2:1) or three (syringe-step volume ratio of 3:1) syringe-steps per loop. Two types of flow profiles were designated within the software. The first, continuous flow, incrementally increased the number of loops, each with the designated number of syringe cycles. As the name suggests, this essentially means that the system runs continuously, pushing reactant through the reactor until stopped by the user. The second type of flow profile, fraction extraction, allowed the user to designate the volume of reactant they would like to extract from the reservoir after a defined number of loops. This extraction allowed the user to perform an offline analysis of the reactant solution to track the reaction rate and determine the reaction's endpoint. In order to more clearly explain how the flow reactor system worked in terms of generating a series of pump step commands to send to the pump each loop, based on the number of syringe cycles, Table 2 shows an example of two full loop cycles, the resultant syringe-step numbers and the corresponding volumes per syringe pump for both continuous and fraction extraction flow profiles.

Loop Number	Syringe-Step Number	Continuous Flow Profile		Fraction Extraction Flow Profile	
		Syringe 1 volume / µL	Syringe 2 volume / µL	Syringe 1 volume / µL	Syringe 2 volume / µL
1 – Type α	1 – Type A	500	-500	500	-500
	2 – Type B	-500	500	-500	500
	3 – Type A	500	-500	500	-480
2 – Type β	1 – Type B	-500	500	-500	480
	2 – Type A	500	-500	500	-500
	3 – Type B	-500	500	-460	500
3 – Type α	1 – Type A	500	-500	460	-500
	…	…	…	…	…

Table 2 - An example of the volumes generated and programmed into the syringe pump for each cycle and each loop, in a 3 steps per loop, 1500 µL total start volume systems. The volumes for the continuous and fraction extraction flow profiles are given, alternating between loop type α & β until the user stops the system. … represents the continuation of the series in the same fashion. A 2-step per loop system generates a similar series for each syringe but with only 2 syringe cycle numbers per loop and the total start system volume split by 2 (750 µL per syringe cycle volume for a 1500 µL total start volume system).

Due to the pump being driven by two syringes, there are two possible states of syringe-step. Type A, where syringe 1 is infusing (positive volume command sent to the pump) and syringe 2 is withdrawing (negative volume command sent to the pump), and type B, where syringe 1 is withdrawing and syringe 2 is infusing. These types are important to define, as the syringe-step type determined how the valves were actuated. For example, if the syringe-step is type A, valve 1, which is connected to syringe 1, will need to direct flow through the reactor at the same time, closing direct access to the reservoir, while valve 2, which is connected to syringe 2, directs flow

from the reservoir while closing direct access to the reactor (Table 2 - Type A and Figure 5.5a). Type B can be defined as the total opposite inverse of the type A profile (Table 2 - Type B and Figure 5.5b). The software actuated the valves accordingly based on the type of syringe-step. In the case of a two syringe-step loop (meaning two syringes performing two steps of the syringes infusing and withdrawing, then inversing), there was only one type of loop, with the step alternating between types A and B. However, in a three syringe-step loop (meaning two syringes performing three steps of infusing and withdrawing), there were two types of loop: type α, consisting of A, B, A syringe-step types (Table 2 - Type α) and type β made up of B, A, B syringe-step types (Table 2 - Type β). For a pumping system to return to the first state of pumping, a three syringe-step loop must undergo a type α and type β cycle to return to the first loop type (type α) (Table 2).

Defining loop types was a vital consideration for the software fraction extraction system. After the user-defined number of loops per fraction extraction had been completed, the user-defined fraction extraction volume was deducted from the total volume of the syringe that was withdrawing during the final syringe step (Table 2 – Fraction extraction column), and the flow rate recalculated so that both the infusion and withdrawal syringes finish at the same time at the end of one loop. The change in withdrawal volume ensured that within the next cycle before extraction, the total system volume for the reactor was reduced by the same volume that had been removed from the system. The flow rates for the withdrawal step were modified to keep the volume within the reservoir close to being constant during this syringe cycle. Regarding the UI, the software paused when reaching the designated number of loops per fraction extraction, and a pop-up prompted the user to extract the defined volume fraction from the reservoir. After the user clicks ‘ok’, the software records the time and loop number within the experiment run log and restarts the system at the next set of steps and loops before the subsequent extraction. Because the system adjusted for loss in total system volume, the solution volume that passed through the reactor also decreased, and, in turn, so did the time for a loop to occur. Ensuring the system compensated for this loss of volume to decrease the time taken for a loop was crucial when determining reaction kinetics based on time, even when comparing reaction kinetics within the context of this flow reactor system; otherwise, the kinetic profile becomes significantly more system-limited than would be occurring just based on flow rate limitations or enzyme kinetics. In addition to the system volume, the UI also allowed the user to define the main phase flow rate, the priming flow rate and the delay time (in seconds) between each syringe cycle prior to valve switching.

The maximum number of extractions, $N_{\mathrm{Max}\,Ex.}$, as defined by the following equation:

$$N_{\mathrm{Max}\,Ex.} = \frac{n \cdot V_{Cycle}}{V_{ext.}} \quad (5.1)$$

Where n is the number of loops per fraction extraction, V_{Cycle} is the start main phase volume and $V_{ext.}$ is the volume of the extracted fraction. This formula limited the total number of fractions that could be taken while the number of loops per fraction extraction controlled the time between extractions. This ability to control the time between extractions is critical when dealing with slow-turnover reactors.

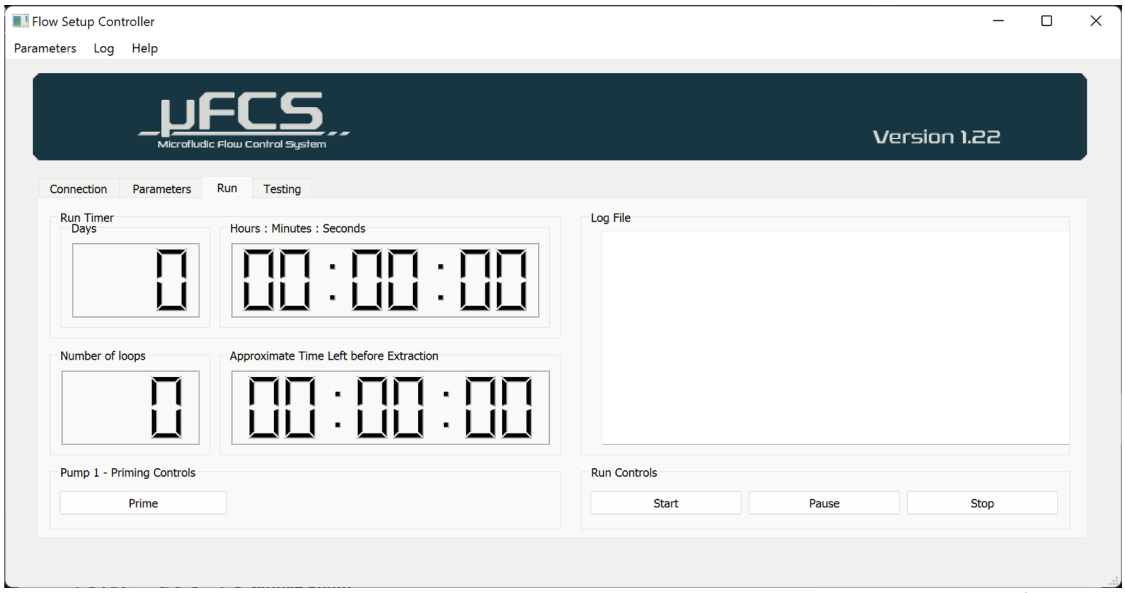

Figure 5.11 - A screenshot of the run page of the µFCS UI, used to initiate priming of the pump, start/stop the flow reaction, monitor the elapsed time, the current number of loops, display the count down timer to the time till the next extraction step and the current information within the log file for the running experiment.

The UI run page allowed the user to prime the syringe pump into the starting configuration, start and stop the flow reactor experiment, display the elapsed time of the experiment and the number of loops completed, and approximate the time till the net extraction, as well as giving a live view of the running experiment log file, which included a copy of the experimental run parameters, and the timestamps for each extraction (Figure 5.11).

As the column was packed outside the flow system, it had to be filled with reaction solution before being placed within the flow reactor system to ensure the volume and concentration were as expected for the experiment. Although this meant some product was potentially formed prior to the start of the experiment, it was a known limitation of the system and deemed preferable to accounting for a dilution of the overall reaction buffer if the beads were packed with non-reactant containing buffer, as the rate of mixing of the two solutions, would be hard to quantify. In order to start a flow reaction experiment, the flow system first required priming, which was performed by filling the reservoir with a volume of solution equal to the total system volume

minus the reactor volume and manually pumping the fluid throughout the system via the syringes. Once primed, the user could fill the syringes via the syringe pump using the prime button of the user interface. A defined priming step ensured that the syringe infusing within the first syringe step was filled according to the main phase volume at the user-defined priming flow rate. Once primed, the user could press the start button, which prompted them to choose a name and location to save the experiment log file. The reaction could be stopped at any given time by pressing the stop button, to which a pop-up asked the user to confirm they want to stop the reaction.

For user convenience and to ensure more consistent experimental practices, the run interface also included a timer that informed the user how long the reaction had been running (days, hours, minutes and seconds) and the number of loops completed during this time. Lastly, the system was programmed to calculate an estimated time for the subsequent extraction using the volumes and flow rates of each syringe step, which were added to the total wait time of all the individual steps until the ensuing extraction. The software allowed the user to save the user-defined parameters for an experiment as a setup file, which could be re-loaded.

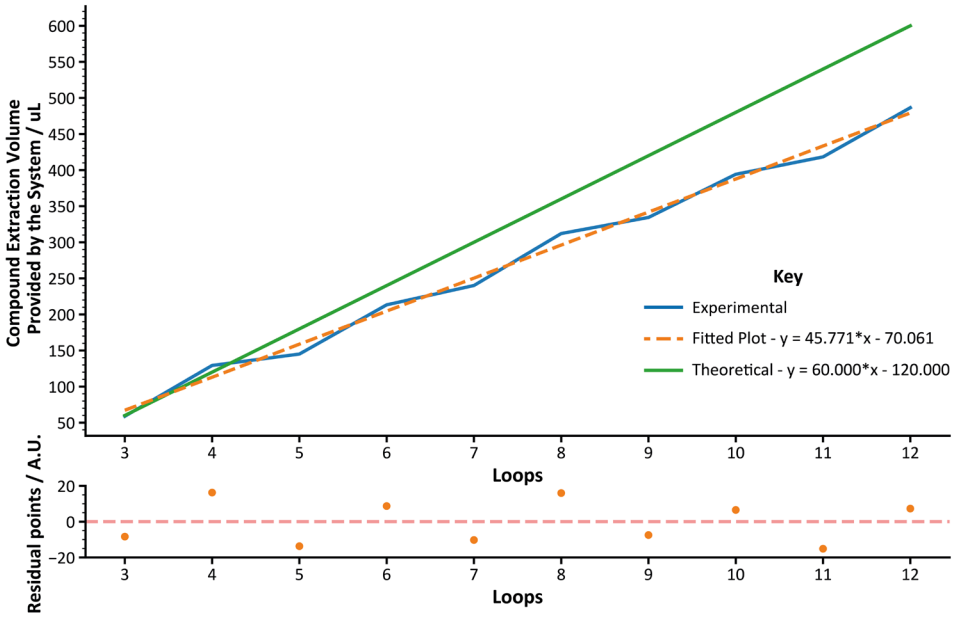

Figure 5.12 - An experiment to determine the system's consistency in maintaining a constant decrease of the reservoir volume for each extraction. The data shows the change in compound extraction volume provided by the flow system per loop, starting at loop 3. Experimental data points (blue line) were plotted as a line graph to indicate the data points' linear yet fluctuating nature. The fitted plot for the experimental data (orange dashed line) was calculated from the experimental data set using OLS linear regression. The theoretical plot was calculated assuming each loop increased the compound extraction volume by exactly 60 µL. A residual analysis of the experimental data points was also performed.

In order to test software reliability, the system was allowed to run continuously without stopping or extraction for 14 days. Although this assessment was not quantitative, the software successfully ran for 14 days without crashing or reporting any errors, with fluid still pumping

throughout the system. To more quantitatively assess the reliability and consistency of the system, a control experiment was performed in which the mass of the reservoir at the start and end was recorded. The experiment used a column reactor packed with unfunctionalised agarose beads and sodium phosphate buffer as the flow medium. Here, the flow rate was set at 150 µL min^{-1}, with a total system volume of 3000 µL. The main phase volume was 1000 µL for a three syringe-step loop with a 60 µL fraction extraction for each loop. The experiment aimed to determine if the software and flow system correctly factored in the volume loss to the flow system for each extraction. By weighing the reservoir before and after each extraction and determining its difference from the previous extraction step, it was possible to determine the compound change in volume for each loop/extraction over the experiment's lifetime (Figure 5.12). This information was presented and considered in this fashion, as it more clearly displayed the overall compound effect on the actual volume of each loop differing from that of the ideal volume of each loop provided to the reservoir for extraction. The plot was considered from the third loop onwards since the first loop gave a highly inconsistent volume, most probably due to the system not yet performing one full syringe-step and due to the values consisting of differences between steps; the third step was the first valid difference (the difference between the second and third step). Instead of the data being plotted as a scatter plot, a point-to-point line plot was chosen to emphasise that from point to point, a fluctuation was observed, but the overall trend was still linear. After fitting a linear relationship via OLS linear regression to these data points, residual analysis was performed to further show the linear but alternating fluctuation pattern, even within the residual points. The origin of this fluctuation can be attributed to the two different syringe-step types, A and B. Discrepancies in the plastic syringes used, the syringe pump motors, and slight volume differences between the microfluidic tubing, over time, cause small accumulated systematic errors so that the two syringe step types give slightly different outputted volumes to the reservoir at the end of each syringe step and therefore each loop, the result of which gives the observed fluctuating pattern. Due to the fact that the extractions are taken from the pooled reactant solution within the reservoir, these slight differences in volume and concentration of product will only be minor, making the systematic error between these two syringe step types an issue not detrimental to the determination of reaction kinetics. Comparison of the fitted plot for the experimental data (Figure 5.12 - Fitted Plot) to that of the theoretical plot (Figure 5.12 - Theoretical plot), which was calculated assuming that the system provided exactly 60 µL extra to the reservoir at the end of an extraction cycle, showed a clear difference in their gradients. This comparison showed that the experimental system delivered approximately ¼ less volume per fraction extraction over the observed period of extractions when compared to the ideal volume delivered. This systematic error is likely due to the use of rubber septum plastic syringes for the flow experiments and the

lack of feedback loop control via pressure or flow sensors, which resulted in less accurate volume delivery per syringe step.

Using the gradient of the theoretical plot and the fitted plot, a compensation correction constant could be calculated and incorporated into the flow control system to accommodate for the loss of volume in the reservoir to syringe and syringe pump system error. However, since reaction kinetics for each reactor type and each experiment were only planned to be performed using this same flow control system, the same systematic error would be applied to all experiments and, therefore, would not affect the comparison of these reactors and experiments. For this reason, the integration of this feature into the flow control software was postponed and has been flagged for a point of further work.

5.2 - Sepharose Bead Column Reactor

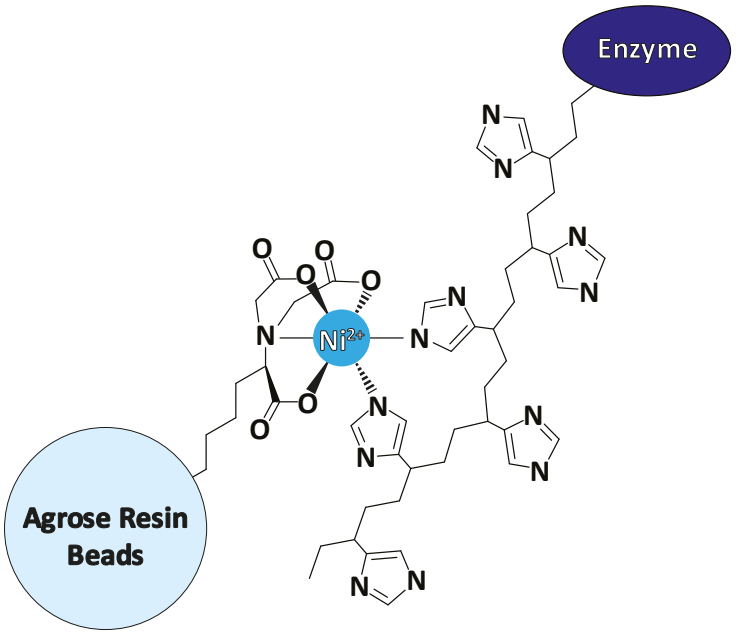

Figure 5.13 - A simplified schematic to demonstrate immobilisation of a His-tagged enzyme, such as CBL used in this study, via NTA Ni functionalised agarose resin beads. Note: A simplified skeletal chemical structure has been illustrated for the 6-His tag motif to maintain greater visual clarity.

After fully developing and testing the flow reactor system and the accompanying µFCS software, it was possible to establish and perform µ-IMER experiments using the immobilised CBL enzyme. One of the key points of this research was to compare a planar enzyme functionalised microfluidic chip reactor to that of a packed bead microcolumn reactor. It was decided that to initially prove the viability of the inflow catalytic system, a bead column reactor would be used due to their higher abundance in the literature and inherent ability to immobilise a far larger concentration of the enzyme due to their three-dimensional surface area.

The physical assembly of the µ-IMER followed the same configuration as the designed reactor model (Figure 5.5), with a PC connected by USB to the valve controller and syringe pump, which ran the µFCS software (Figure 5.14). In order to have a stable platform in which the microfluidic components and tubing could be held, a 3D printed scaffold system was developed, which, via a modular interconnecting approach, allowed the integration of all the microfluidic components used within this work.

The procedure for functionalising the agarose beads with the desired enzymatic species (Figure 5.13) can be found in the method section (3.4.3 - Enzyme Functionalisation and Packing Procedure for Bead Columns). 200 µL of CBL functionalised beads were loaded into the microcolumn reactor described within the methods section. To quantify the protein uptake onto

the agarose beads, an absorbance-based biochemical assay commonly used for the quantification of protein concentrations, called a Bradford assay, was performed on the protein-bead solution before and after the bead incubation step. The Bradford assay solution used for the study was TCI Bradford Assay Solution (B5702).

Figure 5.14 - A picture of the actual microcolumn reactor setup used within this work. Control of the flow system was handled via the µFCS software on the PC (right), which in turn was connected to the dual syringe pump and valve controller via USB (centre) and the flow setup, including the valves, filters, connectors, and reservoir all mounted on a bespoke modular 3D printed microfluidic scaffold (left).

A calibration curve was initially acquired using known concentration dilutions of bovine serum albumin (BSA), which is a common protein standard within biochemistry. 4 µL of each BSA solution was added to 200 µL of the Bradford assay solution. After leaving the solution to incubate for 5 minutes at room temperature, the optical absorbance between 400 nm and 700 nm was recorded with a spectrophotometer, and the peak absorbance at 595 nm, as per the manufacturer's specification, was acquired for each concentration (Figure 5.15).

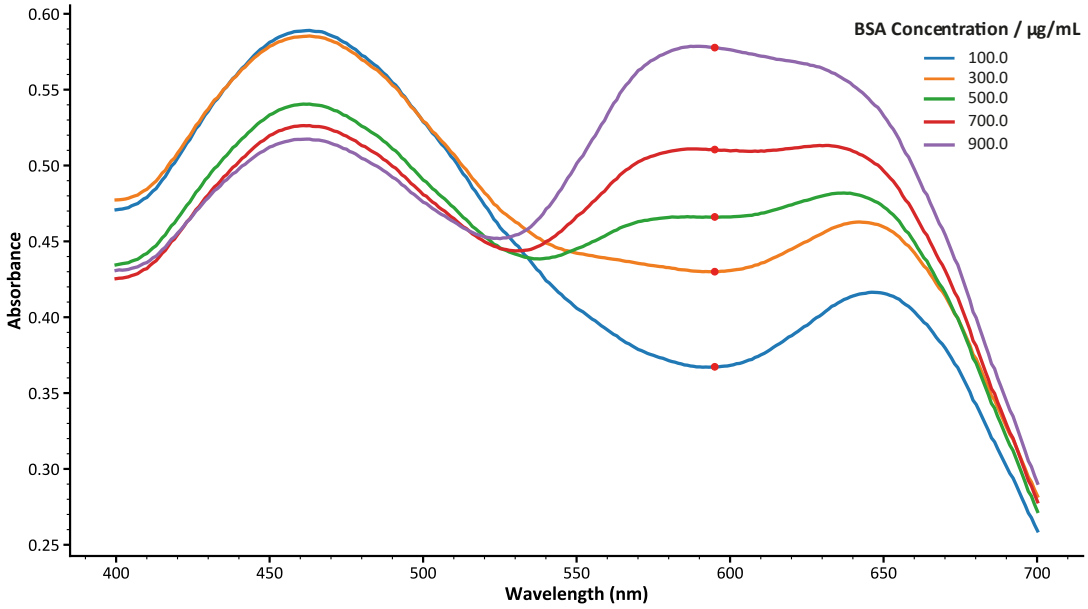

Figure 5.15 - Bradford Assay absorbance vs wavelength plots for BSA at various indicated concentrations, with absorbance values for each plot at 595 nm (red dot) taken for the Bradford Assay calibration curve per the manufacturer's specification sheet.

The absorbance for each concentration at 595 nm was then plotted against the concentration to which OLS linear regression was applied to acquire a linear calibration plot from which unknown protein concentrations could be determined (Figure 5.16).

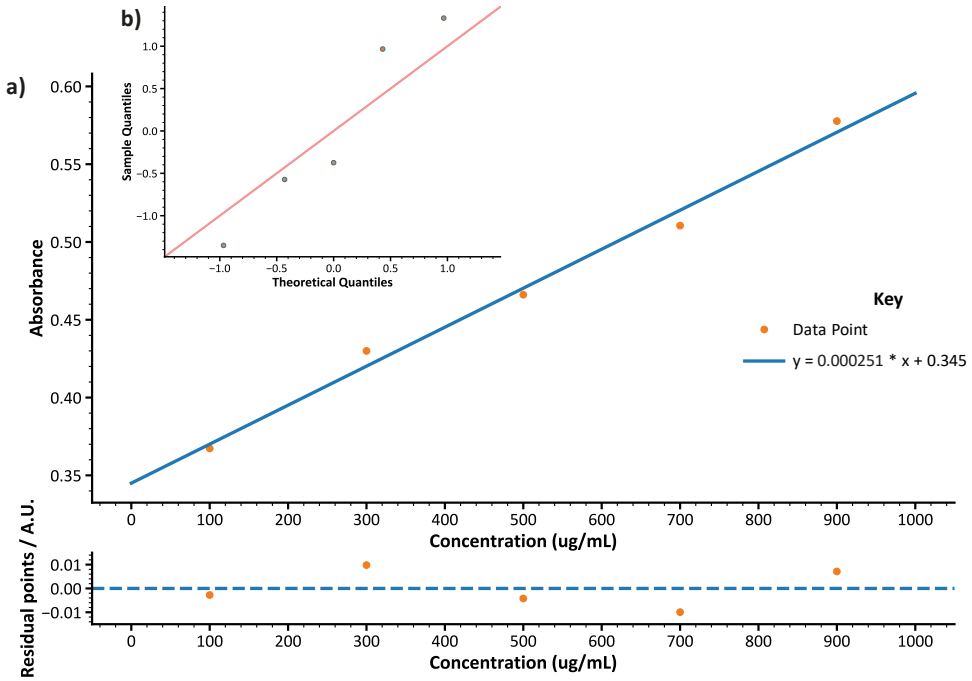

Figure 5.16 - BSA Bradford assay calibration plot showing absorbance at 595 nm against the known concentration of the BSA solution. The linear plot was fitted using OLS linear regression and analysed using a) residual and b) QQ plot statistical analysis.

The resultant linear regression showed a clear linear trend with an R^2 of 0.989, with a narrow, even distribution about the norm for the residual analysis, and a QQ plot which indicated a

quartile distribution for the fitted plot that was significant, especially given the large tolerances afforded a Bradford assay.

Using the same Bradford assay and analysis, the absorbance of the CBL solution before and after the bead incubation step was recorded for three nominally identical individual preparations of the CBL enzyme functionalised beads. Using the BSA calibration curve, it was possible to determine the difference in CBL concentration before and after bead functionalisation and thus the concentration of CBL bound to the 200 µL of stock Agarose bead medium. The average mass of CBL protein bound to 200 µL of stock Agarose bead medium was 668.8 ± 17.1 µg (equivalent to $8.3\times10^{15} \pm 2.1\times10^{14}$ molecules). As only 1/5 of these functionalised beads were packed in the reactor per experiment, the amount of CBL used per flow reactor experiment was 133.8 ± 3.4 µg ($1.67\times10^{15} \pm 4.25\times10^{13}$ molecules of CBL). These beads were then packed as described earlier in the chapter, filled with substrate running buffer, and carefully mounted within the flow reactor system.

Two column reactors were used in this work with a total calculated volume, including the valves and filter, of 133.5 and 120.8 µL, respectively, and the system dead volume, including each column reactor, was estimated at 501.2 and 488.5 µL respectively. As only 40 µL of CBL-functionalised Agarose beads were loaded into the columns, the number of beads packed in each column remained consistent.

5.2.1 - Microcolumn μ-IMER Experiments using CBL Immobilised Agarose Beads

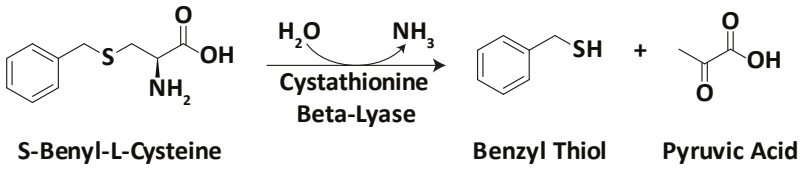

Figure 5.17 - The chemical equation to show the CBL catalysed α, β-elimination reaction of S-benzyl-L-cysteine into ammonia, benzyl thiol and pyruvic acid, used as the reaction to test the kinetics of immobilised CBL enzyme and the μ-IMER system.

L-cystathionine is one of the primary substrates for CBL in a natural biological system. Using the cofactor, pyridoxal-5'-phosphate (PLP), CBL catalyses the α, β-elimination reaction of L-cystathionine to produce ammonia, pyruvate and L-homocystienine[271]. CBL participates in several metabolic pathways, but potentially the most industrially relevant from a μ-IMER standpoint is the metabolism of methionine[272], an essential amino acid for protein synthesis. L-cystathionine is a relatively expensive precursor that would detract from the usefulness of immobilised CBL as a testing standard for reactor systems. Fortunately, CBL displays high substrate promiscuity, working efficiently with other cheaper alternative substrates. The substrate selected here was S-benzyl-L-cysteine, which would produce ammonia, benzyl thiol and pyruvic acid when catalysed by CBL (Figure 5.17).

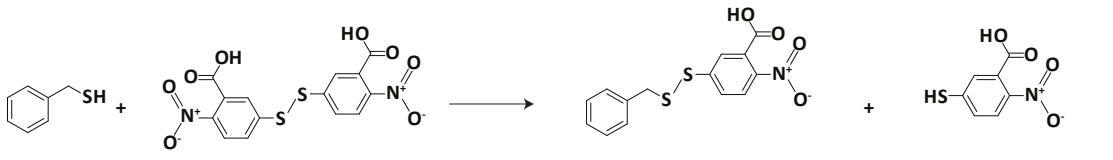

Figure 5.18 - The stoichiometric chemical equation to show the reaction of the benzyl thiol product from the CBL catalysed reaction with Ellman's reagent (DTNB) to form a mixed disulfide and TNB, which has a strong absorbance peak at 406 nm, which can be used to quantify the formation of the thiol product.

Regular access to high-performance liquid chromatography (HPLC) systems was not possible for product analysis of any of the μ-IMER experiments performed in this work. Therefore, an alternative strategy for analysis was achieved via a reaction of the benzyl thiol product with the colourogentic chemical, Ellman's reagent (5,5'-dithiobis-(2-nitrobenzoic acid) or DTNB) (Figure 5.18). DTNB reacts readily and stoichiometrically with small molecular mass thiols, such as the benzyl thiol product of the CBL catalysed cleavage of S-benzyl-L-cysteine, to form a mixed disulfide product and 5-thio-2-nitrobenzoic acid (TNB). TNB has a significant absorbance peak at 406 nm. Therefore, by adding DTNB to the running reaction buffer, it was possible to quantify the catalytic formation of benzyl thiol through the offline UV-Vis analysis of the fractional extractions taken from the flow reactor. The protocol for preparing this standard CBL catalysis

buffer can be found in the methods chapter (3.4.6 - Preparation of the Standard CBL µ-IMER Running Buffer).

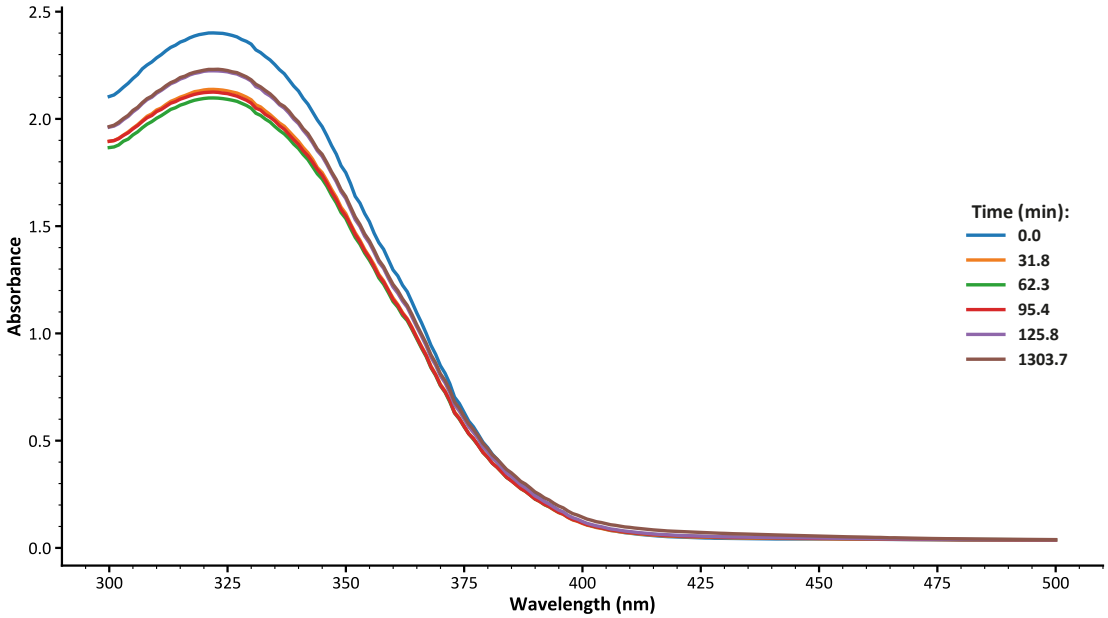

Figure 5.19 - Control experiment where the microcolumn was packed with unfunctionalised Sepharose beads, with S-benzyl-L-cysteine [10 mM], a total system volume of 1.5 mL, a flow rate of 150 µL min^{-1}, 20 µL fraction extractions every loop, and the extraction diluted by 1/5 in standard PBS buffer. Extractions were taken every loop for the first 2 hours, then again after 22 hours.

To ensure the unfunctionalised beads or other components of the experiment did not actively catalyse the cleavage of S-benzyl-L-cysteine, unfunctionalised beads were prepared and loaded into the microcolumn using an identical preparation to that of the CBL functionalised beads, and a control experiment was performed to confirm no catalysis was observed. The conditions for the reaction consisted of S-benzyl-L-cysteine [10 mM], a total system volume of 1.5 mL, a flow rate of 150 µL min^{-1} and 20 µL fraction extractions every loop. Each 20 µL fraction extraction was diluted in 80 µL of standard PBS buffer before UV-Vis analysis. No product peak formation was observed during any fraction taken over the 22-hour monitored period during the control experiment (Figure 5.19), ensuring any catalysis observed in further reactions resulted from the immobilised CBL enzyme. Changes in the magnitude of the DTNB indicator peak at 332 nm were observed, though, which were attributed to the error in precision introduced by the UV-Vis spectrometer and formed the reasoning for some experiments later disclosed having fractions being sampled in triplicate to obtain error bar data.

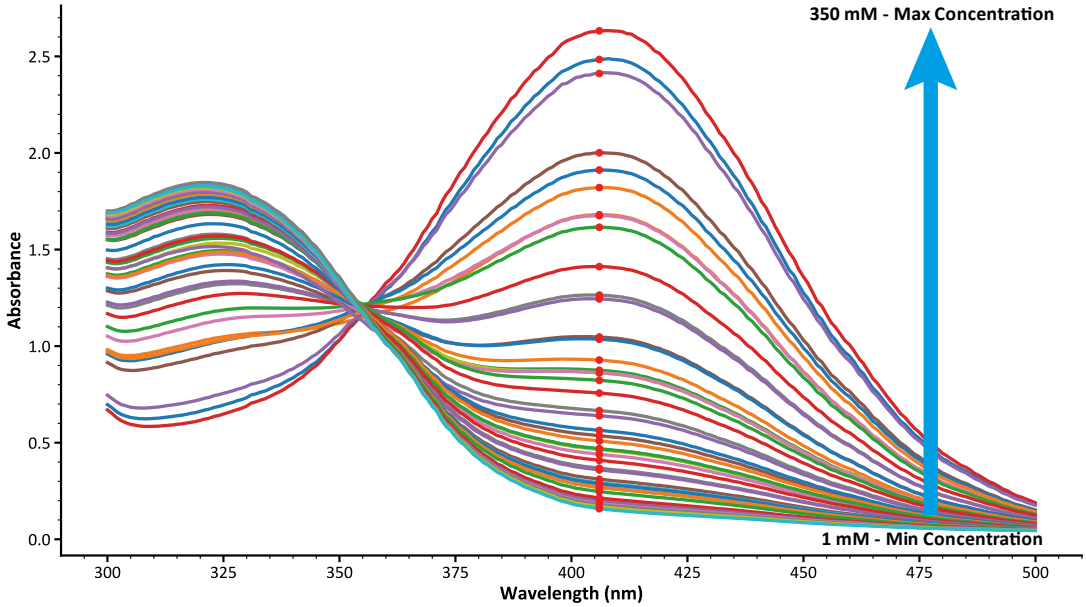

Figure 5.20 - TNB absorbance vs wavelength plots for the DTNB reaction with the reference molecule L-Cystiene at concentrations ranging from a minimum of 1 mM to a maximum of 350 mM, the peak maxima for each plot at 406 nm taken for the calibration curve.

In order to quantify the unknown concentration of benzyl thiol using the analysed absorbance spectra, a concentration curve using pure benzyl thiol was initially attempted. However, a poorly defined linear trend was observed between absorbance and benzyl thiol concentration. This poor trend is believed to be due to the sensitivity of benzyl thiols' to air, leading to the rapid oxidation of the thiol to form a disulfide. This oxidation of the thiol product was not an issue for the catalytically formed benzyl thiol, as upon formation, the product was more likely to react with the high concentration of DTNB instead of with the significantly lower concentration of benzyl thiol in the solution. A calibration curve was instead achieved using an alternative reference thiol compound, L-Cystiene, to acquire the required DTNB calibration plot. In order to obtain absorbance values not exceeding the saturation absorbance of the spectrometer, all UV-Vis spectral analysis of the standard running buffer and the calibration buffer was diluted by 1/5 (20 µL of the analyte with 80 µL of PBS). Like the running buffer, each L-Cystiene analyte solution contained the same concentration of DTNB [1 mM]. After plotting the spectra for L-Cystiene concentrations ranging from 0.78 to 1000 µM, it was ascertained that the absorbance plateaued for concentrations greater than 350 µM. For this reason, the calibration spectra (Figure 5.20) and the resultant calibration plot (Figure 5.21) were limited to a concentration of 350 µM.

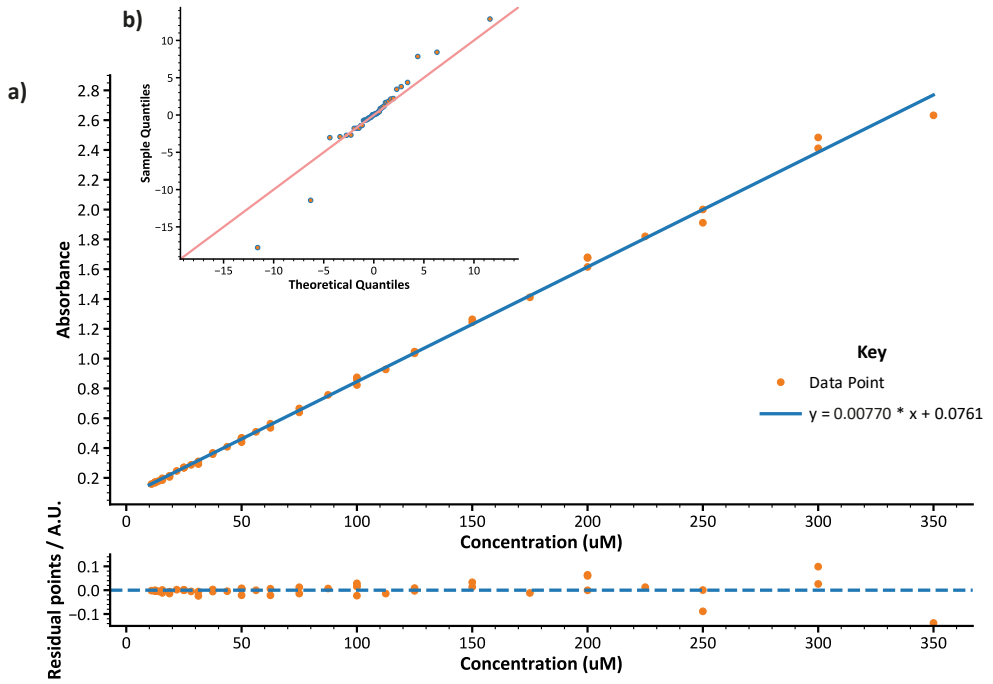

Figure 5.21 - TNB calibration plot for determining an unknown thiol concentration using various concentrations of the standard reference compound, L-Cystiene, with DTNB [1 mM] to obtain the peak absorbance at 406 nm at the known concentration. Analysed solutions were diluted (20 uL of analyte solution with 80 uL PBS) before analysis, but the given concentration in this plot is in reference to the undiluted solution. The linear plot was fitted using OLS linear regression and analysed using a) residual and b) QQ plot statistical analysis.

The resultant OLS linear regression showed a clear linear trend with an R^2 of 0.998, with a slightly increasing spread in the distribution of residuals about the norm with increasing concentration. QQ plot analysis showed that the linear trend well described the normal quartile distribution for the plot.

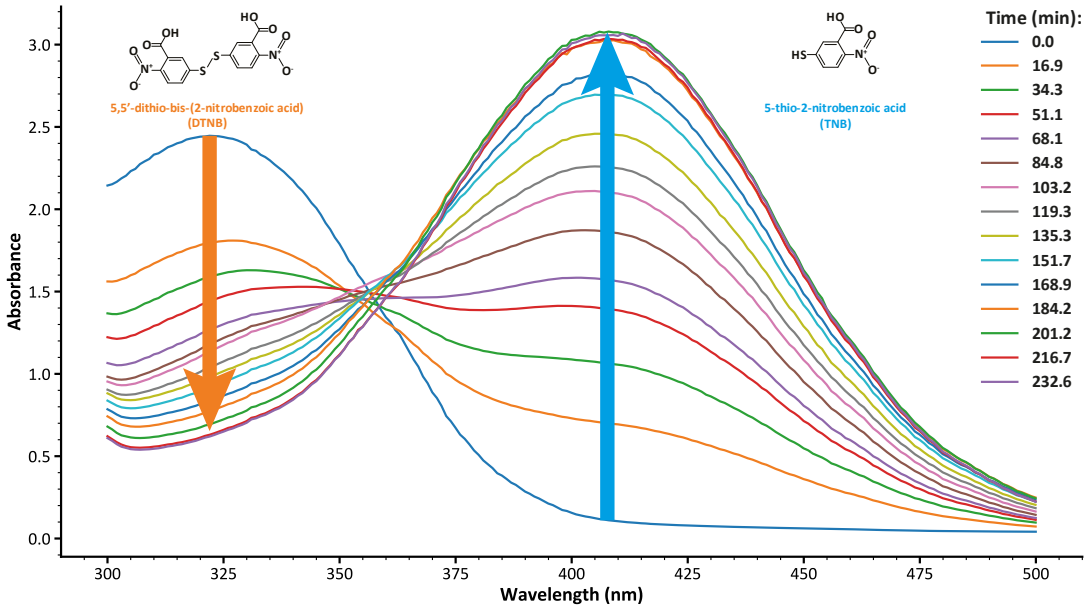

Figure 5.22 - The UV-vis spectra of the decreasing absorbance peak of DTNB (orange arrow) at 332 nm and the increasing absorbance for TNB (blue arrow) at 406 nm over time until the maximum detectable absorbance was reached. This data was from the µ-IMER experiment for the inflow biocatalysts of S-benzyl-L-cysteine [10 mM] by His-tag immobilised CBL within a bead column reactor, a 3.0 mL total system volume, a 150 µL min^{-1} flow rate and 3 × 20 µL fraction extractions.

This higher detectable limit for the spectral analysis of thiol products using DTNB would naturally limit the detectable concentration endpoint of any given reaction. This limitation had little effect in determining reaction kinetics for the enzymatic system. All reactions were performed using the same system and 1 mM concentration of DTNB within the reaction running buffer, leaving kinetics comparable to all experiments performed using this system.

The first µ-IMER experiment for the inflow biocatalysis of S-benzyl-L-cysteine [10 mM] by His-tag immobilised CBL within a bead column reactor, as described, was performed using a larger total system volume of 3.0 mL. The large system volume enabled 3 × 20 µL extractions per loop without exceeding the main phase volume. Multiple extractions per loop were performed to calculate standard deviations for the absorbance data for each extraction. The other system parameters for this experiment were a flow rate of 150 µL min^{-1}, a 240-second delay between syringe steps, a 500 µL min^{-1} priming flow rate and 3 syringe steps per loop. Before this experiment, it was determined through testing that a 240-second delay between syringe steps and the actuation of the valves to their new latching position was required to allow the dissipation of any system backpressure during the system step. The wait step and release of backpressure via the reactor stopped any unwanted pressure release and subsequent backflow into the reservoir upon the valve switching.

By plotting the absorbance spectra of the fraction extractions over time, it is possible to observe the decrease in absorbance at 332 nm for the depletion of DTNB (Figure 5.22 - Orange Arrow) and the increase in absorbance at 406 nm for the formation of TNB (Figure 5.22 - Blue Arrow) as the DTNB reacts with the catalytically formed benzyl thiol. The plot also showed that the highest detectable absorbance was larger than that observed in the calibration curve, allowing for the detection of higher concentrations of the benzyl thiol product. The ability to detect these higher absorbances demonstrated that the higher detectable limit of concentration of the formed benzyl thiol was, in fact, a limitation of the DTNB colourimetric assay itself and not the UV-Vis spectrometer. Since higher absorbances were detected in the experimental results than were obtainable in the L-Cystiene calibration experiment, it was decided that instead of determining kinetics plots calibrated to concentration, the resultant plot would be left in absorbance and the reaction rates in relation to absorbance accordingly. The information regarding the calibration assessment was included to show how viable the assay was for accurately determining concentration. The DTNB thiol assay, although convenient and a valid means of initial assessment, provided too many inconsistencies, such as system error from the UV-Vis spectrometer and limitations and inaccuracies in the concentration calibration. However, it is accepted as a limitation of this analytical method that could be amended using an alternative analysis method, such as HPLC.

The simplified kinetic model used for the fitting of all experimentally obtained data for the biocatalytic turnover of S-benzyl-L-cysteine into benzyl thiol via CBL, using the DTNB thiol determination assay, was of the following form:

$$[C] = [C]_0\{1 - e^{-k_1 t}\} \quad (5.2)$$

Where $[C]$ is the absorbance/concentration, $[C]_0$ is the maximum theoretical absorbance/ concentration, k_1 is the rate of reaction or rate constant, and t is time. The kinetic model is built on the assumption that the maximum theoretical absorbance/ concentration is limited to that of the TNB as per the described limitations of the assay. Secondly, due to the high concentration of DTNB compared to that of benzyl thiol formed, the formation of TNB is not the rate-limiting step, but instead, the observed rate of reaction is defined by the catalysis of the S-benzyl-L-cysteine by CBL. In reality, k_1 is likely an amalgamation of several rate-determining steps relating to experimental setup and system limitations, such as the time taken to pump the total system volume through the reactor at a set flow rate to determine a single loop. Despite this limitation of the reactor system, due to these other contributing rates associated with the reactor setup being kept consistent across experiments, the obtained rate of reaction still functions as a valid means of comparison between each system, as the observable rate change is directly linked to the change in the rate of enzymatic catalysis, which should remain a function of the substrate concentration.

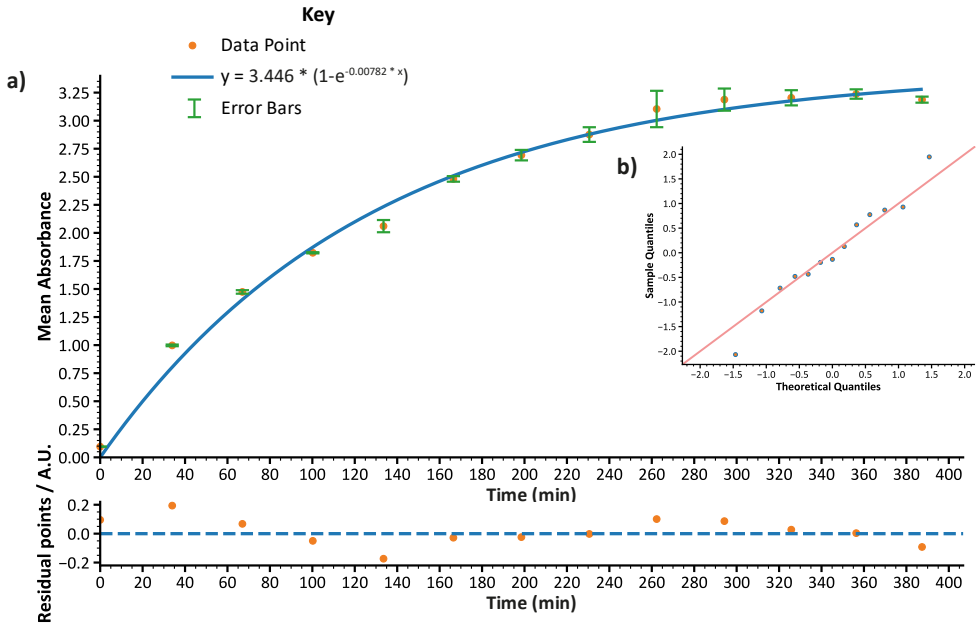

Figure 5.23 - The mean absorbance over time kinetic plot for the immobilised CBL catalysed formation of benzyl thiol via DTNB coupled UV-vis analysis, using a bead microcolumn reactor, with S-benzyl-L-cysteine [10 mM], a total system volume of 3.0 mL, a flow rate of 150 µL min^{-1} and 3 × 20 µL fraction extractions every loop, to determine standard deviation error bars. The curved plot was fitted using NLS regression and analysed using a) residual and b) QQ plot statistical analysis.

The kinetic model (5.2) was applied using non-linear least squares (NLS) regression, explicitly employing the Trust Region Reflective (TRF) algorithm, with solution boundaries set for $[C]_0$ between 0 and 4, and for k_1 between 0 and 1, to ensure successful convergence.

From the first µ-IMER experiment for the inflow biocatalysis of S-benzyl-L-cysteine [10 mM] and a total system volume of 3.0 mL, a kinetic analysis plot was obtained from the experimentally determined peak absorbance for the formation of TNB, which inferred the catalytic formation of benzyl thiol (Figure 5.23). The curve fitted for determining the reaction rate of catalysis using non-linear least squares regression gave an R^2 of 0.990, with a narrow, even distribution about the norm for the residual analysis but with an observable oscillating pattern to the residuals. The QQ plot analysis indicated that the normal quartile distribution for the data was well described by the fitted kinetic model. A rate constant of 0.00782 min^{-1} was obtained from the fitted model, which could then be compared to subsequent catalytic reactions performed using the DTNB quantification of benzyl thiol formation via CBL biocatalysis.

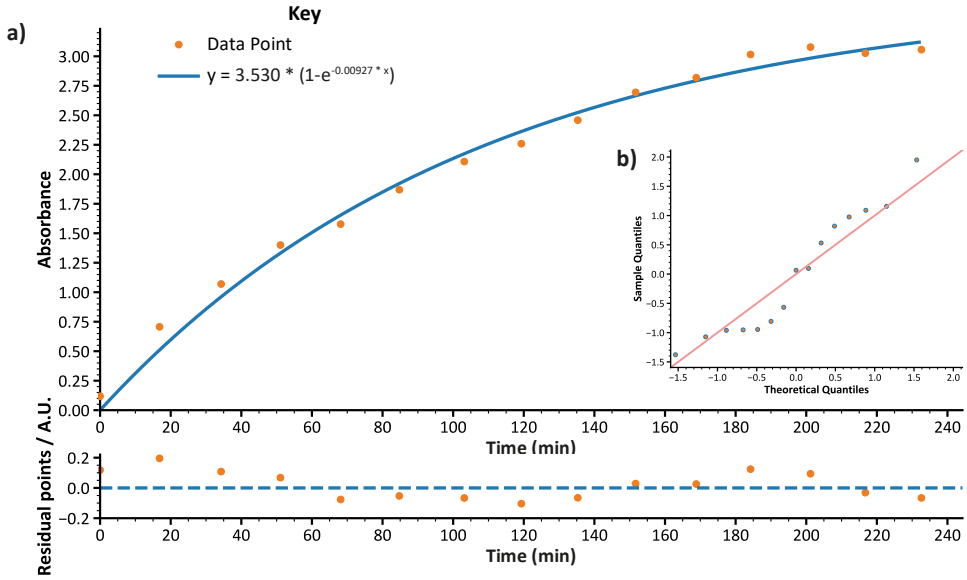

Figure 5.24 - The absorbance over time kinetic plot for the immobilised CBL catalysed formation of benzyl thiol via DTNB coupled UV-vis analysis, using a bead microcolumn reactor, with S-benzyl-L-cysteine [10 mM], a total system volume of 1.5 mL, a flow rate of 150 µL min^{-1} and 20 µL fraction extractions every loop. The curved plot was fitted using NLS regression and analysed using a) residual and b) QQ plot statistical analysis.

The next µ-IMER experiment was performed to quantify the effect of performing inflow biocatalysis of S-benzyl-L-cysteine [10 mM] but at a lower system volume of 1.5 mL (Figure 5.24). Additional parameters of the experiment were a 150 µL min^{-1} flow rate, a 240-second delay between syringe steps, a 500 µL min^{-1} priming flow rate and 3 syringe steps per loop. The curve fitted for determining the rate constant of catalysis gave an R^2 of 0.990, with a narrow and even distribution of residuals around the norm similar to the previous experiment, once more displaying the same pattern. The QQ plot analysis indicated that the normal quartile distribution for the data showed the kinetic model did not fit as well as in the last experiment but still gave a

significant fit overall, with a relatively even total distribution. From the fitted kinetics, a rate constant of 0.00927 min^{-1} was obtained by considering the fitted model, which showed an apparent 18.5 % increase in the reaction rate compared to that of the 3.0 mL total reactor volume system. It was theorised that this observed difference was due to the system limitation of physically pumping the given total system volume through the column for each loop; the kinetics are somewhat limited by the fact that fractions are only taken at the end of a specified number of loop steps, one in the case of all reactions presented in this work. The longer the loop takes, the slower the observed time-dependent reaction rate will be due to a larger volume at the same set flow rate, which will take more time to pass through the reactor column than a smaller volume would under the same conditions.

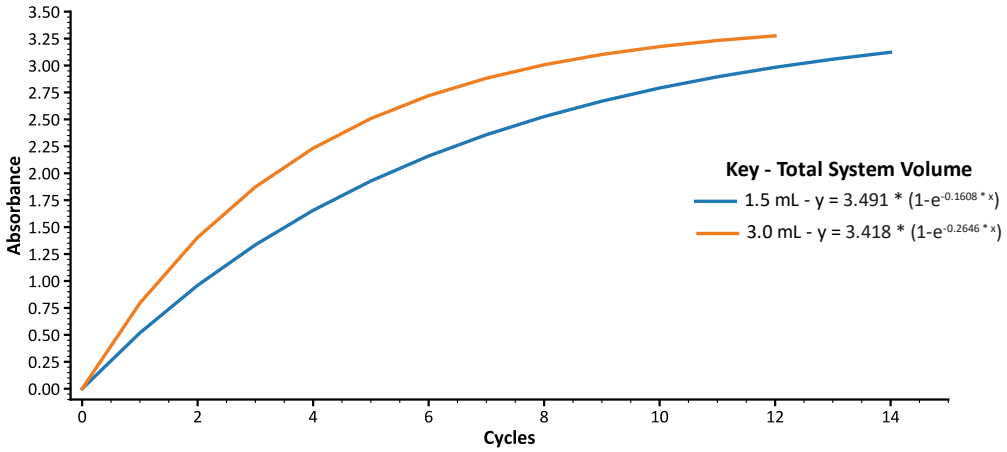

Figure 5.25 - A comparison of how total system volumes of 1.5 mL (blue) and 3.0 mL (orange) varied the kinetic plots for absorbance over cycles for the immobilised CBL catalysed formation of benzyl thiol via DTNB coupled UV-vis analysis, using a bead microcolumn reactor, with S-benzyl-L-cysteine [10 mM] and a flow rate of 150 µL min^{-1} and 20 µL fraction extractions every loop. The curved plots were fitted using NLS regression.

In order to compare the kinetics between the 1.5 mL and 3.0 mL total system volume experiments, the kinetics were plotted as absorbance against cycles (Figure 1.25), which, in theory, would remove the discussed time-based limitation. It would be expected that because potentially influential conditions for kinetics in the experiment, such as analyte concentration, flow rate, reactor volume and temperature, remained constant, the observed kinetics should, in theory, be identical for both experiments. However, this was not the case, and instead, an apparent deviation in the kinetics was still observed, with the 1.5 mL total system volume experiment giving a lower rate constant of 0.1608 $cycles^{-1}$ when compared to that of the 3.0 mL experiment, which gave a higher rate constant of 0.2646 $cycles^{-1}$. The reason for this deviation could result from numerous possible experimental errors, including but not limited to errors introduced by using rubber-plunger syringes at lower volumes, accuracy of the spectrometer and human errors. Due to the system's complexity, disentanglement of these errors is extremely hard to perform based on the limited experimental results collected throughout this work. In order to

more clearly ascertain the origin of this observable difference when different total system volumes are used, further studies would need to be performed, such as the use of online analysis techniques like HPLC with a calibrated internal standard, to remove one possible source of the error and compare the experimental results.

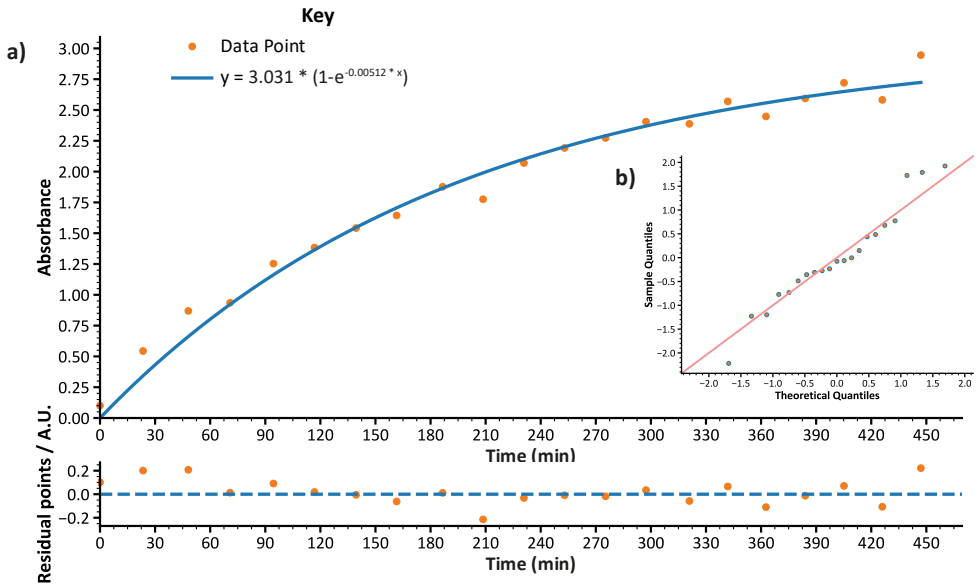

Figure 5.26 - The absorbance over time kinetic plot for the immobilised CBL catalysed formation of benzyl thiol via DTNB coupled UV-vis analysis, using a bead microcolum reactor, with S-benzyl-L-cysteine [8 mM], a total system volume of 1.5 mL, a flow rate of 150 µL min^{-1} and 20 µL fraction extractions every loop. The curved plot was fitted using NLS regression and analysed using a) residual and b) QQ plot statistical analysis.

To obtain insightful biocatalytic parameters such as K_{cat} and V_{max}, Michaelis–Menten kinetic analysis is often applied to the enzymatic system through which these constants can be determined. In order to perform Michaelis–Menten kinetic analysis, the reaction rate for the enzymatic system at various substrate concentrations must first be determined. Therefore, the subsequent comparative inflow biocatalytic experiment was performed using a running buffer containing S-benzyl-L-cysteine at a reduced concentration [8 mM] (maintaining the same 1mM concentration of DTNB), a total system volume of 1.5 mL, a 150 µL min^{-1} flow rate, a 240-second delay between syringe steps, a 500 µL min^{-1} priming flow rate and 3 syringe steps per loop (Figure 5.26). The fitted kinetic model curve gave an R^2 value of 0.980, which was slightly lower than in previous experiments but still indicative of a well-described fit. Residual analysis showed a narrow, even distribution of residuals around the norm and a QQ plot displaying a normal quartile distribution that strongly supports a well-described fit for the experimental data. The kinetic fit gave a rate constant of 0.00512 min^{-1}, 44.8 % slower than that of the same system with a 10 mM S-benzyl-L-cysteine running buffer. The fact that the rate of reaction decreases by such a degree with only a 1/5 decrease in the substrate concentration confirms that the rate of catalysis by the immobilised CBL was the most significant component of the reaction rate monitored using the u-IMER system. Unfortunately, there was not enough time within the scope

of this work to perform more reactions at additional S-benzyl-L-cysteine concentrations to obtain a Michaelis–Menten kinetic analysis of the system. However, the data obtained here indicated that the complete kinetic analysis is obtainable, given further work.

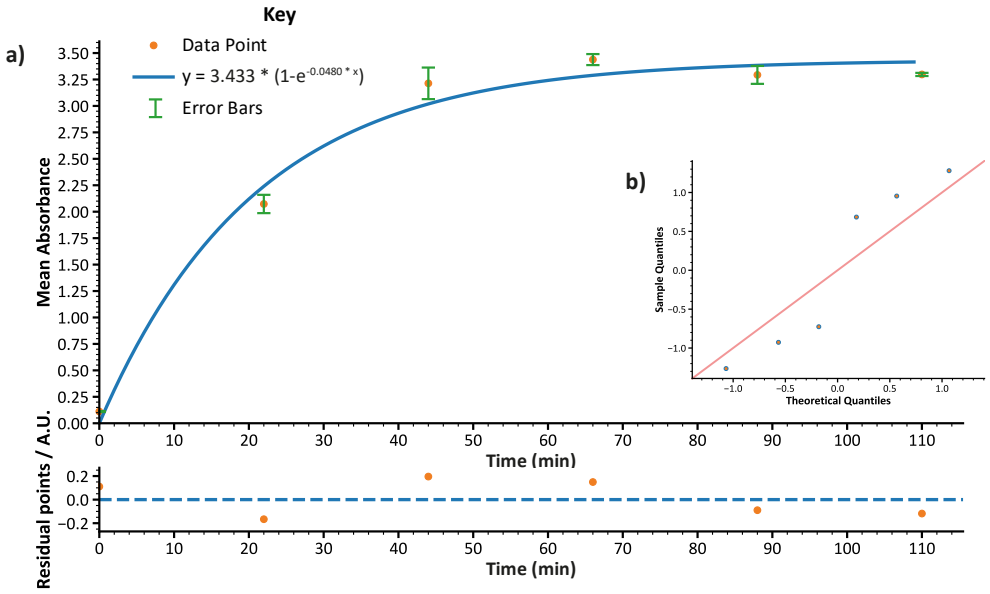

Figure 5.27 - The mean absorbance over time kinetic plot for the immobilised CBL catalysed formation of benzyl thiol via DTNB coupled UV-vis analysis, via free in solution beads shaken at 1000 rpm, with S-benzyl-L-cysteine [10 mM], a total system volume of 3.0 mL, a flow rate of 150 µL min^{-1} and 3 × 20 µL fraction extractions every loop, to determine standard deviation error bars. The curved plot was fitted using NLS regression and analysed using a) residual and b) QQ plot statistical analysis. 0.986

In order to compare the µ-IMER system to an equivalent system not dependent on the inflow looping of the substrate running buffer, an experiment was established where the same 200 µL volume of functionalised beads packed into the reactor microcolumn were instead suspended in S-benzyl-L-cysteine buffer [10 mM] to make up a total system volume of 3.0 mL which was then agitated at 1000 rpm. Every 20 minutes, agitation of the solution was stopped, and the beads were left to settle for 2 minutes. At this point, 3 × 20 µL induvial fraction extractions were taken from the supernatant from the reactor solution and used to obtain a mean absorbance kinetic plot of the unpacked CBL functionalised beads under agitation (Figure 5.27). The kinetic data from this experiment would then provide a point of comparison to the equivalent S-benzyl-L-cysteine [10 mM], 3.0 mL total system volume experiment. The fitted kinetic model gave an R^2 value of 0.986, indicating a robust correlation between the data points and the fit, with the residual analysis showing a comparably narrow and even distribution around the norm to that of the reactor system experiments. The QQ plot analysis showed a more diffuse distribution around the identity line, yet a clear linear trend for the normal quartile distribution, still indicating conformity of the data to the applied kinetic model. Similar to the mean absorbance reactor experiment, the variation in standard deviation, as shown by the error bars, differs significantly from extraction to extraction. From the fitted kinetic curve, a reaction rate of 0.0480

min^{-1} was obtained, which is over five times faster than the reaction rate for the flow reactor system under the same comparable experimental conditions.

The experimental data for the enzymatic reaction not facilitated within the μ-IMER system showed a statistically good fit to the kinetic model used to describe all discussed CBL biocatalytic reactions within this chapter. As the model still described the reaction, despite being facilitated without using the μ-IMER system, it confirmed that the kinetic model matched the CBL biocatalytic reaction and was not just a result of the flow system limitations. Despite confirmation of the kinetic model, the significantly higher rate constant demonstrated by the non-column bound CBL functionalised beads implied that the flow system did have a direct effect on the reaction rate for the established kinetic model. The reactor's effect on the reaction rate was shown throughout the work due to the time required for an entire loop of the total system volume, which limits the reaction kinetics at a fixed flow rate but did not affect the comparison of experiments of differing analyte concentrations, with all other conditions held constant, as was performed. This limitation could be mitigated by increasing the flow rate, which has been highlighted as an area of further work, where the effect of changing the system flow rate for the u-IMER system and the CBL immobilised catalysis is explored.

After successfully demonstrating the viability of the μ-IMER and the inflow CBL-driven biocatalysis of S-benzyl-L-cysteine at various concentrations, exploring additional aspects of this work using the μ-IMER system was possible. The two main areas pursued were testing the CBL enzyme experiments within a planer microfluidic chip reactor for comparison and testing the inflow biocatalysis of the bead microcolumn reactor using the artificial metalloenzyme Gst.

Chapter 6 - Microfluidic Chip Reactor Inflow Biocatalysts

This chapter outlines the design of microfluidic reactor chips used within this research and the approach adopted to systematically and reproducibly fabricate these devices via a bespoke master substrate PDMS jig. Following the production of these chips, this chapter then addresses how the microfluidic chip reactors were integrated into the µ-IMER experimental setup and subsequently used to obtain preliminary results for inflow biocatalytic turnover. Specifically, these studies were made up of preliminary experiments focussed on the biocatalytic production of S-benzyl-L-cysteine within a planar microfluidic chip reactor consisting of a layer of surface immobilised CBL enzyme for a comparative study to the microcolumn reactor.

6.1 - Microfluidic Chip Fabrication

Several design, fabrication, and implementation choices had to be made to successfully implement the microfluidic chip reactor. These include the desired characteristics and features of the device, the method used to fabricate the chip, and how the microfluidic device is sealed and integrated with ancillary fluidic components (e.g. pumps, valves, control system). Multiple fabrication strategies and types of microfluidic devices were investigated to increase the chance of developing a successful microfluidic chip µ-IMER. This subchapter covers the standardisation, fabrication and characterisation of a range of investigated microfluidic devices.

6.1.1 - Standardisation of PDMS Casting

As previously stated, the microfluidic chips exploited here were exclusively fabricated in PDMS as this approach offers fast, consistent, high-resolution, and cheap fabrication of multiple microfluidic chips from a master substrate. An issue commonly observed in PDMS microfluidic devices is the leaking of the fluidics at the interface between the PDMS channels and the underlying substrate. These issues are often attributed to the size scale, high surface area to volume ratios, and high-pressure differentials across the microfluidic chip[273]. Moreover, many PDMS microfluidic chips fabricated in-house suffer from a lack of standardisation, such as chip size and inlet/outlet location, due to them often being cut and punched by hand, and the thickness of the device is dependent on the size of the casting dish and volume used, which can be hard to control. Inconsistencies like these can further exacerbate leaks due to uneven pressure distribution across the chip or a lower-quality seal at the fluidic connection to the inlet/outlet tubing.

In order to minimise these inconsistencies and to give an engineered fit to the chips for integration with ancillary components, such as a microfluidic clamp, it was decided that the size and means of casting the PDMS chips would be standardised across all fabricated master substrates and the subsequent PDMS chips. This standardisation was achieved using a custom-designed and engineered jig for PDMS casting (the original schematic can be found in 8.1 - Appendix 1 - PDMS Microfluidic Chip Jig Schematic). The basic premise of the jig was to create a well-defined cavity, called the casting chamber, of a fixed and known size and thickness above the patterned master substrate. Liquid PDMS could be poured into this casting chamber and cured in situ to create a highly standardised size of microfluidic chip. Additionally, solid metal pins were designed to extend through the cavity defined by the casting chamber at fixed

positions to define the fluidic inlet and outlet points on the cast PDMS chip during the casting process instead of requiring a post-casting hole punch step. The jig was fabricated by technical support staff (Mark Bentley and Becca Neale) within the workshop in the Department of Biology, University of York. The 3D-printed master substrate back plate, master substrates and microfluidic chips were fabricated independently.

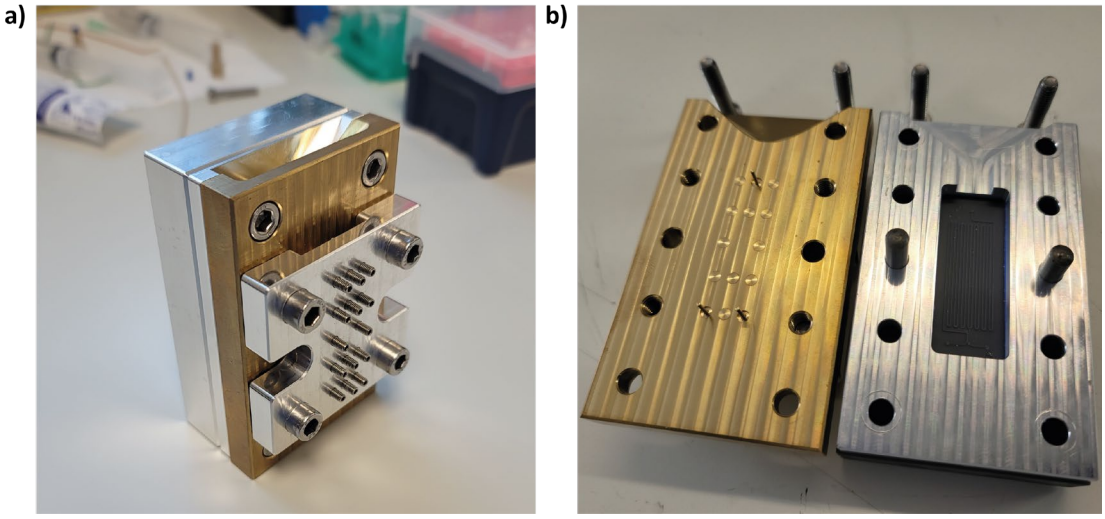

Figure 6.1 - The PDMS microfluidic chip jig was designed to ensure a standardised size for microfluidic chips and incorporate well-defined inlet/outlet holes as part of the casting process. a) The fully sealed mould containing a Si wafer master substrate back plate. b) The internal cavity, with the brass Ø1 mm inlet/outlet and blanking pins on the front plate (left) and the stereolithographic backplate and inserted master substrate (3D printed), sealed via a gasket to the centre plate, the rebate of which determines the thickness of the chip (right).

The jig consisted of three parts that could be slotted together and aligned via guidance pegs. The jig was sealed to make the casting chamber via bolts from the top plate through the centre to threaded holes machined into the back plate (Figure 6.1a). Two varieties of back plates were used, the first for Tough 2000 stereolithographic, 3D printed master substrates (50×20×5 mm) and the second for Si wafer soft-photolithographic master substrates (50×20×0.5 mm). Both plates contained rebates where the master substrate was mounted to ensure it lay flush with the top face of the back plate. A silicon gasket was placed over the edge of the master substrate between the substrate and a back plate to form a seal with the centre plate (Figure 6.1b - right).

Once the device was sealed against the gasket, the centre plate sat almost flush with the top and bottom plate due to a slight recess within the central plate for the gasket. This made each chip cast an almost identical thickness to that of the central plate chip rebate (6 mm), ensuring the casting of standard dimension (49×19×6 mm) microfluidic chips, as defined by the casting chamber. The chip was designed to be this size to fit a standard 75×25 mm microscope slide, with room around the edge of the chip for potential electrode contact points and clamping points and to ensure a clear sealing between the PDMS chip substrate and the mounting substrate. A funnel rebate was placed into the top and centre plate's top section to pour liquid PDMS into the casting chamber. This aperture (10×5 mm) was large enough to allow air to escape from the

casting chamber while liquid PDMS was poured into the mould. The top plate could then be placed onto the centre plate and sealed.

The top plate additionally contained 14 rebated Ø3.2 mm pin holes in which various configurations of inlet/outlet points within the device could be chosen. The master substrate microfluidic pattern was designed with channels that started and ended at points which aligned with the location of one of these pin holes. Corresponding pins could then be placed at these points, which sealed the chamber while extending a precisely engineered pin (Ø1×6 mm) into the casting chamber, contacting the start/end of the channel of the master substrate. If pin holes were not required, the pin holes were blocked with blanking pins to seal the casting chamber (Figure 6.1b - left). Lastly, an additional plate was attached to the top plate (Figure 6.1a), in which individual screws could be adjusted to finger tightness, which clamped the pins, ensuring they did not move during the PDMS baking step. Due to the elastic nature of the PDMS, the uniform and well-defined holes in the cured PDMS chip resulted in a tight seal when standard OD 1/16" (1.5875 mm) tubing was inserted into these ports to integrate the reactor into the flow system.

Following the casting of a PDMS device as per the conditions described in the methods chapter(3.4.1 - Casting of PDMS Microfluidic Chips), the microfluidic chip was removed from the mould, and excess PDMS from the PDMS pouring inlet was removed using a scalpel. The quality and uniformity of the resultant microfluidic chips gave a reliable base for the innovation of a bespoke microfluidic chip clamp, which was then developed and is described later in this chapter.

Using this mould meant the microfluidic devices were required to fit onto a set-sized master substrate within a 49×19 mm area, and the inlet/outlets were positioned at set locations. These conditions did not limit the parameter space for the designs used within this work.

6.1.2 - PDMS microfluidics Cast using Stereolithographic Master Substrates

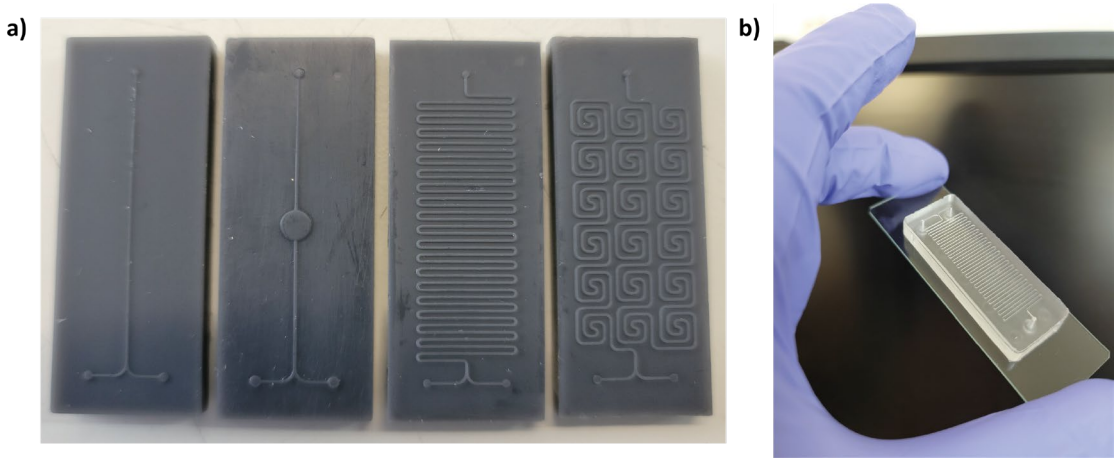

Figure 6.2 - a) Stereolithographic fabricated master substrates of various microfluidic channel designs, all with CAD-specified channel cross-sectional area of 300×300 µm. From left to right: linear channel, linear channel with a circular chamber, serpentine channel and meandros channel. b) a PDMS cast microfluidic chip using the serpentine channel stereolithographic fabricated master substrates.

Once the PDMS casting jig had been developed, it was possible to produce master substrate patterns that adhered to the dimensions of the mould and its potential inlet/outlet pin configuration - the first method of producing master substrates employed stereolithography. In recent years, stereolithography has developed so that numerous 3D printers can achieve a high enough spatial and layer resolution to produce features within the 0.2 - 3.0 mm range. The 3D printer used in this work, a Formlabs form 3+, was quoted to have an XY resolution of 25 µm[274] and a layer thickness of 100 µm for Tough 2000[275] resin, which is the material used here. Despite this, the smallest feature size that could be consistently printed was ca. 300 µm wide with a depth of 300 µm, which remained the standard dimensions used within this work when designing further stereolithographic microfluidic master substrates. Although significantly larger than the minimal achievable features using soft photolithography, stereolithography was a significantly faster means of fabricating wide-channel master substrates, allowing quick prototyping and evaluation of the resultant microfluidic chips.

Four designs of microfluidic reactor chips were developed throughout this work, ranging from a simple linear channel to a much more complicated spiral mixer design that utilised a meandros motif (Figure 6.2a), the design of which is covered in the next section. A 30 µm fillet was applied to the edges at the top and bottom of the serpentine channel feature to help reduce ripping of the PDMS chip after casting, with the knowledge that the achievable resolution of this feature was limited by the resolution limitations of the stereolithographic system. The serpentine channel design was initially chosen as the standard chip for characterising the planer surface chip-based reactor. Serpentine channel microfluidic devices are commonly utilised within the

microfluidic literature, primarily due to their relatively simplistic design and inherent mixing properties due to Dean vortices[276], as discussed within the theory section of this thesis (2.2.1 - What is microfluidics?). Before using the chip as a reactor, both the master substrate and the PDMS chip were characterised to determine the consistency of the fabrication process, including the limitations of the stereolithographic process and the resultant PDMS microfluid chips cast from these masters.

The serpentine master substrate was first imaged using a standard optical microscope to assess the visible surface topography of the channel features. Even by optical assessment, the top surface of the channels displayed a significant degree of surface roughness with clear pitting throughout (Figure 6.3).

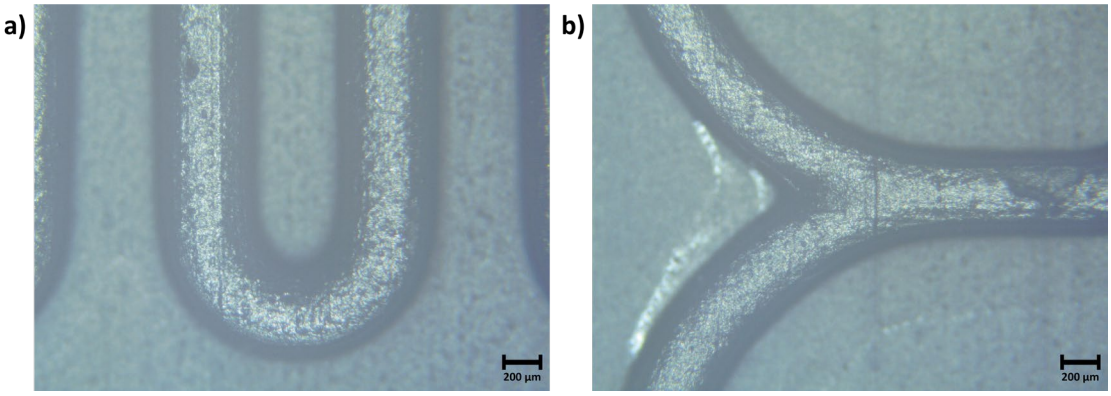

Figure 6.3 - Optical microscope images of the surface features for the Tough 2000 serpentine channel master substrate, outlining a rough surface topography at both a) a u-bend in the channel and b) at the Y-connector junction - images taken at a 5× objective.

In order to determine the step size, which defines the height of the features, the master substrate was analysed using stylus profilometry (Figure 6.4). From the maxima peak height, it was possible to determine the average feature height of the negative channels to be 263.9 ± 4.1 µm. Based on the CAD design, this was approximately 36 µm lower than expected. When profiling the step height, a clear dome was observed leading to the peak maxima, as was determined in the CAD design. Due to the channel height and the stylus having a 2 µm radius and 90° tip angle, obtaining the channel width via stylus profilometry was not accurate. Additionally, the 90° angle of the tip would not account for the surface roughness displayed across these peaks. Therefore, it can be deduced from the stylus profilometry that the channels did have a rough surface topography, as indicated by the optical microscope images, and at the top of the channels, the applied 30 µm fillet resolved as a fully curved arch-like structure.

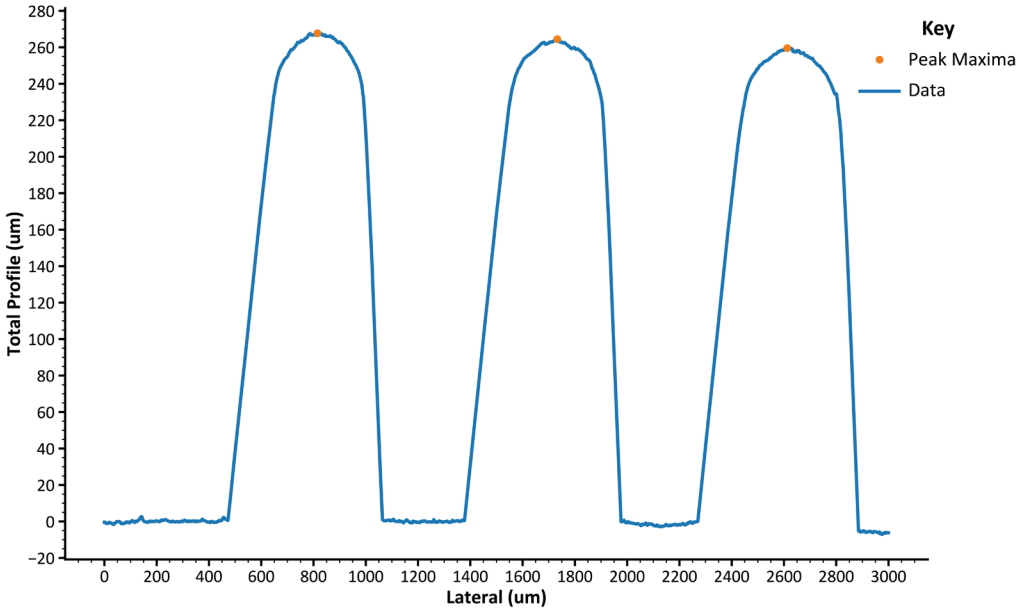

Figure 6.4 - Stylus profilometry of the Tough 2000 serpentine channel master substrate: The scan direction was perpendicular to that of the channels across the middle section of three channels. The peak maxima gave an average feature height of 263.9 ± 4.1 µm.

Following the characterisation of the master substrate, a PDMS chip was cast using the aforementioned jig. The initial PDMS chip was plasma oxygen bonded to a standard glass microscope slide according to the procedure outlined in the method section (3.4.1 - Casting of PDMS Microfluidic Chips) to form a sealed microfluidic device for fluidic testing. Due to the elastic nature of PDMS, it was not possible to perform stylus profilometry on any cast PDMS chip, as the stylus tip readily catches on the surface, even at the lowest applied pressure, which can potentially cause damage to the stylus, as well as erroneous readings.

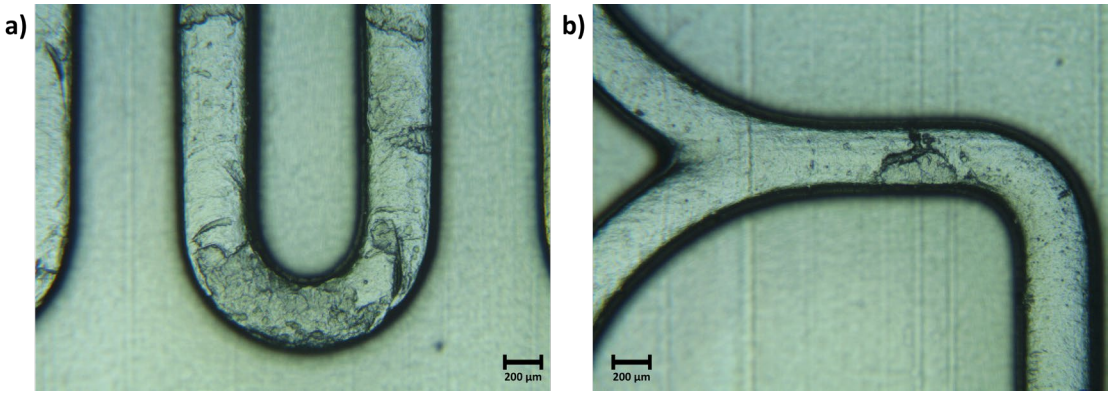

Figure 6.5 - Optical microscope images of the 300.6 ± 21.1 µm wide serpentine channel PDMS chip, outlining how the rough surface topography transferred from the master substrate to the device a) a u-bend in the channel and b) at the Y-connector junction - images taken at a 5× objective.

With a standard optical microscope, it was possible to observe significant surface roughness within the channels of the PDMS chip (Figure 6.5). Notable sections of the channel showed deterioration of the feature edges and faces, with an overall lack of smoothness across the length

of the channel's topmost face. An approximate channel width, calculated from optical microscope images, of 300.6 ± 21.1 µm was determined from an averaged value of user-drawn lines, giving an average width close to what was expected from the initial CAD design but with a high standard deviation in width.

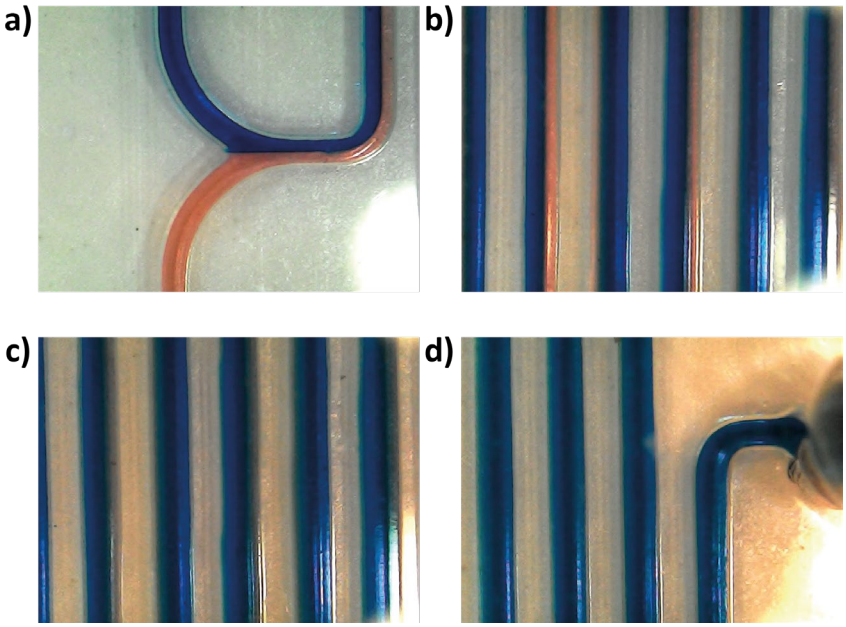

Figure 6.6 - Simple demonstration of the laminar flow of the 300 um serpentine channel PDMS microfluidic chip, with the gradual mixing of the two coloured dyes via Dean's vortices induced from the serpentine channel u-bend features. a) the laminar separation at the inlet y-connector junction, b) the rotation of the laminar separation, c) complete mixing observed slightly over halfway down the length of the channel and d) the fully mixed outlet.

The rough surface topography of the PDMS microfluidic chip, combined with the curved profile of the topmost channel, affects the overall flow profile, potentially increasing chaotic mixing within the fluidic channel. To confirm the flow profile within the microfluidic chip and to ensure that mixing did occur within the serpentine channel, two coloured dye solutions made using mQ water were pumped into the two inlets of the device at 75 µl min^{-1}, and the resultant flow was imaged optically using a digital camera (Figure 6.6). Upon the two solutions meeting at the Y-connector junction, the two flow streams remained segregated, as would be expected for the fluidic system in the laminar flow regime (Figure 6.6a). The separation of the two flow streams continued over several turns of the serpentine channel, with the visibility of the red dye stream alternating between channel loops (Figure 6.6b), which indicated the stream's rotation through the Dean vortices induced at the U-bends of the channel. At six turns of the serpentine channel, any observable presence of the red stream was lost (Figure 6.6c), indicating the efficient mixing of the two solutions.

For this system, the Reynolds number for the overall flow profile could be calculated using the Reynolds equation (2.8), with a flow rate of 75 µl min^{-1} and the assumption that the density (998.2 kg m^{-3}) and dynamic viscosity (1.002×10^{-03} Pa·s) of the dye solution was approximate to

water at 20 °C, given that it makes up the bulk solvent of this solution. Therefore, the Reynolds number of this serpentine chip was 4.153 ± 0.273, which strongly indicates the flow to be laminar, which agrees with the observed initial diffusion limited flow profile of the two dyes entering the chip (Figure 6.6a).

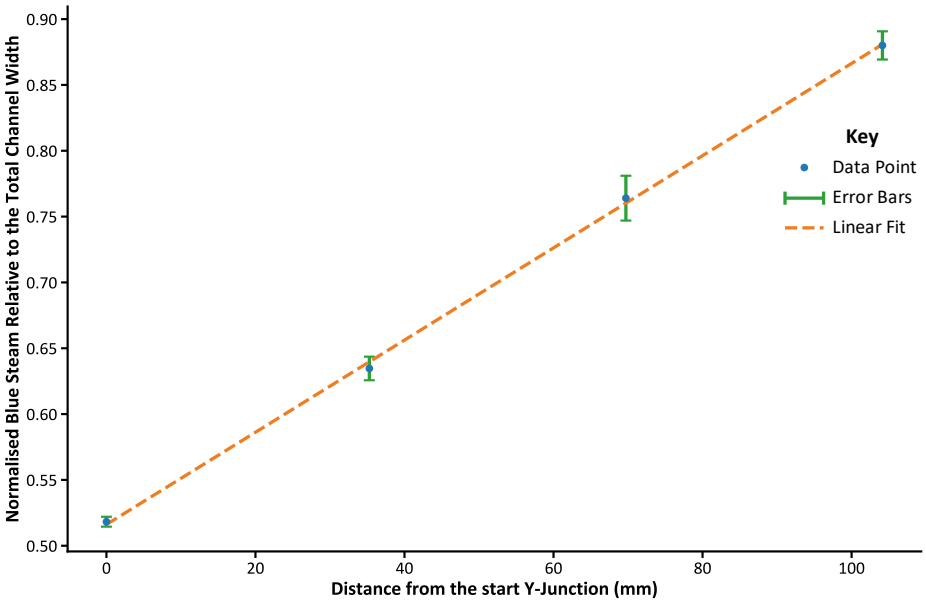

Figure 6.7 - The blue dye stream normalised in relation to the combined width of the blue and red steams at discrete distances along the channel path, with a linear fitting that gave an R^2 of 0.9994. The data points were calculated at the same central point of every other channel based on a manual analysis of the digital camera images.

Using this Reynolds number, it was then possible to calculate Dean's number, which gives a quantitative metric for the degree of secondary flow profile Dean's vortices forming in the device and, therefore, the expected degree of mixing. Assuming that the channel's curvature is taken as the central point of the cross-sectional area, which for this serpentine chip design was 450 µm, the Dean's number was calculated as 3.391 ± 0.114, using Dean's equation (2.11). For this value, a moderate degree of Dean's vortices would be expected for a microfluidic chip of this geometry, meaning for each exposure of the flow to these 180° hairpin bends, a rapid increase in the passive rate of mixing would be expected to occur. It was possible to calculate a normalised value for the blue dye stream in the observed laminar pattern using the digital images of this chip (Figure 6.6), with respect to itself and the red stream, to show how, over distance, the two streams mix to form a homogenous coloured stream. Due to the rotation of these streams, values could only be determined for every consecutive loop of the serpentine channel. They were calculated at the very mid-point of each and recorded as the path length from the start of the channel after the Y-connector junction. This data, shown in Figure 6.7, reveals a clear linear trend, showing a highly quantifiable increase of the predominate blue dye stream as the two

solutions mix. The fact that this mixing is linear demonstrates that the curved hairpin bends and the resultant Dean's vortices induced are the predominant source of the mixing, as predicted by the Dean's number.

6.1.3 - Meandros Pattern Master Substrate and Microfluidic PDMS Chip Fabrication

In addition to simple linear and serpentine channels, additional and novel chip designs that varied in function according to their geometry and cross-sectional area were also fabricated. Inspired by the literature, a possible novel design for a chip that would create a higher Dean's number flow to utilise primary and secondary Dean vortex flow profiles was considered. The theory behind innovating such a microfluidic chip was that through these additional flow profiles, a greater degree of non-chaotic convection currents within the flow would be created, increasing the bulk diffusion rate to and from the enzyme surface. Developing such a design meant that if the observed rate of biocatalysis for the planar surface chip reactor was limited due to the rate of diffusion, the new design would show a difference in reaction rate, improving the system and demonstrating a limitation of the simple linear and serpentine channel design.

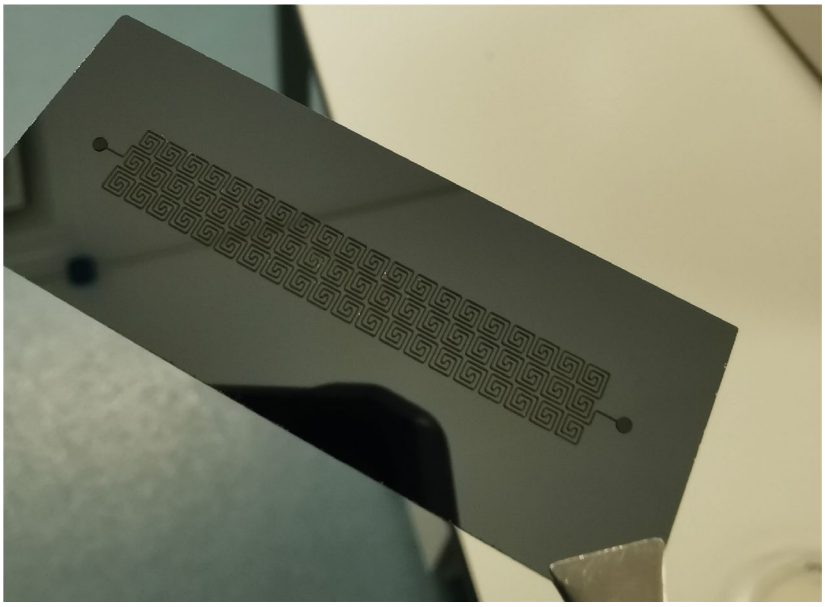

Figure 6.8 - One of the Ø 100 um meandros channel master substrates, produced in SU-8 photoresist on a Si wafer substrate. An additional version with an identical design, except having two inlet channels merging into a y-connector junction.

The chosen design was that of the meandros motif, a pattern commonly used in Greek and Roman architecture and pottery. The design comprises a repeating inward and outward pattern of spirals, each consisting of straight sections, 90° angles and a switchback at its centre. This pattern was hoped to achieve a more extreme form of non-chaotic convection current to increase the bulk transfer advantages of a spiral micromixer with a longer resident time and the use of a more space-efficient pattern. The master substrate was produced using the SU-8 soft-photolithography fabrication method discussed within the methods section (3.3.1 - Soft Photolithography), which required significant optimisation to achieve a device of this complexity

and thickness of resist without issues arising during the development step. Two varieties of Meandros pattern devices were produced with identical central channel patterns, but with one containing a single inlet and outlet (Figure 6.8), while the second contained a single outlet but two inlets merging into a Y connector junction (Figure 6.9a & b).

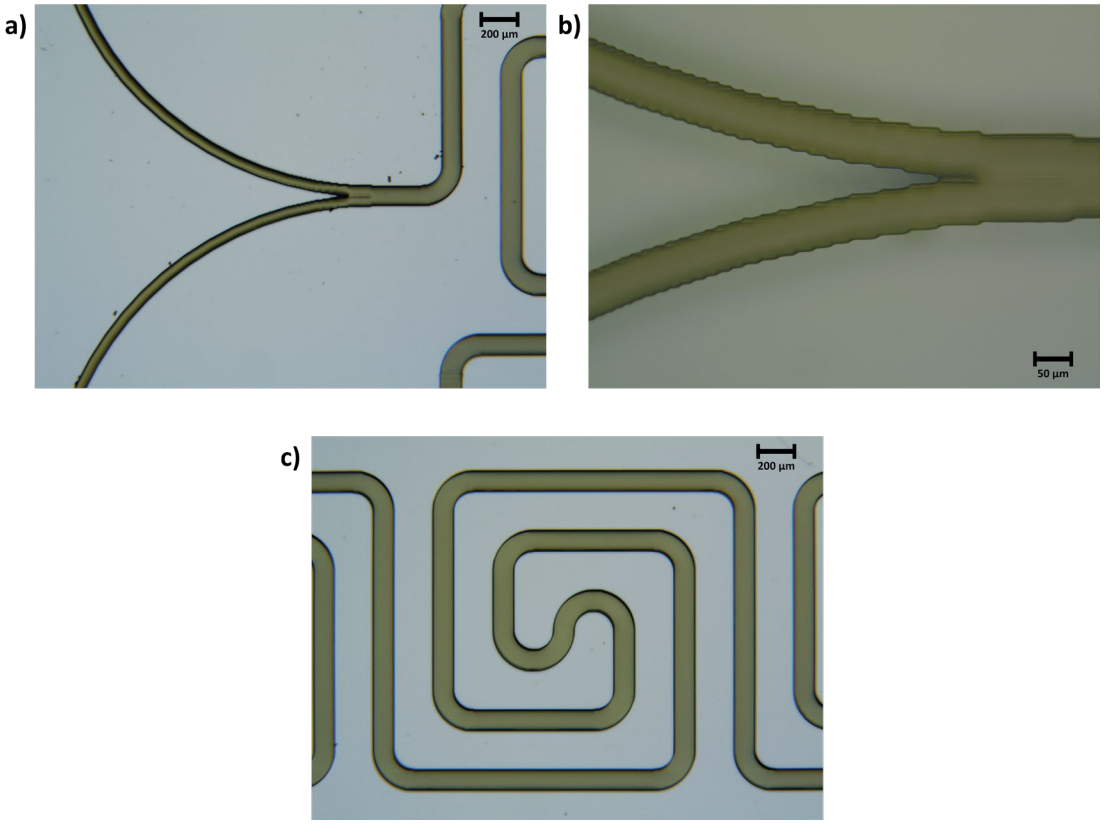

Figure 6.9 - Optical microscope images of the surface features for the SU-8 meandros channel master substrate, at a) & b) the Y-connector junction and c) at a central meandos feature - a) & c) taken using a 5× and b) using a 10× objective lens.

Following the fabrication of the meandros master substrate, the surface was imaged using an optical microscope. Observation of the Y-connector junction showed a stepping feature along the walls of the 50 µm wide inlet channels (Figure 6.9a & b). This stepping feature is a facet of direct laser writing and is due to the movement of the stage relative to the optical beam in linear steps to create the channel curvature. In order to mitigate this aberration, a second optical exposure following the contours of the pattern could have been used. However, the overall effect of such a pattern on the flow profile was deemed minimal due to the laminar nature of the regime. A similar deviation within the corners of the meandros pattern was not observed; instead, the ideal 90° angles within the meandros pattern were well-defined, as were the remaining elements of the master substrate channels (Figure 6.9c).

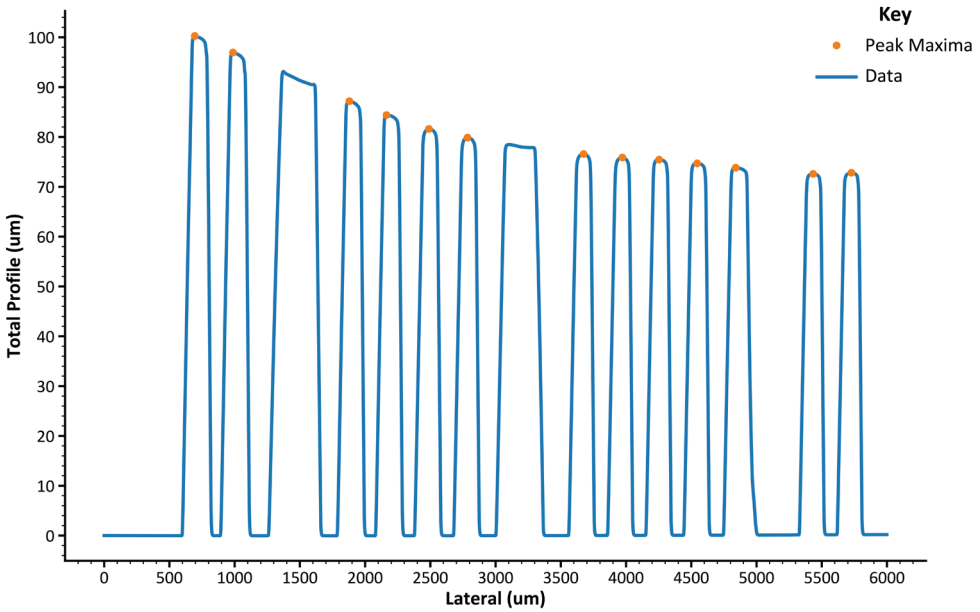

Figure 6.10 - Stylus profilometry of the SU-8 meandros channel master substrate the scan direction perpendicular to the channels, indicated by the thinner width peaks, with the thicker corresponding to sections of the central u-bend channel.

Stylus profilometry was again used for feature step height profiling. The measurement was taken with a 6000 µm lateral scan, which ran from the outer edge of the pattern into the centre, across the middle of several meandros motifs (Figure 6.10). It is clear from the observable decrease in channel height over the lateral scan towards the centre of the design that the channel height lacked uniformity across the device resulting from the fabrication process. The cause of this non-uniformity was isolated to the spin coating process. When using SU-8 to achieve a thick resist layer on a rectangular substrate of this size, the rate at which resist is lost across the surface area of the substrate differs according to the distance from the axis of rotation. This difference in rate leads to a beading of photoresist around the edges of the substrate, where it collects after flowing along the surface from the centre. This beading effect leads to the non-uniform thickness observed within the master substrate, where the outermost features are thickest, decreasing to a more uniform but reduced thickness towards the centre. Considering just the central features of the device, where the thickness was significantly more uniform, the channel height was 72.7 ± 0.1 µm, showing good uniformity in the channel height. Despite the lack of uniformity across the overall chip, the approximate total internal volume of the chip could still be calculated at 18.7 µl using the average channel height of 80.9 µm across all device areas. The effect that the non-uniform height may have on the desired non-chaotic convection currents was complex to predict and was deemed an element that would benefit from rigorous experimental flow profiling and simulations. Initial work on testing an alternative lamination method of applying comparative photoresist to SU-8 was started, hoping to mitigate the non-uniform channel height

entirely. This work, however, was never utilised due to the time restraints of the project. Initial findings are discussed in the chapter on further works.

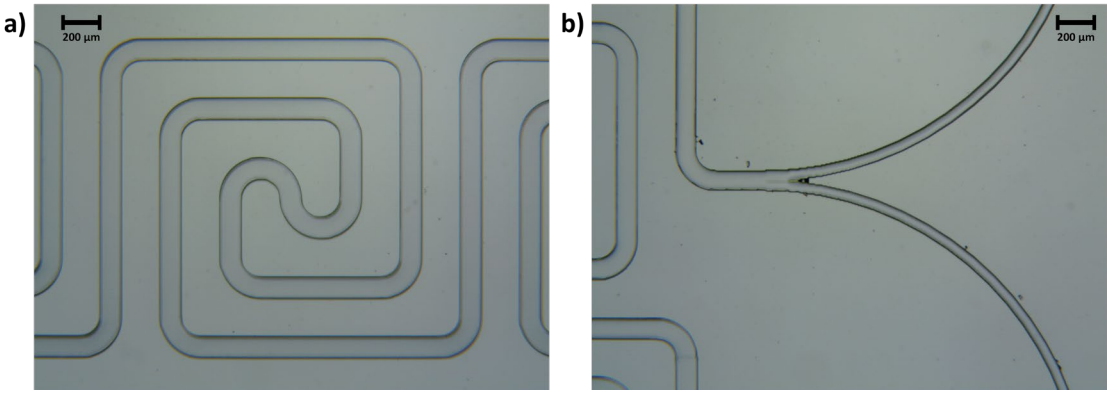

Figure 6.11 - Optical microscope images of meandros channel PDMS chip, at a) 106.5 ± 1.4 µm wide channel central meandros pattern and b) the Y-connector junction with half standard width inlet channels - images taken at a 5× objective.

Following the successful fabrication of the meandros pattern master substrate, a PDMS chip was cast per the instructions in the methods section (3.4.1 - Casting of PDMS Microfluidic Chips). The microfluidic chip was subsequently plasma oxygen bonded to a standard microscope slide glass substrate, as outlined within the method section. Imaging the microfluidic chips channel structure at the PDMS and glass substrate interface showed the channel width to be approximately 106.5 ± 1.4 µm (Figure 6.11). This result was slightly wider than the desired feature width of 100 µm, likely due to a slight overexposure or overdevelopment during the direct laser writing process. The overall uniformity and topology of the PDMS chip were of high quality, with no other visible defects or inconsistencies compared to the original CAD design.

One of the desired outcomes of this work was to test the meandros microfluidic chip against that of a similarly dimensioned serpentine channel chip as a reactor within the µ-IMER system and to evaluate the comparative effects of this novel chip design on the observed reaction rate. Although the sealed device was checked to confirm the viability of the chip to support the continuous flow of PBS buffer at a flow rate of 75 µL min^{-1} without leaking, unfortunately, due to time restraints, the meandros chip was never tested for inflow catalysis purposes but remains an area of future work.

Additional characterisation of all microfluidic chips produced within this work, such as determining the cross-sectional flow profile of the chips at given points in the channel using dyes and confocal microscopy, is also a point of further work. Through performing this characterisation, it is hoped that a greater understanding of how the flow profile could affect the mass transfer of substrates and products to the immobilised enzyme surface will be achieved.

6.2 - In-Flow Biocatalysis in a Planar Surface Microfluidic Chip

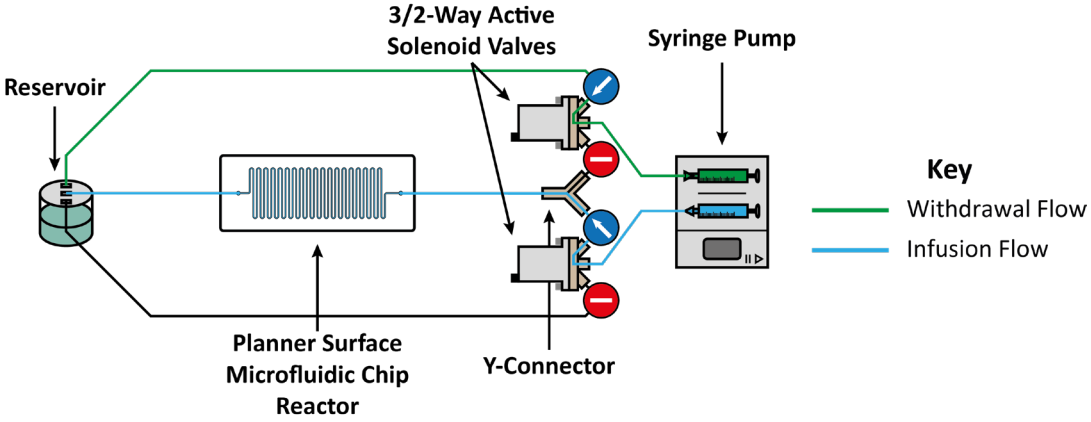

Figure 6.12 - Schematic of the planner surface microfluidic chip reactor µ-IMER system used in this work, where the infusion path of flow through the reactor is represented in blue, and the withdrawal path of flow from the fluid reservoir is represented in green. At the end of a syringe step, these would then invert.

In order to compare the catalytic rates of enzymes immobilised within the bead microcolumn and within a planar surface microfluidic chip reactor (Figure 6.12), a means of non-destructively and reliably forming an enzyme-functionalised microfluidic chip reactor needed to be established. Functionalisation of the 75 × 25 mm Au-on-Si mounting substrate with CBL enzyme was performed using the procedures detailed within the methods chapter (3.4.4 - Lipoic Acid Self-Assembled Monolayer (SAM) Procedure & 3.4.5 - Ni regeneration of the LA-NTA SAM and His-Tagged Enzyme Immobilization Procedure).

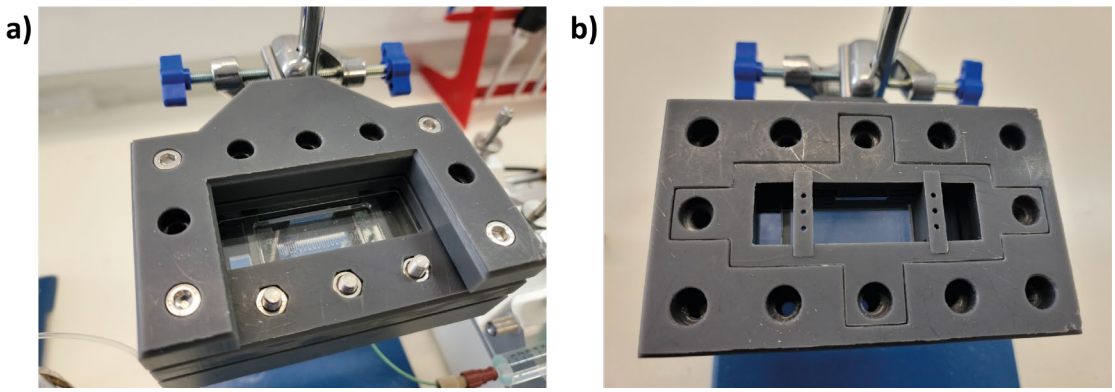

Figure 6.13 - The bespoke microfluidic clamp design for holding microfluidic chip reactors created in this work. The clamp provided an evenly distributed pressure across the chip via its contact with the top and bottom viewing ports. It also included guiding holes for the connecting tubing and the ability to integrate electrode contact points that could interface with the mounting substrate surface at a later date.

The method for forming a sealed microfluidic device described within prior sections of this chapter, namely plasma oxygen bonding, was not a viable option for the creation of the microfluidic chip reactor as the ashing process would damage the immobilisation chemistry and the immobilised enzyme bound to the mounting substrate. For this reason, a clamp was designed and manufactured to hold the PDMS chip and the surface of the enzyme-functionalised

mounting substrate together. The clamp ensured an evenly distributed force across the chip to form a sealed microfluidic reactor chip without the risk of leakage but not so much force that the fluidic channels would collapse.

In order to achieve this systematic and reliable clamping of the microfluidic chip, a bespoke clamp was developed specifically for the size and design of the PDMS chips and mounting substrates used within this work (Figure 6.13). The clamp consists of two sections. The lower section contained a rebate where the mounting substrate could sit securely on a piece of transparent acrylic. Holding clips were placed across the substrate to secure and indicate where the PDMS chip should be placed. After carefully placing the PDMS chip in the indicated location, the upper section of the clamp was aligned to the bottom half via its corresponding outer lip. The upper section sat directly on top of the PDMS substrate via a second transparent acrylic plate, such that when the two sections were tightened together using eight M6 bolts positioned around the rim of the device, the clamping pressure was applied directly to the PDMS chip, forming the sealed reactor. One of the most common causes of leakage in clamped PDMS microfluidic devices is the magnitude and uniformity of the applied clamping force. Too much pressure and the resulting high internal channel pressure can deform the channel walls, leading to leaks; if too low, then the device will not properly seal, causing it to leak upon building internal channel backpressure, and if not distributed uniformly, the pressure differential across the chip can lead to leaking at regions of low clamping force. In order to avoid these issues, the eight evenly distributed M6 bolts around the edge were tightened using a torque screwdriver to ensure all were fastened with equal torque. Experimental trials determined that a torque of 0.05 Nm was optimal to seal the reactor securely without leakage at the flow rates used in this work.

The transparent acrylic central panels allowed the user to observe the fluid flow from the top or bottom face, depending on the transparency of the mounting substrate. The design also included guiding holes for the 1/16” OD PEEK tubing to connect the reactor to ancillary fluidic components, ensuring continued parallel insertion into the PDMS chip. This connection point is often another typical means of leakage in microfluidic chips but was avoided in this work by using the tight sealing pre-cast inlets/outlets, along with the tubing being held in the parallel insertion orientation, which ensured a much more stable connection.

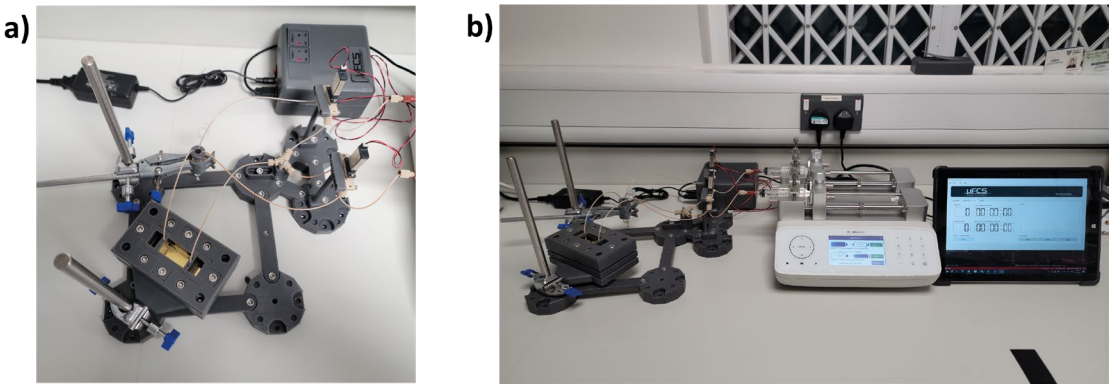

Figure 6.14 - A picture depicting the actual microfluidic chip reactor setup used within this work. a) A top-down view of the clamped microfluidic chip reactor and how it was integrated via peek tubing into the other ancillary components of the reactor. b) the overall view of the reactor system with a clamped microfluidic chip reactor.

Once the enzyme functionalised planner surface microfluidic chip was successfully clamped and the inlet/outlet tubing inserted, the reactor could be integrated into the µ-IMER system (Figure 6.14). The configuration of this setup followed an identical structure to that of the microcolumn reactor setup, except for the reactor itself being exchanged for the microfluidic chip reactor (Figure 6.12). Additional flow setup components were securely held using the 3D-printed scaffold system, demonstrating how its modular design allowed an easy way of adapting the configuration to accommodate the chip reactor instead of the microcolumn reactor.

6.2.1 - Microfluidic Chip µ-IMER Experiment using the LA-NTA SAM

The 300 µm serpentine channel microfluidic chip was used for the fluidic element of the initial planer surface microfluidic chip reactor, with an Au-on-Si mounting substrate functionalised with CBL enzyme using the LA-NTA SAM functionalisation procedure outlined within the method section (3.4.4 - Lipoic Acid Self-Assembled Monolayer (SAM) Procedure & 3.4.5 - Ni regeneration of the LA-NTA SAM and His-Tagged Enzyme Immobilization Procedure). The experimental conditions for this µ-IMER experiment are as follows: The standard reaction buffer was prepared as outlined

within the method section (3.4.6 - Preparation of the Standard CBL µ-IMER Running Buffer) with S-benzyl-L-cysteine [10 mM], a total system volume of 3 mL, 3 × 20 µL extractions per loop, a system flow rate of 150 µL min^{-1}, a 120-second delay between syringe steps, a priming flow rate of 500 µL min^{-1} and three syringe steps per loop. The system was flushed thoroughly with a reaction buffer before priming and initiating the experiment.

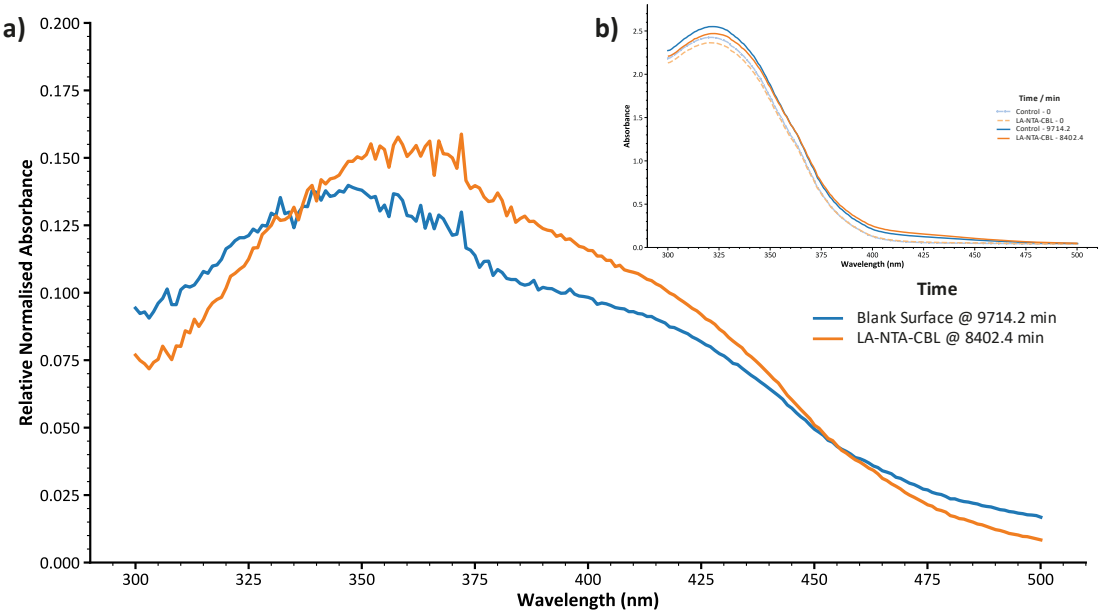

Figure 6.15 - a) Subtraction of the UV-spectra of the analyte solution at 0 mins with no exposure to the surfaces (b - dashed lines) from that of the analyte solution after 6 days of continuous flow exposure to the surfaces, where one spectrum is for blank Au-on-Si mounting substrate (blue) and the other is for the CBL functionalised LA-NTA Au-on-Si mounting substrate (orange). b) Original unsubtracted spectra. The spectra were obtained with a 1 nm scan resolution.

At 6.5 hours into the experiment, the reaction rate was notably slower than that of the previous microcolumn reactor, and a significant colour change in the reaction buffer was observed, which had not occurred during the chip reactor experiment. Therefore, it was clear that monitoring the formation of the product via the microfluidic reactor would require a significantly longer

experimental timescale. In order to ensure the integrity of the scientific method, a control experiment was additionally performed under the same experimental conditions but with an unfunctionalised Au-on-Si substrate, which had undergone only the piranha cleaning protocol. Fractions were taken after day 1, day 2 and day 6 of continuous running. After day 6, a 1.50×10^{-2} AU increase of the TNB product peak at 406 nm was observed for the CBL functionalised reactor. However, the substrate peak at 332 nm did not decrease as expected but instead increased by 8.43×10^{-3} AU (Figure 6.15 - orange line). It should be noted that this peak occurs at a wavelength where the signal-to-noise ratio is poor, making accurate quantification challenging. To contextualise these results, the equivalent microcolumn experiment (Figure 5.23) for the first sample taken at 34 minutes increased at 406 nm by $0.903 \pm 5.88\times10^{-3}$ AU and decreased at 332 nm by $0.397 \pm 2.93\times10^{-3}$ AU, showing both results to be orders of magnitude smaller after six days of recirculated flow in the chip reactor compared to that of the column reactor.

Additionally, an increase in the overall profile across both the product and reactant peaks was seen for the enzyme-free control experiment, albeit with a smaller increase at the 406 nm TNB product peak region than that of the CBL functionalised reactor experiment. From the significantly faster reaction rates observed in the microcolumn reactor experiments, it could be determined that the increase in absorbance recorded within these planer surface microfluidic chip reactor experiments comparatively only captured the initial reaction rates. For this reason, fitted kinetics for both the control and the CBL functionalised microfluidic chip reactor were modelled as a linear relationship under the assumption that the initial rate of reaction follows a linear trend often assumed in enzymatic kinetic plots[277].

The kinetic analysis of the absorbance at 406 nm over time across four fraction extractions for the control surface (Figure 6.16) gave a fitted linear regression with an R^2 value of 0.902. Residual analysis displayed a deviation from the fitted trend across the first three data points, with the last data point aligning closest to the norm. QQ analysis indicated a diffuse but linear quartile distribution, but it is hard to draw more conclusions from only four data points.

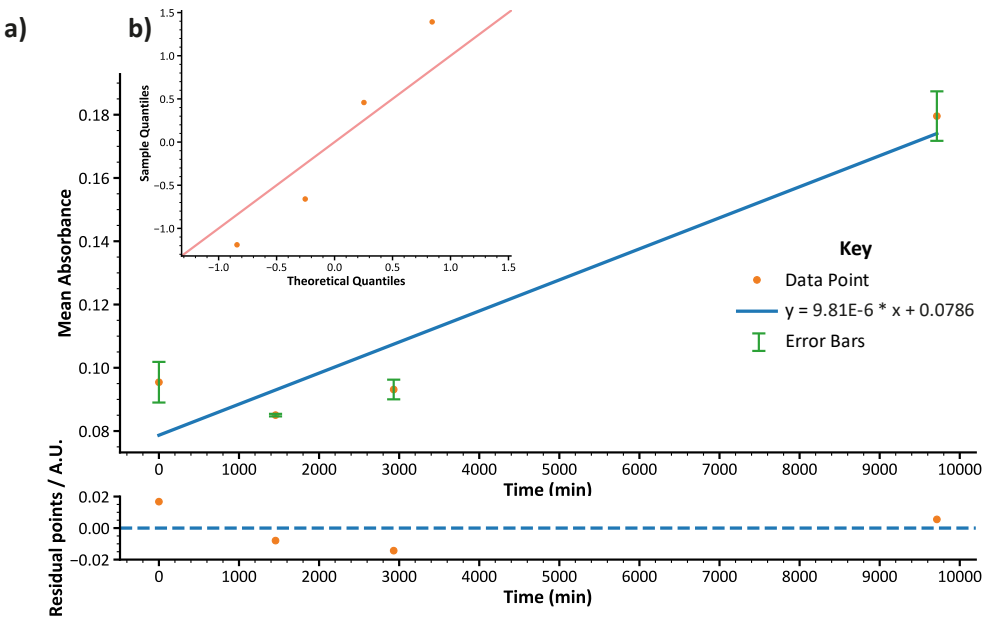

Figure 6.16 - The absorbance over time kinetic plot for the blank Au-on-Si substrate for a control experiment of benzyl thiol formation via DTNB coupled UV-vis analysis, using a planer surface serpentine microfluidic chip reactor, with S-benzyl-L-cysteine [10 mM], a total system volume of 3.0 mL, a flow rate of 150 µL min^{-1} and 3 × 20 µL fraction extractions every loop. The curved plot was fitted using OLS linear regression and analysed using a) residual and b) QQ plot statistical analysis.

Critically, the control plot revealed no change in the absorbance at 406 nm for approximately the first 3000 minutes; the increase was only apparent at approximately 9700 minutes with a marginal increase of $8.41\times10^{-2} \pm 1.14\times10^{-3}$ AU. Although this did not entirely rule out evaporation as a cause for the increased absorbance across the entire spectrum, as evaporation would show a slow increase in absorbance as a function of time, the data suggested that the major contributor to the increase in absorbance at 406 nm at approximately 9700 minutes is likely due to decomposition of DNTB into other compounds which result in the overall increased absorbance.

The kinetic analysis of the absorbance at 406 nm across four fraction extractions for the CBL functionalised Au-on-Si surface (Figure 6.17) revealed a fitted linear regression with an R^2 value of 0.980, which is comparatively higher than that of the control sample, indicating a better fitting of the data to the applied linear regression. The residual analysis also displayed less deviation from the norm across the data, further supporting a more closely fitting relationship than the control plot. QQ analysis indicated a similar pattern in the diffuse but linear quartile distribution.

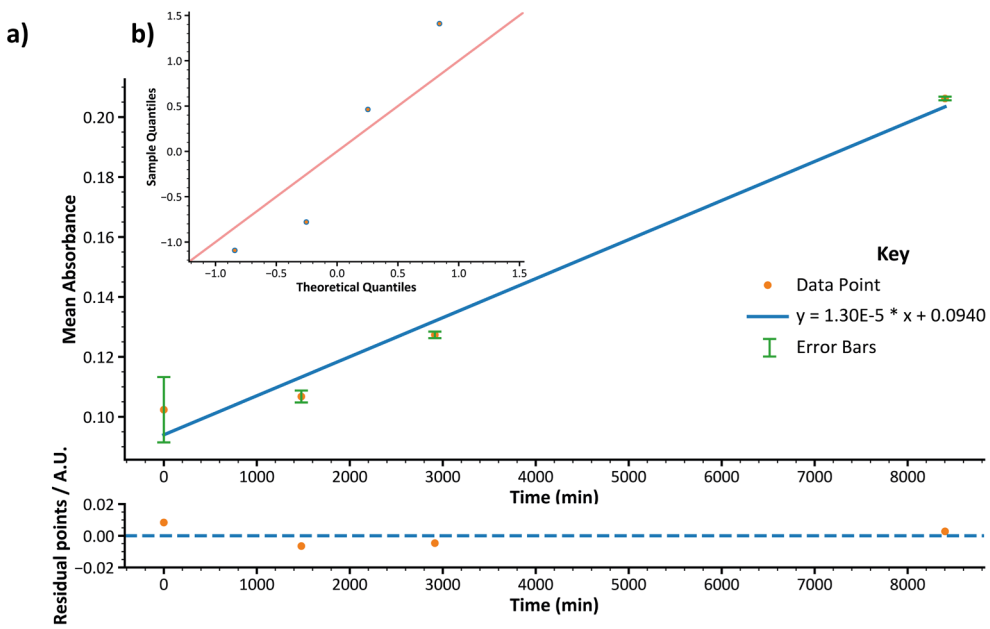

Figure 6.17 - The absorbance over time kinetic plot for the immobilised CBL substrate for the catalysed formation of benzyl thiol formation via DTNB coupled UV-vis analysis, using a planer surface serpentine microfluidic chip reactor, with S-benzyl-L-cysteine [10 mM], a total system volume of 3.0 mL, a flow rate of 150 µL min^{-1} and 3 × 20 µL fraction extractions every loop. The curved plot was fitted using OLS linear regression and analysed using a) residual and b) QQ plot statistical analysis.

Due to the overall profile of the UV-Vis spectrum also increasing in the CBL functionalised experiment (Figure 6.15), the final peak likely has some contribution from decomposition and evaporation. Despite this, the rate constant of 1.35×10^{-5} min^{-1} for the CBL functionalised surface was more significant than that of the control (pseudo-rate constant of 9.81×10^{-6} min^{-1}) and an increasing, linear absorption at 406 nm within the first 3000 minutes, which was not observed with the enzyme-free control. The simplistic comparison of the difference in start and end point showed that the increase in absorption at 406 nm for the functionalised surface substrate was still only $0.104 \pm 9.40\times10^{-3}$ AU, only 1.97×10^{-2} AU higher than for the blank substrate. This difference indicates that if catalysis occurred within the microfluidic chip reactor, it was undetectable within the experimental errors and would still be three orders of magnitude slower than the column reactor under the same reaction conditions (reaction rate of 0.0480 min^{-1}).

The surface area of the functionalised chip exposed within the microfluidic serpentine design was calculated to be 8.13 cm^2. When using the calculated CBL surface coverage acquired on the QCM-D studies, the approximate number of enzymes present within the microfluidic chip reactor is 5.6×10^{12} molecules. Considering that within the microcolumn reactor, an approximate value of 8.3×10^{15} molecules was calculated for the number of CBL enzymes present within the reactor, it is unsurprising that a potentially undetectable amount of biocatalysis was observed within the planer surface microfluidic chip reactor. Despite this, several more optimisations can be made to the microfluidic chip reactor that could increase the rate of reaction, which will be considered in the section on further work.

Chapter 7 - Conclusions and Outlook

7.1 - Summary and Conclusions

To summarise the work presented in this thesis, the key findings and achievements have been structured by addressing each of the initial goals outlined in 1.2 - The Goals of this Work and highlighting where further work is required.

Immobilisation strategies capable of anchoring His-Tag containing enzymes and protein structures to solid surfaces were critical objectives to progress further aspects of the work. Two main strategies were pursued. The first strategy was built on the diazonium electrografting of a protected benzylamine species. The resulting dendritic multilayer could then be cleaved via the amine deprotection to leave a near-monolayer of phenylamine groups, para to the immobilised bond. As part of this work, the electrografting procedure was optimised, and the successful immobilisation of redox-active ferrocene groups via NHS-Ester coupling chemistry was experimentally demonstrated, giving an estimated surface coverage of $3.29\times10^{14} \pm 1.95\times10^{13}$ molecules cm^{-2}, surpassing similar electrografted chemical immobilisation strategies which demonstrated 1.51×10^{14} molecules cm^{-2} reported by Yates *et al.*[172] and 2.41×10^{14} molecules cm^{-2} reported by Bellare *et al.*[20]. The amenability of this surface for further functionalisation was also demonstrated through the production of a terminal maleimide functionalised surface. The development of these procedures and their characterisation contribute on their own to the wider field of surface functionalisation chemistry and aid in the progression of others' work in pursuing various immobilisation strategies from the foundations provided in this work. Despite the electrografting strategy reliably producing a robust and densely packed near-monolayer, the strategy was ultimately abandoned due to the time-consuming and hazardous nature of the procedure. A faster and safer functionalisation method was established to progress further aspects of the work.

The second immobilisation strategy utilised gold-thiol bonding interactions to form a self-assembled monolayer (SAM) on the surface of a gold-coated substrate, using a lipoic acid and nitrilotriacetic acid terminated molecule (LA-NTA). The resulting LA-NTA functionalised SAM substrate could then be primed for His-Tag immobilisation by exposing the NTA surface with Ni^{2+} ion species and subjecting the surface to a His-Tag containing enzyme or protein molecule. In contrast to the electrografting method of surface functionalisation, the LA-NTA SAM procedure

was a significantly lower risk, with no required diazonium or hydrazine deprotection chemistry, and more expedient, taking only two days as opposed to approximately five days to prepare. The surface was characterised using PM-IRRAS and QCM-D. PM-IRRAS revealed broad C=O stretch peaks for the unfunctionalised SAM layer at 1736 cm^{-1}. After drop-casting of the $NiCl_2$ buffer solution, a significant (128 cm^{-1}) downshift of the C=O peak was observed, confirming the successful coordination of the Ni ions to the NTA groups. Immobilisation of a His-tag enzyme was also observed after drop-casting of the CBL enzyme solution. IR absorption peaks characteristic of amide I and II functional groups at 1662 cm^{-1} and 1547 $cm^{-1,}$ respectively, were observed. While these indicate enzyme immobilisation, the measurement does not directly confirm the specificity of interaction between the Ni-NTA and the engineered His-tag motif.

Successful specific immobilisation of the CBL enzyme was confirmed using QCM-D through the change in resonant frequency, indicative of the change in immobilised mass, observed upon binding and dissociation of the enzyme from the surface. During the optimisation process, it was found that the preexposure of the LA-NTA surface to EDTA was highly effective in reducing the non-specific binding of CBL enzyme to a surface not exposed to Ni ions, as shown by a significant frequency decrease (11.2 Hz to 1.6 Hz) after EDTA pretreatment, negating an approximate 2.28×10^{11} molecules cm^{-2} layer of CBL non-specifically bound. It has been hypothesised that this effect may be due to either the removal of non-specific metal ions coordinated to the NTA groups or modification of the surface by EDTA, such as its insertion into the layer or hydrogen bonding interactions with the NTA terminal groups. Further studies are required to confirm the origin of this observed effect. Regardless, this discovery has the potential for applications in anti-fouling surface treatment technologies, depending on the protein specificity and longevity of the EDTA pretreatment. From the QCM-D frequency shift observed in the final optimised procedure, the approximate surface coverage of the surface-bound CBL enzyme was calculated at 6.86×10^{11} molecules cm^{-2} (6.86×10^{-3} molecules nm^{-2}) using the Sauerbury equation. This result shows the feasibility of an enzyme monolayer when considering the calculated approximate CBL enzyme cross-sectional area of 18.2 nm^2. Further investigations to support the formation of a monolayer will need to be performed to confirm this hypothesis.

Subsequent exposure of the surface to EDTA stripping buffer in flow showed close to total removal of the bound CBL enzyme, with only a slight mass on the surface still observed, indicated by a variation in frequency (5.8 Hz) from the pre-CBL exposed surface, assumed to be due to fouling of the surface with non-specifically bound CBL. The negligible low-frequency drop observed for the EDTA pretreated NTA functionalised surface compared to one predisposed to Ni ions confirmed the specificity of the binding interaction. Refunctionalisation of this surface with CBL enzyme additionally demonstrated an approximated surface coverage of 6.28×10^{11}

molecules cm^{-2} for the LA-NTA-EDTA-Ni, showing that the surface could be used for chemically switchable enzyme functionalisation inflow, which represents a step towards achieving a switchable immobilisation surface for the long-term vision of this work.

In order to perform biocatalysis inflow, an immobilised enzyme reactor system was designed and innovated as part of this work that could accommodate slower flow rates via means of the dual syringe driver setup and allowed for the use of both a 52.5 µL packed bed microcolumn and a planar surface serpentine microfluidic chip reactors. A continuous flow system consisting of a syringe pump, valves for directional control, a reactor and a reservoir was developed so that the reaction solution could be repeatedly passed through the reactor to obtain biocatalysis with the minimum required amounts of biocatalyst per experiment. Active solenoid valves and a bespoke valve controller were required to achieve the continuous flow system, alongside purpose-built flow control software that automated the system for regular analyte extraction for offline analysis. Both the control system and reactor setup were demonstrated to run for 14 days without hardware or software failure, demonstrating the system's robust nature. There is currently no other open-access software solution available to researchers for performing continuous inflow catalysis using an IMER system in this manner. Therefore, by providing open access to the software developed as part of this work, it is hoped that this work will enable researchers to develop and automate other IMER systems. Quantifying the system's consistency in volume delivery showed limitations, with a ¼ volume loss per fraction extraction after 12 reactor loops. These inconsistencies suggest further work is required to adjust the software's working to accommodate this discrepancy caused by the physical limitations of this system, which are relatively minor adjustments.

One of the overall visions of the work was to demonstrate the viability of a microfluidic scale immobilised enzyme reactor system for high throughput screening of inflow biocatalytic parameters. In order to demonstrate such a system, the CBL enzyme was immobilised onto Sepharose beads, and approximately 4 mg of the functionalised beads were packed in a microcolumn reactor in order to perform the inflow α,β-elimination reaction of S-benzyl-L-cysteine [8 and 10 mM] to produce ammonia, benzyl thiol and pyruvic acid. Due to the lack of access to an inline or offline HPLC system, a thiol quantification assay that utilised Ellman's reagent was used in conjunction with an offline UV-Vis spectrometer to analyse the kinetics of the inflow biocatalytic reaction. A calibration curve was created to equate UV absorbance to the concentration of the product. Unfortunately, the accuracy of this assay was insufficient to enable the concentration of the product to be calculated with confidence. Assessment of this calibration data highlights the limitations of this assay that should not be overlooked when performing more exact studies. Despite this, the devised system viability was clearly demonstrated, allowing for

its use in further work where it would be advised that a more accurate inline analytical system, such as HPLC, be used.

The first inflow biocatalytic reaction was performed using a large volume of reaction buffer (3 mL) with an S-benzyl-L-cysteine concentration of 10 mM. The larger volume enabled multiple fraction extractions for each cycle to obtain a combined experimental error at each sample point. This experiment yielded a reaction rate constant of 0.00782 min^{-1}. A repeat experiment under the same conditions but with a reduced total system volume (1.5 mL) resulted in a moderate increase in the rate constant to 0.00927 min^{-1}. This discrepancy is associated with experimental error or a combination of errors in the experimental setup. Due to the system's complexity, isolating the exact source of the error was not possible for the data acquired and is an area of study that should be further explored. However, this observed difference should not affect the direct comparison of reactions performed at the same volume with differing substrate concentrations. When a reaction was performed once again at the reduced system volume (1.5 mL) but with a lower S-benzyl-L-cysteine concentration of 8 mM, the kinetic fit gave a rate constant of 0.00512 min^{-1}, 44.8 % slower than that of the same system with a 10 mM S-benzyl-L-cysteine running buffer. Unfortunately, due to time limitations, analysis of immobilised CBL within the IMER system being tested for this reaction across multiple substrate concentrations was not possible. Therefore, Michaelis–Menten kinetics was not obtained, but based on the results of the system, with additional concentration data points, the demonstrated continuous flow μ-IMER system could be used to determine these parameters.

The rate constant of the bead surface immobilised CBL enzyme was also measured in static, i.e. non-flow conditions. Critically, when the same quantity of CBL functionalised agarose beads that were packed into the microcolumn reactor were agitated within 1.5 mL of 10 mM S-benzyl-L-cysteine buffer, a significantly higher rate constant of 0.0480 min^{-1} was observed. A more detailed analysis of the flow system, including screening of the expansive parameter space, is required to optimise the inflow reaction rate and elucidate the observed difference in reaction kinetics.

To develop a planer microfluidic chip reactor, soft photolithography and stereolithography were used to fabricate several designs of master substrates from which PDMS microfluidic substrates could then be cast and used to create the reactors. As part of standardising the setup, a PDMS microfluidic jig was engineered alongside a bespoke microfluidic clamp. These minimised variations across experiments and ensured the tight sealing of the microfluidic chip to the biocatalyst functionalised substrate surface without leaking or the need for plasma oxygen bonding that would damage the functionalised surface. Although a rather practical contribution to the field, prior to this work, an open-source PDMS microfluidic jig and clamping system was unavailable to researchers. Fabricated devices and master substrates were assessed using optical

microscopy and surface profilometry. Surface profilometry of a serpentine channel stereolithographic master substrate showed that the profile was relatively uniform, with a 263.9 ± 4.1 µm feature height, approximately 37 µm shorter than expected.

Additionally, the soft photolithographic fabricated meandros channel master substrate was shown to have an uneven distribution of channel heights ranging from approximately 100 µm for channels in the outer edges of the chip to a much more uniform height of 72.7 ± 0.1 µm in the centre, which was likely caused by the photoresist beading on the outer edges. The overall effect of the flow profile that this discrepancy would cause is complex and cannot be determined without significant further studies. In order to mitigate any complexity this inconsistency may cause for the assessment of the meandros flow pattern, alternative means of creating a photoresist layer have been pursued as further work to form microfluidic master substrates with channels of a consistent height.

Over the six-day reaction of a CBL functionalised planer substrate microfluidic reactor, with the system in a continuous flow mode, with 3.0 mL of 10 mM S-benzyl-L-cysteine running buffer, the difference between the control study of an unfunctionalised surface and the CBL-functionalised surface showed a marginal overall difference in the rate constant, with the functionalised surface giving a rate constant of 1.35×10^{-5} min^{-1}. It is hard to justify that this constant rate equates to a detectable level of biocatalysis, but instead, it demonstrates that further experimentation would be required to confirm the feasibility of this system. An area for further investigation is the surface density of immobilised enzymes. A comparison between the estimated 5.6×10^{12} molecules of CBL enzymes immobilised on a planar surface to that of 8.3×10^{15} molecules of the CBL enzymes immobilised on Sepharose beads within the microcolumn showed a difference in the number of CBL enzymes present to be over three orders of magnitude more within the column reactor. Therefore, it is unsurprising that the rate constant measured experimentally is comparatively undetectable in the planar surface microfluidic chip reactor, unlike that of the microcolumn reactor, where it was easily quantifiable. Therefore, this work concludes that further development of the planar surface microfluidic chip reactor should focus on increasing the surface area of the microfluidic chip reactor to increase the concentration of immobilised enzymes alongside further optimising the reaction conditions.

Arguably, the microcolumn sepharose bead system would be adequate for many applications requiring high throughput screening of enzymes for inflow biocatalysis. However, a flow reactor based on a microfluidic chip may be more appropriate to pursue electrode-actuated ‘catch and release’ enzyme coordination or highly multiplexed enzyme screening. This work demonstrates that such systems are viable but would require significant system optimisation past the point demonstrated here.

7.2 - Outlook and Further Work

7.2.1 - The Effect of Flow on Non-specific Binding for the LA-NTA Immobilisation Strategy and the Role of EDTA in its Inhibition

QCM-D analysis of the LA-NTA functionalised Au surfaces for the immobilisation of the CBL enzyme revealed that when the LA-NTA surface was pre-treated with EDTA before Ni loading, non-specific binding was suppressed entirely. However, this was not the case when the surface did not undergo EDTA pretreatment. It was hypothesised that this may be due to the EDTA chelating and removing non-specifically bound ionic metal species, the EDTA altering the LA-NTA surface in such a way that it acts to inhibit the interaction of proteins with the surface, or a combination of these two factors. The reduction of biofouling and non-specific binding is an important area of research, with non-specific binding a common cause for lower enzyme activity of μ-IMER systems[278], as well as reducing with the specificity of medical biosensor technologies[279]. Through testing the non-specific binding properties of alternative proteins, with and without a His-tagged binding motif, on the same LA-NTA surface in flow, it is hoped that further information regarding the anti-fouling properties of the EDTA pretreatment can be ascertained or demonstrated to be exclusively observed for the CBL enzyme.

Another observation relating to non-specific binding of CBL was that significant non-specific binding was observed when the surface was challenged with CBL enzyme inflow, as employed in QCM-D experiments. In contrast, when the surface was exposed to an identical CBL solution via drop-casting (as used for PM-IRRAS experiments), the same LA-NTA surface showed minimal non-specific binding of the enzyme.

Two hypotheses to explain this observation are proposed. First, the flow conditions promote interaction and non-specific binding of CBL to the surface functionalised LA-NTA layer. Second, the non-specific binding results from experimental procedures, such as metal ion contamination within the QCM-D flow system or turbulence due to the drop-casting procedure, which induces more stringent substrate washing. The ability to inhibit the non-specific binding of proteins to functionalised surfaces is of significant interest to the biosensor community. It would thus be of interest to elucidate the reduction in surface fouling observed here.

In order to test these two hypotheses, two further experiments are proposed. The first is to perform QCM-D using an open cell module, in which the LA-NTA functionalised Au QCM-D sensor

could be exposed via drop-casting of the CBL enzyme solution rather than the traditional flow module. The second experiment would be to perform functionalisation of the PM-IRRAS Au substrates inflow to characterise if amide I and II absorption peaks associated with CBL are evident in the PM-IRRAS spectra. These two experiments, in conjunction, would confirm if the non-specific binding is a function of the flow conditions or a result of the experimental procedures.

7.2.2 - Microcolumn µ-IMER Experiments using Gst Immobilised Agarose Beads

Due to the time limitations of the project, a complete study into the use of ArM's with a µ-IMER system immobilised within a microcolumn Sepharose bead reactor as shown with CBL enzyme was not possible, but initial work was performed.

In collaboration with colleagues in the Department of Chemistry, University of York (Dr Alex Miller), initial experiments were performed using a novel ArM named Gst. This artificial enzyme has been demonstrated to turnover harmaline via an asymmetric hydrogenation reaction into (+/-)-tetrahydroharmine in solution. This catalytic turnover decreases the concentration of harmaline in the solution, which could be quantified by the corresponding decrease in optical absorption at 375 nm (harmaline has a strong absorbance peak at 375 nm) when monitored using UV-Vis spectrometry.

In order to test this catalytic reaction within the microcolumn µ-IMER system, Gst was immobilised onto the agarose beads using the same procedure developed for the CBL enzyme. The functionalised beads were subsequently loaded into the microcolumn reactor. The Gst catalysis was tested in flow using the same experimental reactor parameters used for CBL but with a 10 mM harmaline running buffer, and the reactor was placed in a water bath at 50 °C, which had been demonstrated to increase the reaction rate when in solution. Within the first 4 hours of the experiment, no observable change to the harmaline absorbance peak was observed. The reactor was left running in continuous flow mode for a further 17.5 hours. However, even after this time, no change was observed in the absorbance peak at 375 nm. The result, or lack of it, suggests that no catalysis occurred or that the concentration of product formed over the timeframe of the experiment was below the limit of detection for the UV-Vis analysis.

As discussed in the literature review of the CBL metalloenzyme (2.1.2 - Artificial Metalloenzymes), the low TON often reported for ArMs, even in solution, implies that their immobilisation within such a small volume microcolumn may have resulted in a reaction rate for the system being too low to be detected experimentally. If so, this means that inflow biocatalysis using the Gst ArM

would require significant optimisation, such as an increased concentration of Gst functionalised beads, higher system flow rates and lower total system volumes. Therefore, it is suggested that to further this research, focusing on optimising these areas would be highly prudent in the first instance, using the methods and system discussed within this work.

7.2.3 - Integration of a Correction Factor to the µ-IMER system

Analysis of the flow system consistency at delivering consecutive user-set extraction volumes to the reservoir at the end of the extraction cycle showed a deviation from the ideal volume the system was expected to deliver. It will be possible to calculate a correction factor using the data acquired from this experiment, which could be implemented within the flow control software to compensate for deviations in the volume withdrawn from the reservoir at each extraction step. Although not essential to producing a quantifiable µ-IMER system, the correction factor would give a more consistent and universally comparable flow setup.

7.2.4 - Inline Spectrometer Integration for Further Kinetic Analysis

The CBL immobilised bead column µ-IMER systems demonstrated within this work were only characterised at two substrate concentrations (8 mM and 10 mM S-benzyl-L-cysteine). Complete characterisation of the system would require measurements at a wider range of substrate concentrations, enabling quantification of Michaelis-Menten kinetic values for this µ-IMER system, such as K_{cat}, K_M and V_{max}. Due to the significant length of time required to perform one of these experiments when using low substrate concentrations, integration of an inline spectrometer would allow for analysis of the Ellman's reagent thiol assay without the need for operator intervention and fraction extraction required by offline UV-Vis spectroscopic analysis. In addition to enabling long reaction times without user intervention, an inline spectrometer would additionally reduce experimental error, allow experiments to be performed at a lower total system volume, as volume compensation for extraction is not required and would allow for the acquisition of more data points throughout the experiment allowing for more accurate interpretation of kinetic trends within the data.

7.2.5 - Further Screening of the Enzyme Immobilised Column Reactor Experimental Parameter Space

Although inflow catalysis for the CBL immobilised column reactor system was successfully demonstrated, the experimentally determined reaction rates were significantly lower than those observed for CBL functionalised beads agitated freely within the substrate solution. In addition, no clear inflow biocatalysis was observed for the immobilised Gst ArM in an IMER system under the experiment's current parameters. Further optimisation of the wider experimental parameter space for both biocatalysts is clearly required. Optimisation conditions such as testing a range of flow rates, using different-sized column cross-sectional areas, testing the enzymatic system at various temperatures using a water bath and adjusting the CBL immobilised bead volume to system volume ratio are all areas still to be explored which have the potential to increase the overall rate of reaction for the column μ-IMER system.

Once optimisation for the CBL enzyme μ-IMER system has been performed, it is hoped that some of the more fundamental system parameter optimisations, such as optimal flow rate, packing density and microcolumn size, can be applied to the Gst artificial metalloenzyme bead microcolumn reactor system in order to demonstrate the use of an artificial metalloenzyme in a μ-IMER.

7.2.6 - Profiling of the Cross-Sectional Area of Microfluidic Chip Devices

The meandros microfluidic chip designed and fabricated in this work was developed to produce a pressure differential across the microfluidic channels, forming primary and secondary Deans' vortices. The resultant non-chaotic convection currents would help increase the diffusion of the substrate to the surface-immobilised enzymes. To fully understand the potential and characteristics of the flow profile produced by the meandros pattern, further work should be performed to determine the cross-sectional flow profile of the chip at various points within the flow channel. Commonly, profiling of this kind is achieved using confocal microscopy using two distinct dyes or a dye and a standard buffer injected via a Y-connector junction inlet. As the two solutions move through the flow channel, it is possible to observe the dye movement and the resultant convection currents within the cross-sectional area of the channel. Performing such an experiment helps better understand how the complex meandros pattern fluidic channel could

be used to regenerate saturated surface diffusion sites and determine its performance as a microfluidic mixer.

7.2.7 - Acquiring Lower Variance in the Thickness of Master Substrates using SUEX Laminated Photoresist

The undesirable side effect of spin coating a layer of photoresist onto a sizeable rectangular substrate is that the resist layer has inconsistent thickness due to resist beading at the substrate's edges. As a result, the resultant exposed pattern tends to have a 'bowl-like' profile, with the outer features being higher than those closer to the centre of the substrate. Although often not detrimental to the microfluidic performance, this inconsistency in channel height decreases the accuracy of calculating the chip's internal dead volume and may have undesired effects on the microfluidic flow profile. Additionally, the surface topography of the stereolithographic master substrates was observably rough, which once again was not innately detrimental but had the potential to affect the fluid flow unpredictably. For these reasons, initial work was performed on an alternative method of producing high aspect ratio microfluidic master substrates using the laminated photoresist SUEX described in the methods chapter (3.3.1 - Soft Photolithography).

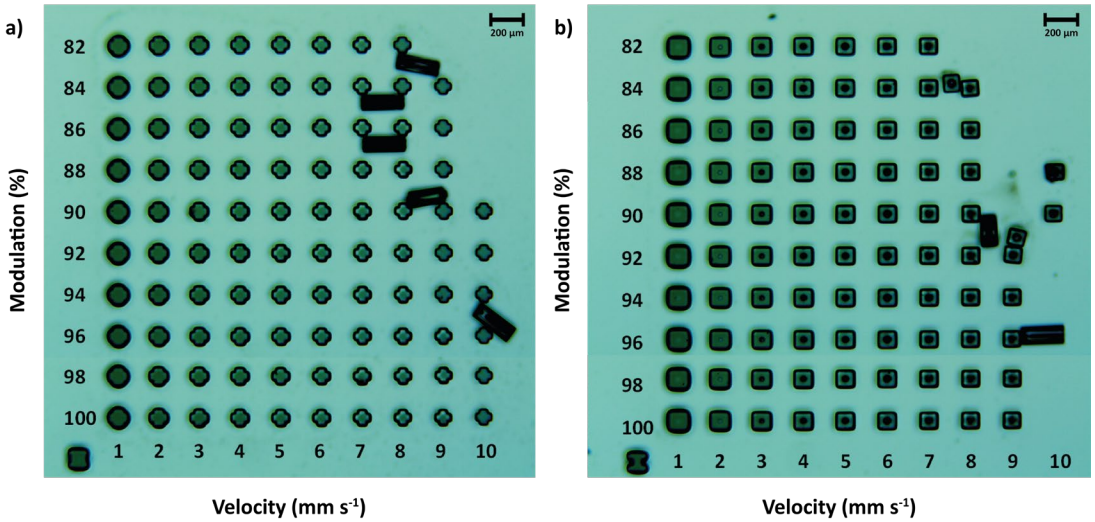

Figure 7.1 - Optical microscope images of the initial dose testing for SUEX K-200 laminated photoresist of two test features, a) ⌀80 µm cross structures and b) ⌀100 µm squares with ⌀40 µm wells. Lower exposure pillars, which had poor substrate adhesion, can be seen scattered across both images. Both Images were taken with a ×5 objective lens.

In order to establish the correct exposure dosage for the 200 µm thick SUEX photoresist (SUEX K-200), a set of dose tests was devised, one using an ⌀80 µm cross structure (Figure 7.1a) and the other a ⌀100 µm squares with ⌀40 µm well (Figure 7.1b). A testing grid was established for each, starting from the bottom left corner, with write velocity increasing from 1-10 in increments of 1 mm s^{-1} along the X axis and beam modulation decreasing from 100-82 % in increments of

2 % along the y-axis. From the corresponding patterns, a dose of 88% beam modulation and 5 mm s^{-1} was selected owing to the fast write speed while still demonstrating high feature resolution, substrate adhesion, and lack of overexposure.

From the microscope images of the completed patterns, the approximate size of the cross feature at the chosen dosage was calculated at approximately 80 µm, in agreement with the original design. However, a more complex pattern should be generated with multiple features at this dosage to determine a more accurate optical assessment of the feature's width.

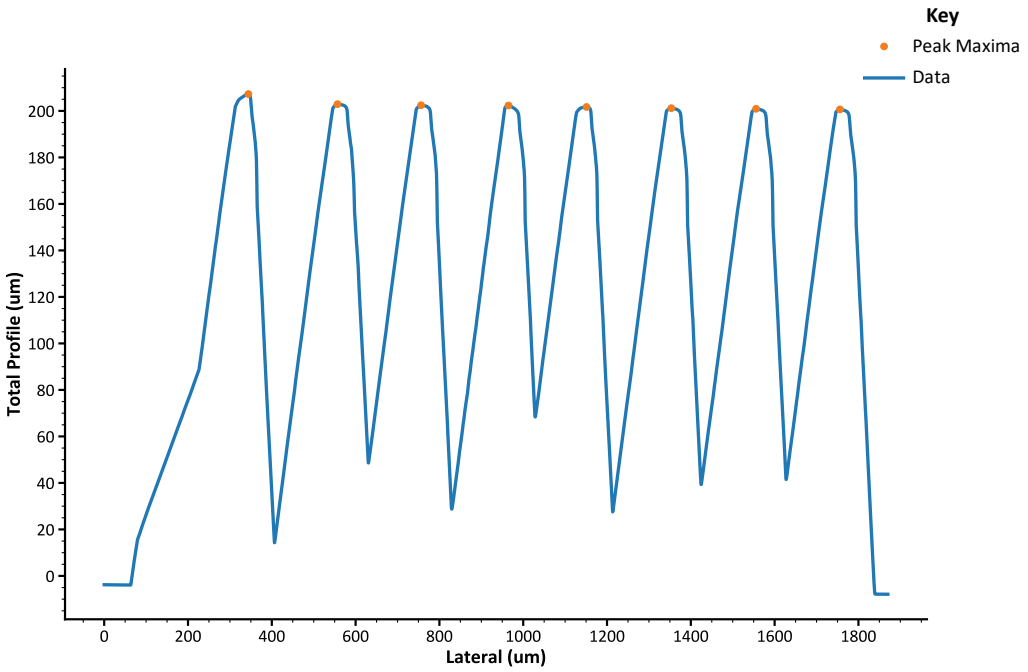

Figure 7.2 - Stylus profilometry of the SUEX K-200 ⌀80 µm cross structure with the scan running across the central section of the 82 % modulation row. The peak maxima gives an average feature height of 202.4 ± 2.1µm.

Due to the close packing of the patterns and height of the ⌀80 µm cross features, the stylus profilometry system could not accurately determine the full height of a single cross feature (Figure 7.2). However, the peak height of the features was obtainable using the peak maxima and minima values, giving an average of 202.4 ± 2.1 µm. Even with each of these peaks being a product of a differing exposure dosage, observation of the visually flatter peak profile and the significantly smaller standard deviation of 2.1 µm, compared to 9.0 µm seen for the SU-8 profile, demonstrates the significantly more consistent feature height that can be obtained using the SUEX laminated photoresist for the 75 × 25 mm Si substrates.

In order to achieve 200 µm resist thickness using SU-8, multiple layers of spin coating are required, from which the results can be varied and optimisation of the process time-consuming. The consistency and ease at which a 200 µm layer of photoresist could be achieved using the SUEX K-200 fabrication process makes it ideally suited to producing high aspect ratio microfluidic devices while maintaining low surface roughness and consistent thicknesses. The production of

master substrates for both the meandros pattern and standard Serpentine channel, both of cross-sectional areas of 200 × 200 µm, would provide microfluidic devices with significantly less fabrication error deviation, such as was seen for master substrates and resultant devices produced using stereolithographic and SU-8 fabrication. It would therefore be recommended that SUEX K-200 master substrate production be utilised to produce comparable meandros and Serpentine channel microfluidic devices, which could then be characterised, used in additional planar surface microfluidic chip reactor experiments and compared to determine the advantages and disadvantages of each.

7.2.8 - Demonstration of Electrochemically Actuated His-tag Affinity Binding

One of the potential avenues of research left unexplored due to the broad scope of the project was that of demonstrating the potential selective electrochemical reduction of the His-tag coordinating Ni^{2+} species instead of the more traditional EDTA chemical stripping of his tagged proteins from a Ni-NTA surface. Electrochemically actuated reduction and oxidation of Ni ion species at designated electrode areas would allow for the selective immobilisation of different His-tagged enzymes in series to achieve an enzyme cascade reaction. Flowing the product of one of the enzyme reactions into the next in a predetermined order would achieve an enzymatic microfluidic chemical production line. Such work would be considered highly novel and has the advantage of delivering a nonchemically driven means of recycling the immobilised enzyme or ArM, which would not require a purification process.

Chapter 8 - Appendixes

8.1 - Appendix 1- PDMS Microfluidic Chip Jig Schematic

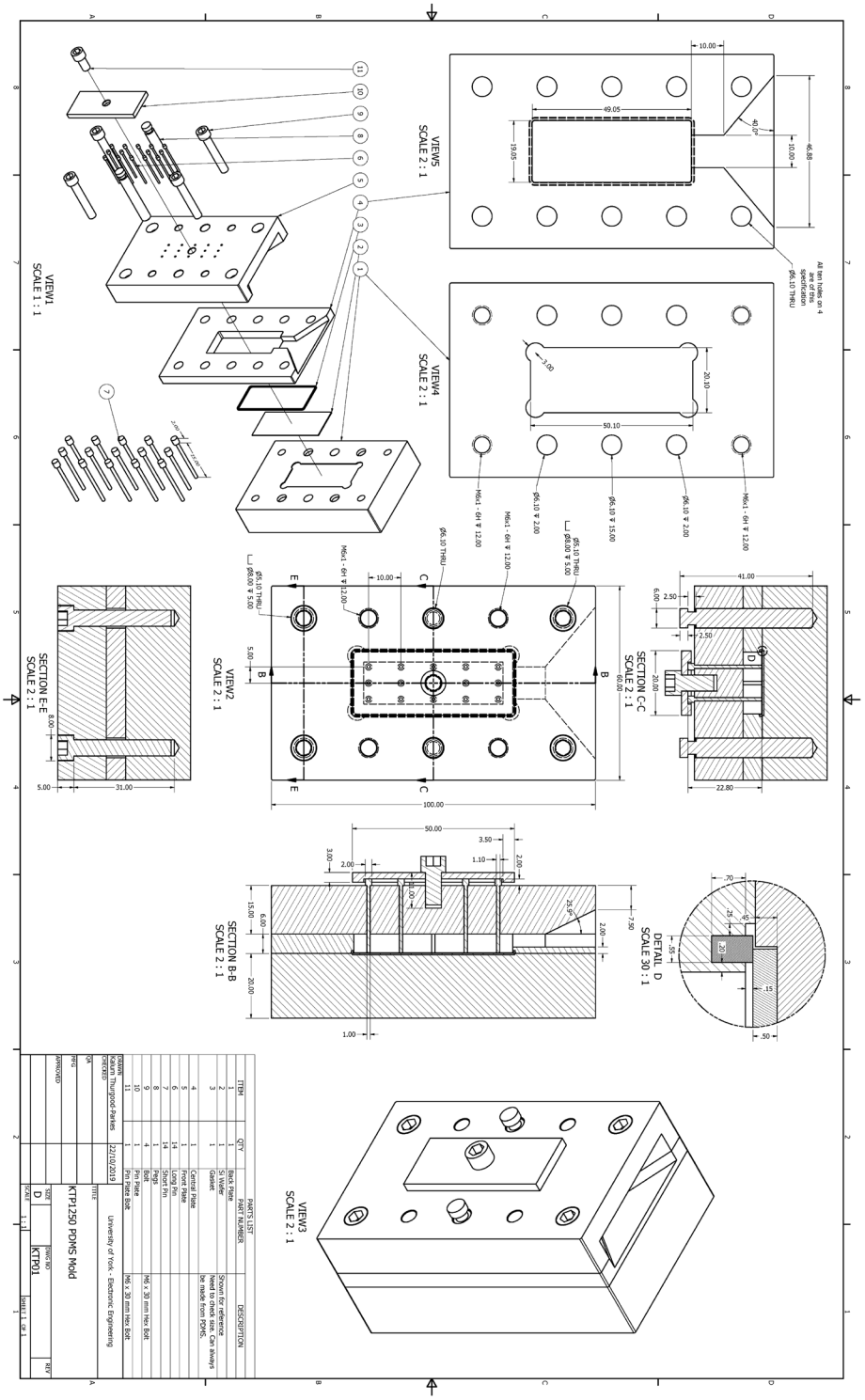

Link to file - https://drive.google.com/file/d/1ap9ZpDe78_BUR9e8s_r7NkHY8cq-CZkP/view?usp=sharing

8.2 - Appendix 2- Flow Control System Code

Python Environment 3.7 was used for this project.

The packages required for the software are as follows:

brotli==1.1.0

ConfigParser==6.0.1

cryptography==42.0.5

Cython==3.0.8

dl==0.1.0

HTMLParser==0.0.2

importlib_metadata==4.12.0

ipaddr==2.2.0

keyring==24.3.1

lockfile==0.12.2

lxml==5.1.0

machine==0.0.1

mypy_extensions==1.0.0

numpy==1.21.6

ordereddict==1.1

protobuf==4.25.3

pyOpenSSL==24.0.0

PyQt5==5.15.10

PyQt5_sip==12.11.0

pyserial==3.5

thread==0.1.3

utime==1.1.7

wincertstore==0.2.1

xmlrpclib==1.0.1

zipp==3.8.1

Link to files -

https://drive.google.com/file/d/1Pvi7GVe2eQrl4Q9FXUEZXZAG1DQLVRo9/view?usp=sharing

Chapter 9 - Abbreviations

3-PGA - 3-phosphoglyceric acid

ACE - Angiotensin-converting enzyme

AFM - Atomic force microscopy

ALP - Alkaline phosphatase

AMG - Amyloglucosidase

anti-IgG - Anti-Immunoglobulin G

ArM - Artificial metalloenzyme

CA - Carbonic anhydrase

CAD - Computer-aided design

CALB - Candida antarctica lipase B

CAS - Chemical assembly systems

CBL - Cystathionine beta-lyase

CNT - Carbon nanotube

COF - Covalent-organic framework

COM - Common

CPM - Cycles per minute

CV - Cyclic voltammetry

DAQ - Data acquisition

DDI - DNA-directed immobilisation

DiFMU - 6,8-difluoro-4-methylumbelliferyl

DMF - Dimethylformamide

DMSO - Dimethylsulfoxide

DNA - Deoxyribonucleic acid

DTNB - 5,5’-dithiobis-(2-nitrobenzoic acid

e.e - Enantiomeric excess

EDC - 1-Ethyl-3-(3-dimethylaminopropyl)carbodiimide

EDTA - Ethylenediaminetetraacetic acid

EM - Electromagnetic

FDM - Fused deposition modelling

FITC - Fluorescein isothiocyanate

FT-IR - Fourier-transform infrared spectroscopy

GA - Glutaraldehyde

GC - Gas chromatography

GOD - Glucose oxidase

Gox - glucose oxidase

HA - Hippuric acid

HDB - Hexadimethrine bromide

HHL - hippuryl-His-Leu

His-tag - Polyhistidine tag

HPLC - High-performance liquid chromatography

HRP - Horseradish peroxidase

IgG - Immunoglobulin G

IMAC - Immobilised metal affinity chromatography

IMER - Immobilised enzyme reactor

IR - Infrared

IUPAC - International Union of Pure and Applied Chemistry

LA - Lipoic acid

LED - Light-emitting diode

LHS - Left-hand side

MOF - Metal-organic framework

MS - Mass spectrometry

MWNT - Multi-walled carbon nanotube

NADH - Nicotinamide adenine dinucleotide (NAD) + hydrogen (H)

NaPB - Sodium phosphate buffer

NC - Normally closed

NHS - N-Hydroxysuccinimide

NLS - Nonlinear least squares

NMR - Nuclear magnetic resonance

NO - Normally open

NTA - Nitrilotriacetic acid

OEM - Original equipment manufacturer

OLS - Ordinary least squares

PA - Polytetrafluoroethylene

PBP - Periplasmic binding protein

PCNA - Proliferating cell nuclear antigen

PDA - *Ortho*-phenylendiamine

PDB - Protein data bank

PDDA - Polyelectrolyte polydiallyldimethylammonium

PDMS - Polydimethylsiloxane

PEB - Post-exposure bake

PEG - Polyethylene glycol

PEI - Polyethylenimine

PEM - photo-elastic modulator

PET - Polyethylene terephthalate

PFA - Perfluoroalkoxy polymer

PGMEA - 2-methoxy-1- methylethyl acetate

PM-IRRAS - Polarisation Modulation Infrared Reflection Absorption Spectroscopy

PMMA - Poly(methyl methacrylate)

PS-PIAT - polystyrene-poly(isocyanoalanine-(2-thiophene-3-yl-ethylamide))

PTFE - Polytetrafluoroethylene

QCM-D - Quartz Crystal Microbalance with Dissipation monitoring

QQ - Quartile-quartile

RHS - Right-hand side

RIMR - RuBisCO immobilised microfluidic reactor

rpm - Revolutions per minute

RuBisCO - Ribulose-1,5-bisphosphate carboxylase/oxygenase

RuBP - Ribulose 1,5-bisphosphate

SAM - Self-assembled monolayer

SDS - Sodium dodecyl-sulfate

SEC - Size exclusion column

SEM - Scanning electron microscopy

SLA - Stereolithography

SLS - Selective laser sintering

SOP - Standard operating procedure

ssDNA - Single-strand DNA

sSMCC - Sulfo-succinimidyl-4-(*N*-maleimido-methyl)-cyclohexan-1-carboxylate

SWNT - Single-walled carbon nanotube

TCEP - Tris(2-carboxyethyl)phosphine hydrochloride

TNB - 5-thio-2-nitrobenzoic acid

TON - Turnover number

TTN - Total turnover number

UI - User Interface

UV-Vis - Ultraviolet-visible

ZIF-8 - Zeolitic imidazolate framework-8

µFCS - Microfluidic flow control system

µ-IMER - Microfluidic immobilised enzyme reactor

Chapter 10 - Bibliography

1. O. E. Dictionary, *Journal*, 2023, DOI: https://doi.org/10.1093/OED/1070073972.
2. Reaxys, https://www.elsevier.com/products/reaxys, (accessed 17/12/2023).
3. N. N. Gandhi, *Journal of the American Oil Chemists' Society*, 1997, **74**, 621-634.
4. R. A. Young, *Annual Review of Biochemistry*, 1991, **60**, 689-715.
5. R. H. A. Plimmer, *The Chemical Constitution of The Proteins*, Longmans, Green and Co., London, 1908.
6. H. B. Vickery and T. B. Osborne, *Physiological Reviews*, 1928, **8**, 393-446.
7. I. Wagner and H. Musso, *Angewandte Chemie International Edition in English*, 1983, **22**, 816-828.
8. D. Seebach, A. K. Beck and D. J. Bierbaum, *Chemistry & Biodiversity*, 2004, **1**, 1111-1239.
9. B. Palecz, *Journal of the American Chemical Society*, 2002, **124**, 6003-6008.
10. W. S. Horne, J. L. Price and S. H. Gellman, *Proceedings of the National Academy of Sciences of the United States of America*, 2008, **105**, 9151-9156.
11. U. Breitinger, T. Clausen, S. Ehlert, R. Huber, B. Laber, F. Schmidt, E. Pohl and A. Messerschmidt, *Plant Physiology*, 2001, **126**, 631-642.
12. T. Shafee, File:Alpha beta structure (full).png, https://en.wikipedia.org/wiki/File:Alpha_beta_structure_(full).png, (accessed 30/09/23).
13. T. Shafee, File:Protein structure (3)-en.svg, https://en.wikipedia.org/wiki/File:Protein_structure_(3)-en.svg, (accessed 30/09/23).
14. P. D. Sun, C. E. Foster and J. C. Boyington, *Current Protocols in Protein Science*, 2004, **35**.
15. C. M. Roth, B. L. Neal and A. M. Lenhoff, *Biophysical Journal*, 1996, **70**, 977-987.
16. H.-X. Zhou and X. Pang, *Chemical Reviews*, 2018, **118**, 1691-1741.
17. P. T. Wingfield, *Current Protocols in Protein Science*, 2015, **80**.
18. E. Hochuli, W. Bannwarth, H. Döbeli, R. Gentz and D. Stüber, *Nature Biotechnology*, 1988, **6**, 1321-1325.
19. A. Spriestersbach, J. Kubicek, F. Schäfer, H. Block and B. Maertens, *Methods Enzymol*, 2015, **559**, 1-15.
20. M. Bellare, V. K. Kadambar, P. Bollella, M. Gamella, E. Katz and A. Melman, *Electroanalysis*, 2019, **31**, 2274-2282.
21. E. M. Ciszak, L. G. Korotchkina, P. M. Dominiak, S. Sidhu and M. S. Patel, *Journal of Biological Chemistry*, 2003, **278**, 21240-21246.
22. S. Ravanel, D. Job and R. Douce, *Biochemical Journal*, 1996, **320**, 383-392.
23. Michelle, Roy, Michael and R. Eisenthal, *Biochemical Journal*, 2007, **402**, 331-337.
24. D. Kishore, S. Kundu and A. M. Kayastha, *PLoS ONE*, 2012, **7**, e50380.
25. H. Bisswanger, *Perspectives in Science*, 2014, **1**, 41-55.
26. H. Bey, W. Gtari, A. Aschi and T. Othman, *International Journal of Biological Macromolecules*, 2016, **92**, 860-866.
27. T. Shafee, File:Enzyme structure.svg, https://commons.wikimedia.org/wiki/File:Enzyme_structure.svg, (accessed 30/09/23).
28. E. Fischer, *Berichte der deutschen chemischen Gesellschaft*, 1894, **27**, 2985-2993.
29. D. E. Koshland, *Proceedings of the National Academy of Sciences*, 1958, **44**, 98-104.
30. T. Shafee, File:Hexokinase induced fit.svg, https://commons.wikimedia.org/wiki/File:Hexokinase_induced_fit.svg, (accessed 30/09/23).
31. L. B. Spector, *Covalent Catalysis by Enzymes*, Springer New York, 2012.
32. U. Ermler, W. Grabarse, S. Shima, M. Goubeaud and R. K. Thauer, *Current Opinion in Structural Biology*, 1998, **8**, 749-758.

33. A. Warshel, P. K. Sharma, M. Kato, Y. Xiang, H. Liu and M. H. M. Olsson, *Chemical Reviews*, 2006, **106**, 3210-3235.
34. M. Eigen, *Angewandte Chemie International Edition in English*, 1964, **3**, 1-19.
35. J. Gao, *Current Opinion in Structural Biology*, 2003, **13**, 184-192.
36. G. G. Hammes, *Biochemistry*, 2002, **41**, 8221-8228.
37. T. C. Bruice, in *The Enzymes*, ed. P. D. Boyer, Academic Press, 1970, vol. 2, pp. 217-279.
38. N. A. Campbell and J. B. Reece, *Biology*, Pearson / Benjamin Cummings, San Francisco, Calif. ; London, 8th / Neil A. Campbell ... [et al.]. edn., 2008.
39. T. D. Bugg, *Introduction to enzyme and coenzyme chemistry*, John Wiley & Sons, 2012.
40. E. Frieden, *Journal of Chemical Education*, 1985, **62**, 917.
41. A. Martínez-Limón, M. Alriquet, W.-H. Lang, G. Calloni, I. Wittig and R. M. Vabulas, *Proceedings of the National Academy of Sciences*, 2016, **113**, 12156-12161.
42. H. K. Chenault, E. S. Simon and G. M. Whitesides, *Biotechnology and Genetic Engineering Reviews*, 1988, **6**, 221-270.
43. A. W. Munro and K. J. McLean, in *Encyclopedia of Biophysics*, ed. G. C. K. Roberts, Springer Berlin Heidelberg, Berlin, Heidelberg, 2013, DOI: 10.1007/978-3-642-16712-6_41, pp. 601-606.
44. A. D. Goldman and B. Kacar, *Journal of Molecular Evolution*, 2021, **89**, 127-133.
45. C. K. Prier and F. H. Arnold, *Journal of the American Chemical Society*, 2015, **137**, 13992-14006.
46. J. M. Berg, J. L. Tymoczko and L. Stryer, *Biochemistry, Fifth Edition*, W.H. Freeman, 2002.
47. K. A. Johnson and R. S. Goody, *Biochemistry*, 2011, **50**, 8264-8269.
48. L. Michaelis and M. L. Menten, *Biochem. z*, 1913, **49**, 352.
49. A. Cornish-Bowden, *Fundamentals of Enzyme Kinetics*, Elsevier Science, 2014.
50. W. W. Chen, M. Niepel and P. K. Sorger, *Genes & Development*, 2010, **24**, 1861-1875.
51. A. Bhagi-Damodaran, P. Hosseinzadeh, E. Mirts, J. Reed, I. D. Petrik and Y. Lu, in *Methods in Enzymology*, ed. V. L. Pecoraro, Academic Press, 2016, vol. 580, pp. 501-537.
52. R. Roskoski, in *Reference Module in Biomedical Sciences*, Elsevier, 2015, DOI: https://doi.org/10.1016/B978-0-12-801238-3.05143-6.
53. G. P. Moss, *Pure and Applied Chemistry*, 1996, **68**, 2193-2222.
54. J. R. Cossy, in *Comprehensive Chirality*, eds. E. M. Carreira and H. Yamamoto, Elsevier, Amsterdam, 2012, DOI: https://doi.org/10.1016/B978-0-08-095167-6.00101-4, pp. 1-7.
55. N. Vargesson, *Birth Defects Research Part C: Embryo Today: Reviews*, 2015, **105**, 140-156.
56. J. Isac-García, J. A. Dobado, F. G. Calvo-Flores and H. Martínez-García, in *Experimental Organic Chemistry*, eds. J. Isac-García, J. A. Dobado, F. G. Calvo-Flores and H. Martínez-García, Academic Press, 2016, DOI: https://doi.org/10.1016/B978-0-12-803893-2.50007-3, pp. 207-238.
57. 18.14 Stereochemistry of Nucleophilic Addition Reactions: Re and Si Faces, https://chem.libretexts.org/@go/page/18923, (accessed 02/10/23).
58. D. R. Klein, *Organic chemistry*, Wiley, Hoboken, NJ, Second edn., 2015.
59. A. Zaks, *Current Opinion in Chemical Biology*, 2001, **5**, 130-136.
60. A. L. Margolin, *Enzyme and Microbial Technology*, 1993, **15**, 266-280.
61. A. Bozan, R. SongÜr and Ü. MehmetoĞlu, *Turk J Chem*, 2020, **44**, 1352-1365.
62. A. Abate, E. Brenna, C. Fuganti, F. G. Gatti and S. Serra, *Journal of Molecular Catalysis B: Enzymatic*, 2004, **32**, 33-51.
63. A. Babtie, N. Tokuriki and F. Hollfelder, *Current Opinion in Chemical Biology*, 2010, **14**, 200-207.
64. J. Haseloff and W. L. Gerlach, *Nature*, 1988, **334**, 585-591.
65. V. Stepankova, S. Bidmanova, T. Koudelakova, Z. Prokop, R. Chaloupkova and J. Damborsky, *ACS Catalysis*, 2013, **3**, 2823-2836.
66. F. Schwizer, Y. Okamoto, T. Heinisch, Y. Gu, M. M. Pellizzoni, V. Lebrun, R. Reuter, V. Köhler, J. C. Lewis and T. R. Ward, *Chemical Reviews*, 2018, **118**, 142-231.
67. K. C. Nicolaou, P. G. Bulger and D. Sarlah, *Angewandte Chemie International Edition*, 2005, **44**, 4442-4489.

68. R. H. Grubbs and S. Chang, *Tetrahedron*, 1998, **54**, 4413-4450.
69. D.-S. Wang, Q.-A. Chen, S.-M. Lu and Y.-G. Zhou, *Chemical Reviews*, 2012, **112**, 2557-2590.
70. D. J. Raines, J. E. Clarke, E. V. Blagova, E. J. Dodson, K. S. Wilson and A.-K. Duhme-Klair, *Nature Catalysis*, 2018, **1**, 680-688.
71. F. Yu, V. M. Cangelosi, M. L. Zastrow, M. Tegoni, J. S. Plegaria, A. G. Tebo, C. S. Mocny, L. Ruckthong, H. Qayyum and V. L. Pecoraro, *Chemical Reviews*, 2014, **114**, 3495-3578.
72. V. M. Cangelosi, A. Deb, J. E. Penner-Hahn and V. L. Pecoraro, *Angewandte Chemie International Edition*, 2014, **53**, 7900-7903.
73. U. T. Bornscheuer, G. W. Huisman, R. J. Kazlauskas, S. Lutz, J. C. Moore and K. Robins, *Nature*, 2012, **485**, 185-194.
74. H. Yang, A. M. Swartz, H. J. Park, P. Srivastava, K. Ellis-Guardiola, D. M. Upp, G. Lee, K. Belsare, Y. Gu, C. Zhang, R. E. Moellering and J. C. Lewis, *Nature Chemistry*, 2018, **10**, 318-324.
75. P. S. Coelho, E. M. Brustad, A. Kannan and F. H. Arnold, *Science*, 2013, **339**, 307-310.
76. T. A. Rogers and A. S. Bommarius, *Chemical Engineering Science*, 2010, **65**, 2118-2124.
77. M. Tamás, S. Sharma, S. Ibstedt, T. Jacobson and P. Christen, *Biomolecules*, 2014, **4**, 252-267.
78. Q. Jing, K. Okrasa and R. J. Kazlauskas, *Chemistry – A European Journal*, 2009, **15**, 1370-1376.
79. J. A. Laureanti, G. W. Buchko, S. Katipamula, Q. Su, J. C. Linehan, O. A. Zadvornyy, J. W. Peters and M. O'Hagan, *ACS Catalysis*, 2019, **9**, 620-625.
80. G. Roelfes, *Accounts of Chemical Research*, 2019, **52**, 545-556.
81. T. K. Hyster, L. Knörr, T. R. Ward and T. Rovis, *Science*, 2012, **338**, 500-503.
82. T. Heinisch and T. R. Ward, *Accounts of Chemical Research*, 2016, **49**, 1711-1721.
83. E. V. Blagova, A. H. Miller, M. Bennett, R. L. Booth, E. J. Dodson, A.-K. Duhme-Klair and K. S. Wilson, *Acta Crystallographica Section D Structural Biology*, 2023, **79**, 694-705.
84. S. C. Terry, J. H. Jerman and J. B. Angell, *IEEE Transactions on Electron Devices*, 1979, **26**, 1880-1886.
85. H. T. G. Van Lintel, F. C. M. Van De Pol and S. Bouwstra, *Sensors and Actuators*, 1988, **15**, 153-167.
86. D. J. Harrison, A. Manz, Z. Fan, H. Luedi and H. M. Widmer, *Analytical Chemistry*, 1992, **64**, 1926-1932.
87. Laminar vs Turbulent Flow, https://www.nuclear-power.com/nuclear-engineering/fluid-dynamics/flow-regime/laminar-turbulent-flow/, (accessed 25/09/23).
88. O. Reynolds, *Philosophical Transactions of the Royal Society of London*, 1883, **174**, 935-982.
89. A. Sommerfeld, *International Congress of Mathematicians*, 1908, **3**, 116–124.
90. B. E. Rapp, in *Microfluidics: Modelling, Mechanics and Mathematics*, ed. B. E. Rapp, Elsevier, Oxford, 2017, DOI: https://doi.org/10.1016/B978-1-4557-3141-1.50009-5, pp. 243-263.
91. *DOE Fundermentals Handbook - Thermodynamics, Heat Transfer, and Fluid Flow*, U.S. Department of Energy, 1992.
92. C. C. Miller, *Proceedings of the Royal Society of London. Series A, Containing Papers of a Mathematical and Physical Character*, 1924, **106**, 724-749.
93. W. R. Dean, *The London, Edinburgh, and Dublin Philosophical Magazine and Journal of Science*, 1927, **4**, 208-223.
94. H. Fellouah, C. Castelain, A. Ould El Moctar and H. Peerhossaini, *European Journal of Mechanics - B/Fluids*, 2006, **25**, 505-531.
95. N. Nivedita, P. Ligrani and I. Papautsky, *Scientific Reports*, 2017, **7**, 44072.
96. A. D. Stroock, S. K. W. Dertinger, A. Ajdari, I. Mezić, H. A. Stone and G. M. Whitesides, *Science*, 2002, **295**, 647-651.
97. L. Y. Yeo, H. C. Chang, P. P. Y. Chan and J. R. Friend, *Small*, 2011, **7**, 12-48.
98. S. Scott and Z. Ali, *Micromachines*, 2021, **12**, 319.

99. C. R. Friedrich and M. J. Vasile, *Journal of Microelectromechanical Systems*, 1996, **5**, 33-38.
100. Z. Isiksacan, M. T. Guler, B. Aydogdu, I. Bilican and C. Elbuken, *J Micromech Microeng*, 2016, **26**, 035008.
101. J. Tu, Y. Qiao, H. Feng, J. Li, J. Fu, F. Liang and Z. Lu, *RSC Advances*, 2017, **7**, 31603-31609.
102. A. Muck, J. Wang, M. Jacobs, G. Chen, M. P. Chatrathi, V. Jurka, Z. Výborný, S. D. Spillman, G. Sridharan and M. J. Schöning, *Analytical Chemistry*, 2004, **76**, 2290-2297.
103. S. Metz, R. Holzer and P. Renaud, *Lab on a Chip*, 2001, **1**, 29.
104. M. A. Holden, S. Kumar, E. T. Castellana, A. Beskok and P. S. Cremer, *Sensors and Actuators B: Chemical*, 2003, **92**, 199-207.
105. K. Jo, Y.-L. Chen, J. J. De Pablo and D. C. Schwartz, *Lab on a Chip*, 2009, **9**, 2348.
106. F. Y. Ushikubo, F. S. Birribilli, D. R. B. Oliveira and R. L. Cunha, *Microfluidics and Nanofluidics*, 2014, **17**, 711-720.
107. S.-Y. Teh, R. Lin, L.-H. Hung and A. P. Lee, *Lab on a Chip*, 2008, **8**, 198.
108. T. S. Kaminski, O. Scheler and P. Garstecki, *Lab on a Chip*, 2016, **16**, 2168-2187.
109. P. Rodriguez‐Mateos, B. Ngamsom, C. E. Dyer, A. Iles and N. Pamme, *ELECTROPHORESIS*, 2021, **42**, 2246-2255.
110. J. Zhang, S. Yan, R. Sluyter, W. Li, G. Alici and N.-T. Nguyen, *Scientific Reports*, 2014, **4**.
111. E. E. Tsur, *Annual Review of Biomedical Engineering*, 2020, **22**, 285-307.
112. J. N. Lee, C. Park and G. M. Whitesides, *Analytical Chemistry*, 2003, **75**, 6544-6554.
113. P. M. Van Midwoud, A. Janse, M. T. Merema, G. M. M. Groothuis and E. Verpoorte, *Analytical Chemistry*, 2012, **84**, 3938-3944.
114. I. Oita, H. Halewyck, B. Thys, B. Rombaut, Y. Vander Heyden and D. Mangelings, *Analytical and Bioanalytical Chemistry*, 2010, **398**, 239-264.
115. A. A. S. Bhagat, H. Bow, H. W. Hou, S. J. Tan, J. Han and C. T. Lim, *Medical & Biological Engineering & Computing*, 2010, **48**, 999-1014.
116. A.-G. Niculescu, D. E. Mihaiescu and A. M. Grumezescu, *International Journal of Molecular Sciences*, 2022, **23**, 8293.
117. R. Chauhan, N. Minocha, P. Coliaie, P. G. Singh, A. Korde, M. S. Kelkar, M. Langston, C. Liu, N. Nazemifard, D. Patience, D. Skliar, N. K. Nere and M. R. Singh, *Chemical Engineering Research and Design*, 2023, **197**, 908-930.
118. S. N. Bhatia and D. E. Ingber, *Nature Biotechnology*, 2014, **32**, 760-772.
119. P. S. Dittrich and A. Manz, *Nature Reviews Drug Discovery*, 2006, **5**, 210-218.
120. Y. Zhu, Q. Chen, L. Shao, Y. Jia and X. Zhang, *Reaction Chemistry & Engineering*, 2020, **5**, 9-32.
121. M. Guidi, P. H. Seeberger and K. Gilmore, *Chemical Society Reviews*, 2020, **49**, 8910-8932.
122. M. B. Plutschack, B. Pieber, K. Gilmore and P. H. Seeberger, *Chemical Reviews*, 2017, **117**, 11796-11893.
123. K. F. Jensen, *AIChE Journal*, 2017, **63**, 858-869.
124. Modern HPLC Pumps: Perspectives, Principles, and Practices, https://www.chromatographyonline.com/view/modern-hplc-pumps-perspectives-principles-and-practices, (accessed 19/10/2023).
125. Tubular reactor – Part numbers, https://www.vapourtec.com/products/flow-reactors/tubular-reactor-part-numbers/, (accessed 19/10/23).
126. Superdex 200 Increase small-scale SEC columns, https://www.cytivalifesciences.com/en/us/shop/chromatography/prepacked-columns/size-exclusion/superdex-200-increase-small-scale-size-exclusion-chromatography-columns-p-06190, (accessed 19/10/23).
127. M. A. Burns, B. N. Johnson, S. N. Brahmasandra, K. Handique, J. R. Webster, M. Krishnan, T. S. Sammarco, P. M. Man, D. Jones, D. Heldsinger, C. H. Mastrangelo and D. T. Burke, *Science*, 1998, **282**, 484-487.
128. A. B. Wood, S. Plummer, R. I. Robinson, M. Smith, J. Chang, F. Gallou and B. H. Lipshutz, *Green Chemistry*, 2021, **23**, 7724-7730.

129. A. R. Bogdan and N. W. Sach, *Advanced Synthesis & Catalysis*, 2009, **351**, 849-854.
130. M. N. Moore, M. Andrade, A. N. Scozzari and A. H. Krotz, *Organic Process Research & Development*, 2004, **8**, 271-274.
131. Y. Zhu, Z. Huang, Q. Chen, Q. Wu, X. Huang, P.-K. So, L. Shao, Z. Yao, Y. Jia, Z. Li, W. Yu, Y. Yang, A. Jian, S. Sang, W. Zhang and X. Zhang, *Nature Communications*, 2019, **10**.
132. P. Sagmeister, R. Lebl, I. Castillo, J. Rehrl, J. Kruisz, M. Sipek, M. Horn, S. Sacher, D. Cantillo, J. D. Williams and C. O. Kappe, *Angewandte Chemie International Edition*, 2021, **60**, 8139-8148.
133. A. D. Clayton, *Chemistry–Methods*, 2023, DOI: 10.1002/cmtd.202300021.
134. N. Zotova, K. Hellgardt, G. H. Kelsall, A. S. Jessiman and K. K. Hii, *Green Chemistry*, 2010, **12**, 2157.
135. J. De M. Muñoz, J. Alcázar, A. De La Hoz and A. Díaz‐Ortiz, *European Journal of Organic Chemistry*, 2012, **2012**, 260-263.
136. L. Babich, A. F. Hartog, M. A. Van Der Horst and R. Wever, *Chemistry – A European Journal*, 2012, **18**, 6604-6609.
137. D. Dallinger and C. O. Kappe, *Nature Protocols*, 2017, **12**, 2138-2147.
138. R. A. Maurya, K.-I. Min and D.-P. Kim, *Green Chem.*, 2014, **16**, 116-120.
139. Y. Liu, I. Okada and A. Tsuda, *Organic Process Research & Development*, 2022, **26**, 3336-3344.
140. D. Ghislieri, K. Gilmore and P. H. Seeberger, *Angewandte Chemie International Edition*, 2015, **54**, 678-682.
141. S. Chatterjee, M. Guidi, P. H. Seeberger and K. Gilmore, *Nature*, 2020, **579**, 379-384.
142. J. Liang, J. Ruan, B. Njegic, A. Rawal, J. Scott, J. Xu, C. Boyer and K. Liang, *Angewandte Chemie*, 2023, **135**.
143. H.-P. M. De Hoog, I. W. C. E. Arends, A. E. Rowan, J. J. L. M. Cornelissen and R. J. M. Nolte, *Nanoscale*, 2010, **2**, 709.
144. T.-H. Wei, S.-H. Wu, Y.-D. Huang, W.-S. Lo, B. P. Williams, S.-Y. Chen, H.-C. Yang, Y.-S. Hsu, Z.-Y. Lin, X.-H. Chen, P.-E. Kuo, L.-Y. Chou, C.-K. Tsung and F.-K. Shieh, *Nature Communications*, 2019, **10**.
145. K. Liang, R. Ricco, C. M. Doherty, M. J. Styles, S. Bell, N. Kirby, S. Mudie, D. Haylock, A. J. Hill, C. J. Doonan and P. Falcaro, *Nature Communications*, 2015, **6**, 7240.
146. W.-H. Chen, M. Vázquez-González, A. Zoabi, R. Abu-Reziq and I. Willner, *Nature Catalysis*, 2018, **1**, 689-695.
147. J. C. Davis, *Biotechnology and Bioengineering*, 1974, **16**, 1113-1122.
148. X. Yang, L. Hua, H. Gong and S. N. Tan, *Analytica Chimica Acta*, 2003, **478**, 67-75.
149. M. S. Mohy Eldin, H. A. El Enshasy, M. E. Hassan, B. Haroun and E. A. Hassan, *Journal of Applied Polymer Science*, 2012, **125**, 3820-3828.
150. S. J. Novick and J. D. Rozzell, Humana Press, 2005, DOI: 10.1385/1-59259-846-3:247, pp. 247-271.
151. M. Karimi Alavijeh, A. S. Meyer, S. L. Gras and S. E. Kentish, *ACS Sustainable Chemistry & Engineering*, 2020, **8**, 16205-16216.
152. T. Honda, M. Miyazaki, H. Nakamura and H. Maeda, *Chemical Communications*, 2005, DOI: 10.1039/B510605B, 5062-5064.
153. J. T. Cang-Rong and G. Pastorin, *Nanotechnology*, 2009, **20**, 255102.
154. O. A. Mogil'Naya and V. S. Bondar, *Nanotechnologies in Russia*, 2012, **7**, 658-665.
155. F. Zhang, B. Zheng, J. Zhang, X. Huang, H. Liu, S. Guo and J. Zhang, *The Journal of Physical Chemistry C*, 2010, **114**, 8469-8473.
156. J. J. Virgen-Ortíz, J. C. S. Dos Santos, Á. Berenguer-Murcia, O. Barbosa, R. C. Rodrigues and R. Fernandez-Lafuente, *Journal of Materials Chemistry B*, 2017, **5**, 7461-7490.
157. Z.-M. Tang and J.-W. Kang, *Analytical Chemistry*, 2006, **78**, 2514-2520.
158. Z. Tang, T. Wang and J. Kang, *ELECTROPHORESIS*, 2007, **28**, 2981-2987.
159. C. Bourdillon, C. Demaille, J. Gueris, J. Moiroux and J. M. Saveant, *Journal of the American Chemical Society*, 1993, **115**, 12264-12269.

160. T. Matsumoto, Y. Isogawa, T. Tanaka and A. Kondo, *Biosensors and Bioelectronics*, 2018, **99**, 56-61.
161. T. G. M. Schmidt and A. Skerra, *Nature Protocols*, 2007, **2**, 1528-1535.
162. C. M. Niemeyer, L. Boldt, B. Ceyhan and D. Blohm, *Analytical Biochemistry*, 1999, **268**, 54-63.
163. L. Fruk, J. Müller, G. Weber, A. Narváez, E. Domínguez and C. M. Niemeyer, *Chemistry - A European Journal*, 2007, **13**, 5223-5231.
164. A. Burrows, J. Holman, A. Parsons, G. Pilling and G. Price, *Chemistry3*, Oxford University Press, 2013.
165. J. Porath, *Protein Expression and Purification*, 1992, **3**, 263-281.
166. IMAC Resins Selection Guide, https://marvelgent.com/pages/imac-selection-guideline, (accessed 10/10/23).
167. The His-Tag: Fundamentals And Principles, https://cube-biotech.com/knowledge/protein-purification/his-tag/, (accessed 10/10/23).
168. V. Balland, C. Hureau, A. M. Cusano, Y. Liu, T. Tron and B. Limoges, *Chemistry - A European Journal*, 2008, DOI: 10.1002/chem.200800368, NA-NA.
169. J. M. Abad, S. F. L. Mertens, M. Pita, V. M. Fernández and D. J. Schiffrin, *Journal of the American Chemical Society*, 2005, **127**, 5689-5694.
170. R. Blankespoor, B. Limoges, B. Schöllhorn, J.-L. Syssa-Magalé and D. Yazidi, *Langmuir*, 2005, **21**, 3362-3375.
171. H. Xu, B. Wei, X. Liu, Y. Huang, W. Zhou and H. Liang, *Biochemical Engineering Journal*, 2022, **180**, 108362.
172. N. D. J. Yates, M. R. Dowsett, P. Bentley, J. A. Dickenson-Fogg, A. Pratt, C. F. Blanford, M. Fascione and A. Parkin, *Langmuir*, 2019, DOI: 10.1021/acs.langmuir.9b01254.
173. H. P. Erickson, *Biological Procedures Online*, 2009, **11**, 32-51.
174. M. Cvjetko, J. Vorkapić-Furač and P. Žnidaršič-Plazl, *Process Biochemistry*, 2012, **47**, 1344-1350.
175. M.-Y. Lee, A. Srinivasan, B. Ku and J. S. Dordick, *Biotechnology and Bioengineering*, 2003, **83**, 20-28.
176. B. Ku, J. Cha, A. Srinivasan, S. J. Kwon, J.-C. Jeong, D. H. Sherman and J. S. Dordick, *Biotechnology Progress*, 2006, **22**, 1102-1107.
177. A. Rodzik, V. Railean, P. Pomastowski, B. Buszewski and M. Szumski, *Scientific Reports*, 2023, **13**.
178. B. Wouters, B. W. J. Pirok, D. Soulis, R. C. Garmendia Perticarini, S. Fokker, R. S. Van Den Hurk, M. Skolimowski, R. A. H. Peters and P. J. Schoenmakers, *Analytica Chimica Acta*, 2019, **1053**, 62-69.
179. S. Matosevic, N. Szita and F. Baganz, *Journal of Chemical Technology & Biotechnology*, 2011, **86**, 325-334.
180. K. Meller, M. Szumski and B. Buszewski, *Sensors and Actuators B: Chemical*, 2017, **244**, 84-106.
181. J. Křenková and F. Foret, *ELECTROPHORESIS*, 2004, **25**, 3550-3563.
182. J. G. Rivera and P. B. Messersmith, *Journal of Separation Science*, 2012, **35**, 1514-1520.
183. H. Lee, S. M. Dellatore, W. M. Miller and P. B. Messersmith, *Science*, 2007, **318**, 426-430.
184. D. P. Woodruff, *Modern techniques of surface science*, Cambridge University Press, Third edn., 2016.
185. M. Edvardsson, S. Svedhem, G. Wang, R. Richter, M. Rodahl and B. Kasemo, *Analytical Chemistry*, 2009, **81**, 349-361.
186. J. Kou and S. Xu, *Colloids and Surfaces A: Physicochemical and Engineering Aspects*, 2016, **490**, 110-120.
187. A. A. Feiler, A. Sahlholm, T. Sandberg and K. D. Caldwell, *Journal of Colloid and Interface Science*, 2007, **315**, 475-481.
188. W. G. Cady, *Piezoelectricity : an introduction to the theory and applications of electromechanical phenomena in crystals*, McGraw-Hill Book Company, Inc. New York, New York, 1st edn., 1946.

189. M. C. Dixon, *J Biomol Tech*, 2008, **19**, 151-158.
190. G. Sauerbrey, *Zeitschrift für Physik*, 1959, **155**, 206-222.
191. D. Johannsmann, *Physical Chemistry Chemical Physics*, 2008, **10**, 4516.
192. C. Modin, A.-L. Stranne, M. Foss, M. Duch, J. Justesen, J. Chevallier, L. K. Andersen, A. G. Hemmersam, F. S. Pedersen and F. Besenbacher, *Biomaterials*, 2006, **27**, 1346-1354.
193. P. Ekholm, E. Blomberg, P. Claesson, I. H. Auflem, J. Sjöblom and A. Kornfeldt, *Journal of Colloid and Interface Science*, 2002, **247**, 342-350.
194. M. T. Zumstein, H.-P. E. Kohler, K. McNeill and M. Sander, *Environmental Science & Technology*, 2016, **50**, 197-206.
195. S. M. Knudsen, J. Lee, A. D. Ellington and C. A. Savran, *Journal of the American Chemical Society*, 2006, **128**, 15936-15937.
196. X. Wang and V. V. Tarabara, *Chemical Engineering Journal*, 2022, **429**, 132085.
197. G. Liu and G. Zhang, in *QCM-D Studies on Polymer Behavior at Interfaces*, eds. G. Liu and G. Zhang, Springer Berlin Heidelberg, Berlin, Heidelberg, 2013, DOI: 10.1007/978-3-642-39790-5_1, pp. 1-8.
198. A. D. Easley, T. Ma, C. I. Eneh, J. Yun, R. M. Thakur and J. L. Lutkenhaus, *Journal of Polymer Science*, 2022, **60**, 1090-1107.
199. P. W. Atkins and R. Friedman, *Molecular quantum mechanics*, Oxford University Press, Oxford, 4th edn., 2004.
200. Vibrational spectroscopy – Introduction, https://www.chemtube3d.com/vibrational-spectroscopy-introduction/, (accessed 14/09/2023, 2023).
201. A. M. C. Davies, *NIR news*, 2005, **16**, 9-11.
202. P. R. Griffiths, in *Encyclopedia of Analytical Science (Second Edition)*, eds. P. Worsfold, A. Townshend and C. Poole, Elsevier, Oxford, 2005, DOI: https://doi.org/10.1016/B0-12-369397-7/00274-0, pp. 385-402.
203. B. C. Smith, The Carbonyl Group, Part I: Introduction, https://www.spectroscopyonline.com/view/carbonyl-group-part-i-introduction, (accessed 14/09/23).
204. O. Faix, in *Methods in Lignin Chemistry*, eds. S. Y. Lin and C. W. Dence, Springer Berlin Heidelberg, Berlin, Heidelberg, 1992, DOI: 10.1007/978-3-642-74065-7_7, pp. 83-109.
205. B. C. Smith, *Fundamentals of Fourier transform infrared spectroscopy*, CRC press, 2nd edn., 2011.
206. A. A. Ismail, F. R. van de Voort and J. Sedman, in *Techniques and instrumentation in analytical chemistry*, Elsevier, 1997, vol. 18, pp. 93-139.
207. A. Dutta, in *Spectroscopic Methods for Nanomaterials Characterization*, eds. S. Thomas, R. Thomas, A. K. Zachariah and R. K. Mishra, Elsevier, 2017, DOI: https://doi.org/10.1016/B978-0-323-46140-5.00004-2, pp. 73-93.
208. W. G. Golden and D. D. Saperstein, *Journal of Electron Spectroscopy and Related Phenomena*, 1983, **30**, 43-50.
209. E. A. Monyoncho, V. Zamlynny, T. K. Woo and E. A. Baranova, *Analyst*, 2018, **143**, 2563-2573.
210. J. D. Kestell, K. Mudiyanselage, X. Ye, C.-Y. Nam, D. Stacchiola, J. Sadowski and J. A. Boscoboinik, *Review of Scientific Instruments*, 2017, **88**.
211. Bruker PMA50 Flyer EN, https://www.bruker.com/en/products-and-solutions/infrared-and-raman/ft-ir-research-spectrometers/pma50-polarization-modulation-module/_jcr_content/root/sections/more_information/sectionpar/search.download-asset.pdf/55f12122-5df1-4f1c-b836-454031d67950/PMA50_Flyer_EN.pdf, (accessed 14/09/23).
212. D. M. Meier, A. Urakawa and A. Baiker, *Physical Chemistry Chemical Physics*, 2009, **11**, 10132.
213. M. Moskovits, *The Journal of Chemical Physics*, 1982, **77**, 4408-4416.
214. R. Ranjan and M. Trenary, Springer International Publishing, 2023, DOI: 10.1007/978-3-031-07125-6_3, pp. 53-73.

215. W. G. Golden, D. D. Saperstein, M. W. Severson and J. Overend, *The Journal of Physical Chemistry*, 1984, **88**, 574-580.
216. N. Elgrishi, K. J. Rountree, B. D. McCarthy, E. S. Rountree, T. T. Eisenhart and J. L. Dempsey, *Journal of Chemical Education*, 2018, **95**, 197-206.
217. L. R. Faulkner, *Electrochemical methods : fundamentals and applications*, John Wiley, New York ; Chichester, 2nd edn., 2000.
218. G. Jerkiewicz, *ACS Catalysis*, 2022, **12**, 2661-2670.
219. M. R. Hasan, P. Sharma, S. Shaikh, S. Singh, R. Pilloton and J. Narang, *Biosensors*, 2022, **13**, 1.
220. A. R. Harris, D. B. Grayden and S. E. John, *Micromachines*, 2023, **14**, 722.
221. M. Glanc-Gostkiewicz, M. Sophocleous, J. K. Atkinson and E. Garcia-Breijo, *Sensors and Actuators A: Physical*, 2013, **202**, 2-7.
222. E. L. Anderson, B. K. Troudt and P. Bühlmann, *Analytical Sciences*, 2020, **36**, 187-191.
223. R. R. Gagne, C. A. Koval and G. C. Lisensky, *Inorganic Chemistry*, 1980, **19**, 2854-2855.
224. A. M. Bond, K. B. Oldham and G. A. Snook, *Analytical Chemistry*, 2000, **72**, 3492-3496.
225. Cyclic Voltammetry Applications and Uses, https://www.ossila.com/pages/cyclic-voltammetry-applications, (accessed 15/09/2023).
226. Cyclic Voltammetry of Ferrocene, [Ru(bpy)3]2+, [Co(bpy)3]2+ and Iodide http://alpha.chem.umb.edu/chemistry/ch371/documents/7Cyclicvoltammetry.pdf, (accessed 15/09/23).
227. EXPERIMENT 5. CYCLIC VOLTAMMETRY, https://www2.chemistry.msu.edu/courses/cem419/cem372cyclicvoltammetry.pdf, (accessed 15/09/23).
228. A. L. Eckermann, D. J. Feld, J. A. Shaw and T. J. Meade, *Coordination Chemistry Reviews*, 2010, **254**, 1769-1802.
229. E. C. Teague, F. E. Scire, S. M. Baker and S. W. Jensen, *Wear*, 1982, **83**, 1-12.
230. L. Blunt, *Three-dimensional surface topography*, Penton, London, 2nd edn., 2000.
231. How does a spectrophotometer function?, https://www.ssi.shimadzu.com/service-support/faq/uv-vis/instrument-design/1/index.html, (accessed 15/09/23).
232. J. Franck and E. G. Dymond, *Transactions of the Faraday Society*, 1926, **21**, 536.
233. E. Condon, *Physical Review*, 1926, **28**, 1182-1201.
234. J. Johnston and N. Reed, *Modern chemical techniques*, Education Division, Royal Society of Chemistry, 1992.
235. T. G. Mayerhöfer, S. Pahlow and J. Popp, *ChemPhysChem*, 2020, **21**, 2029-2046.
236. R. Bunsen and H. Roscoe, *Annalen der Physik*, 1857, **176**, 43-88.
237. R. Luther and A. Nikolopulos, *Zeitschrift für Physikalische Chemie*, 1913, **82U**, 361-384.
238. A. M. Jones, R. Reed and J. D. B. Weyers, *Practical skills in biology*, Pearson/Benjamin Cummings, Harlow, 4th edn., 2007.
239. Y. Xia and G. M. Whitesides, *Angewandte Chemie International Edition*, 1998, **37**, 550-575.
240. Glass Surface Roughness, https://www.eckop.com/resources/scatterometer-resources/optical-scattering-versus-surface-roughness/, (accessed 01/10.24).
241. Wafer Processing Services, https://www.pi-kem.co.uk/services/wafer-processing-services, (accessed 28/08/24).
242. J.-M. Jung, K. Y. Kwon, T.-H. Ha, B. H. Chung and H.-T. Jung, *Small*, 2006, **2**, 1010-1015.
243. SUEX® Thick Dry Film Sheets (TDFS) Product Data Sheet, https://djmicrolaminates.com/wp-content/uploads/2020/06/Thick-SUEX-Data-Sheet-June-2020.pdf, (accessed 15/09/23).
244. SU-8 2000 Permanent Epoxy Negative Photoresist Datasheet, https://kayakuam.com/wp-content/uploads/2019/09/SU-82000DataSheet2025thru2075Ver4.pdf, (accessed 19/09/23).
245. in *Hybrid Microcircuit Technology Handbook (Second Edition)*, eds. J. J. Licari and L. R. Enlow, William Andrew Publishing, Westwood, NJ, 1998, DOI: https://doi.org/10.1016/B978-081551423-7.50005-5, pp. 63-103.

246. V. K. Johns, P. K. Patel, S. Hassett, P. Calvo-Marzal, Y. Qin and K. Y. Chumbimuni-Torres, *Analytical Chemistry*, 2014, **86**, 6184-6187.
247. What Is A Mask Aligner?, https://www.inseto.co.uk/what-is-a-mask-aligner-ikb-068/, 15/09/23).
248. N. Anscombe, *Nature Photonics*, 2010, **4**, 22-23.
249. M. A. Eddings, M. A. Johnson and B. K. Gale, *J Micromech Microeng*, 2008, **18**, 067001.
250. C. F. Chen and K. Wharton, *RSC Advances*, 2017, **7**, 1286-1289.
251. Guide to Stereolithography (SLA) 3D Printing, https://formlabs.com/uk/blog/ultimate-guide-to-stereolithography-sla-3d-printing/, (accessed 15/09/23).
252. A. C. Brown and D. De Beer, presented in part at the 2013 Africon, 2013.
253. SLA basic finishing steps, https://support.formlabs.com/s/article/SLA-basic-finishing?language=en_US, (accessed 15/09/23).
254. Using Tough 2000 Resin, https://support.formlabs.com/s/article/Using-Tough-Resin?language=en_US, (accessed 24/09/23).
255. *US Pat.,* WO2005016511A1, 2005.
256. *Zeitschrift für Angewandte Chemie*, 1898, **11**, 815-846.
257. A. C. Alting, W. Engels, S. v. Schalkwijk and F. A. Exterkate, *Applied and Environmental Microbiology*, 1995, **61**, 4037-4042.
258. M. Rudden, R. Herman, M. Rose, D. Bawdon, D. S. Cox, E. Dodson, M. T. G. Holden, A. J. Wilkinson, A. G. James and G. H. Thomas, *Scientific Reports*, 2020, **10**.
259. T. Menanteau, M. Dias, E. Levillain, A. J. Downard and T. Breton, *The Journal of Physical Chemistry C*, 2016, **120**, 4423-4429.
260. M. Sheng, D. Frurip and D. Gorman, *Journal of Loss Prevention in the Process Industries*, 2015, **38**, 114-118.
261. K. K. Cline, L. Baxter, D. Lockwood, R. Saylor and A. Stalzer, *Journal of Electroanalytical Chemistry*, 2009, **633**, 283-290.
262. L. Lee, P. A. Brooksby, P. Hapiot and A. J. Downard, *Langmuir*, 2016, **32**, 468-476.
263. I. Mahlooji, M. Shokri, R. Manoochehri, M. Mahboubi‐Rabbani, E. Rezaee and S. A. Tabatabai, *Archiv der Pharmazie*, 2020, **353**, 2000052.
264. Y. Ji, X. Yang, Z. Ji, L. Zhu, N. Ma, D. Chen, X. Jia, J. Tang and Y. Cao, *ACS Omega*, 2020, **5**, 8572-8578.
265. H. A. Alhazmi, M. Al Bratty, A. M. Meraya, A. Najmi, M. S. Alam, S. A. Javed and W. Ahsan, *Acta Biochimica Polonica*, 2021, DOI: 10.18388/abp.2020_5462.
266. R. Lanfranco, J. Saez, D. Abati, T. Carzaniga, F. Benito-Lopez and M. Buscaglia, *Microchimica Acta*, 2021, **188**.
267. R. D. Franklin, J. A. Whitley, A. A. Caparco, B. R. Bommarius, J. A. Champion and A. S. Bommarius, *Chemical Engineering Journal*, 2021, **407**, 127065.
268. Ni Sepharose 6 Fast Flow histidine-tagged protein purification resin, https://www.cytivalifesciences.com/en/us/shop/chromatography/resins/affinity-tagged-protein/ni-sepharose-6-fast-flow-histidine-tagged-protein-purification-resin-p-06004#tech-spec-table, (accessed 15/11/23).
269. Type 6724 data sheet | solenoid valve Whisper Valve with media separation, https://www.burkert.com/en/Media/plm/DTS/DS/ds6724-standard-eu-en.pdf, (accessed 18/11/2023).
270. Chemyx Fusion 4000 Updated Serial Commands, https://www.chemyx.com/downloads/fusion_4000_updated_serial_commands.pdf, (accessed 20/11/23).
271. C. M. Dwivedi, R. C. Ragin and J. R. Uren, *Biochemistry*, 1982, **21**, 3064-3069.
272. M. P. Ferla and W. M. Patrick, *Microbiology*, 2014, **160**, 1571-1584.
273. V. Silverio, S. Guha, A. Keiser, R. Natu, D. R. Reyes, H. Van Heeren, N. Verplanck and L. H. Herbertson, *Frontiers in Bioengineering and Biotechnology*, 2022, **10**.
274. Formlabs Stereolithography 3D Printers Tech Specs, https://formlabs.com/uk/3d-printers/form-3/tech-specs/, (accessed 26/11/23).

275. formlabs - Choosing the right material, https://support.formlabs.com/s/article/Choosing-the-Right-Material?language=en_US#tough-2000, (accessed 26/11/23).
276. Q. Zhao, D. Yuan, J. Zhang and W. Li, *Micromachines*, 2020, **11**, 461.
277. R. G. Duggleby, in *Methods in Enzymology*, Academic Press, 1995, vol. 249, pp. 61-90.
278. H. R. Luckarift, G. R. Johnson and J. C. Spain, *Journal of Chromatography B*, 2006, **843**, 310-316.
279. C. Sanchez-Cano and M. Carril, *International Journal of Molecular Sciences*, 2020, **21**, 1007.